Microstructural analysis of atomic mechanisms of metal plasticity under machining conditions: case study of AISI 1045 steel and 7475 aluminum

Bentejui Medina Clavijo

Supervisors:

Pedro José Arrázola Arriola*

Andrey Chuvilin**

A thesis submitted for the degree of Doctoral Program in Engineering

Mechanical and manufacturing department

Mondragon Unibertsitatea

May 2018

* MGEP, High performance machining group

** CIC NanoGUNE, Electron Microscopy Laboratory

The present thesis would not be possible without the fruitful collaboration between the High-performance machining group, of Mondragon Unibersitatea, and the Electron microcopy laboratory of CIC NanoGUNE.

Declaration of originality

Hereby I, Bentejuí Medina Clavijo

declares, that this paper is my original authorial work, which I have worked out by my own. All sources, references and literature used or excepted during elaboration of this work are properly cited and listed in complete reference to the due source.

“Listen with the intent to understand, not the intent to reply”

Stephen Covey

Acknowledgments

I would like to thank the **Basque Government** for supporting **Micromaquinte** research project, collaboration between **Mondragon Unibertsitatea** and **CIC NanoGUNE**.

I want to express my special thanks to my thesis supervisors **Prof. Dr. Pedro Jose Arrázola**, leader of the High-Performance Machining group at Mondragon Unibertsitatea, and **Prof. Dr. Andrey Chuvilin**, leader of the Electron Microscopy group at CIC NanoGUNE, for giving me the opportunity to work in this research project, for their support and for productive discussions.

I gratefully acknowledge **Christopher Tollan** for the daily support to this thesis. This work would not be possible without all his help and advises in the laboratories. I also want to thank **Mikel Saez de Buruaga Echeandia** and **Daniel Soler** for the work and time spent in our common projects.

Furthermore, I thank to my colleague **Jörg** for the support on the writing of the thesis, advises and informal discussions. I also thank **Alexander** for the advises and interesting scientific discussion.

Very special thanks to Lisa for all the motivation and daily support over these three years. I appreciate the encouragement transmitted to complete this research work.

Finally, I would like to express my thanks to my parents and my sister, as without their support and advises this thesis would not be possible.

Table of Contents

Index of figures

Index of tables

Symbols

Machining

Symbol	Nomenclature	Units
F_{sh2}	Normal force according to the shear layer of SSZ	N
F_{sh1}	Normal force according to the shear layer of PSZ	N
N_{sh2}	Normal force according to the shear layer of SSZ	N
N_{sh1}	Normal force according to the shear layer of PSZ	N
A	Area	m^2
$\emptyset$	Shear angle of the PSZ	(º)
A_f	Area of material uncut (for Kc calculations)	mm^2
a_p	Depth of cut	mm
F_n	Force normal to a surface	N
F_t	Force tangential to a surface	N
F_c	Cutting force	N
F_f	Feed force	N
t_1	Feed per revolution	mm/rev
t_2	Chip thickness	mm
K_c	Specific cutting enery	N/mm^2
l_c	Contact length	mm
R	Resultant Stress	Pa
r	Tool tip radius	µm
T	Temperature	ºC
V_c	Cutting speed	m/min
α	Clearance angle	(º)
ε	Strain	-
γ	Rake angle	(º)

Material recrystallization

Symbol	Nomenclature	Units
σ	Stress	Pa
τ	Material shear modulus	Pa
θ	Rotation of a subgrain	(º)
γ	Surface energy of a grain	J/m^2
δ	Grain boundary thickness	m
L	Length of the grain face	m
k	Boltzmann constant	J/K
R	Gas constant	J/K·mol
Q	Activation energy for grain boundary diffusion	J/mol
D	Grain boundary diffusion coefficient	m^2/s

Abstract

The goal of this PhD thesis is discovering the potential of nanostructure characterization for revealing atomic mechanisms of metal plasticity under machining conditions. This approach has been used to reconstruct the phenomena in the tool-chip contact by a composite study of chips utilizing advanced microscopy techniques in combination with a fundamental description of plasticity. There are collected multiple evidences for existence of two qualitatively different cutting regimes in orthogonal machining of annealed AISI-1045 steel with uncoated P15 carbide cutting tool in dry conditions at cutting speed between 5 and 200 m/min. These regimes are characterized by two different phenomena controlling the tool-chip contact, i.e. severe plastic hardening at low velocities, and dynamic recrystallization at high speed. This last phenomenon has induced a structure in the tool-chip contact area with unique properties. Morphological, chemical and mechanical studies have revealed a nanostructured material with shifted properties in comparison with the original material.

The analysis of previously cut chips provides an average picture of the mechanisms that govern tool-chip contact. However, some aspects like grain orientation and microstructural features may have differentiated roles. Hence, the analysis of the cut over individual features could feed a deeper understanding of metal cutting. In order to address this, the present thesis studies the potential of direct observation of the machining process in high-magnification microscopes. For that, a device to perform lineal cutting of aluminum inside an electron microscope's vacuum chamber has been designed and constructed. Based on this device, experiments of machining in-situ have been successfully performed, shown a coherent chip generation. First results have shown that the crystallographic orientation may increase the layer of material deformed under the cutting tool. Furthermore, experiments of cutting in the sub-micrometer regime has demonstrated that this layer is proportionally larger in smaller cuts, consequence of a deeper tool-chip interaction in comparison with macroscopic cutting.

At deeper scales, a method for simulations down to the atomic level has been proposed to model machining. This initiative relies in the capability of atomistic simulations to reproduce the mechanisms of plasticity that govern the deformation of crystalline materials, like dislocations and grain boundary effects, which cannot be reproduced by other techniques based on continuum mechanics. In this study a set of molecular dynamics simulations in different conditions of tool-chip friction and feed size have been carried out. The results have shown the effects of localized recrystallization observed experimentally, largely dependent on the friction with the tool. Moreover, it has been observed that a large friction value reduces the mobility of the atoms up to certain distance to the tool. This produces a gradient of

velocities in the proximity of the cutting edge, thus supporting the appearance of specific deformations mechanisms in the area of contact.

In summary, the present work describes the mechanics of machining based on different atomic mechanisms of plasticity, what has been afforded by experimental and simulation approaches. In addition, this thesis provides new methodologies for the research of the cutting process, with potential application to study other conditions and materials of interest.

Resumen

El objetivo de esta tesis de doctorado es investigar el potencial de la caracterización de la nanoestructura para revelar los mecanismos atómicos de plasticidad en metales presentes en condiciones de mecanizado. Esta aproximación ha sido usada para reconstruir los fenómenos en el contacto viruta-herramienta mediante un estudio de las virutas utilizando técnicas avanzadas de microscopía en combinación con la descripción atomística fundamental de la plasticidad. Se han recolectado varias evidencias de la existencia de dos regímenes de corte cualitativamente diferentes durante el mecanizado ortogonal de acero recocido AISI 1045 con herramientas de corte de carburo P15 sin lubricación a velocidades de corte entre 5 y 200 m/min. Estos regímenes están caracterizados por dos fenómenos distintos controlando el contacto viruta-herramienta, i.e., endurecimiento plástico severo a baja velocidad, y recristalización dinámica a alta velocidad. Este último fenómeno ha inducido una estructura única en la zona de contacto con propiedades. Estudios morfológicos, químicos y mecánicos han revelado un material nanoestructurado con propiedades diferentes en comparación con el material de origen.

El análisis de virutas previamente cortadas proporciona una imagen general del mecanismo que gobierna el contacto viruta-herramienta. Sin embargo, algunos aspectos particulares como la orientación del grano y otros elementos microestructurales podrían tener roles diferenciados. Por tanto, el análisis del corte sobre determinados elementos microestructurales puede alimentar un entendimiento más profundo del corte en metales. Para abordar esto, esta tesis estudia qué potencial proporciona una observación directa del mecanizado en microscopios de alta magnificación. Para ello, se ha diseñado y construido un dispositivo para el corte lineal de aluminio dentro la cámara de vacío de un microscopio electrónico. Este dispositivo se ha mostrado satisfactorio para realizar experimentos de corte in-situ. Los primeros resultados han mostrado que la orientación cristalográfica puede influir en la capa de material deformada bajo la herramienta de corte. Más aún, el análisis del corte en el régimen submicrométrico ha demostrado que esta capa es proporcionalmente más grande en cortes pequeños, consecuencia de una interacción viruta-herramienta más profunda que a escalas macroscópicas.

A una escala inferior, se ha propuesto un método de simulación a escala atómica para modelizar el mecanizado. Esta iniciativa responde a la capacidad de las simulaciones atomísticas para reproducir los mecanismos de plasticidad que gobiernan la deformación de los materiales cristalinos, como las dislocaciones y los efectos de bordes de grano. Efectos que no pueden ser reproducidos por otras técnicas basadas en mecánica continua. En el presente estudio se ha efectuado una serie de simulaciones de dinámica de moléculas en

diferentes condiciones de fricción y avance. Los resultados han mostrado los efectos de recristalización localizada observados experimentalmente, altamente dependientes de los valores de fricción. Más aún, se ha observado que una alta fricción reduce la movilidad de los átomos alrededor de la herramienta hasta cierta distancia. Esto crea un gradiente de velocidades en el área cercana al borde de corte, conllevando por tanto la aparición de mecanismos de deformación específicos en el área de contacto.

En resumen, esta tesis describe la mecánica del mecanizado basándose en diferentes mecanismos de plasticidad a nivel atómico, tanto con experimentos como con simulaciones. Además, en este trabajo se describen nuevas metodologías para el estudio del proceso de corte con potencial uso en otras condiciones y materiales de interés.

Laburpena

Doktoretza tesi honen helburua da, nanoegituren karakterizazioak mekanizazio baldintzetan metalen plastikotasun mekanismo atomikoak bistaratzeko duen potentziala ikertzea da. Estrategia hau erabili da txirbil-erreminta kontaktuan ematen diren fenomenoak berreraikitzeko. Txirbilak mikroskopiako teknika aurreratuak nahiz plastikotasunaren oinarrizko deskribapen atomistikoak erabiliz aztertu dira. Kualitatiboki desberdinak diren bi ebaketa erregimenen existentzia erakusten duten zenbait ebidentzia bildu dira. Honetarako, AISI 1045 altzairu galbanizatuaren mekanizatu ortogonala aztertu da P15 karburozko ebaketa erreminta lubrikatzailerik gabe eta 5 eta 200 m/min arteko ebaketa abiaduran erabiliaz. Erregimen hauek bi fenomeno desberdinen bitartez karakterizatuak daude txirbil-erreminta kontaktua kontrolatuaz, hots, abiadura baxuko plastiko gogortze larria eta abiadura handiko ber-kristalizazio dinamikoa. Azken fenomeno honek ezaugarri bereziak dituen estruktura bat induzitu du kontaktu zonan. Azterketa morfologiko, kimiko eta mekanikoek erakutsi dute material nanestrukturatu berri honek oinarrizko materialarekin alderatuz ezaugarri desberdinak dituela.

Aurretik ebakitako txirbilen azterketak txirbil-erreminta kontaktuan parte hartzen duten mekanismoen informazio orokor bat ahalbidetzen du. Aldiz, beste zenbait aspektuk eragin desberdinduak izan ditzakete; hala nola, grano edo beste elementu mikroestrukturatu batzuen orientazioak. Beraz, zenbait mikroestrukturatutako elementuren ebaketen azterketak metalen ebaketaren inguruko ulermen maila sakonago bat ahalbidetu dezake. Hau dela eta, tesi honek handitze altuko mikroskopio bidezko behaketa zuzenak ze potentzial eskaintzen duen aztertzen du. Honetarako, gailu berezi bat diseinatu eta eraiki da, zeinak elektroi bidezko mikroskopio batetako huts ganbera batean aluminioaren ebaketa lineala egitea ahalbidetzen duen. Dispositibo honetan in-situ esperimentuak egin ahal izan dira. Lehen emaitzek erakutsi dute orientazio kristalografikoak ebaketa erremintaren azpiko deformaturiko material geruzan eragina izan dezakeela. Are gehiago, erregimen azpi-mikrometrikoko ebaketaren analisiak frogatu du material geruza hau proportzionalki handiago dela ebaketa txikietan, ebaketa makroskopikoekin alderatuta txirbil-erreminta interakzioa sakonagoa delako.

Eskala txikiago batean, eskala atomikoko simulazio metodo bat proposatu da mekanizatua modelizatzeko. Simulazio atomistikoek material kristalinoen deformazioa zehazten duten plastikotasun mekanismoak erreproduzitzeko gaitasuna dute, esaterako, ihardukitzeak eta grano hertz efektuak. Efektu hauek ezin dira erreproduzitu mekanika jarraian oinarritutako beste teknikekin. Lan honetan, marruskadura eta aitzinamendu egoera desberdinetako molekulen dinamikak simulatu dira. Emaitzek esperimentalki ikusitako ber-

kristalizazio lokalizatuko efektuak erakutsi dituzte, zeinak marruskadura baloreekiko oso menpekoak diren. Are gehiago, marruskadura altu batek erremintaren inguruko atomoen mugikortasuna gutxitzen duela ikusi da, distantzia jakin batera arte. Honek, ebaketa hertzaren gertuko zonan abiadura gradiente bat sortzen du, kontaktu gunean deformazio mekanismo espezifikoak sortuz.

Laburbilduz, tesi honek mekanizatuaren mekanika deskribatzen du maila atomikoko hainbat plastikotasun mekanismotan oinarrituta, esperimentu nahiz simulazio bidez. Horrez gain, lan honetan ebaketa prozesuaren azterketarako metodologia berriak deskribatzen dira, zeinak beste material nahiz baldintzetan erabilgarri izan daitezkeen.

1 Introduction

The goal of this PhD thesis is discovering the potential of nanostructure characterization for revealing atomic mechanisms of metal plasticity under machining conditions.

Fundamentally, machining is a process in which parts are fabricated removing material by the action of a cutting tool. The extensive use of machining techniques started in the so-called “Machine age” (1880-1945), and it has been under development since that times. Nowadays, machining is treated as a high-quality finishing technique. According to Eurostat (2016), machining represents one of the most added-value manufacturing methods for quality metal components (Figure 1-1).

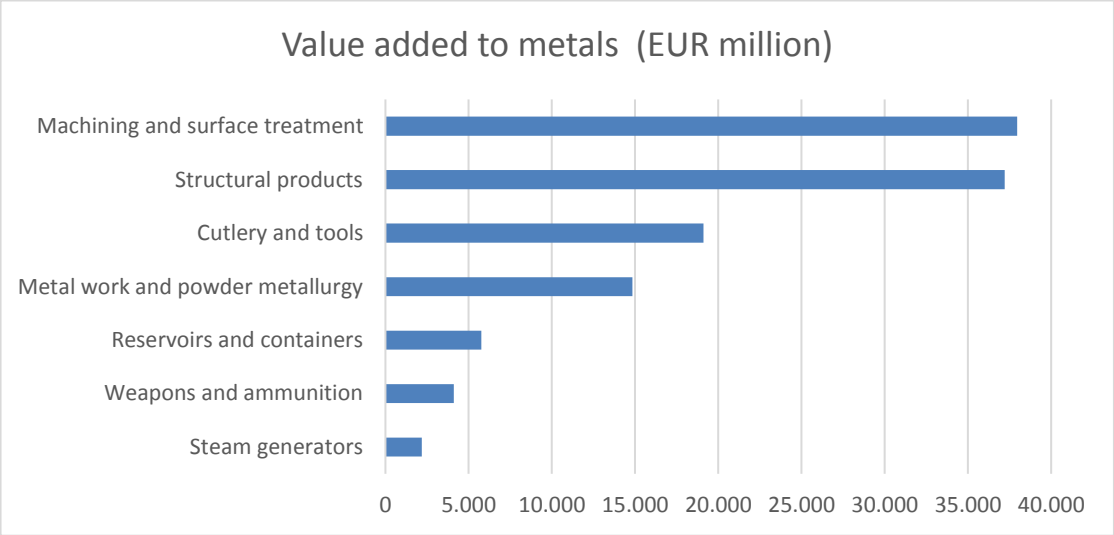

Figure 1-1 Manufacture of fabricated metal products. The blue bars indicates value added (Eurostat, 2016).

The added value of machining is related to the accurate control of this manufacturing method. Three technical aspects are of particular relevance in the manufacture by machining: high dimensional precision, material integrity and quality finishing. These aspects have pushed machining to be the manufacturing technique of entire parts and moreover, to be an essential assisting method for most of others which are unable to provide necessary precision and finishing.

Today, the world production value of machining reachs 80 billion ($8 \cdot 10^{10}$) euros each year. This economic relevance in the worldwide manufacture market leads to a significant research founding. At this regard, much effort has been done in different aspects of machining. As it is an added value technique, any of the parts involved are carefully treated, both the quality of the fabricated parts and the energy cost of the whole technique.

In the manufacturing of metal parts by machining, most of the energy cost is generated in the cutting process itself. This process is performed by the action of a hard tool, which removes material of the workpiece surface layer by layer to constitute the final shape. In this process material is removed by a mechanical shear induced through the cutting edge. Hence, the action of cutting is governed by the tool-workpiece interaction. This interaction is controlled by the material in the close proximity to the cutting edge, which suffers particular conditions of stress and temperature, which may affect energy consumption, parts quality and tool wear. Thus, understanding of these processes at the tip is the key for increasing the efficiency of the whole industry.

During machining, material hits the tool at velocities over 1 m/s and deforms more than 100 % in a fraction of millisecond, this happening locally in front of the tool edge. Such conditions have represented a major challenge in terms of phenomena understanding. This has pushed some of the research effort to a cause-effect methodology, which have been of great help for detecting the influence of input parameters in the machined parts. More recently, successive advances in materials characterization techniques have facilitate the investigation of the microscopic details involved in metal cutting, thus giving access progressively to the phenomena of tool-workpiece interaction and chip generation. This last aspect has kept much attention, since it has been pointed that most of the machining energy is indeed spent in the chip generation. Thus, while the chip is wasted during the cutting process, chip generation analysis is an aspect of major importance.

The process of chip generation, and particularly the contact between the cutting tool and the chip of material, has been matter of huge research effort. This part of the chip contains the so-called secondary shear zone (SSZ). In this zone the mechanism of tool-chip friction is developed, where the largest values of temperatures are reached, and where the material suffer extreme values of strain-rate (up to 10^5 s^{-1}). In addition, it is also the less accessible area for experimental observations. Thus, while tool-chip contact understanding is experimentally hampered, the phenomena occurring in this area is still matter of much attention.

In the last decades there has been a continuous request of techniques and methodologies to structurally characterize the traces of material's fiction produced during machining. However, a full development of these methodologies is still a work in progress in many cases. Recently, a few authors have pioneered the reconstructive study of chip microstructure. At this regard, Courbon et al. have observed that the friction between tool and chip induces microstructural changes in the SSZ (Courbon et al. 2013). These changes point out that certain mechanisms of plasticity are activated in this region, which may offer valuable

information about the conditions of the material during cutting. Experiments with the same material carried out by Kümmel et al. (2014) have reported a different microstructural behavior in the same region, thus pointing that different mechanisms of plasticity could be activated depending on the cutting conditions. Thus, a microstructural analysis in terms of plasticity could shed light on the phenomena of tool-chip interaction.

The present work approaches the disclosure of the tool-chip contact processes by a reconstructive analysis of the material nanostructure present in material in close contact with the tool. Based on a structural study utilizing advanced microscopy techniques in combination with the fundamental atomistic description of metals plasticity, the phenomena in the SSZ will be investigated.

The analysis of previously cut chips provides an average picture of the mechanisms that govern tool-chip contact, while some aspects like grain orientation and boundaries may play a role. Hence, the analysis of individual material features could feed a deeper understanding the behavior. In order to address it, this thesis studies the potential of direct observation of metal cutting in a scanning electron microscope. For that, a device to perform linear cutting inside an electron microscope's vacuum chamber will be designed and constructed. Based on this device, experiments of machining in-situ in an electron microscope have been performed.

At deeper scales, a method for simulations down to the atomic level will be proposed to model machining. The purpose of this initiative relies in capability of atomistic simulations to reproduce the mechanisms of plasticity that govern the deformation of crystalline materials, like dislocations and grain boundary effects. These effects cannot be reproduced by other techniques based on continuum mechanics, what motivates approaching machining by a model based on individual atoms. This will be carried out by a set of molecular dynamics simulations in different conditions in the tool-chip contact.

This thesis focuses on structural steel and aluminum, materials with two distinct strengthening mechanisms. On the one hand, it has been selected AISI 1045 steel, an alloy with large industrial significance, widely used for machine building. The strengthening mechanism in this case relies in the composite structure of hard (pearlite) and soft (ferrite) phases. On the other hand, aluminum 7475 is of particular importance as a low-density material, which is commonly used for fabrication of aeronautic parts. In this case, the material develops strengthening by homogeneous precipitation of intermetallic particles.

These aspects are organized in this thesis through the following chapters structure:

Chapter 2 gives the fundamentals and terminology of the research areas covered in this thesis and provides a literature review and the state of the art. This chapter provides basics about the machining technique, steel and aluminum alloys and atomic mechanisms of metal plasticity. Then, the state of the art focuses on investigations correlating the metal plasticity involved in machining, following by the progress of in-situ cutting in electron microscopes, and subsequently points the most relevant research of machining simulations by molecular dynamics. Finally, they are provided conclusions of the review, and the motivation.

Chapter 3 defines the methods of use during this thesis to characterize materials. Optical microscopy, electrons microscopy (SEM, EBSD, FIB EDX) as well as mechanical techniques (nanoindentation, pillar compression and beam bending) are described here. Then, the equipment and setup used for macroscopic metal cutting is explained. Lastly, an initial characterization and properties of the materials of use during this thesis will be provided.

Chapter 4 represents a composite mechanical and structural study of the high speed dry orthogonal cutting of annealed AISI-1045 steel with uncoated P15 carbide cutting tool, typical combination in the industry. This study focuses on experimental evidences which in last decades have suggested the existence of different cutting regimes at increasing machining speed. In this chapter mechanical tests confirms such evidences with a sharp transition accordingly expressed in cutting characteristics. The microstructural characterization of the chips, generated at different velocities, will be used to disclose the governing mechanisms of plasticity that controls chip generations on each regime.

In chapter 5 a material generated in SSZ is subject of an extensive study. Due to its very specific micro/nano structure developed in the conditions of high strain and temperature, its mechanical properties are of particular interest, especially because similar material defines the finishing of the workpiece surface. This may affect the behavior of machined parts, since the characteristics of the surface can affect strength and fatigue resistance. To determine the properties of this layer of 10 µm of thickness it has been performed a localized chemical, microstructural and mechanical analysis by means of electron microscopy, nanoindentation and pillar/beam testing.

Chapter 6 covers the design, construction and proof of concept use of a plain cutting device for in-situ cutting directly in a scanning electron microscope (SEM). This device allows for high-magnified visualization of the tool-chip interaction in-line with imaging of the grain structure of the workpiece and measurement of the cutting force. Along with initial experimental data in aluminum, we also discuss theoretical aspects of downscaling of the tool-chip interface from 10 µm of feed in industrial cutting to 200 nm in in-situ setup, and thus

evaluate an applicability of the in-situ obtained data for up-scaling. In this task aluminum suits for micro-cutting due to its homogeneity, which leads to forces of cut relatively low and stable. In addition, aluminum alloys induce low wear in the micro-tool.

Chapter 7 addresses specific aspects for the application of molecular dynamics (MD) for the cutting process. Traditionally finite elements methods are used for machining simulations and provide a vast of crucial information about the process parameters not accessible experimentally. Nevertheless, this method based on continuum mechanics is agnostic to the mechanisms of plasticity in crystalline matter and requires proper parametrization. In turn, MD does not require knowledge of macroscopic properties of materials, but rather derives these properties based on calculations of individual atoms, whose trajectories are determined by the Newton's law of motion and where forces are calculated using interatomic potentials. Though this approach ignores the quantum nature of atoms, it can approach a large fraction of the lattice phenomena. Application of MD for simulation of processes of metal plasticity is to a large extend limited by the high computational cost. Here we explore the approaches to optimize MD simulations on aluminum, underline the new atomistic understanding of tool-workpiece interaction and relate the results of simulations to macroscopic parameters.

In summary, the present work describes the mechanics of machining based on the atomic mechanisms of plasticity, what is afforded by experimental and simulation approaches. Microstructural aspects of tool-chip contact are investigated by electron microscopy techniques, ex-situ and in-situ, with the emphasis in the non-continuum phenomena that govern the interaction. Furthermore, the micro-mechanics of the unique resultant structure is evaluated by a complex composite study. Finally, a new simulation approach is proposed to deep in the understanding of chip generation accordingly to mechanics of atoms interaction.

It should be remarked that the present PhD thesis is enrolled in the project **MICROMAQUINTE** (acronym of: estudio de la influencia de la MICROestructura de aceros y superaleaciones base níquel en la MAQUinabilidad e INTEgridad superficial de componentes mecanizados), funded by the **Basque Government** (Departamento de Educación, Política Lingüística y Cultura).

2 Fundamentals and literature review

This chapter describes fundamental aspects of machining, metal alloys, and mechanisms of material plasticity. Subsequently, attention is paid to connect these fundamentals with recent research concerning metal cutting.

In the first section, the machining technique and an overview of common research approaches are briefly introduced. A further section concentrates on microstructural aspects of steel and aluminum alloys. The third section shows fundamentals of mechanics of plasticity of crystalline materials. The most recent research works on linking metal plasticity and machining is presented in the fourth section. Section five is devoted to the recent effort on performing cutting experiments in-situ in an electron microscopy. Finally, conclusions of the literature review and thesis motivation are proposed.

2.1 The machining technique

Machining is a process in which a cutting tool is used to remove small chips of material from the working piece (often called “workpiece” or "work"). To perform the operation, relative motion is required between the tool and the workpiece. This relative motion is achieved in most machining operation by means of a primary motion, called "cutting speed" and a secondary motion called "feed per revolution" (often called “feed”). The shape of the tool and the feed size, combined with the system motions, determine the resulting workpiece surface.

The cutting process mechanism during machining refers to a process where part of the material is separated by shear from the workpiece surface. This mechanism involves material deformation work in the three dimensions of space (3D). However, in order to reduce the complexity of the problem, in certain conditions orthogonal cutting can be represented by a two-dimensional (2D) problem, as shown in Figure 2-1. This simplification is considered to be accurate enough for making a representative analysis of the cutting process when the depth of cut (“a_p” in Figure 2-1) is 10 times larger than the feed per revolution (“t_1” in Figure 2-1) (Arrazola et al. 2005). In that circumstances, the material in the center of the chip suffers plain deformation, and the material flow is well described by a 2D model.

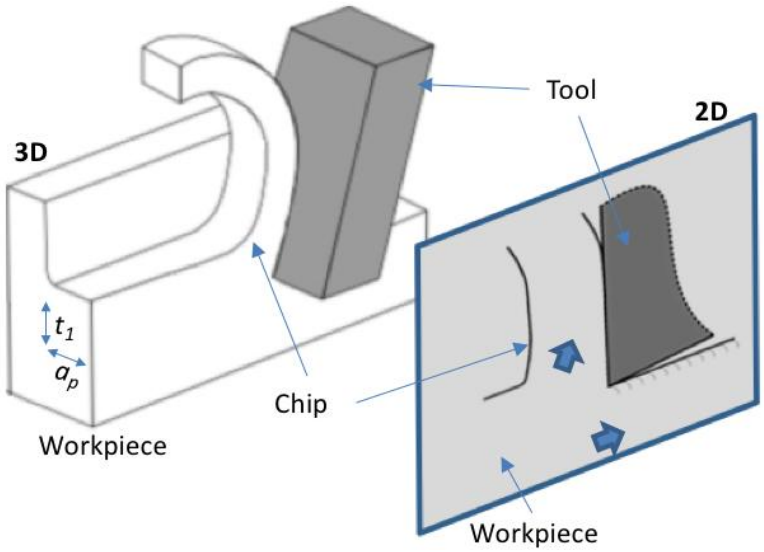

Figure 2-1 3-dimensional (3D) and 2-dimensional (2D) representation of metal cutting.

The 2D model has been widely used for an analytical approach of metal cutting. The sketch in Figure 2-2 depicts the most important variables of the model, where t_1 and t_2 are respectively feed and chip thickness, ϕ is the shear angle of the thin layer, and γ is the angle of the chip-tool sliding face of the tool, known as the rake face. The total machining force R can be decomposed into the cutting force F_c and the feed force F_f. Nevertheless, R can be

decomposed according other criteria, F_{sh1} and N_{sh1} according to the shear layer in the primary shear zone (PSZ) from the tool edge to the free surface, and F_{sh2} and N_{sh2} according to the shear layer in the SSZ. When applying the minimum energy to the workpiece-tool system (Ernst and Merchant 1941; Merchant 1945), the cutting force can be approximated by Equation 2-1, and the material shear angle by Equation 2-2.

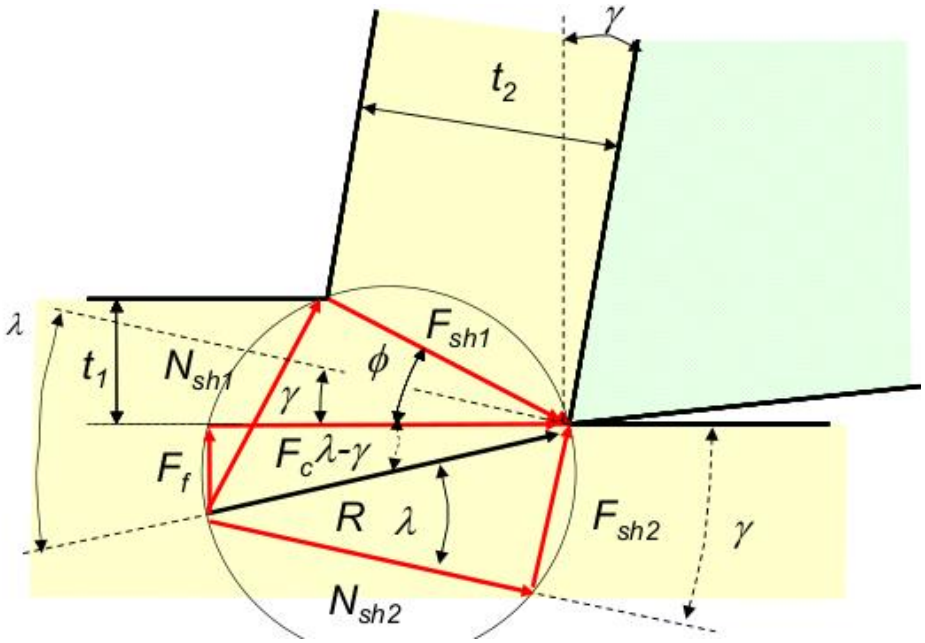

Figure 2-2 Sketch of orthogonal cutting. Cut of a layer of material t_1, and chip with thickness t_2. The total force of cutting R is decomposed into F_c and F_f according to workpiece axis, F_{sh1} and N_{sh1} according to the shear layer in the PSZ, or F_{sh2} and N_{sh2} according to the shear layer in the SSZ.

$$F_c = \frac{a_p \cdot t_1 \cdot \tau}{sin\emptyset} \cdot \frac{cos(\lambda-\gamma)}{\cos(\emptyset+\lambda-\gamma)} \qquad \text{Eq. 2-1}$$

$$\emptyset = \frac{\pi}{4} - \frac{\lambda-\gamma}{2} \qquad \text{Eq. 2-2}$$

where a_p is the depth (width) of cut, τ is the material shear modulus, and λ is the angle between the total machining force R and N_{sh2}.

In order to resolve the model of Merchant, given by Equations 2-1 and 2-2, an initial cutting test on the material has to be done measuring both forces and chip geometry. Such test should be made for each couple material / cutting-parameters in order to make further calculations (that are valid only in that system).

The model presented above requires some simplifying assumptions: thin shear zone, continuous chip generation and homogeneous properties of the chip material. However, while Merchant's model could approximate real problems, the shear mechanism, chip shape and material properties differ widely from the ones proposed. This is in part consequence of the

very specific conditions that the material suffers during machining. The existence of a restricted area where most of the deformation work is done entails large strain ratios present only there. This process occurs typically in a fraction of a second. Thus, the kinetics of material response plays a major role during machining.

- **Kinetics of machining**

In terms of production, the fabrication of machined parts involves two key aspects, the machinability and the surface integrity of the fabricated parts (workpiece). Machinability is related to the productivity, i.e. parts fabricated per journey, energy consumption, the wear of the cutting tools and the overall cost needed along the manufacturing process. On the other hand, the surface integrity is related to the quality of the parts, i.e. dimensional accuracy, fatigue life and visual aspect. Experimentally, typically both machinability and surface integrity obtain benefit from medium and large cutting speeds. Thus, kinetics strongly determines the mechanisms involved in material removal.

Comparing to other techniques, the industrial process of machining leads to very specific deformation conditions, i.e. high temperature and high strain rates, which both affect the response of the material. Under these conditions the classical knowledge about the microstructure and material strength might be not useful, as long as the kinetics and the temperature change the deformation mechanisms of metals (Ashby, 1979).

Table 2-1 shows different working conditions depending on the mechanical treatment. There are some remarkable differences between them, particularly in terms of kinetics. The strain-rate developed during machining stays one order of magnitude over any other technique, what makes this technique unique.

Table 2-1 The conditions of metal forming (Frost and Ashby 1982)

	True strain (range)	*Velocity range (m/s)*	*Strain rate range (s^{-1})*	*Temperature range*
Cold working (rolling, forging,)	0.1→0.5	0.1→100	1→2 x 10^3	298 K (slight adiabatic heating)
Wire drawing (sheet, tube drawing)	0.05→0.5	0.1→100	1→2 x 10^4	298 K to 0.3 T_M (adiabatic heating)
Explosive forming	0.05→0.2	10→100	10→10^3	298 K
Machining	~ 1	0.1→100	10^2→10^5	298 K to 0.5 T_M (adiabatic heating)
Warm working (rolling, forging)	0.1→0.5	0.1→30	1→10^3	0.35→0.5 T_M
Hot working (rolling, forging,)	0.1→0.5	0.1→30	1→10^3	0.55→0.85 T_M
Extrusion	~ 1	0.1→1	0.1→10^2	0.7→0.95 T_M

Kinetics, temperature and stress of the deformation work largely influence the material behavior, leading to variations in material ductility, hardening or softening trends. These variations depend on the microstructural mechanisms that govern material plasticity. In metals it has been observed a number of mechanisms which may control the deformation, typically represented in an Ashby diagram. Such diagram (also known as deformation mechanism map) marks the deformation mechanism of a material under different conditions of temperature, stress and strain-rate. Figure 2-3 depicts an Ashby diagram for a pure metal (titanium). Note the discontinuity observed at 0.65 T_m because of the titanium allotropy (Babu, 2008).

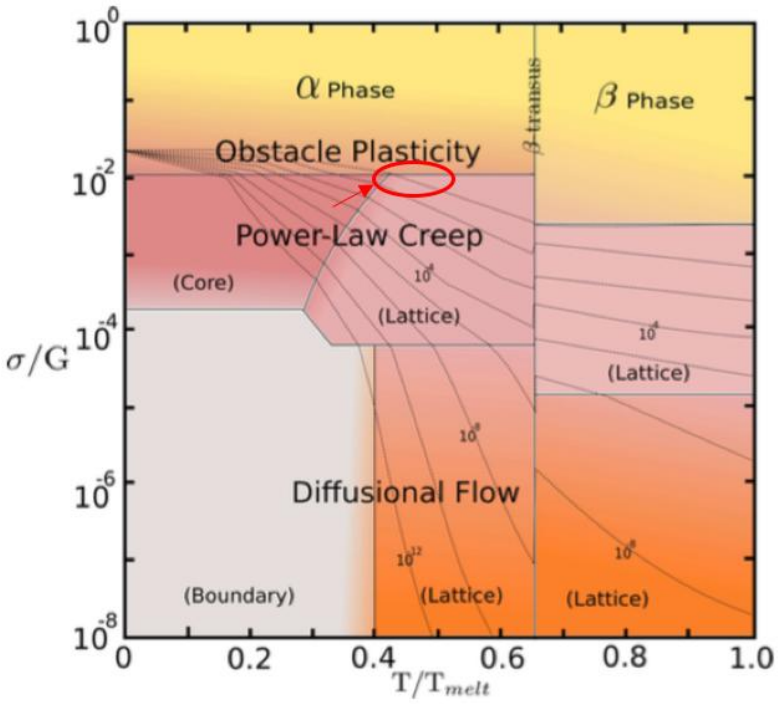

Figure 2-3 Representation of deformation mechanisms in titanium under different conditions. Stress is normalized with the shear modulus and temperature with melting temperature. According to Table 2.1, machining is presented as a high strain rate, medium temperature and high stress process (Babu 2008).

The figure depicts three fundamental strain mechanisms depending on the shear stress in the ordinate axis (normalized with the shear modulus) and on the temperature in the abscise axis (normalized with the melting temperature). At low temperatures deformation is controlled by lattice obstacles (detailed in Section 2.3). However, at higher temperatures and lower stress defects interaction (power-law) and ultimately atom diffusion may be the governing mechanism even a very low mechanical loading. Thus, variations in the process condition make materials react fundamentally different in terms of crystal mechanics. While this Ashby diagram focus on titanium, such mechanisms maybe depicted for other metals following a different distribution.

In the Ashby diagram of Figure 2-3, machining is represented as a singular red point with high strain rate, medium temperature and high shear stress process, this also according to Table 2.1. However, in contrast to that, most of the characterization already made in structural alloys refers to low strain rate, low temperature and high shear stress conditions. Thus, in machining it is roughly possible to use data from classical characterizations in the modeling of material response, since it may represent a flow law not present during machining, limiting data applicability.

In order to overcome the limitations of the machining process study a set of methodologies around the particularities of machining has been developed. These methods focus on the process of metal cutting.

- **Chip generation**

During metal cutting, material is deformed and separated from the workpiece as a chip. The way chip generates has been matter of great scientific interest, however, there has been conflicting evidence about the nature of the deformation zone in metal cutting. This has led to a number of schools of thought in the approach to analysis. Most of the attention has been reached by the thin-shear plane model and the plastic region deformation model.

Models describing a thin-shear plane (TSP) were developed already at 40ths by Piispanen (Piispanen 1948) and Merchant (Ernst and Merchant 1941), whose pointed that chip deformation occurs in a very localized plane (Figure 2-4a). Later, it was an attempt to introduce a more complicated model involving, a plastic deformation region model (PDR) where the material progressively deforms as in following Figure 2-4b (Oxley 1961).

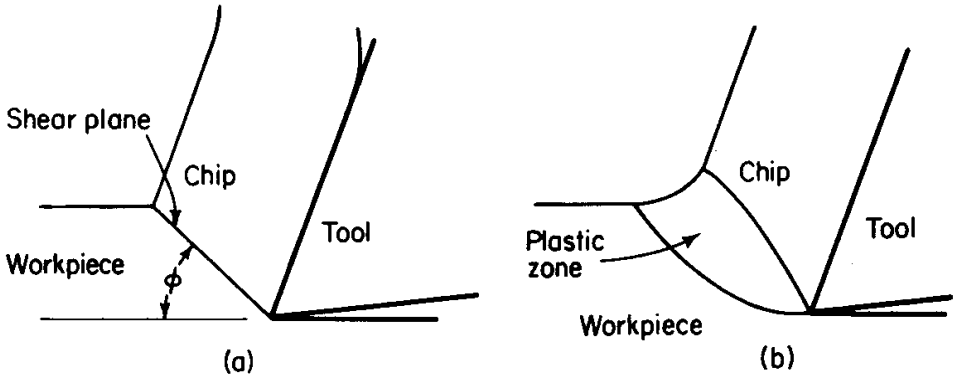

Figure 2-4 (a) shear model of the machining process, (b) plastic-zone model for machining (Sutherland, 2016).

The available experimental evidence indicates that the PDR model (Figure 2-4b) may describe the cutting process at very low speeds, but at higher speeds most evidence indicates that TSP model better describes experimental results. Hence, the TSP model is assumed for high-speed industrial cutting conditions. In addition, this model leads to far simpler mathematical treatment than does the PDR model. For these two reasons the analysis of the thin shear zone has received far more attention and is more complete than that of the thick zone.

While the development of the theory of the TSP can explain the generation of most of the chip section, it has been observed that a part of the chip, the one in close contact with the tool, develops particular shear properties. This has made the thin zone to be referred as the primary shear zone (PSZ), and the layer of chip in contact with the tool as the secondary shear zone (SSZ). For a better understanding, in this model is usually first considered the case of orthogonal cutting, i.e., cutting with the tool edge perpendicular to the relative velocity between work and tool, as depicted in Figure 2-5.

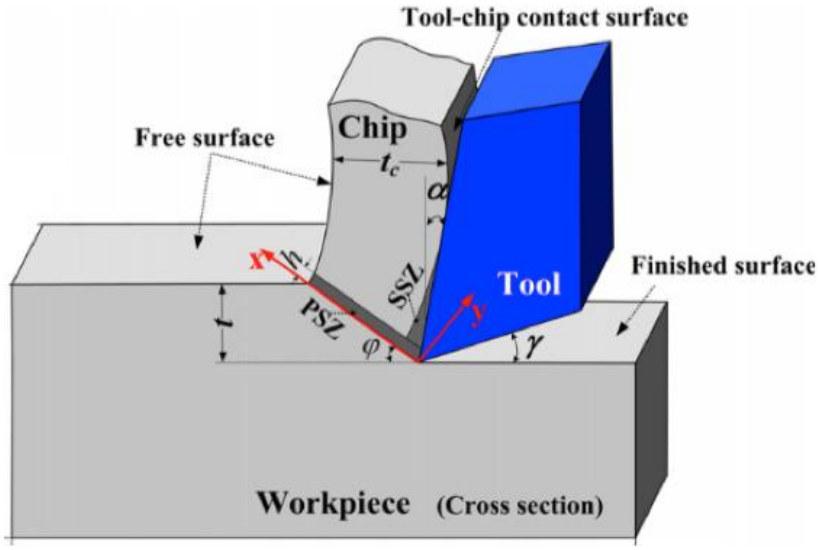

Figure 2-5 Basic Workpiece-tool interaction in the machining process (Ye, 2012).

The existence of a thin layer (PSZ or SSZ) where most of the deformation work is done entails large strain ratios present only in restricted areas. Since this process occurs typically in fraction of a second, such scenario may lead to localized conditions of extreme temperature, strain and stress. These conditions are not covered by the model proposed by Merchant, which assumes ideal thin shear zone, continuous chip generation and homogeneous properties of the chip material. Thus, while this model could approximate real problems, the shear mechanism, chip shape and material properties differ widely from the ones proposed. Figure 2-6 shows a set of chip morphologies depending of the material and the cutting speed (Ye et al. 2014). There, non-continuous chips or high microstructural anisotropy can be observed.

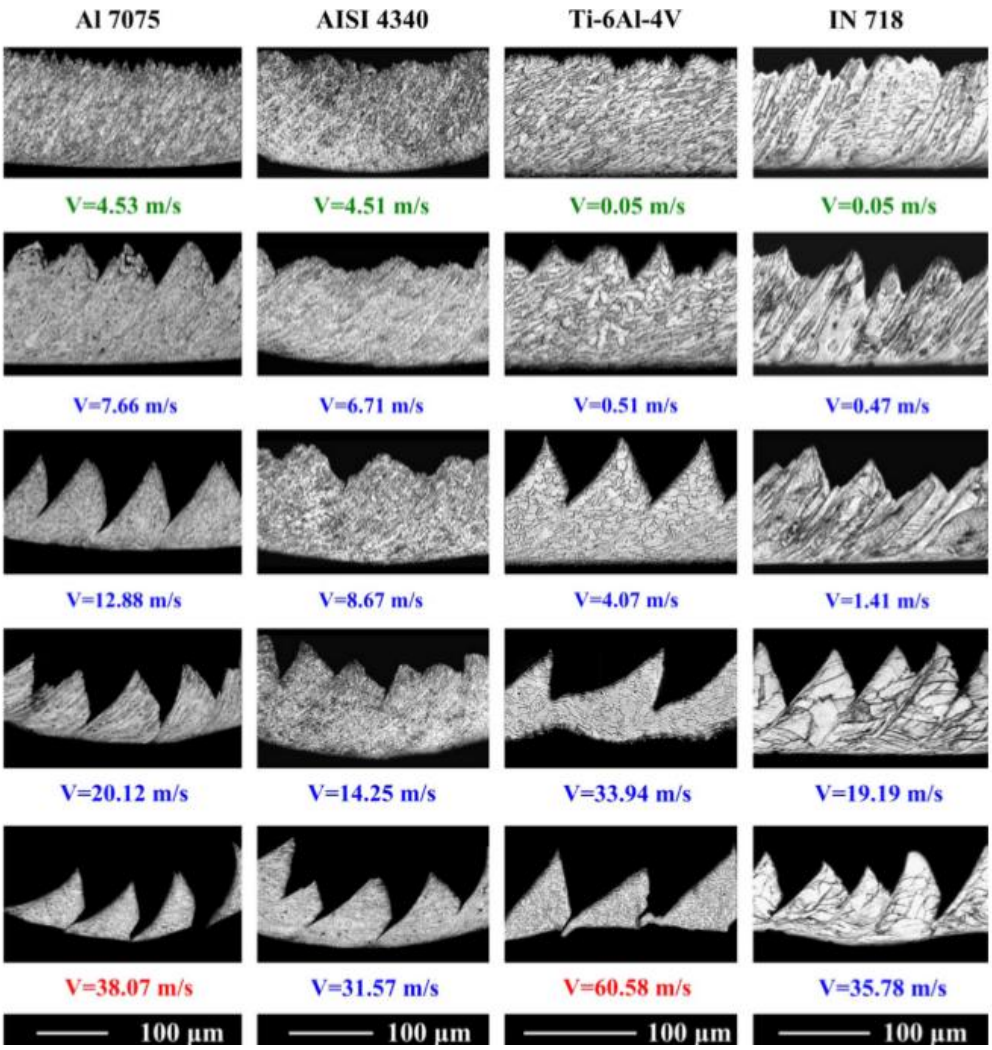

Figure 2-6 Chip flow pattern evolves with cutting speed for Al 7075, AISI 4340, Ti–6Al–4V and IN 718 (Ye, 2014).

The experiments of Ye *et al.* (2014) show that when the cutting speed increases, in some metals the continuous chip disappears and becomes a serrated chip. Such chip morphology is produced by prominent shear bands that absorb most of the shear deformation in the thin shear zone (known as primary shear zone, PSZ). The origin of this bands still generates controversy, however most of the authors point out that they are the consequence of thermal instabilities produced when the material does not have enough time to diffuse the heat along the material. In this case, an adiabatic shear band (ASB) nucleates and propagates through the shear plane.

Typically, the process of shearing in front of the tool lasts units of milliseconds (depending on the cutting speed). Hence, the term “adiabatic” refers to the fact that there is not enough time to make the heat to abandon the shear area during the short temporal window. Simulations of heat transfer by the finite element method (FEM) of the adiabatic effect during orthogonal cutting have predicted the formation of ASB, what reinforce the

theory of thermal instabilities as the primary trigger (Ye et al. 2013). Figure 2-7 shows the good agreement of the simulations and experiments in terms of chip shape.

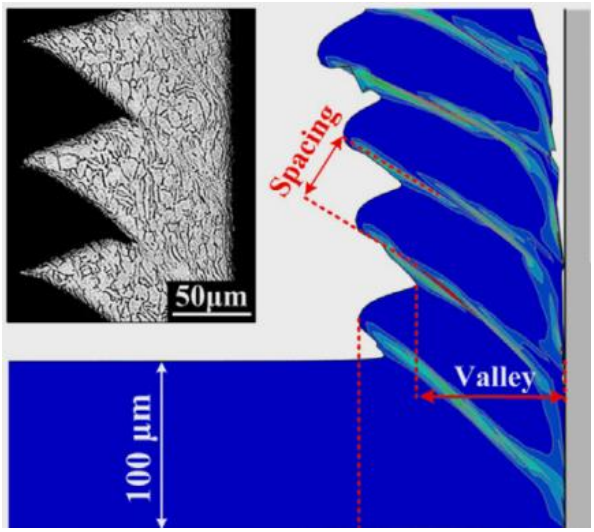

Figure 2-7 FEM simulation of the chip morphology in Ti machining (Ye, 2013)

While some of the thermal phenomena have been successfully reproduced by FEM simulations, the exact thermal conditions in the tool edge during real cutting are still unknown and can be hardly approximated by non-experimental methods. Since this is a key aspect with relevance to predict tool wear, workpiece surface integrity and chip mechanical properties, much effort has been devoted to measure temperatures during machining. This has pushed the use of high-speed infrared (IR) cameras. With these cameras it is possible to measure the temperature in the side face of the tool during cutting. While this is not the section with the largest temperature, further data analysis is typically used to estimate the temperature in the area of chip-tool contact. Calculations from (Arrazola et al. 2015) pointed out that the temperature in the center of the cutting contact tends to be 1.4 - 2.3 times higher than the one measured on the side (Figure 2-8).

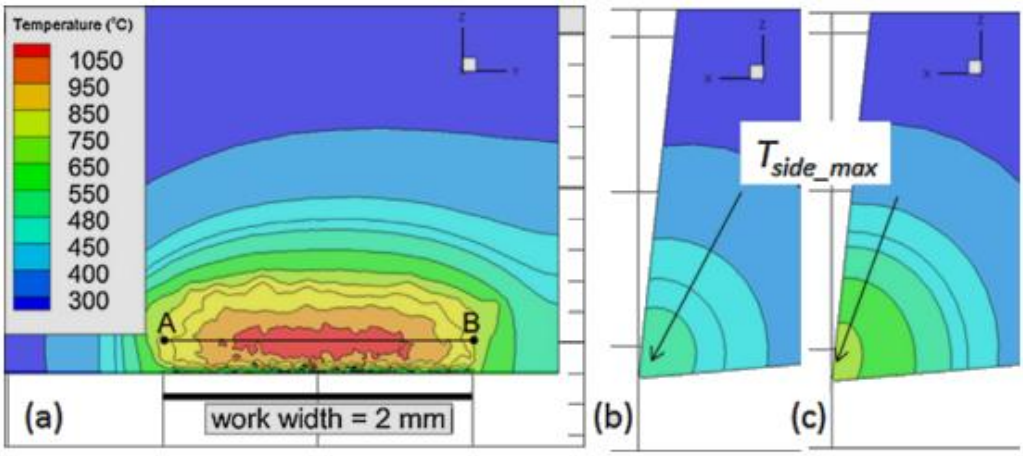

Figure 2-8 (a) tool rake face temperature distribution up to 1050 °C, (b) and (c) tool side temperature measured at 55 and 22 µm from workpiece (Arrázola, 2015).

Large temperatures in the cutting edge would be responsible of large chip heating on the one hand, and an increased tool wear on the other hand. This last aspect of key importance since, as demonstrated, WC-Co tools integrity can be thermally degraded at temperatures over 900 ºC (Yang et al. 2016).

Another important factor for the understanding of the chip flow is the strain and strain-rate along the cutting area. Figure 2-9 depicts an orthogonal cutting configuration where some features of a mild steel AISI 1018 sample are optically tracked during high speed machining to estimate strain of the different parts of the chip (List et al. 2013).

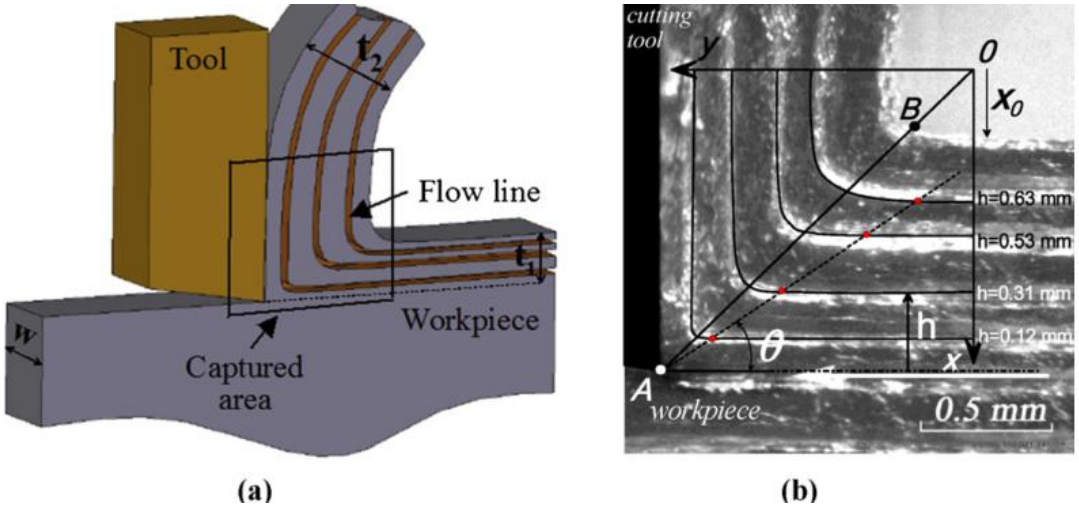

Figure 2-9 Orthogonal cutting configuration. (a) Definition of the chip cross-section observed during the test with the flow lines design. (b) Experimental observation at *Vc* = 1020 m/min (List, 2013).

The measurements of List *et al*. (2013) concluded that depending on the distance to the surface, the strain-rate changes significantly, approximately one order of magnitude (Figure 2-10b). As this result remarks, near the cutting edge the strain-rate increases several times the one near the material surface. Hence, there is a severe strain-rate gradient that promotes the material shear and rotation and promotes large values of heating by work deformation close to the cutting tool.

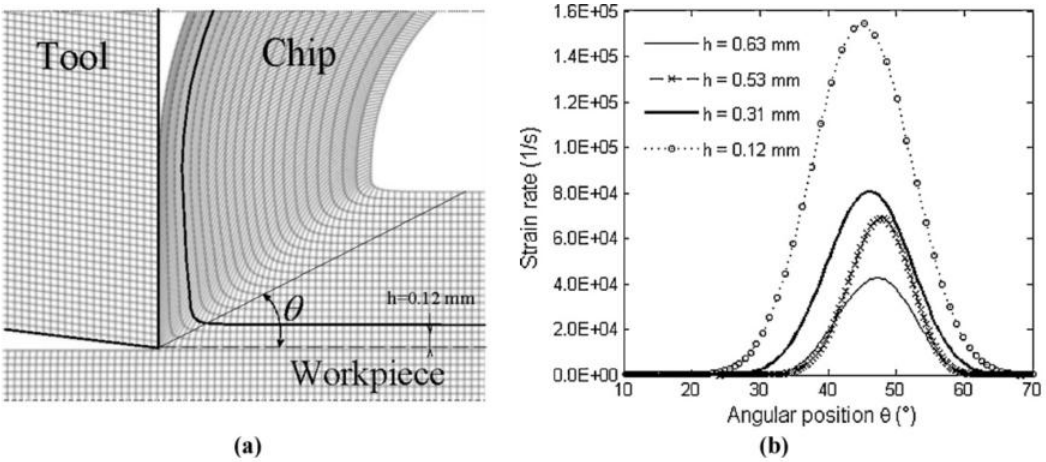

Figure 2-10 (a) sketch of tool-chip system, (b) strain-rate at different depth of the non-cut chip (List et al. 2013).

Further research of the strain in the primary shear zone has been carried out by (Y. Guo, Compton, and Chandrasekar 2015), whom exploited high-speed video post-processing. By this technique the motion of distinct features of the material are tracked in order to predict differential strain along the tool-chip-workpiece interaction. Figure 2-11a depicts the pathway of seven features from the workpiece to the chip. With data post-processing for several features a map of strain can be built (shown in Figure 2-11b), where it is shown larger values of strain close to the tool.

It should be noted that, while this methodology has resolved the strain field in the primary deformation zone, the deformation field in the close proximity to the tool is not depicted. This part of the secondary shear zone develops a strain behavior where features can hardly be tracked.

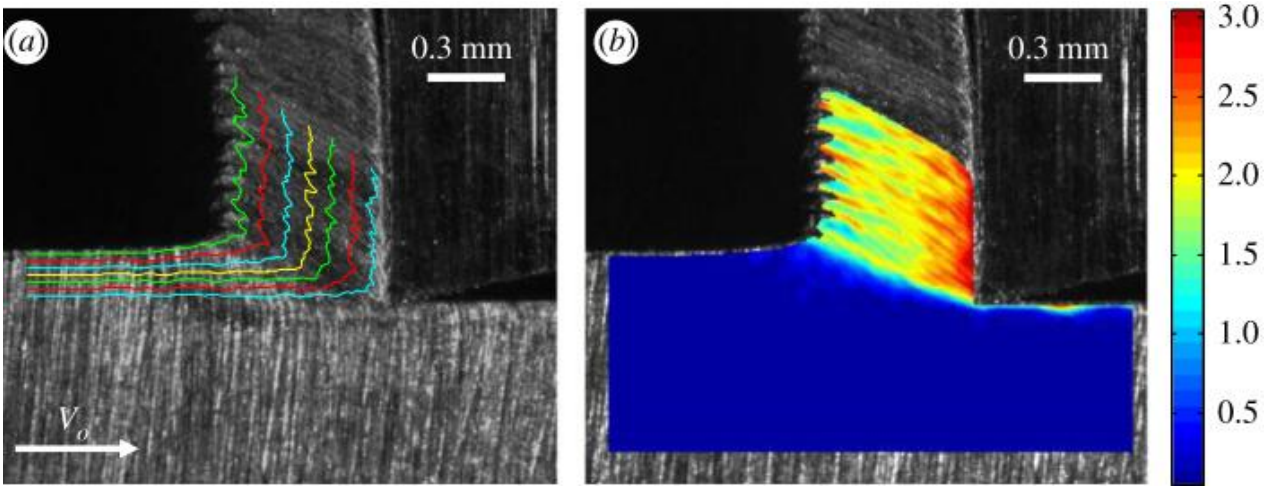

Figure 2-11 (a) Path of sample features from the workpiece to the chip. (b) observable strain field produced during chip generation (Y. Guo, Compton, and Chandrasekar 2015).

In terms of material behavior, results from different authors have shown that workpiece and chip form a system of mutual thermal-mechanical interaction. Friction and deformation work represent the main sources of heating. Nevertheless, while temperature field has been calculated in the tool, and the deformation distribution has been disclosed in the primary shear zone, the phenomena in the secondary shear zone, where chip material is in close contact with the tool, is still uncertain. In this area the behavior strongly depends on the conditions of cutting, on the cutting material and the properties of material to be machined. The present work takes especial attention to the material of the workpiece, in particular two structural alloys typically shaped by machining: steel and aluminum.

2.2 Microstructure of steel and aluminum alloys

2.2.1 Iron and steel

Iron is a chemical element that exists in three different structures at ambient pressure: alpha ferrite (α), austenite (γ) and delta ferrite (δ). The α phase, with a body centered cubic (BCC) crystal structure, is stable at room temperature and up to 910°C. At higher temperatures, it transforms into the face centered cubic (FCC) austenite γ, and it reverts to delta ferrite at 1390°C. This high-temperature ferrite is traditionally called δ, although its crystal structure is not different from the α phase. The δ-ferrite remains stable until melting occurs at 1536°C. The γ- to α-transformation is also accompanied by an atomic volume change of approximately 1 % (Bhadeshia and Honeycombe, 2006).

The term steel is associated with an iron-based alloy containing carbon in amounts less than about 2 % of weight. Higher concentrations are referred to as cast iron, where bulk iron-carbide (Fe_3C) or graphite are the main components. The introduction of carbon in the iron lattice modifies the phases present in pure iron as shown in the equilibrium diagram illustrated in Figure 2-12. Depending on the temperature and the carbon concentration, iron atoms arrange in different lattice structures.

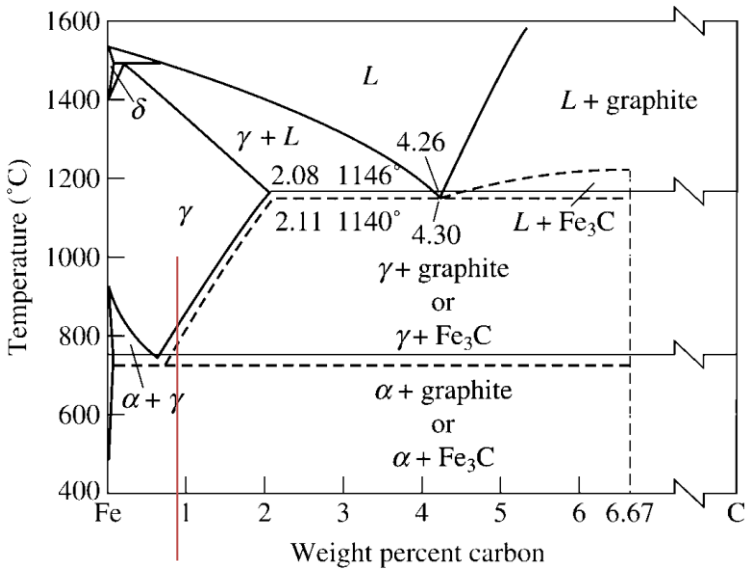

Figure 2-12 Stable Iron-Carbon diagram (solid line); Meta-stable Iron-Cementite diagram (dashed line). Up to 2 wt% carbon, the alloy is called steel. The vertical line at 2% C separate steels and cast iron. *L* refers to the liquid state (Askeland, Fulay, and Wright 2010).

In Figure 2-12, the area of alpha ferrite (α) is small compared to austenite (γ). That means that pure ferrite is only possible for small concentrations of carbon. The reason for that is the low solubility of carbon in ferrite, in contrast to a much bigger one in austenite. In turn, this low solubility in the BCC lattice is produced by the small size of the tetrahedral interstitial between iron atoms in ferrite.

The stress produced by carbon atom interstitials in austenite and ferrite lattices differs significantly (Table 2-2). In the octahedral holes of an austenite lattice, carbon atoms introduce less lattice deformation than in a ferrite lattice. Thus, the solubility of carbon is much higher in austenite.

Table 2-2. Accommodation stress and solubility of carbon atoms in ferritic and austenitic structures. The stress of carbon atoms in ferrite is 10 times higher than the stress of carbon atoms in austenite. This causes a considerable difference in the carbon solubility (Bhadeshia, 2006)

	Ferrite	**Austenite**
Stress of C interstitial	$\delta\sigma_y/\delta c = 79000\ MPa$	$\delta\sigma_y/\delta c = 7300\ MPa$
Solubility of C at 723°C	0.02 wt%	0.8 wt%

The difference in carbon solubility, the changes in volume and the change of the structure itself (BCC to FCC) imply that the restructuration from austenite to ferrite lead to atom segregation of the supersaturated element. However, the mechanism of segregation is highly time-dependent. Hence, if a material that is heated up to the austenite temperature is cooled fast enough to hinder the lattice accommodation, phases of steel may be formed out of the Fe-Graphite diagram (Figure 2-12). This lead to the generation of the so called metastable phases. Some of these phases remain at room temperature and have different mechanical properties compared to the stable ones.

Currently, the solid-state transformation of austenite can produce a broad range of different structures and lead to a range of property combinations. Such large variety of structures that can be generated in steels is, in part, responsible for their success as engineering materials.

One of the most used steel structures is the pearlitic one. Steels with that structure have mechanical properties often required by the industry, like toughness, high strength and resistance to wear. The term ‘Pearlite’, or more specific ‘pearlitic steel’, refers to an iron-based compound phase, which is characterized by the joint arrangement of thin layers of ferrite and cementite (Figure 2-13). Pearlite is formed during sufficiently slow cooling in an iron-carbon system at the eutectoid point in the Fe-C phase diagram (723 °C, eutectoid temperature). In a pure pearlitic alloy (Fe-Fe_3C) it is contained about 88 % of mass of ferrite and 12 % of cementite, corresponding to a total of 0.76% of carbon in terms of mass.

The term ‘pearlite’ refers to the appearance of this alloy phase when studied under the microscope. It resembles the laminar pearl structure (nacre), a natural lamellar structure. While pearlite was first identified by Henry Clifton Sorby and hence it was initially named “sorbite”, this similarity of microstructure to nacre and especially the optical effect caused by the successive piling of layers made the alternative name 'pearlite' more popular.

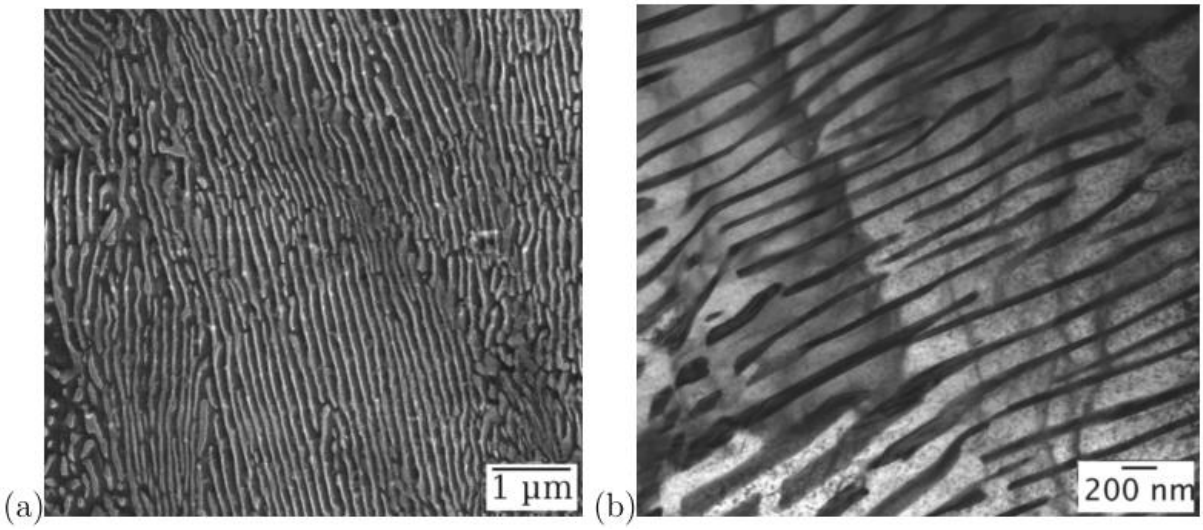

Figure 2-13 (a) SEM image of fine pearlite, (b) TEM image of fine alternate arrangement of ferrite and cementite (Bakshi, 2014)

While most of the plates of pearlite develops in parallel, the usual lamellar appearance of pearlite shown in micrographs is typically misleading since the individual plates within a pearlite colony are commonly inter-connected. A single colony is therefore an interpenetrating bicrystal of ferrite and cementite. Moreover, cementite tends to growth in multiple directions and may develop discontinuities along the plates, as shown in Figure 2-14 (internal 3D reconstruction of a pearlite colony by imaging successive ion-milling-steps).

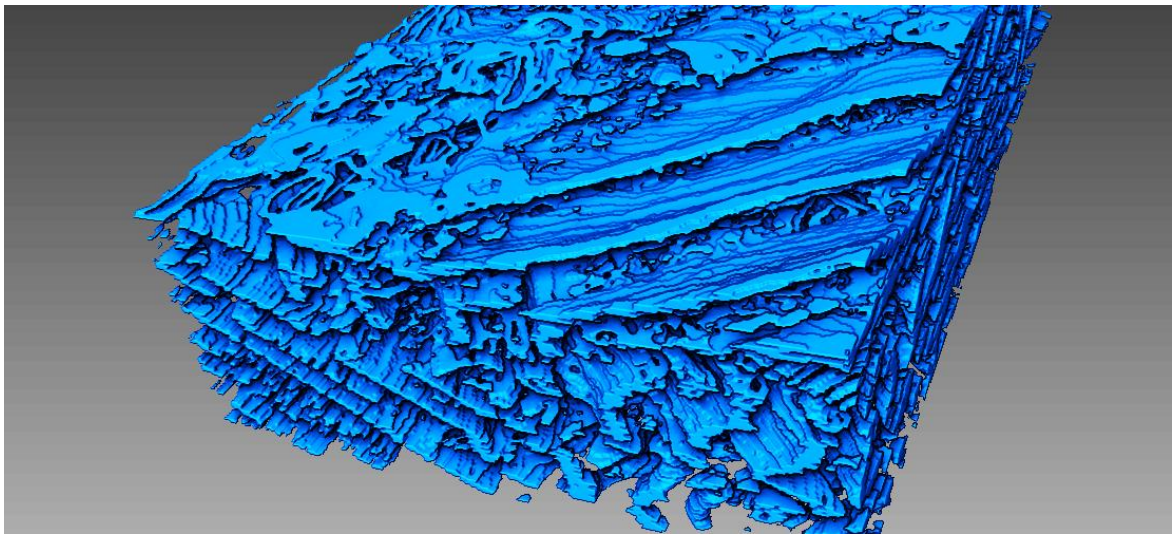

Figure 2-14 3D reconstruction of the structure of a block of pearlite in AISI 1060 steel (7x15x30 µm).

Furthermore, the pearlitic reaction during austenite cooling may lead to different values of interlaminar space, the distance between plates ebbed in the ferrite matrix. The interlaminar space has shown to be determinant in the mechanical properties. The reduction of this distance is largely determined by the degree of undercooling during the austenite-

pearlite transformation. As shown in Figure 2-15, different interlaminar spacing promoted by undercooling influences yield strength in steel (Bhadeshia and Honeycombe 2006).

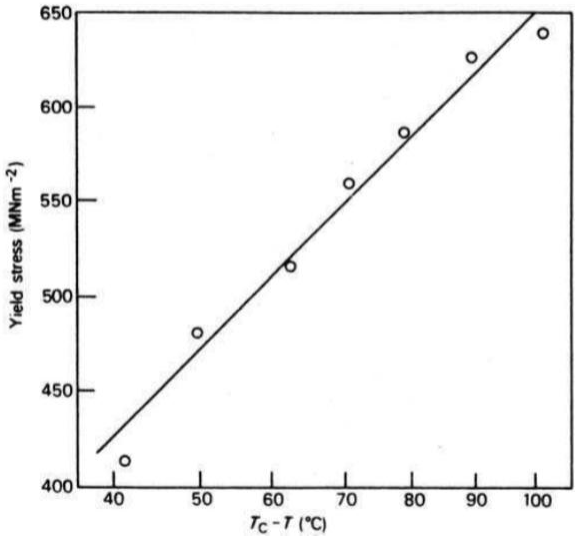

Figure 2-15 Effect of undercooling (respect to eutectoid temperature) on the strength of a pearlitic steel (Bhadeshia and Honeycombe 2006).

Pearlitic structures may coexist with other softer structures. In case the chemical amount of carbon is under the one of the eutectoid point, the alloy develops a combination of pure ferrite with perlite islands. These alloys are referred as medium-carbon steels and are commonly used in structures and machines. They develop mechanical properties in between the ones of ferrite (soft and ductile) and the corresponding of pearlite (hard and brittle).

2.2.2 Aluminum alloys

Aluminum is a chemical element that in solid state develops a face centered cubic lattice that remains stable until melting occurs at 660 °C. It is a low-density metal (2.7 g/cm^3) that develops a corrosion-protecting coating in presence of oxygen. Aluminum is commonly alloyed and thermally treated to reach mechanical properties of a structural metal.

The predominant reason for alloying aluminum is to increase strength, hardness, resistance to wear, creep or fatigue. Effects of alloying elements are related to their alloy phase diagrams, to microstructures and to substructures which they form as a result of solidification and thermo-mechanical history. Among the heat treatment existing for aluminum alloys, the solution heat treatment is used to produce a supersaturated structural single-phase without precipitates. Such target structure is used as a precondition for aging heat treatment. In the industry, solid solution ageing is widely extended when aluminum is design for structural purposes.

Typical elements of alloying are Mg, Mn, Si, Cu and Zn, placing mostly as substitutionals in the aluminum lattice. These elements have some solid solubility in aluminum and, in all cases, the solubility increases when temperature rises (Figure 2-16). This opens the possibility of inducing hardening following two different strategies, by second phase precipitation or by supersaturated solid solution.

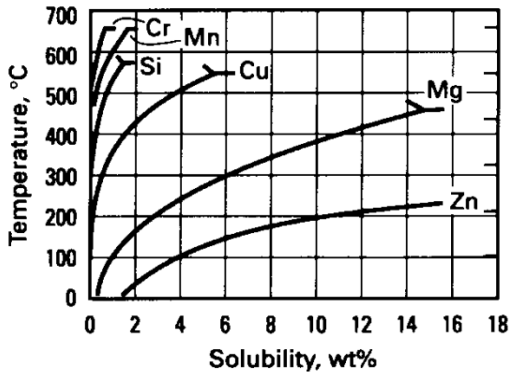

Figure 2-16 Solubility of different alloying elements in the aluminum depending on the temperature (Davis 2001).

The first strategy takes advantage of the most stable situation. When an element overcomes the saturation limit a new specie emerges by precipitation of a second phase, which is an intermetallic compound in the form of a particle. The presence of intermetallic phases generally increases the material strength, since these second-phases are generally harder than the host matrix. These irregularly shaped particles form during slow solidification and mostly along grain boundaries.

In the second strategy, saturated states at high temperature are fast-cooled to retain alien elements in the original position, which leads to a homogeneous supersaturated state. That produces some misfits in the matrix lattice which enhance the properties of the alloy by solution strengthening.

For those elements that form solid solutions, the strengthening effect when the element is in solution tends to increase with increasing difference in the atomic radii of the solvent (Aluminum) and solute (alloying element) atoms (Table 2-3). This factor is observed in high-purity binary solid-solution alloys in the annealed state, but partially disappears in complex alloys since other effects are involved, principally which promote electronic bonding to form other species.

Table 2-3 Strengthening effect of elements in solid solution in aluminum (Davis 2001).

Element	Difference in atomic radii %	Yield strength increase by adding 1 wt. %
Si	-3.8	9.2
Zn	-6.0	2.9
Cu	-10.7	13.8
Mn	-11.7	30.3
Mg	11.8	18.6

The presence of homogeneously distributed alloying elements in the aluminum matrix has been traditionally exploited to induce metastable nanosized-scale precipitates embedded in a host, which promotes enhanced properties. The most common method is the precipitation of Guinier-Preston particles, which relies on the progressive association of host and alien element assisted by controlled heating (Guinier 1938; Preston 1938). This mechanism is observable in the system Al-Cu (Figure 2-17). Contrary to stable second phase precipitation, this mechanism promotes precipitates homogeneously distributed along the host matrix, instead of precipitation in grain boundaries. This represents a more effective method to reach strength (Gornostyrev and Katsnelson 2015).

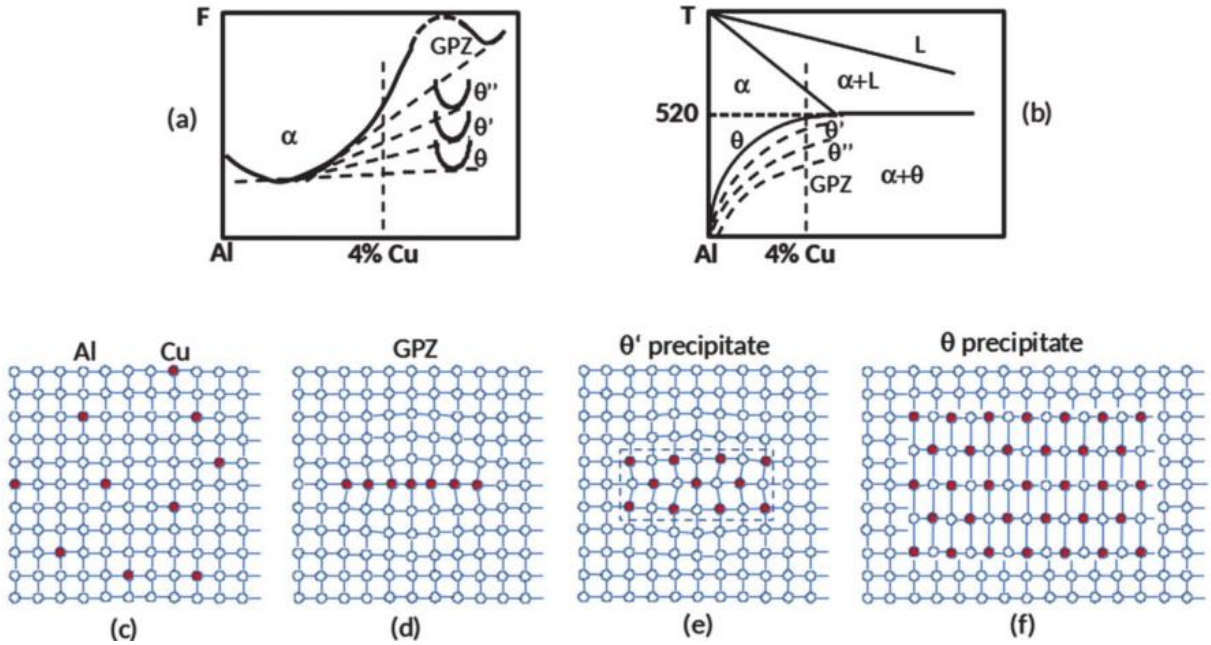

Figure 2-17 (a) Solid line shows the system free energy, which increases with the Cu solid solution concentration and dashed lines point to energy of particle precipitations; (b) corresponding phase diagram; (c) solid solution and (d,e,f) progressive association of Al and Cu to create a Guinier-Preston precipitate (Gornostyrev, and Katsnelson, 2015).

In binary aluminum-copper alloys the mechanism of nucleation and growth of particles follow successive steps triggered thermally from a solid solution of Cu in Al (Figure 2-17c). In a first step precipitates are atomically thin Cu platelets on the {100}-planes in FCC Aluminum; they are called Guinier-Preston zones (GPZ). Further tempering of the AlCu alloy above room temperature leads to the growth of GPZ and the progressive transformation by several steps: GPZ to Θ'' particles, then Θ' particles, and finally Θ particles. The GPZ has only one Cu layer in the {100} plane (Figure 2-17d). The Θ'' particles contain two or more {100} Cu layers separated by three aluminum planes. GPZ and Θ'' are features coherently conjugated with the host. The Θ' particles are larger and semi-coherent with the Al host, since they are conjugated with the host via the formation of misfit dislocations (Figure 2-17e). Finally, the Θ

particles are inclusions of a thermo-dynamically stable intermetallic Al_2Cu incoherent with the host (Figure 2-17f).

The highest strength of the alloy in the Al-Cu system is reached just before the precipitates loss coherency, when the compensation of long-range internal stresses takes place. These alloys (thermally aged aluminum) have been largely investigated as low-density structural metal, particularly important in the sector of aeronautics. Further explanations of the ground to explain mechanical properties and the hardening mechanisms are given in the following section.

2.3 Metal plasticity

Metals tend to be assembled as crystals, an arrangement of atoms packed together in a regularly repeating pattern. These periodical arrangements commonly have different defects in them, which in many cases determine the mechanical properties. In the same way as the strength of a chain is determined by the strength of the weakest link, the strength of a crystalline material is given by strain mechanism with the weakest energy consumption, mainly defects nucleation or propagation. The dislocation is a particular type of defect that has the effect of allowing materials to deform plastically (yielding) at stress levels that are much less than the theoretical strength.

During deformation, while a rearrangement of all the atoms in a material would have a huge energetic cost, moving just one line of atoms at once is a preferable mechanism of plasticity. In the more basic model, the effective deformation will be produced when the last line of atoms reaches a side of the piece of material. The Burgers vector of a dislocation is the misfit of the lattice between both sides of the dislocation, and also represent the unit of strain propagated by a dislocation. This is represented in Figure 2-18.

Dislocation lines propagate in crystallographic planes, preferably in planes where the density of atoms is large (close packed planes), which reduce the energy of that linear defects. In the case of face-centered cubic lattices (FCC), there are 12 slip systems. In body-centered cubic lattices (BCC) there are no proper close packed planes, which develops up to 48 slip planes at the cost of requiring some extra energy to be activated.

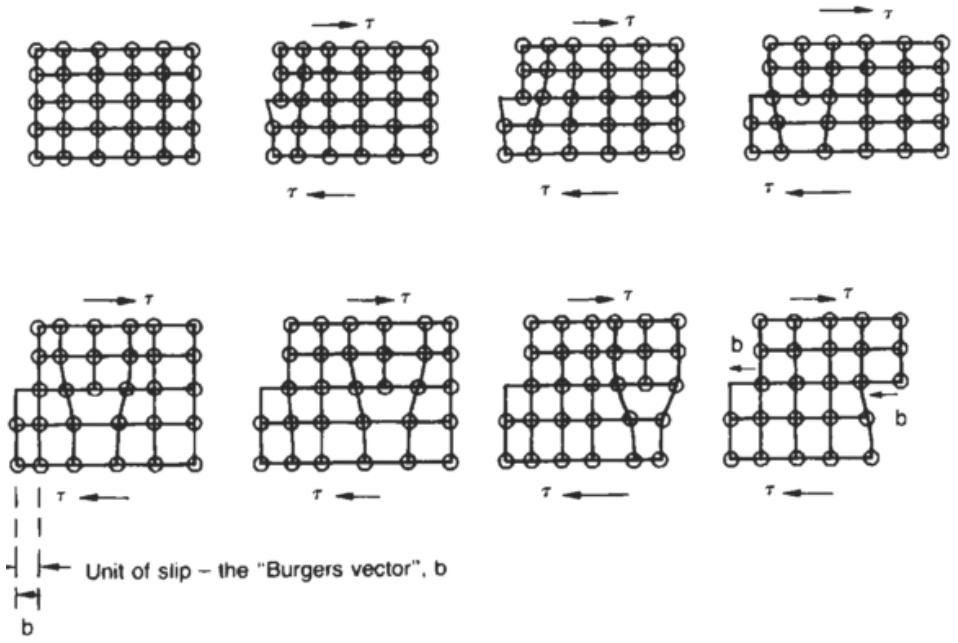

Figure 2-18 From top-left to bottom-right, nucleation and propagation of a dislocation in a crystal in presence of shear force. The minimum unit of slip between lines is called “Burgers vector” (Michael F. Ashby and Jones 1996).

In order to produce continued strain, it is necessary to overcome intrinsic friction in opposition to the dislocation progress. Geometrically, the propagation of a dislocation is facilitated by a perfect lattice where at both sides of the dislocation stress symmetry is present. Contrary to this, the introduction of geometry-breaking elements will represent an obstacle that will increase the needed stress to obtain strain. This elucidates different strategies to increase the strength of an alloy.

The most obvious lattice asymmetry is given by grain boundaries, where each side of the boundary develops a different lattice orientation (Figure 2-19). In addition to lattice discontinuity, the atomic disorder increases close to grain boundaries, increasing further the energy to cross this area. Thus, a grain boundary would likely stop the propagation of a dislocation.

In the case of a second dislocation reaching the grain boundary, during deformation it would probably stop propagation and tend to “pile up” (or back up) on the previous dislocation at grain boundaries. Successive pile-ups of dislocations introduce stress concentrations ahead of their slip planes, which eventually generate a dislocations source in the other side of the boundary. Hence, in general grain boundaries are effective obstacles against dislocation movement, since crossing them will have an energy cost. A fine-grained material (one that has small grains) is harder and stronger than one with coarse grains, since the former has a greater total grain boundary area to impede dislocation motion.

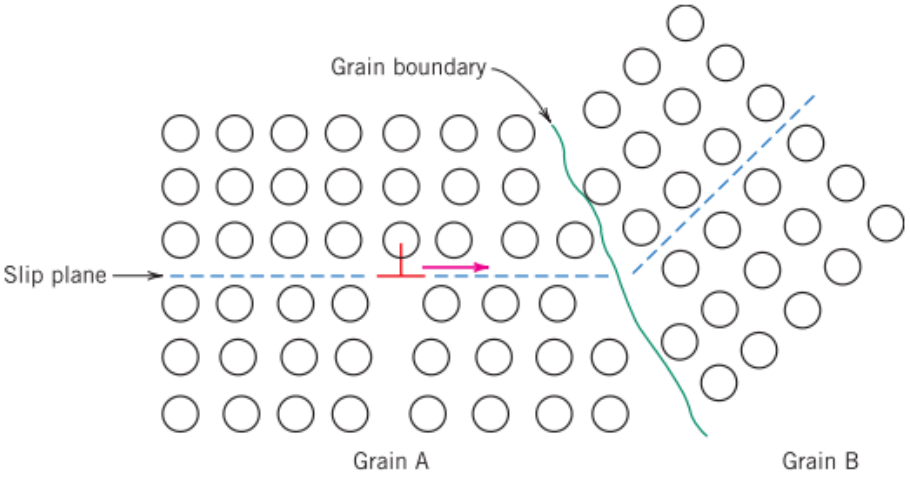

Figure 2-19 Dislocation approximating a grain boundary. The slip planes are discontinuous and change orientation across the boundary (Callister and Rethwisch 2007).

Another technique to strengthen and harden metals is alloying with alien atoms that go into either substitutionals or interstitials solid solutions. High-purity metals are almost always softer and have less strength than alloys composed of the same base metal. Alloys are stronger than pure metals because impurity atoms that go into solid solution ordinarily impose geometric discontinuities and lattice strains on the surrounding host atoms. Hence, these impurity atoms promote restrictions in dislocation movement, increasing yield stress.

Alloying also offers a set of other mechanisms to enhance mechanical properties. Metal alloying over solubility limits will end up with the precipitation of a second phase to recover stable equilibrium. Usually this second phase is a stoichiometric combination of host and alloy element, leading to an intermetallic or ceramic phase. These phases tend to be more brittle than the host matrix with a few, if any, active mechanism of plasticity. Hence, if dislocations energy is not large enough to produce the fracture of the precipitate, second phases tend to abruptly stop dislocation propagation in the boundary of the hard second phases. The presence of second phases typically makes the material harder but more brittle, since the mechanisms of plasticity can act only in the volume fraction occupied by the matrix of ductile metal. Once the matrix is saturated of dislocations, fracture could be energetically favorable. This is the case of pearlitic steel, since the intermetallic phase of cementite (Fe_3C) strongly stops propagation of strain in the material. Moreover, smaller interlamellar distances in pearlite increase the number of boundaries, leading to larger values of hardness at the cost of a reduced ductility (Modi et al. 2001).

In opposite to strengthening by precipitation of large hard phases, another strategy consists on promoting much smaller precipitates in the host lattice. These precipitates act as non-impassable dislocation barriers, making the dislocations spend energy to pass through with a small cost in ductility. This mechanism is generally used in aluminum alloys by the

precipitation of Guinier-Preston particles, as explained in previous section. In such alloys, particles nucleate and progressively grow from solid solution to coherent precipitate (Θ''), then semi-coherency (Θ') and finally to a particle with no lattice connections with the host (Θ). The size of the particles can be engineered by thermal ageing to reach the optimum strength. As it is shown in Figure 2-20a for the Al-Cu system, the highest strength of the alloy is reached when annealing rounding 100 hours at 150 ºC, just before the precipitates loss coherency, when the compensation of long-range internal stresses takes place (Michael F. Ashby and Jones 1998).

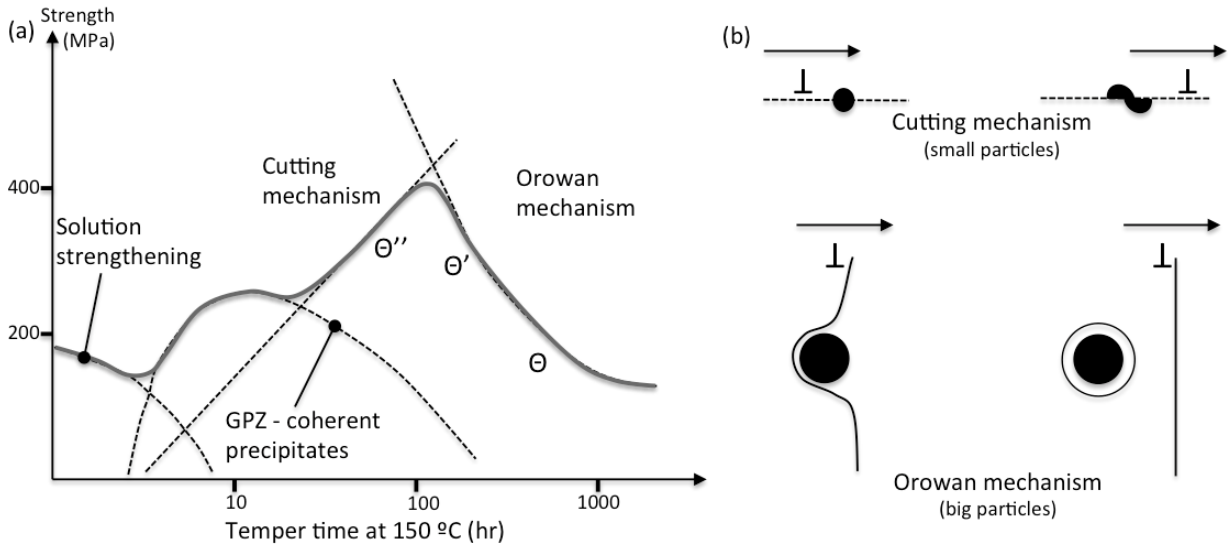

Figure 2-20 (a) Approximate evolution of the strength of AlCu alloy depending on the ageing time. The mechanism of hardening is pointed for each segment. (b) sketch of cutting and Orowan mechanisms when a dislocation reaches a particle - plotted from data of (Michael F. Ashby and Jones 1998).

Figure 2-20b shows two different ways a dislocation interacts with a particle, cutting or Orowan mechanism. In the first case when particles are small enough dislocations can cut through. Nevertheless, further ageing induce particle merging to reach a larger size, representing harder obstacle, and thus activating a second mechanism. In that case, dislocations can bow particles overcoming then to follow propagating. This is referred as the Orowan mechanism. To activate the cutting mechanism the energy needed increases with the particle size. However, the Orowan mechanism depends on the distance between particles, which decreases with the particle size. Thus, there is an optimum particle size that leads to maximum strengthening. For each alloy there is a characteristic ageing point.

2.3.1 Strain hardening

The strain-hardening phenomenon is generally explained on the basis of dislocation-to-dislocation interactions. The dislocation density in a metal increases with deformation due to

dislocation multiplication or the formation of new dislocations, since this would absorb further strains. Consequently, the average distance of separation between dislocations decreases with increasing strain, i.e., the dislocations are positioned closer together and can mutually clamp by two mechanisms. On the one hand, dislocations itself represent a discontinuity in terms of lattice continuity, which hampers dislocation propagation. Additionally, on average dislocation-to-dislocation strain interactions are repulsive (Durst et al. 2006). The net result is that the motion of a dislocation is hindered by the presence of other dislocations. As the dislocation density increases, this resistance to dislocation motion by other dislocations becomes more pronounced. Thus, the imposed stress necessary to deform a metal increases with increasing cold work.

Normally alloys develop more hardening than pure metals. Generally, in pure metals dislocations can propagate easily across the whole material. Then, they can reach boundaries, annihilate and produce effective strain without obstacles. Hence, only a fraction of the dislocations interacts with other dislocations. In contrast, metal alloys have plenty of obstacles where dislocations clamp, being afterwards an obstacle for following dislocations, thus promoting work hardening. Hence, the capacity of hardening increases rapidly with the density of lattice obstacles. However, in the opposite side, too many obstacles would make the material saturate of dislocations rapidly. This makes the material reaching easily the energy necessary for fracture with few hardening. In industrial alloys the factor of hardening capacity is typically engineered to reach the needed properties.

2.3.2 Material relaxation and dynamic softening

Sometimes, cold working leads to effects that are undesirable. Loss of ductility or development of residual stresses may not be desirable in some applications. Since strain hardening results from increased dislocation density, it is possible to assume that any treatment to rearrange or annihilate dislocations partially or totally reverses the effects of hardening.

Annealing is a heat treatment used to eliminate some or all of the effects of cold working. Generally annealing consists of increasing the material temperature to facilitate atom diffusion, hence allowing the atoms to migrate from a high-energy position to a less stressed place. At higher temperatures annealing may be performed to completely eliminate the strain hardening achieved during cold working. However, annealing at a lower temperature may be used to eliminate the residual stresses produced during strengthening without seriously affecting the mechanical properties. This treatment is suitable for materials with efficient

dynamic recovery mechanisms based in the stacking fault energy, normally in BCC and some FCC metals (Hosford 2010).

The concept of staking fault energy is linked to the effect of partial dislocations. In some materials it can be observed an interruption of the normal stacking sequence of atomic planes when a dislocation propagates. This is because in some metals a one-step dislocation movement represents a larger energy barrier than a two-step path by an intermediate position with lower energy (green position in Figure 2-21) (Hosford 2010). The energy of this intermediate stacking position is called the stacking fault energy (SFE). If the SFE is too high, one-step dislocations are favored. In contrast, when the SFE is low, dislocations will propagate by two partial dislocations with a stacking fault in between. The width of stacking fault is a consequence of the balance between the repulsive forces between two partial dislocations on the one hand, and the attractive force due to the energy of the stacking fault on the other hand.

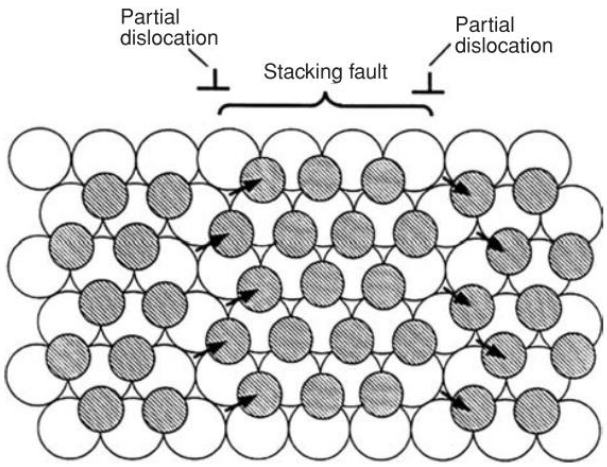

Figure 2-21 Illustration of two partial dislocations with an stacking fault in between (Hosford 2010).

The efficiency of dynamic recovery in high SFE metals is given by the possibility of dislocations to associate to absorb further strain. The dynamic character refers to the continuous rearrangement of dislocation to absorb continuous strain. This factor is not favored in lower stacking fault energy materials since they tend to display partial dislocations. They require some energy for cross-slip and climb to other slip plane, being more easily clamped in obstacles (Püschl 2002). In contrast, in high stacking fault materials the dissociation of a full dislocation into two partial dislocations is energetically harmed. This facilitates dislocation climb to another slip plane when an obstacle is reached, or to accommodate strain in a new direction. Hence, high SFE materials like ferritic steel and aluminum will redistribute dislocations relatively easy to accommodate strain, being that the basis of dynamic recovery, where the original grains get increasingly strained, but the

dislocations sub-boundaries remain more or less equiaxed by larger dislocation mobility (Guo-zheng 2013).

As shown in Figure 2-22, after cold working grains largely deform, but sub-structures of dislocations inside the grain remain largely equiaxed. A process of partial annealing would transform some of the sub-structures into proper grains, leading to a refined structure partially relaxed. This last step is known as static recrystallization.

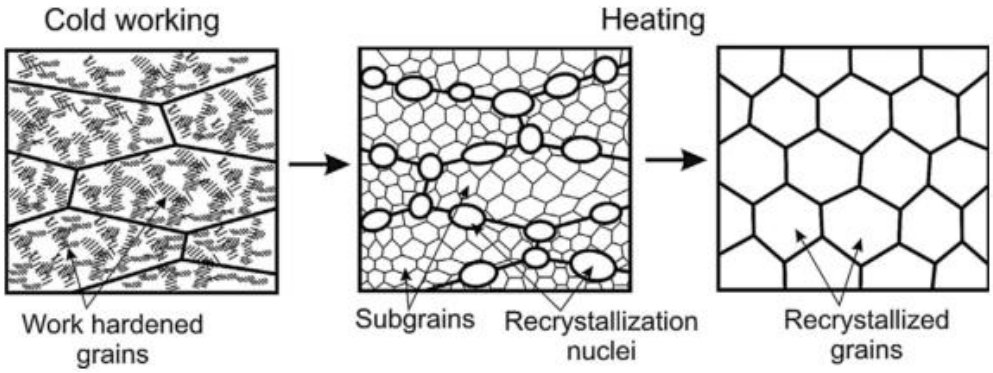

Figure 2-22 Schematic representation of the static recrystallization taking place during the annealing of strain hardened materials. Note the equiaxed distribution of sub-grains previous heating (Sakai et al. 2014).

A similar mechanism can be used to reach more refined structures by a continuous working-and-heat process, i.e., dynamic recrystallization. This is a process where a crystalline material continuously changes its grain distribution by sustained thermomechanical loads. In addition, from the mechanical point of view, during recrystallization material's ductility increases, while develops a drastic decrease of strength during the process (Landau et al. 2016; Rittel, Landau, and Venkert 2008).

However, it should be mention that the process of dynamic recrystallization is still under certain controversy. The understanding of metals and alloys behavior at hot deformation condition has a great importance for designers of hot metal forming processes, like rolling, forging and extrusion. Additionally, because of its effective role on metal flow pattern in harsh conditions, fields like high speed machining or ballistics largely feed from fundamental knowledge of extreme thermomechanical behavior. However, in these last cases, the kinetics nowadays is not clear.

Generally, during a hot deformation process a metal is liable to undergo work hardening (WH), dynamic recovery (DRV) and dynamic recrystallization (DRX), metallurgical phenomena for controlling microstructure and mechanical properties (Ihara and Miura, 2004). At a microstructural level DRX begins when strain hardening in addition to dynamic recovery can no longer store more immobile dislocations. At this point, when this critical strain is reached in a ductile metal at certain temperature, mechanisms of strain-hardening and

dynamic recovery cease to be the principle responsible of the strength-strain behavior, and DRX accompanies the process.

In practical metallurgy, the activation of DRX affects the crystallographic texture and thus, the material anisotropy. For example, DRX eliminates some crystal defects, such as part of dislocations resulting from work hardening, which will improve hot plasticity, refine microstructure, and reduce the deformation resistance for further strain. Thus, recrystallization can be considered to be a microstructural softening mechanism.

The present work will concentrate on the group of metals that express high stacking fault energy, i.e., metals that tend to avoid partial dislocations. From a fundamental point of view high stacking fault energy (SFE) metals, such as aluminum alloys, alpha titanium alloys, and ferritic steels, undergo a continuous dynamic recrystallization during high temperature deformation. In particular, due to the high efficiency of dynamic recovery, new grains are not formed by a classical nucleation and grow mechanism. Instead, the recrystallized microstructure develops by the progressive transformation of subgrains into new grains, within the deformed original grains. This relies on the plasticity mechanisms promoted by strain hardening and dynamic recovery, which progressively accumulate dislocations in low-angle (subgrain) boundaries. However, at high temperatures mobility of dislocations would facilitate the movement of sub-grains walls to accommodate more strain. In addition, at these temperatures many alloy obstacles for dislocations are eventually dissolved favoring mobility. These two factors enhance the capacity of dislocation to associate. Hence, even if the dynamic character of the DRX process would introduce a huge amount of simultaneous dislocations, mobility of these defects would facilitate the rearrangement of sub-grains walls to accommodate large strains. At the point the angle among subgrains reach a value to make they have certain incoherency in the boundary, final transformation into proper grains is promoted by the re-arrangement of atoms by diffusional processes favored at high temperatures). Thus, on each step, dynamic recrystallization leads to a relatively relaxed lattice with micro-sized microstructure of equiaxed grains ready to absorb further strain. Once a new grain is shaped, the process starts again by the development of subgrains. Thus, giving the dynamic character of this recrystallization.

This succession of events has been used to describe the process commonly seen in industrial DRX. However, it should be mention that, while the process is diffusional-related, it should express strong time dependence. This has been matter of controversy, since it is not clear how dynamic recrystallization develops in high-speed machining or ballistics tests.

2.4 Mechanisms of plasticity in metal cutting

The effects of metal hardening and softening described in previous section have been exploited industrially for different tasks. Industrial work hardening and recrystallization has been mainly used to engineer the properties of structural alloys for specific purposes. Ductility, yield stress and ultimate tensile strength (UTS) can be largely enhanced by proper control of the microstructure. However, the same mechanisms are known to be produced in other scenarios. Processes of extreme hardening and recrystallization have been reported in metal forming, machining or terminal ballistics.

In the case of machining, such process presents one of the largest strain-rates of the whole range of materials processing. While the industrial relevancy has pushed metal cutting research for decades, the unique conditions and the small area of contact in the proximity of the cutting edge have made invisible the phenomena. There, the material hits the tool at velocities well over 1 m/s, and deforms more than 100 % in a fraction of millisecond (M. F. Ashby, Gandhi, and Taplin 1979). There, traces of large microstructural hardening and softening in the proximity of the tool edge has been recently reported (Childs 2013, Kümmel et al. 2013, Courbon et al. 2013).

An example of remarkable hardening during machining is given by a process known as built-up edge (BUE). This effect refers to progressive accumulation of ultra-refined and layered material in front of the cutting edge. These depositions that cover the tool harden to the point of acting as effective cutting edge against the workpiece material (Figure 2-23b).

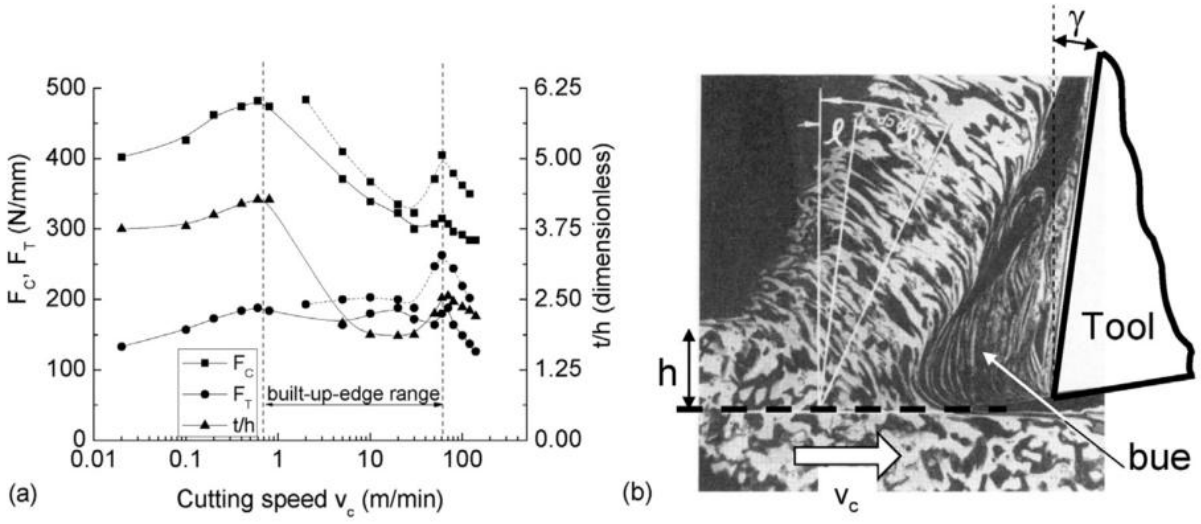

Figure 2-23 Built-up edge (BUE) during machining. (a) effect of appearance of BUE in forces and chip thickness. (b) image of a BUE acting as effective cutting edge (Childs, 2013).

Figure 2-23a depicts the effect of BUE appearance in the cutting and feed force, and in the chip thickness. As shown, forces and chip thickness reduce during the appearance of

BUE, what is related to the change in the effective rake angle. Once BUE disappear forces and thickness obtain larges values (Childs 2013).

Kümmel et al. (2014) analyzed in detail the microstructure of the built-up edge (BUE) after medium-speed cutting of AISI 1045 steel. They reported a layered and lamellar structure of reinforced metal (Figure 2-24). The fibril structure denotes a remarked direction reallocation of the microstructure. They are sings of extreme work hardening with no relaxation. The hardness value of the deposits grew up to 6200 of Martens hardness (MH). An extreme value in compression to the average value of 2766 MH present in pearlitic phase in the original material.

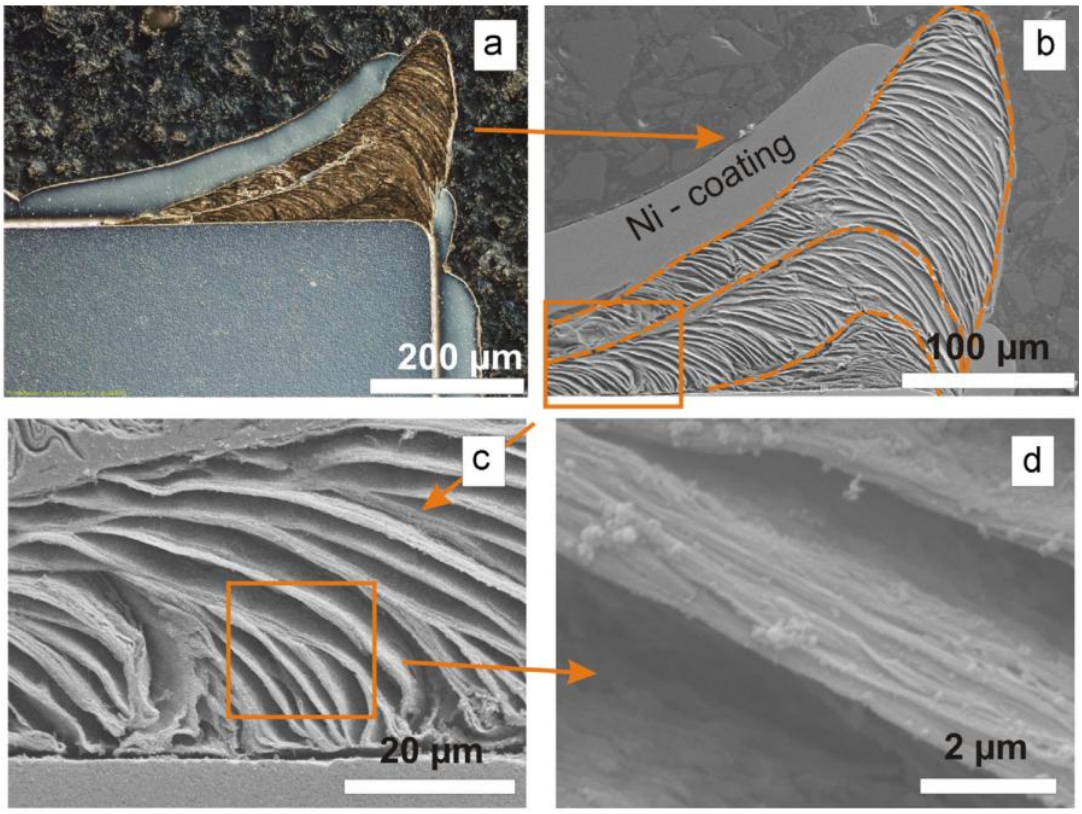

Figure 2-24 (a) Optical and (b,c,d) electron micrographs of a section of the a built-up edge in from of the cutting tool after an etching process (Kümmel et al. 2013).

On the other hand, effects of softening have been seen during machining as well. At large cutting speeds traces of equiaxial grains in the chip side in contact with the cutting tool has been recently reported. Grains of SSZ are refined to about 200 nm and tend to equiaxity in the proximity of the tool, in contrast to rest of the chip. Appearance of equiaxial grains in SSZ was proposed to be due to recrystallization or phase transition (Pu et al., 2015; Subramanian et al., 2002). However, resent research denoted a reduction of the residual stress in this region, thus pointing that recrystallization plays a roll (Courbon et al., 2013).

The study of Courbon et al. (2013) pointed out that the machining of AISI 1045 steel at speeds over 200 m/min induce a particular refinement of the structure in the secondary shear zone of the chip, present as micrometric and sub-micrometric grains with an equiaxed aspect and no signs of crystallographic texture, as shown in Figure 2-25.

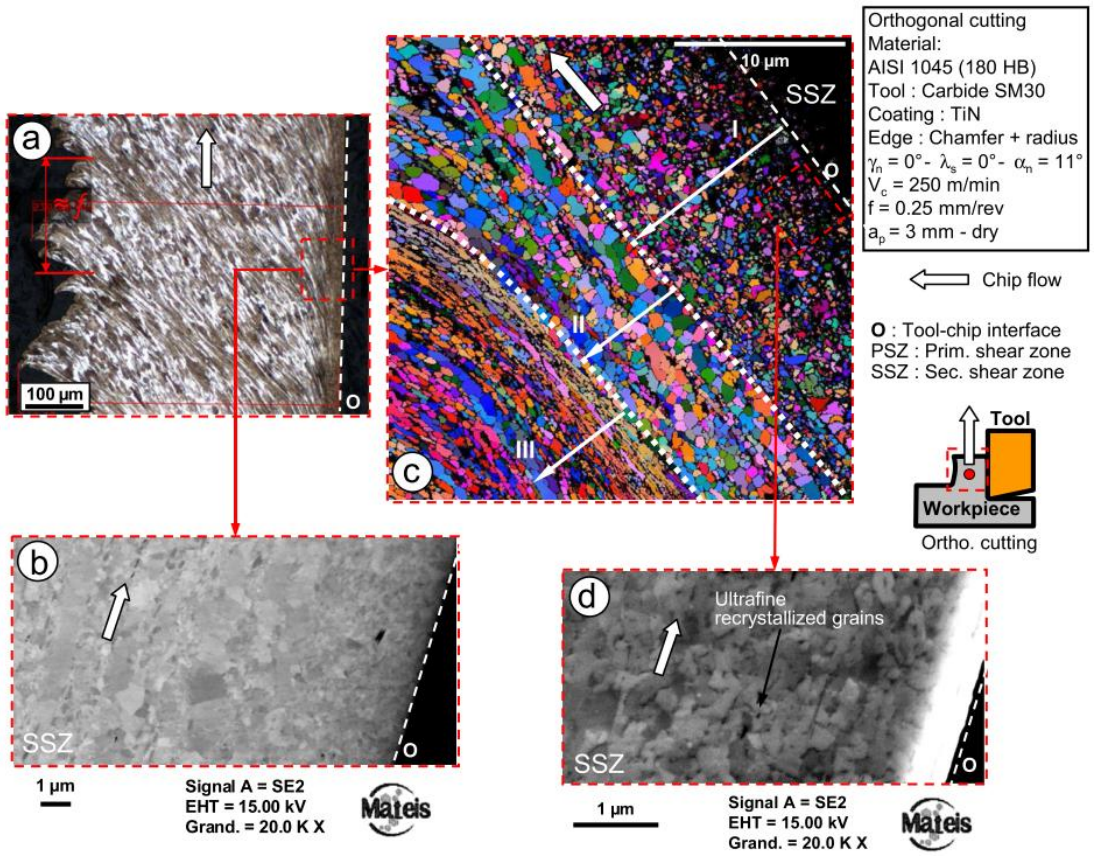

Figure 2-25 (a) Overview of a chip cut at 250 m/min. (b,d) SEM micrographs of the SSZ side of the chip with signs of structure decomposition. (c) image depicting crystallographic distribution in SSZ (Courbon et al. 2013).

While these two examples show traces of large microstructural hardening and softening, it can be argued the necessity of developing of further understanding of the processes occurring in the close proximity of the tool. It should be mention that most of the energy of the cutting process is spent in chip deformation and chip-tool friction, however a relevant part of the processes has not been revealed.

2.5 Mechanical machining at SEM

The microstructure study presents many aspects that need to be investigated with high-resolution devices. Furthermore, modern steels present features that can be studied only in the micrometer and nanometer regime (Ma, 2006). Hence, the use of electron microscopes is becoming relevant for these purposes. Several publications in the last years have shown a

renewed interest in the observation of workpiece and chip generation under the electron microscopes. In this field Heo *et al.* presented an extensive research on the tool wear in scanning electron microscopes (SEM) (Heo, 2015) In that case, hard metal was cut under the SEM. Their experiments (Figure 2-26) show a clear shear in front of the tool-workpiece interface.

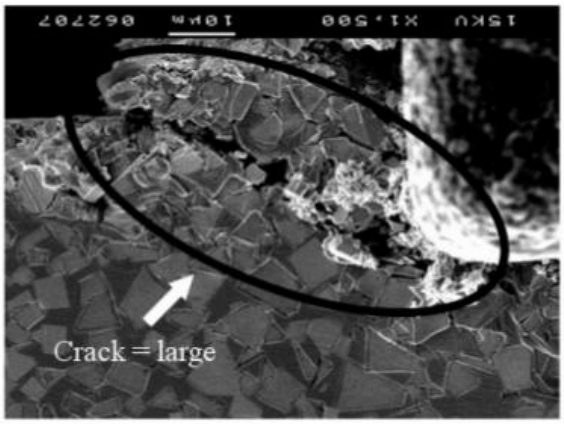

Figure 2-26 Tungsten carbide cutting under SEM at 10um/s (Heo, 2008).

In a more recent publication, Ye *et al.* (2014) went into relative high-speed cutting chips analyzed with the same technique. Both papers demonstrated the potential of the technique in this field and opened a niche for extensive analysis with further electron microscopy methods.

More recently, Fang *et al.* presented a self-constructed device able to perform cuts with a feed size in the nanometer regime under the electron column (Figure 2-27). Cutting experiments with such device have shown chip generation down to 10 nm, which has led to a particular morphology. Such device ensembles multiple positioners and manipulator in a compact structure (Fang, Liu, and Xu 2015).

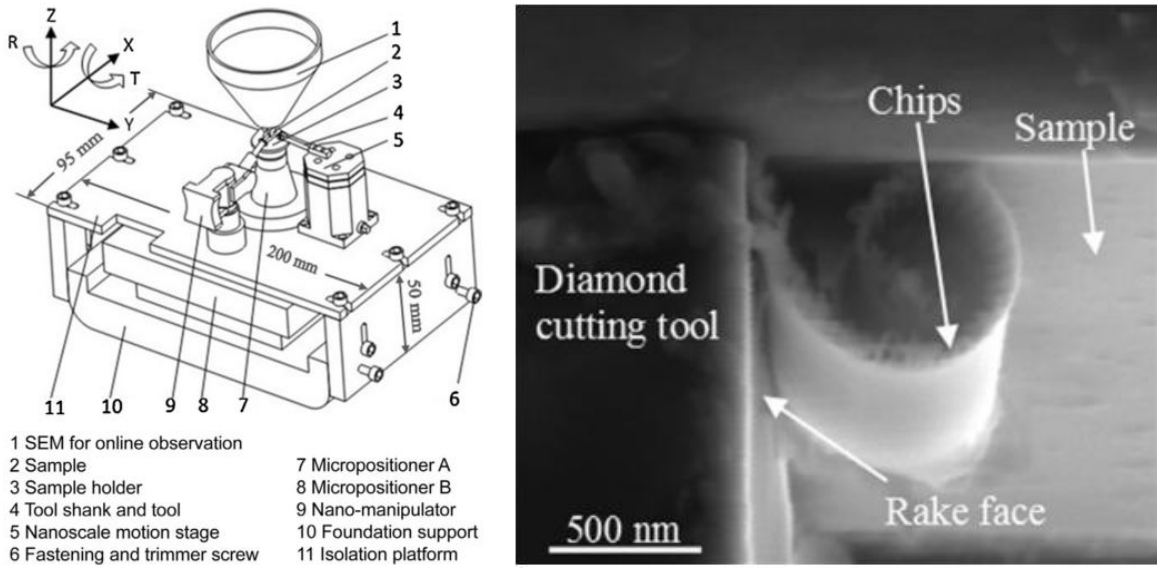

Figure 2-27 Cutting process imaged by scanning electron microscopy. The cutting tool is moving to the right creating a rounded chip (Ye, 2012).

These recent publications open an opportunity to study the evolution of the microstructure during the machining process. The very small features present in steel and nickel superalloys can be studied with modern high precision devices, in particular electron microscopes. In addition, it was already demonstrated, that a cutting process could be directly scanned inside one of these microscopes. Thus, the state of the art supports this new approach to study the microstructure during the cutting process. The present work makes use of this approach (see Chapter 6) to increase the fundamental knowledge of the relation between microstructure and machining.

2.6 Simulations of machining

In machining science, there are a number of phenomena that are not easily observed or not subject to direct experimentation, so that initially the influence of a number of process parameters has to be studied by empirical correlation. In the last decades different models to predict a number of cutting parameters has been developed (Arrazola et al. 2013). These predictive physics-based models are used to estimate fundamental process variables (strain, stain-rate, stress, temperature), which are used to calculate industry-relevant outcomes such as tool wear, residual stress, burr, chip breakability, etc. Predictive models span numerous methods: analytical models, finite element models or atomic-based models (Melkote et al. 2017). While analytical models represent a fast approach to predict cutting forces, strains, strain-rates and temperatures, they have some limitations to predict complex non-linear behaviors. Thus, numerical methods have reach great attention to obtain values of the

fundamental variables distributed in the space. Common models used are based on Eulerian or Lagrangian finite element methods (FEM).

FEM techniques use a representation of workpiece and cutting edge based on a mesh of nodes in which certain boundary conditions are implemented. This can be observed in Figure 2-28a, where a model and input parameters leads to results which can be plotted as a distribution over the original mesh (Arrazola et al. 2005). In order to determine the distribution of temperature, stress or strain in the mesh, and subsequently flow of material, these techniques base on the assumption of continuity between adjacent nodes. This continuity is represented by the equations that describe the variation of parameters among nodes. Thus, by FEM physical phenomena occurring through experiments of machining are expressed with the base of continuum mechanics.

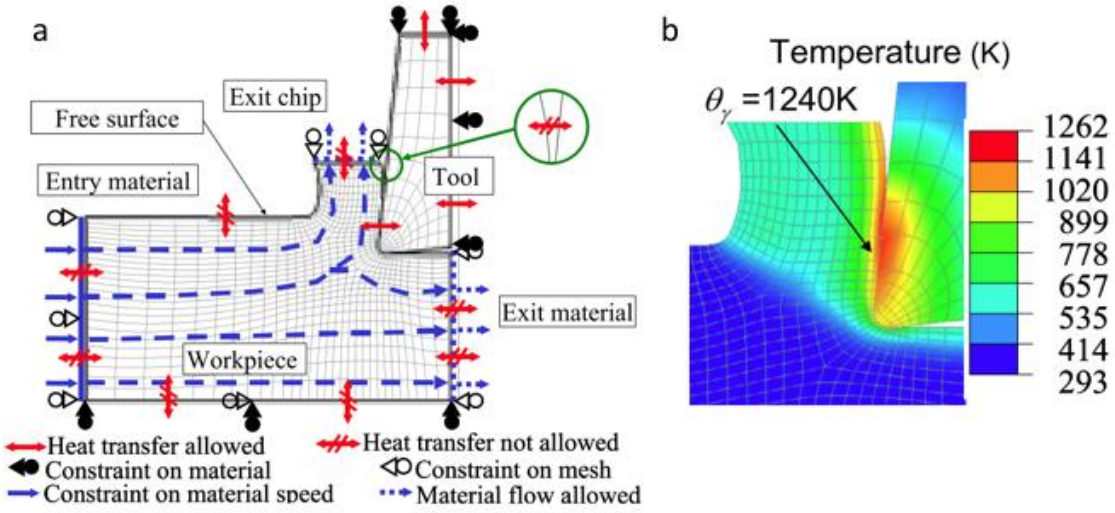

Figure 2-28 (a) Discretization of workpiece and tool by a mesh of elements, where certain boundary conditions are implemented. (b) Results of the simulation in which it is plotted the distribution of temperatures as function of the position, where 1240 K is the maximum temperature (Arrazola et al. 2005).

The coupling of the material of study and the mesh of nodes has been matter of research in terms of model coherency. In a first approach it should be consider that during machining material seriously deform, and this makes necessary a non-linear method to consider geometry evolution. The typical approaches consider coordinates linked to the material geometry (Lagrangian approach) or consider material geometry changes across a fixed mesh of nodes (Eulerian approach). Since coordinates linked to the material could induce errors on large deformations (unless proper re-meshing), Eulerian formulations has been largely chosen for workpiece materials, being possible to handle arbitrarily large deformations and the generation of new free surfaces (Benson 1997). However, Eulerian approach under-represents the contact between unequal materials, what hampers traction across material interfaces and limits the shear stress according to a Coulomb friction law,

being this last effect better represented with the Lagrangian approach. Thus, methods to assign Eulerian or Lagrangian approach to different parts of the scene has been proposed (Benson and Okazawa 2004). This last strategy has been widely used to simulate the workpiece and chip material in the community of machining and has been used un chapter 4.

The difficulties for representing a process like machining, in which solid material flows, by continuum mechanics has deviated some attention to other techniques based on another approach. In the last two decades a number of authors have used atomistic simulations, mainly molecular dynamics (MD), to simulate the mechanics of cutting. This technique takes the base of individual atoms which are connected by a potential. It presents a computation cost much larger than the one in FEM. In contrast, this approach has the advantage of permitting large deformations without incoherencies, while being the solid nature of the model well stablish.

In initial efforts of atomistic simulations of cutting, the computational experiments proposed by (Inamura and Takezawa 1992) pointed to the influence of crystallographic orientation, what can be expected according to the nature of lattice deformation (chapter 2). Nevertheless, the influence of grain boundaries represents a less obvious problem. The authors observed that deformation occur first in the boundaries, and then propagates across grains. These simulations highlight the role of lattice phenomena in the material response to machining, however they are not representative of real experiments (only 204 atoms were simulated).

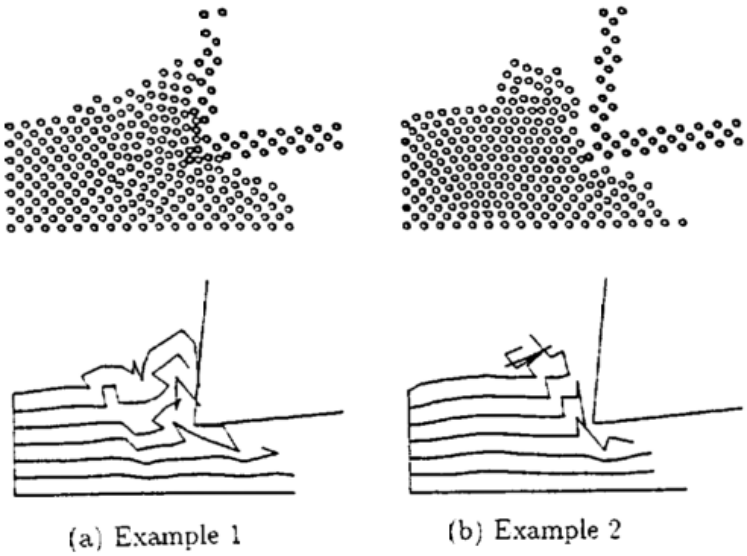

Figure 2-29 Molecular dynamics simulation of 204 atoms of copper with (a and b) two different force distribution between workpiece and tool. Upper side is atoms view, and bottom side trajectories representation (Inamura and Takezawa 1992).

More recently (Pei et al. 2007) made use of a system of 4 million atoms of cooper to study the introduction of defects in the workpiece by the action of a cut of 2 nanometers of feed (Figure 2-30). They have pointed that the dislocations that govern the deformation of cooper stick to the <110> family of directions, expected for this material as shown by (Kim and Moon 1996). Thus, the progression of defects into the metals strongly depend on lattice planes available to transmit dislocations into the workpiece.

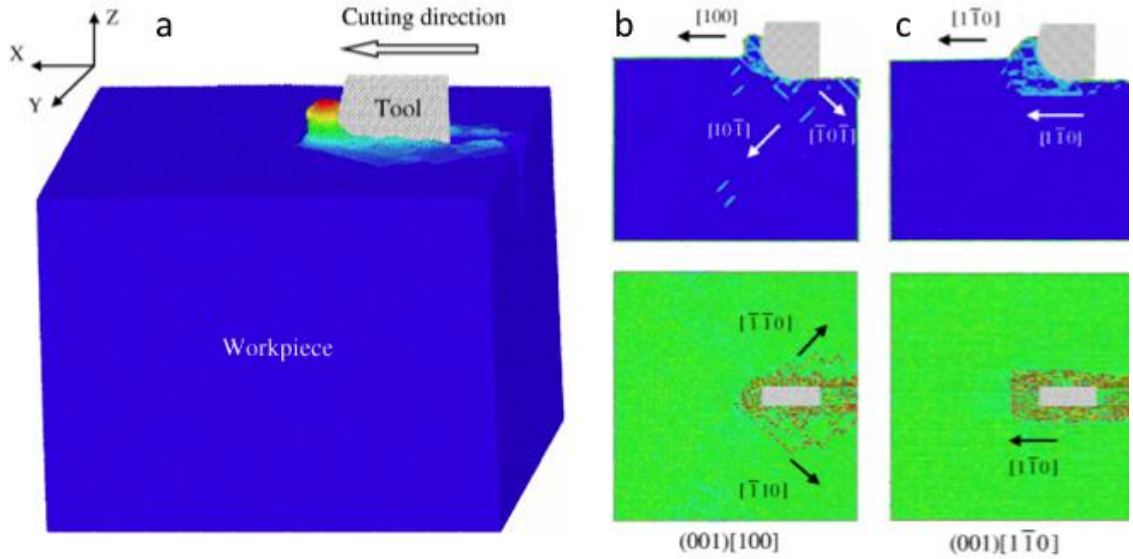

Figure 2-30 Block of 4 million atoms of copper cut by a moving tool (a). The atoms at the bottom of the block are defined to maintain a constant temperature, so called thermostat atoms. (b and c) effect of cutting against different crystallographic orientations (Kim and Moon 1996).

Pei et al. (2007) also treated some other complexities connect MD and realistic effects, like heat dissipation. In MD all the heat generated remains in the system. A typical strategy to simulate a flow of heat is to force certain temperature in the atoms of the boundary. Hence, these atoms act as heat drains. Another element to be addressed is the interaction of workpiece material and tool material (typically carbon). The materials of both sides use to interact by potentials defined for pairs of atoms. The same kind of interaction has been used by Goel et al. (2015) to simulate dry and lubricated cutting (Figure 2-31). However, in both cases the interacting surface free of the tool (the rake face) lacks features and topography. Thus, the tool-chip friction is based on atomic forces.

Goel et al. also make use of periodic conditions in the plane perpendicular to the cut. This technique induces mirror forces at both sides of the plane, leading to conditions similar to the ones in the center of a chip. This allows to reduce the number of atoms of the simulation on the one hand, and to force a situation of plane deformation, hence similar to the 2D Merchant model.

While the last examples show the potential of this technique of simulation to address the effect of material crystallinity, it can be argued the necessity of developing the technique to develop mechanisms that affect a large volume of atoms. The contributions of last authors have pushed the techniques closer to real experiment, however relevant aspects of the cutting process should be considered for further development.

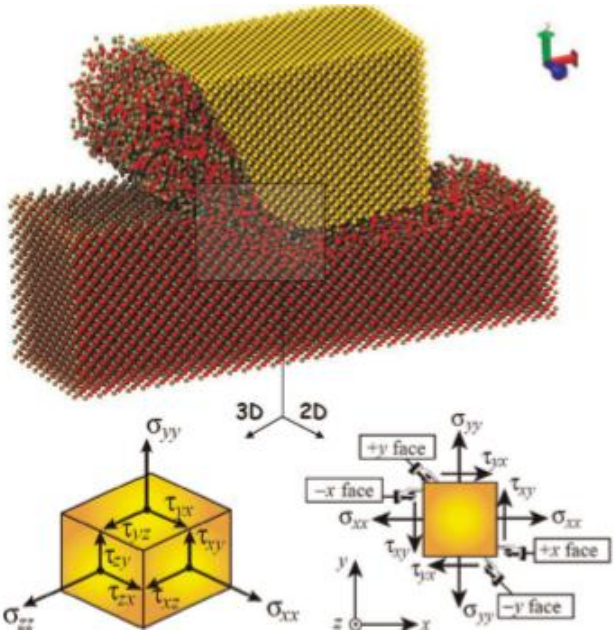

Figure 2-31 Periodic conditions in the direction perpendicular to the cut entails mirror forces in that direction. In that case deformation restricted to a 2D plane (Goel et al. 2015).

In summary, FEM is a computationally efficient approach, with simulations in real scale and time, and producing directly interpretable results. However, it deeply depends on the primary models (cannot predict new phenomena) and on the input parameters, which must be determined by other means. In turn MD has a high computation cost and cannot be easily up-scaled to the real world. From the other hand side MD is not bound to any macroscopic model and predicts processes from the basic principles (interatomic potentials). As such it is suited to reveal the atomic mechanisms of deformation, and thus to predict the new phenomena.

This thesis makes use of FEM modeling in chapter 4 for simulations of machining in real size and time scales, and addresses in chapter 7 the potential of MD for reproducing several atomic mechanisms of plasticity in the close proximity of the cutting tool.

2.7 Review conclusions and motivation

The review of the literature presented in this chapter shows that a great effort has been applied to disclose the conditions and the behavior of the material during the cutting process.

As shown, temperature and strain have been recently disclosed in the tool and in the primary shear zone respectively. However, the interaction between material and tool in the proximity of the contact under conditions of industrial machining are roughly resolved. In addition, the influence of each kind of microstructural feature is missing. The impact of the different metal phases has been under empirical study for a long time (Brunzel and Fomin 1997; Simoneau, Ng, and Elbestawi 2006; Abouridouane, Klocke, and Lung 2014). However, the physical details of the grain distribution, the volume fraction of phases and their morphology, or the chemical distribution along grains are examples of microstructural aspects that have not been extensively studied for the dynamic conditions imposed by machining. Thus, the lack of certain phenomena understanding has hampered a model constructed from the fundamentals.

In many cases, the present knowledge of crystalline metals and their mechanisms of plasticity provide a powerful tool to reconstruct difficult-to-observe phenomena. Courbon et al. (2013) have shown signs of microstructural recrystallization in the secondary shear zone during steel cutting. The observation of an area of high grain refinement, previously marked as white layer, could bring some light to the mechanics of the tool-chip contact. However, the origin and consequences of this process of recrystallization has not been disclosed.

Some authors have proposed new approaches to disclose the chip-tool interaction. Fang *et al.* (2015) pointed out some advantages of in-situ cutting watching inside electron microscopes. Unfortunately, just a few parameters were extracted from those measurements. On the other hand, Heo et al. (2015) have shown in more detail the mechanism of cutting of tungsten carbides. However, any of the experiments until now have afford in-situ micro-machining on structural materials like steel or aluminum.

The main motivation for the present work relies on disclosing the thermo-mechanic phenomena that govern the process of cutting, particularly in the shear zone in the proximity of the tool contact. These phenomena should be linked to the atomic mechanisms of plasticity activated during metal deformation. As observed by Courbon et al. (2014), theses mechanisms produce some traces in the resultant microstructure and plasticity. Based on that, the approach proposed in this thesis consists on acceding the mechanics of contact between chip and tool by a microstructural analysis down to the nanometer regime.

For that, an extended work of microscopy has been planned. In a first stage, a number of experiments on structural steel will be made for subsequent microscopic analysis; both the contact mechanics and the properties (morphological and mechanical) of the microstructure produced. The experiments focus on the evolution of the microstructure in contact with the cutting tool down to the nanometer size when the cutting speed increases. It has been

previously reported an increase in the velocity induce some change in the cutting regime, however this effect has not been documented from the microscopic point of view.

In a second stage, the area of the chip in close contact with the tool has been matter of a full characterization. As some authors have pointed, there is a unique structure there. However, the small dimension of this area has hampered a concise study. This has been addressed in this work using *state-of-the-art* techniques to perform morphological, structural, chemical and mechanical characterization in localized areas.

In a third stage, effort has been applied on building a testing device for micro-cutting in-situ in a scanning electron microscope. Until now, a number of authors have performed experiments of machining in the SEM chamber with success. This has led to observed certain effect at high resolution, while being further in-situ analysis troubled by complex devices. In order to solve that, in this stage it have been designed a cutting setup that permits perform metal cutting, and subsequent operations of characterization with electron microscopy, and thus accessing the microstructure in unaltered conditions.

In a final stage, it has been tested the technique of molecular dynamics to reproduce part of the phenomena of cutting. As shown, FEM does not allow to reproduce the effect of deformation in crystals, being an atomistic method appropriate for that. In spite of the effort of the community, most of the attention has been applied in simulations roughly applicable to experimental machining. This stage attends such approach.

Besides the interest of solving the scientific questions, this project has a remarkable industrial interest. This project focuses on two industrial materials with very different strengthening mechanics, ferritic-pearlitic steel and aeronautic aluminum. In the case of steel, the alloy of use is AISI 1045 with 0.45 % wt. of carbon. Steel widely used in the automobile industry, machine fabrication and structural constructions, as long as it provides appropriate mechanical properties and relative low prices. On a further step, the interest is focused to aluminum 7475, a relative soft alloy which will be used in micro-cutting. This alloy is also widely used in machining methods for parts fabrication in the aeronautics.

3 Methods and materials

This chapter describes experimental methods and materials that have been employed along this thesis.

As soon as structural characterization is the main experimental approach used in this thesis description of the methods starts from introduction in micro/nano structure characterization techniques. The first section is focused on the set of techniques used to characterize material microstructures, which includes optical, scanning (electron or ion) microscopy, and data post-processing. Of the same importance are the techniques for nano-mechanical characterization: nanoindentation, nano-pillar compression and bending, described in section 3.2. The third section focuses on the application of the above techniques for complete structural and micromechanical characterization of the AISI 1045 steel and 7475 Aluminum used for cutting experiments in this work. Finally, the forth section describes experimental setup for macroscopic cutting tests, that served as a source for the samples for microstructural analysis.

3.1 Characterization methods

The present work, which addresses fundamental aspects of tool-chip interaction, is strongly linked to materials and process characterization. Due to the complexity and different length-scales involved, details of materials microstructure have been revealed by different techniques. Light microscopy, scanning electron and ion microscopy, electron back-scattered diffraction, X-ray microanalysis, have been used to characterize the structure and composition of the samples. In this section, before detailing each technique, an introduction of image formation in microscopes is firstly addressed. Subsequently, for each technique a brief introduction is provided, along with the aspects to consider in metals characterization, the way how they have been applied and the equipment used.

3.1.1 Image formation in microscopes

The process in which a two-dimensional image of an object is constructed may differ from one microscopy technique to another. The most natural one, since it follows the system of perception of the eye, is the one present in typical optical microscopes. In that case an object is illuminated, and the optical response reach lenses that project the image over a light-sensitive surface; this could be a human eye, a photographic film or a two-dimensional optical sensor. The complete two-dimensional image intensity distribution is projected simultaneously. Digital optical sensors for this class of the microscopes are constituted by surfaces covered by ordered arrays of light-to-charge transducers.

Another strategy of image formation is scanning, i.e. successive compilation of the points of an image array one by one. In this case, only one point of the object/sample of interest is exited at a time. This excitation may be by a sharp hard probe (like in scanning probe microscopy or in nanoindentation), or by a focused electron/ion beam (like in scanning electron/ion microscopy). Excitation results in a local site-specific generation of a number of responses that can be recorded by corresponding scalar detector. In order to construct the image, the probe scans the surface of the object point by point, and for each one a detector records the respond signal. In this way, an image corresponding to each particular signal is constructed pixel by pixel. Contrary to the previously described strategy, each pixel of the image corresponds to a different moment in time. Detector is usually of scalar type, yet it should have reasonably small respond time to allow fast image acquisition. Among the benefits of this strategy is the ability to collect and differentiate a broad variety of signals at the same time simply by utilizing multiple detectors for different response signals. This strategy is used by scanning electron microscopes (SEM).

In the present work optical microscopy is used mostly for preliminary inspection, being most of the material characterization made by SEM-based techniques. Here the microscope resolution is described in the sense of *minimum resolvable distance*, which is the minimum distance between distinguishable objects in an image.

3.1.2 Optical microscopy

In optical microscopes, a system of lenses is used to reach magnifications up to 1000x (limited by the wavelength of the light). This leads to an image resolution in metallographic microscopes of the order of 1µm, which is generally enough for a rough analysis of the microstructural features in industrial alloys. A big advantage of an optical microscope is the simplicity of operation in comparison to e.g. electron microscopes. Thus, it operates at ambient conditions on air and does not require a complex electronic and vacuum systems.

A relevant benefit of this technique is an ability to examine a large area of the specimen in a short time. Since the magnification is generally high enough to distinguish grain boundaries and the field of observation is broad enough to cover a statistically representative sample surface, optical microscopy is broadly used to investigate the general parameters that characterize a specimen with medium-to-large grain size (Mukhopadhyay, 2003).

The images in optical microscope are formed by contrast determined mainly by topography and difference in light reflectivity of different phases. In Figure 3-1 this contrast has been enhanced by the material specific sample preparation, since the preparation method is designed to act on specific features, which are removed faster than other, inducing certain topography. In that image, a chemical method (etching with Nital: nitric acid and alcohol) leads to differential etching rate depending on crystal orientation or metals phase, what makes grain boundaries fully visible optically (Pardal et al. 2009; Bytyqi et al. 2011; Boneti-Toldo et al. 2017).

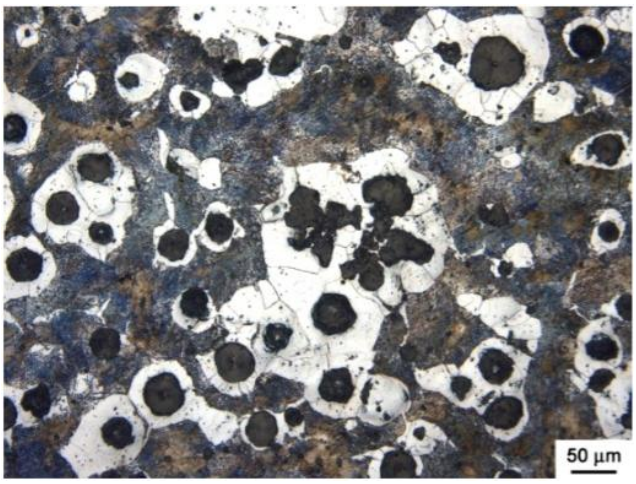

Figure 3-1 Alloy treated with Nital to reveal pearlite, graphite (black) and ferrite (white) (Boneti-Toldo et al. 2017).

In the present work optical microscopy have been used for two main tasks: to acquire the statistical grain size and phase distribution of the materials as received, and to investigate the topography of the chips and the rake surface of the tools. The features like chip thickness or tool-chip contact length, can be accessed optically without major sample preparation. These inspections have been carried out by the microscope Leica DM4000M. Samples have been polished mechanically with sandpaper down to 1 µm grain size with subsequent chemical attack by Nital (5 % nitric acid) to reveal the different sample features.

3.1.3 Scanning electron microscopy

Microscopes based on scanning electrons overcomes easily the spatial resolution of optical microscopes. This, at the cost of being able to inspect smaller areas, and the requirement of working in a controlled atmosphere of low-pressure or vacuum. Typical image resolution of SEMs reaches sub-nanometric values, what allows to distinguish details no accessible by optical microscopes, like intra grain details, precipitates or nano-crystalline microstructures.

A scanning electron microscope (SEM) uses a focused beam of high-energy electrons that hits the surface and produces a variety of signals. Generation and propagation of the electron beam essentially requires vacuum down to 10^{-7} mbar inside the microscope chamber. As mentioned above, in SEM a highly focused electron beam (the size of the focus can be below 1 nm) travels on the surface of the sample in a raster manner, and image formation is achieved by collecting of a point specific signal intensity. Thus, a SEM consists of an electron gun, a set of electromagnetic lenses to focus and orientate electron beam, and detectors.

Scanning electron microscopy is typically used to reveal the topographic features of samples. The spatial resolution overcomes largely the one in optical microscopes and, in the case of SEM, resolution is limited by the magnetic lens aberrations and the wavelength of the incident electrons. Typical image resolution of SEMs reaches sub-nanometric values, what allows to distinguish intra grain details, even of nano-crystalline metals.

Figure 3-2 shows a schematic representation of a modern SEM. After the electrons are ejected from the gun, they are accelerated, focused and directed to the sample surface via different electromagnetic lenses. The interaction between the impinging electrons and the sample produces different imaging signals, such as secondary electrons, back-scattered electrons and x-rays, which are collected using several detectors.

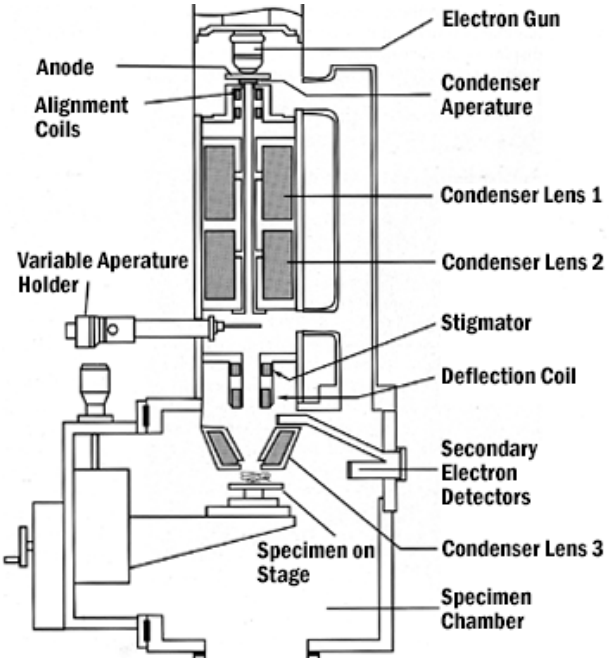

Figure 3-2 Sketch of a scanning electron microscope. The basic electron microscope system mainly consists of an electron gun, condenser lenses and a detector. The electron beam scans the surface in a raster manner, and a detector collects the emitted electrons. A processing unit analyses the data (location and intensity) to produce an image of the scanned area. ((University of Iowa 2016).

Commonly, in these microscopes the specimen response to the incident beam is collected in form of secondary electrons (SE). These electrons have energies of less than 50 eV and are formed by inelastic scattering. As the SEs possess very low energies, they are able to escape from the very surface of the sample and thus provide a high surface sensitivity. The intensity of the SEs emitted by the material depends on the topography, the atomic weight and the material structure. Thus, the image can reveal in sample surface features, chemical composition and grain orientation.

SEM is very good in revealing the topographic features of samples, as the intensity of secondary electron (SE) emission is strongly dependent on the local inclination of the surface feature to the detector, as observed in Figure 3-3, where peaks and valleys are highlighted by brightness and shadows.

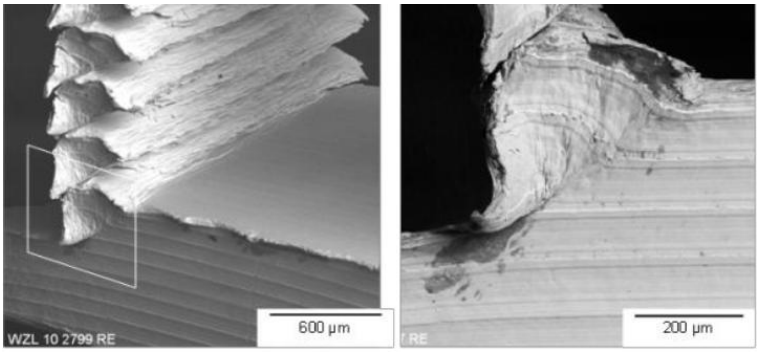

Figure 3-3 SEM image by secondary electrons acquisition.

As in other techniques, the sample preparation plays an important role in the characterization of alloy phases, since the material removal rate of a specific polishing method may be different depending on the phase (Mukhopadhyay, 2003), or even the crystallographic orientation (Szabó, 2012). Figure 3-4 presents a SEM image of dual phase steel where the martensite, ferrite and cementite particles show different contrast because of the surface preparation method used. In this case, the surface was electro-polished with an ethanol-2-butoxyethanol electrolyte.

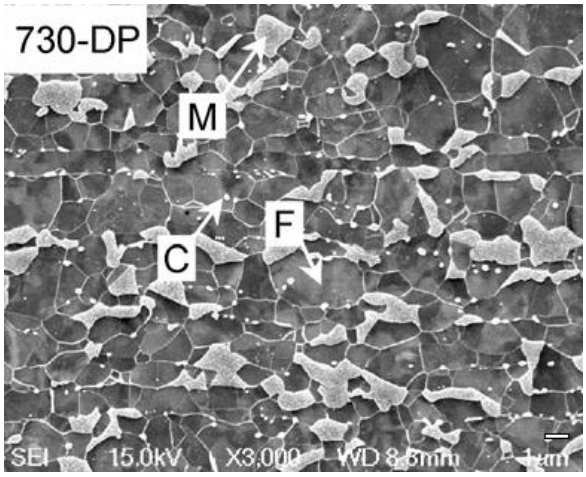

Figure 3-4. SEM image of a dual phase steel. Martensite(M), ferrite(F) and cementite(C) phases are distinguishable because of the preferential chemical attack caused during electro-polishing (Calcagnotto, 2010).

In crystalline materials SEs may additionally supply information about lattice orientation. The depth of penetration of the incoming electrons is affected by the regular arrangement of atoms in crystalline materials. If the incoming electrons encounter a low density of atoms, e.g. when they travel along crystallographic rows of atoms in the crystal, they can penetrate deeper in the material than for randomly oriented crystal. This effect is called electron "channeling". If primary electrons channel deep into the crystal, SEs which they produce cannot penetrate to the surface and corresponding crystal grain looks darker on SE image. This contrast is called "channeling contrast" and is used for visualizing grains of the same material with different orientation. Figure 3-5 images show enhanced contrast by channeling by using two different detectors.

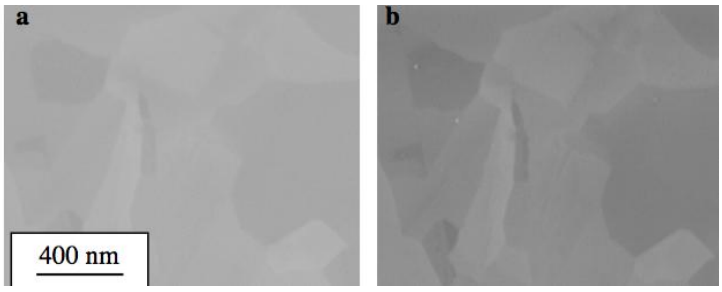

Figure 3-5 Electron channeling contrast between different Ti grains with two different detectors (a) E-T detector, (b) in-lens detector (Canovic, 2008).

Electron channeling can be utilized even in a more intelligent way: when the sample is strongly tilted, e.g. by 70° scattered electrons start to escape from the surface. In contrary to the primary electrons, having one defined propagation direction, scattered electrons travel in all directions. In the directions of crystal lattice planes, they experience channeling resulting in a shadow image of the local lattice at some distance of the sample. That is the basis for the electron back-scattered diffraction technique, where the electrons are collected after a fraction of them pass through a tilted sample.

3.1.4 Electron Back-Scatter Diffraction (EBSD)

Derivative techniques from SEM have demonstrated to be very useful for metal characterization. Electron back-scatter diffraction (EBSD) is a SEM based technique, which can be used to reveal the crystallographic orientation of grains present in the sample surface.

EBSD technique uses the pattern produced by the back-scattered electrons diffracted from the crystal lattice to analyze the sample crystal structure and orientation. The diffraction pattern is made of a combination of Kikuchi bands (Maitland and Sitzman 2006), where the centerline of each band represents the intersection of the diffracting planes with the EBSD camera. Measuring the positions of these Kikuchi bands on the image provides an unambiguous measurement of crystal orientation with extremely high accuracy.

Practically, in EBSD a suitably placed phosphor screen continuously registers the electron diffraction patterns to produce an orientation map as the electron beam scans the surface of the material. Figure 3-6 shows the basic configuration of an EBSD setup in a SEM (Klocke, 2014). The sample is tilted at approximately 70° relative to the normal incidence of the electron beam to maximize the back-scattered diffraction. The recorded diffraction patterns are subsequently analyzed by specific EBSD data software, so that different crystal-dependent parameter maps can be depicted.

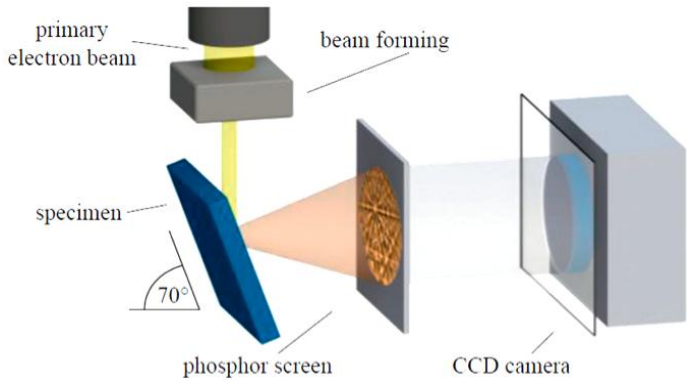

Figure 3-6 Typical EBSD configuration in a SEM. When the electron beam hits the surface, the diffracted electrons produce a pattern on the phosphor screen related to the lattice. Then, a piece of software is used to analyze the images and to map the orientation (Klocke, 2014).

The scanning of the sample with the electron beam and the simultaneous detection of the electron diffraction patterns by EBSD camera, after computer post-processing leads to orientation maps, that represent orientation of every grain. Statistical treatment of the orientation maps may reveal preferential orientations or microstructure.

Figure 3-7 depicts the result of EBSD mapping of a crystalline aluminum sample before and after a high deformation process (note scale difference).

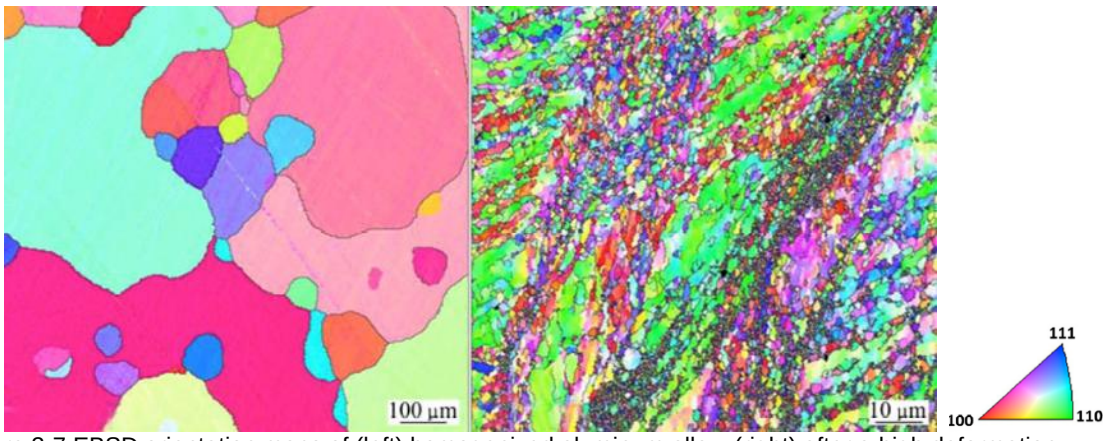

Figure 3-7 EBSD orientation maps of (left) homogenized aluminum alloy, (right) after a high deformation compression (Y. Chen, 2012).

Apart from grain orientation, raw data from EBSD scans provide valuable information about metal alloys. Various analytical tools have been developed to post-process such data. If the data is sufficiently precise, detailed map of small crystal orientation deviations (even inside grains) can be used to create the so called misorientation maps, which exhibit areas with a lattice distortion. For this purpose, the distortions in the registered Kikuchi bands have to be measured and compared with the pattern of a perfect lattice, revealing lattice deviations. These deviations were attributed to a large amount of geometrically needed dislocations in the material (Wright, 2011).

The information revealed by misorientation maps is qualitative and does not lead to a precise dislocation quantification. However, areas of metastable phases, material under stress or defect-induced distortions may be identified.

Figure 3-8 shows a fraction of a crystal-like atom arrangement, in which a dislocation produces a distortion in the lattice, which generates three sub-regions with different orientations. In this case, the EBSD pattern quality is degraded, as it is essentially a superposition of the patterns from the individual sub-regions. The degree of pattern degradation depends on the deformation degree within the interaction volume.

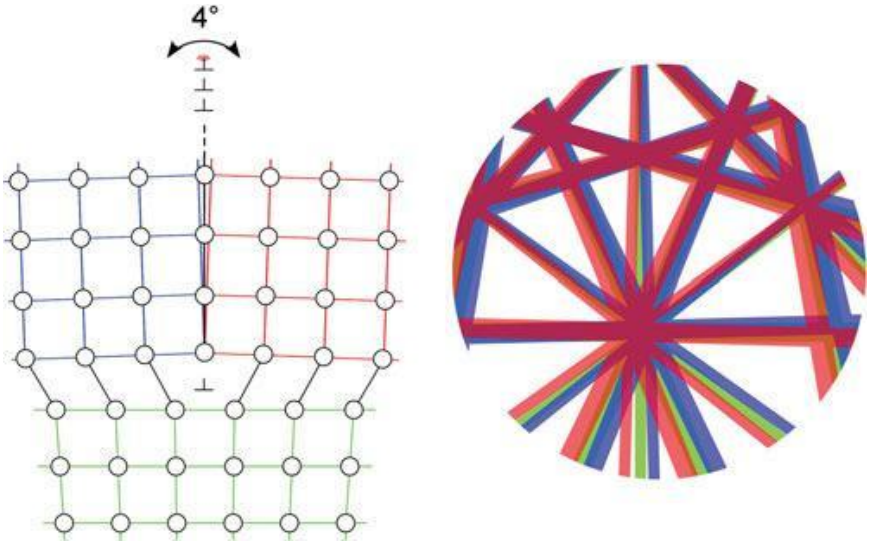

Figure 3-8 (left) how an edge dislocation deforms the lattice, and (right) shows the effect on an EBSD pattern (Wright, 2011).

In order to represent the degree of misorientation in a material, different analytical approaches may be used. The most important ones are the grain and kernel-based approaches. On the one hand, the grain-based approach uses the rotation of all the points inside a grain to assign a misorientation value to the whole grain. On the other hand, as represented in Figure 3-9, the kernel-based approaches use only groups of points (kernel) to calculate the misorientation. Accordingly, in every point an average misorientation is calculated as the difference between a certain point and all of its neighbors. The misorientation of the point (the kernel) would be the mean value of the points included (Calcagnotto, 2010).

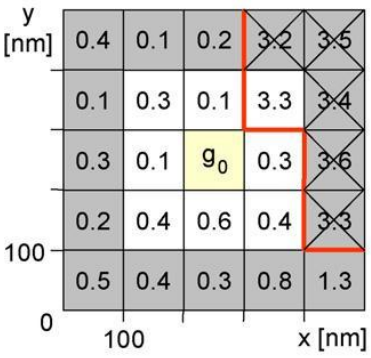

Figure 3-9 Misorientation processing using the kernel average misorientation approach. The software compares the orientation differences among different points, and it then assigns a misorientation mean value to a point or group of points (Calcagnotto, 2010).

An example of EBSD post-processing is depicted in Figure 3-10, which shows misorientation maps generated by EBSD on a dual phase steel sample (ferrite and martensite). In Figure 3-10a, the grain boundaries of the material are colorized in yellow and red. The yellow boundaries present high angle grain boundaries, whereas the red ones indicate small angle grain boundaries. Figure 3-10b demonstrates the misorientation map of the sample area in which the areas of high dislocation density (red) indicate the location of

martensite. High misorientation values are generally related to martensite and areas close to grain boundaries.

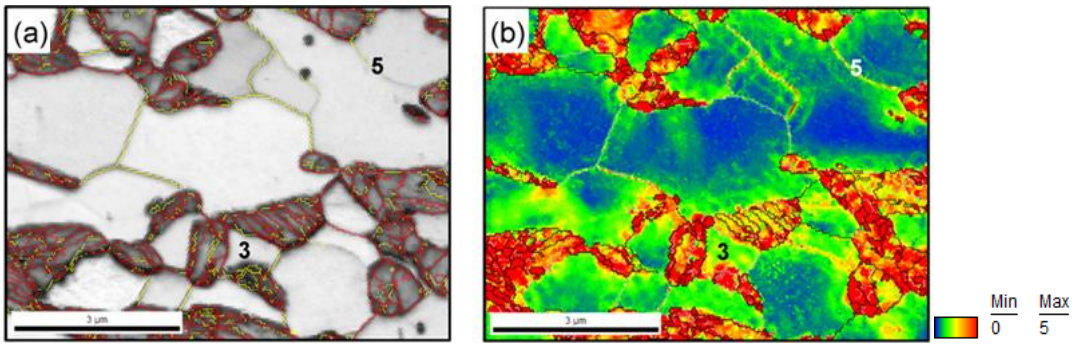

Figure 3-10. (a) is a grain boundary map of a dual phase steel. The yellow lines are related to high angle grain boundaries, and in red to low angle grain boundaries. (b) image shows the misorientation map, in which the range is from zero (blue) to five (red) degrees. The misorientation is generally related to the dislocation density, which is high at grain boundaries and in martensite islands (Calcagnotto, 2010).

In the present thesis an electron microscope Zeiss Sigma equipped with an EBSD camera from Oxford Instruments has been used. With this technique the microstructure of the workpiece and chips in terms of crystals distribution, texture and density of defects has been analyzed. Test has been performed with an electron acceleration up to 30 kv, and step size of 50 nm.

3.1.5 Focused Ion Beam

A focused ion beam (FIB) technique works in a similar way as a SEM, both techniques share multiple components. However, while the SEM uses a focused beam of electrons to scan the sample in the chamber, a FIB setup uses a focused beam of ions instead. In both cases, when imaging, the detector collects electrons.

FIB uses the same scanning principle as SEM does. However, as long as the mass of ions is at least 3 orders of magnitude larger than that of electrons, by carefully controlling the energy and intensity of the ion beam, it is possible to perform very precise nano-milling to produce minute components or to remove unwanted material. In addition, ion beam assisted chemical vapor deposition can be used to deposit material with a level of precision similar to FIB milling.

An ion beam setup is commonly added to a scanning electron microscope as a dual beam system. When an electron and ion beam system are built together, some synergies emerge. Both have corresponding system of lenses; however, they can share the same detectors. In typical configuration, the electron and ion beams intersect at a 52° angle at a coincident point near the sample surface, allowing for example immediate, high resolution

SEM imaging of the FIB-milled surface. Such systems combine the benefits of both the SEM and FIB and provide complementary imaging and beam chemistry capabilities.

While electron scans lead to refined imaged resolution, a relevant advantage of using ions instead of electrons for imaging is having a substantially enhanced channeling contrast. The increase in case of ions is related to the size of the beams. On the one hand, the electrons are light and small particles that can easily penetrate the surface through the space between atoms, and the orientation of the arrangement does not take a big role. On the other hand, the ions have a size comparable to the sample atom size. Thus, depending on the orientation, the sample lattice can be very restrictive or very permissive to the progression of the ions. The ions that do not travel deep in the sample will produce electrons that easily reach the surface, and the SE produced by ions that travel deep in the sample will not reach the surface. Then, the brightness on each case will greatly differ, more than in the case of electron bean scanning (N. Yao 2007).

Figure 3-11 shows an image taken with FIB secondary electron mode. The contrast of a fully annealed, nominally pure poly-crystalline aluminum specimen changes the intensity (gray level) of each grain as a function of deviation from normal incidence as the specimen is tilted with respect to the gallium beam. The same region is imaged at angles of 0, 15, and 30 degrees tilt (foreshortening due to tilt angle is evident) with remarkable differences in the contrast. The change in intensity (in arbitrary "gray level" units) is plotted as a function of tilt angle in one-degree increments. Dark grains (low intensity) represent significant channeling of the primary ions. The angular width of channeling "troughs" and the angular distance between troughs can be used to calculate the relative orientation of different grains.

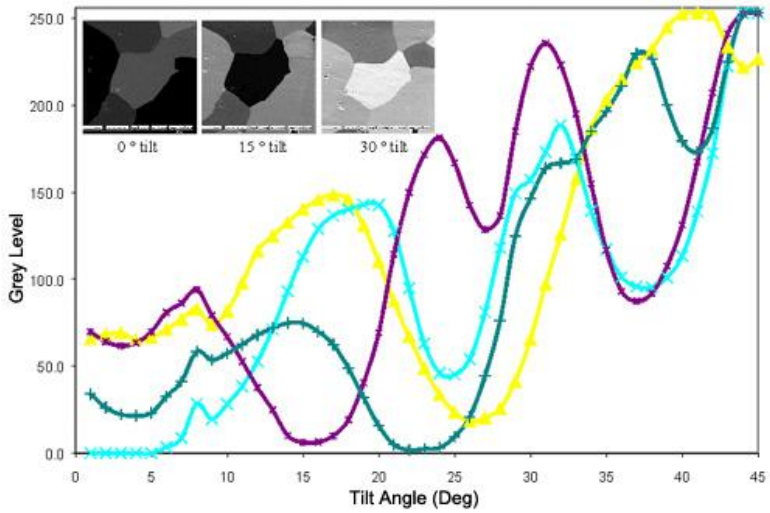

Figure 3-11 In the upper side, three images of the same grain took from different angles. As the density of atoms change depending on the relative orientation, the contrast also changes. In the diagram, the intensity of electron received for different grains depending on the tilt angle (Fibics-Incorporated, 2016).

3.1.6 X-ray chemical analysis

In electron microscopy imaging, the response of the material to the scanning beam is generally collected as electrons. However, the interaction of the electron beam with the specimen leads to a number of other signals. One of that signals is the characteristic X-ray emission.

When an electron from the beam hits another one of an atoms in the specimen, a hole can be induced in the electronic structure of the atom. If an electron from an upper level fill that hole, a photon is emitted. The energy of the emitted photon (the wavelength) exactly corresponds to the difference of energy between two electronic levels and relays in the energy range of X-rays. Since the exact positions of the electron levels is already known for all elements, the energy of the emitted photons allows to identify the presence of specific elements in the sample. This is represented in Figure 3-12.

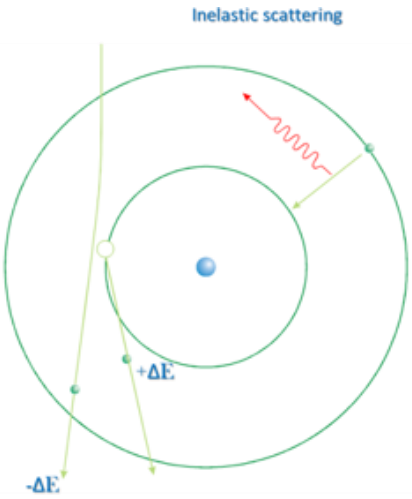

Figure 3-12 Inelastic interaction between beam and atom electrons, which induces a hole in the electronic structure. Subsequently, an electron from an upper level fulfil the hole, emitting characteristic X-rays.

The energy of X-rays photons can be analyzed in two ways. In wavelength dispersive X-ray spectroscopy (WDX) for a point of analysis a detector scans each frequency, counting the impinging X-rays in terms of its characteristic wavelengths. On the other hand, energy dispersive X-ray spectroscopy (EDX) collects one spectrum covering all the elements, within limits, of the sample, where the number and energy of the X-ray photons are evaluated by an energy-dispersive spectrometer (Goldstein et al. 2003). Since the energy of this photons are characteristics of the energy between atomic levels of each elements, EDX permits the composition of the specimen to be measured. This has been used in Figure 3-13 to identify the elements of an aluminum 6063 sample, where an intermetallic precipitate depicts different spectrum than the holding matrix.

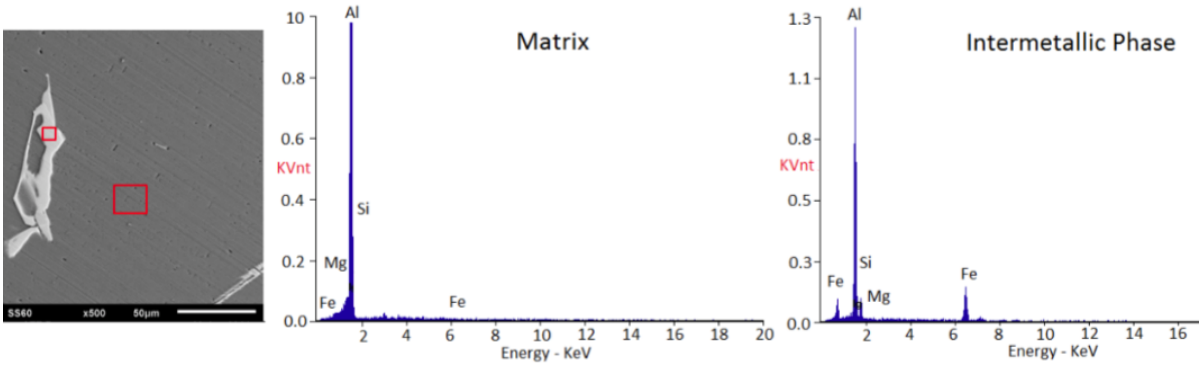

Figure 3-13 X-ray chemical analysis of Aluminum 6063 of the metal matrix, and an intermetallic particle(Espinosa-Zúrñiga et al. 2016).

The spatial resolution reach by these X-ray acquisition techniques relies in the size of the area responsible of photon emission, which in turn depend on the beam energy and the mass of the sample atoms. As described in Figure 3-14, a lower beam energy will make depth and width of interaction to decrease, hence increasing the spatial resolution of the scan. However, the amount of material affected by the beam also depend on the mas of the elements under investigation, being the data more representative of the surface composition in case of heaver atoms.

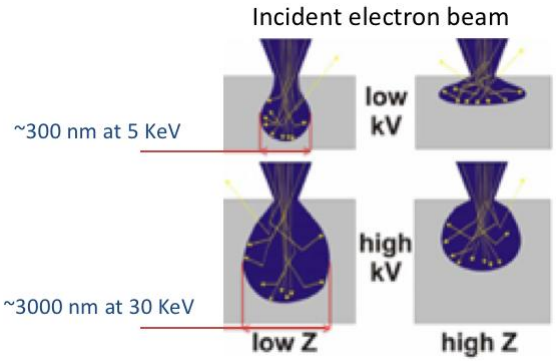

Figure 3-14 Volume of interaction of the incident beam and the sample surface.

An X-rays detection system can be accomplished to a SEM to collect the photons emitted during electron scanning. This leads to qualitative information about the elements and species present along the sample surface. In the present work it has been used an EDAX working in STEM mode, which has been used to detect the composition of a lamellae (details in chapter 5.2).

3.1.7 Nanoindentation

While electron microscopes have been used widely to characterize the structure and the composition of materials in the nanometer regime, the mechanical characterization at this

scale can be acceded by mechanical methods based in nano-actuators. This is the case of nanoindentation, which has become a main technique to determine nanomechanics of alloys.

This technique can measure elastic and plastic properties of the sample surface with sub-micron resolution. Due to the high precision of the nanoindenters, it is possible to test the mechanical properties of a material at the length-scale of a single grain or even smaller.

In nanoindentation, a tip is pressed into the sample surface while the indenter load and penetration depth are recorded. Contrary to a conventional indentation, the print left by the tip is not needed in nanoindentation to calculate the hardness. If the geometry of the tip is known, only the load-displacement curve recorded during indentation is needed to evaluate the mechanical properties of the specimen. From the load-displacement curve, both the elastic modulus (E) and the hardness (H) of the tested specimen can be measured.

Figure 3-15 shows a typical load-displacement curve of an indentation experiment. While loading, the tip produces elasto-plastic deformation in the material. However, during unloading, the response of the material is only elastic, so that there is some degree of recovery due to the relaxation of elastic strains within the specimen. According to the method postulated by Oliver and Pharr, the hardness and the elastic modulus of a specimen can be calculated by the equations (3-1) and (3-2) using the loading curve data (Oliver and Pharr 2011).

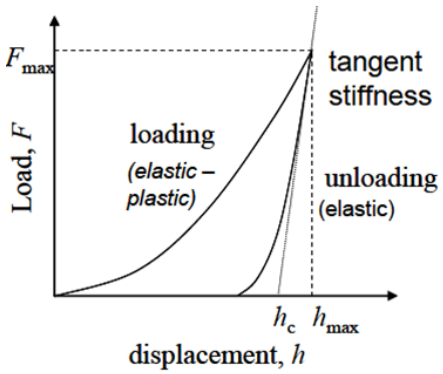

Figure 3-15 Load-displacement curve of a single indentation. The hardness of the specimen is related to the maximum force, while the elasticity is proportional to the unloading slope (Oliver and Pharr, 2011).

$$H = \frac{Fmax}{A(h_C)} \qquad \text{Eq. 3-1}$$

$$E_r = \frac{S \cdot \sqrt{\pi}}{2 \cdot \sqrt{A} \cdot \beta} \qquad \text{Eq. 3-2}$$

where *Fmax* is the maximum force during indentation, $A(h_c)$ is the contact area determined from the value of h_c (see Figure 3-15) and the geometry of the indenter, *S* is the stiffness, determined from the slope of the unloading curve at the maximum penetration depth,

and *ß* is a correction factor dependent on the geometry of the tip. Equation 3-1 describes the hardness (*H*), which is expressed as the pressure under the tip.

The reduced elastic modulus (*Er*) is calculated by the stiffness (the slope of the unloading curve), the contact area and a tip factor (Equation 3-2). Generally, only the upper part of the unloading curve is taken into account to measure the elastic modulus. The reduced elastic modulus is a combined modulus related to the elastic properties of the indenter and the sample. The relationship between *Er*, the indenter modulus (*Ei*) and the sample modulus (*Es*) is described by equation:

$$\frac{1}{E_r} = \frac{1-\upsilon_i^2}{E_i} + \frac{1-\upsilon_s^2}{E_s} \qquad \text{Eq. 3-3}$$

where υ_i and υ_s are the Poisson ratios (coefficient of transversal expansion after an axial compression) of the indenter and the sample, respectively (Courtney 2005).

In the nanoindentation technique the most frequently used tip is the Berkovich type, which is shown in Figure 3-16. This tip has the advantage that it is geometrically equivalent to the macroscopic Vickers indenter. Thus, measurements performed with both kinds of tips are readily comparable through Equation 3-4, which is only valid for materials with low elastic recovery (Aarnts et al. 2011).

$$H(Berkovich) = H\,(Vickers)/92.65 \qquad \text{Eq. 3-4}$$

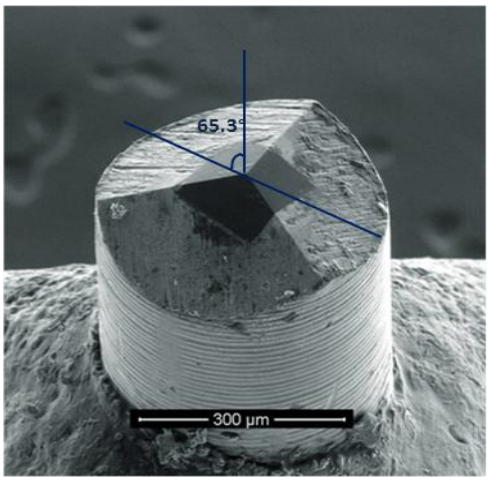

Figure 3-16 Berkovich tip, commonly used for mid-hard and hard materials. The centerline-to-face angle is 65.3º (Goponenko 2014).

In order to calculate the hardness and elastic modulus, the actual contact area of the performed nanoindent is needed. However, the size of the residual print for nanoindentation testing is usually too small to measure accurately with optical techniques. Therefore, the tip

shape is defined instead, so that a projected area given at a certain penetration depth can be calculated.

Since determining the geometry of the tip (i.e., tip area function) is essential for reliable measurements, it should be calibrated prior testing. In this thesis tip has been calibrated for indentations above 20 nm by series of indents in a fused quartz standard.

3.1.7.1 Grid methods

Normally, nanoindenters allow automating a set of indentations over an area. Automations can be programed to perform series of indentations, a regular distribution of indents over the sample surface. Grids have been used in this thesis for two purposes: point counting to determine the statistical average of a variable (point count method)., and grids plot the hardness distribution along a surface (mapping method).

The mapping method uses a matrix of indentations to calculate the hardness and elastic distribution over a specific area. The lateral resolution of the grid should be high enough to reproduce the microstructure of the sample, that is, the hardness of individual grains.

3.1.7.2 Artifacts in nano-indentation measurements

There are a number of effects that can deviate the measured hardness from the values of the bulk material. The artifacts may differ from one material to another and require some attention from the operator to ensure the correctness of measurements.

One of the fundamental aspects to be taken into account in crystalline materials is the indentation size effect (ISE). ISE is a well-documented effect where the measured hardness increases when the indentation depth is in the order of tens of nanometers (Durst et al. 2006). This effect is explained by the large strain gradient produced by the tip at very shallow depths. If the tip radius size approximates to the lattice Burger's vector, this sharp tip will induce large values of curvature in the surface to be absorbed in a very localized area. Since such local load will not make crystallites rotate, to accommodate the geometry of the tip a high amount of dislocations has to be created in front to the tip (Figure 3-17). These geometrically necessary dislocations (GND) increase the hardness locally in the material. As the tip goes deeper into the material, the strain gradient decreases and fewer new GNDs are needed to accommodate the tip. Thus, after a certain depth the hardness stabilizes and approaches the bulk value (Nix and Gao, 1998).

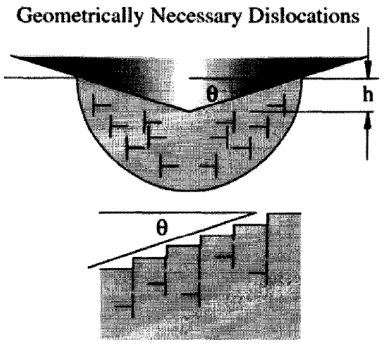

Figure 3-17 Sketch of geometrically necessary dislocations created during an indentation. The plastic area extends far from the indentation itself.(Nix and Gao 1998).

In steel, it has been reported that indentations made with a Berckobich tip below 60-70 nm depth tend to show some size effect, hence not showing bulk values of hardness (Durst et al. 2006).

Another common source of unrepresentative results comes from indentations made in de proximity of a previous one. In the case of inter-indent distance, it is generally admitted that, for work hardening materials, the plastic deformation produced by an indentation increases the residual stress stored near the indent (Durst, Mathias, and Pharr 2008). Thus, a minimum distance between adjacent indentations must be considered in order to have no artifacts in the measurement coming from former indentations. Table (3-1) shows the distance between indentations, as well as between indentations and the sample edge, recommended by the International Organization for Standardization (ISO) and American Society for Testing and Materials (ASTM).

Table 3-1 Recommended minimum distance between indentations and sample edges as a function of the indentation diameter (d), according to the standards ISO 6507-1 and ASTM E384.

Standard	Distance between indents	Distance to the edge of the sample
ISO 6507-1	> 3 d for steel and copper > 6 d for light metals	> 2.5 d for steel and copper > 3 d for light metals
ASTM E384	2.5 d	2.5 d

In case of a matrix or indentation vector, the minimum distance between indentations can be referred to as the lateral resolution. This distance is also related to the diameter of the print. Thus, the shallower is the penetration, the higher is the resolution of the measurement. However, the hard limit of the resolution is pointed by the ISE.

In addition to ISE and inter-indent distance, it should be taken into account the field of influence of hardness and elastic modulus. As proposed by (Durst et al. 2006), the field of plastic deformation tend to be three times the indentation radius, however elastic field is much broader and theoretically expand to the whole piece (Constantinides and Ulm 2004). Hence,

hardness measurements are local, but elastic modulus can be easily influenced by particles and defects far from the indent point. Thus, nanoindentation's elastic modulus can be measured to study the material trend, but typically values should be treated statistically.

In the present work values has been measured with a Berkovich tip, indentations of 140 nm of depth (footprint diameter of rounding 600 nm), and an inter-indent distance of 3 - 4 µm. These parameters are established to avoid the artifacts presented above.

3.1.8 Mechanical tests of micro pillars and beams

The recent advances in nano-fabrication by ion milling with precise control of material dimensions have catalyzed the emergence of new mechanical characterization techniques, specifically in the area of structural materials. Rather than relying on the classical characterization of bulk materials, fabrication and subsequently testing of micro-pillars and micro-beams have provided full access to the characteristics of individual metal phases, individual orientations or even individual plasticity mechanisms.

3.1.8.1 Advantages and experimental setup

While nano-indentation allows to obtain values of hardness directly on the surface of interest with great control of force and displacement, it is not convenient for elastic modulus or strength calculations. In the first case because the elastic field expands far from the measuring point, and uncontrolled underlying features may vary largely the values (Haušild, Materna, and Nohava 2013). In the second case because nano-indentation acts on the material with a complex distribution of stress, being complicate to extract axial-like strain-strength values. In contrast, pillar compression and beam bending can directly be used to construct the strength-strain response of a specific area of material, phase or crystallographic orientation, in a more accurate manner. In addition, the side walls of deformed pillars and beams usually provides information of the mechanisms involve (Torrents Abad et al. 2016).

Pillar compression is commonly used to study the strain-stress response in terms of plasticity. However, this technique is generally not used to evaluate the elastic response since small tills between the punch device and the pillar has a large influence in the calculation of elastic modulus, leading to certain scattering of the results. On the opposite, beam bending is relatively insensitive to small misalignments, thus providing the elastic modulus measurements with better reproducibility. The drawback of the bending approach is that strain develops in a more complex manner once deformation begins, since bending leads to non-homogeneous distribution of stress along the beam section.

In the present work micro-beams have been milled by FIB and used to test the elastic properties of the materials. On the other hand, micro-pillars have been also fabricated by FIB to extract the compression response in the plastic regime, with special interest in the deformation mode and the flow stress.

3.1.8.2 Artifacts by extrinsic size effects

Practically both techniques could lead to several measuring artifacts. Poor preparation, testing misalignments, or in-homogeneous pillar/beams may deviate the results significantly. These experimental defects can be overcome by a rigorous methodology of preparation and alignment prior testing. From the other hand side extrinsic size effects (W. Guo et al. 2014), should be considered. Measurements obtained with micro/nano dimensional samples may differ substantially from the bulk values depending on the pillar/beam size, the material, the microstructure and the type of the test.

While pillar compression has been widely investigated to understand properties of local areas, it has been demonstrated that small pillars depict a behavior deviating from the expected for the bulk material. This is a relevant size effect, where pillars of units of micrometers of diameter tend to depict much larger strength values than the macroscopic equivalent. The more extended theory is the dislocation starvation, a state where initial dislocations rapidly annihilate at the free surface, leaving the crystal dislocation starved (Greer and Hosson 2011). Then, in order to develop new strain, new dislocations have to be nucleated. Since classical Taylor hardening (defects interaction) would not play a role, the paradigm in small scales refers to the probability to generate new defects (Demir, Raabe, and Roters 2010). In other words, the dislocation starvation model postulates that the mobile dislocations inside a small nano-pillar have a greater probability of annihilating at a free surface than of interacting with another defect, thereby shifting plasticity into nucleation-controlled regime.

In the case of nano-crystals much smaller than the pillar diameter, dislocation starvation is disabled by the large amount of grain boundaries retained. As observed by (Fritz et al. 2016), the number of defects gradually decreases the size effect factor. Their experiments with nano-crystalline materials showed that by grains of hundreds of nanometers, size effects are pushed down to pillars under 2 µm of diameter. Thus, pillar compression experiments in pillars made of nano-crystalline metal would reveal bulk mechanical properties of the material.

In the case of beam bending, a pronounced size effect has been also reported. The stress distribution in the bending test is not homogeneous and the size effect could have multiple sources. Microstructural effects that could be responsible for the size effect are

dislocation starvation, strain gradients, geometrically necessary dislocations, pile-up effects or defect source truncation (Demir and Raabe 2010). In addition, the effect of grain size has not been analyzed in detail. Thus, size dependent effects cannot be by-passed and bulk values are hidden in small-scale tests.

Extrinsic size effects are revealed by measuring the pillars and beams of gradually increasing cross-section size. At the size when the strength does not change anymore the absence of size effects may be concluded.

Experimentally (for micro-mechanical analysis), an ex-situ nano-indenter Hysitron Triboindenter Ti 900 has been used for pillar compression. Nano-indenter has been equipped with a flat-punch tip of 10 µm and it has been used sink-in correction of the base material deformation (Sneddon 1965). In the case of beam bending tests, they have been made in-situ by an Asmec UNAT-SEM2, inside a Zeiss Sigma SEM.

3.1.9 Summary of techniques

As described, a number of techniques have been used to characterize different aspect of the materials of use. The following table briefly summarizes these techniques. In the top they are shown microscopy techniques based on signals, while in the bottom part techniques for mechanical tests. As mention, the microscope resolution is the minimum distance between distinguishable objects in an image (minimum resolvable distance).

Table 3-2 Characterization techniques used for materials characterization

Microscopy	Pixel resolution	Use in the present work
Optical Microscopy	250 nm	Phases volume fraction, grain size
SEM (imaging SE)	Sub-nm	Sample features and microstructure
EBSD	200 nm	Reveal crystallographic orientations
X-rays (SEM)	1 - 12 nm	Chemical analysis of the species
FIB (ion scanning)	2 -6 nm	High contrast grain distribution
TEM (transmission)	0.01 nm	Detailed crystallographic defects

Mechanical	Area of test	Material property
Nanoindentation	500 nm	Hardness and E-mod approximation
Pillar compression	2 - 6 µm	Yield stress
Beam bending	2 - 5 µm	E-mod, yield stress

3.2 Materials

This thesis presents the experimental study of the metal cutting process in two different materials, AISI 1045 steel and aluminum-based alloy. The purpose the present work is to elucidate how different mechanisms of plasticity govern the interaction between tool and materials with two different hardening mechanisms on the base of the comprehensive analysis of material's microstructure. On the one hand AISI 1045 steel, an alloy developing strengthening by large volume fractions of a hard phase. Such alloy, a workhorse material in machine design, included hard pearlitic colonies in approximately 75 % of the volume, surrounded by a softer ferritic phase. This leads to a strong and ductile behavior. On the other hand, series 7000 of aeronautic aluminum bases the strengthening on a homogeneous distribution of nanometric particles in the lattice. In the case of aluminum 7475, Mg3 (Al, Cu, Zn)5 intermetallic particles nucleate and growth along the whole lattice after an annealing process (Yoshida, 1991). That retains hardening by dislocation trapping.

Both alloys have been characterized previous any machining test. The following section shows the mains characteristics of as-received steel AISI 1045 and aluminum 7475.

3.2.1 AISI 1045 Steel

The supplier of the samples provided the following chemical composition of the AISI 1045 steel sample:

Table 3-3 Chemical composition (%) of the sample of AISI 1045 steel

C	Mn	Si	S	Cr	Ni	Mo	P
0.45	0.78	0.33	0.025	0.12	0.09	0.02	0.014
V	Cu	Al	Sn	Ti	O	N	Ca
0.004	0.11	0.007	0.0007	0.001	10	58	7

The material, as a rod, has been treated thermally. The steel has been austenized, and subsequently has been subject of an isothermal annealing process at 600 ºC in order to develop a structure of pearlite and ferrite.

The workpiece for further microstructural study have been extracted from the rod following the radial direction of the section, as described in Figure 3-18.

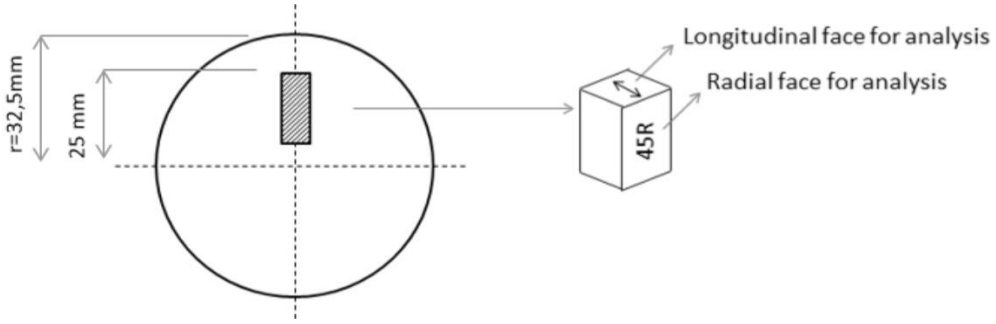

Figure 3-18 Section of material's rod. The sample has been extracted following rod radial direction.

A first study has been made by optical imaging techniques. Figure 3-19 shows micrographs of the microstructure in the external surface, in the rod center and in between them. While the microstructure is lightly refined in the surface, no major changes in the structure morphology is present along the sample. It has been observed a grain size rounding 7-9 µm, and a volume fraction of 25 % of ferrite (white under the optical microscope), as it is depicted in Table 3-4.

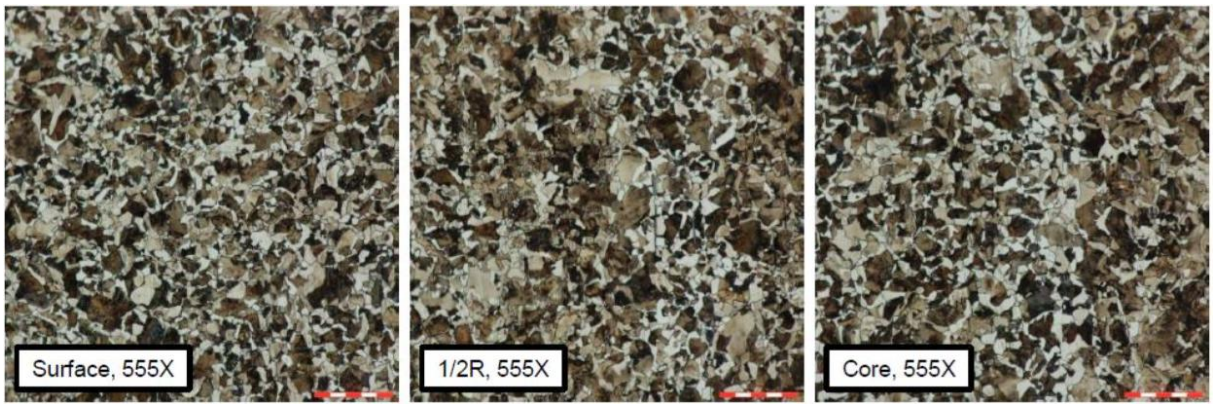

Figure 3-19 AISI 1045 microstructure by optical microscopy. Images have been made in the external surface of the rod (left), at ½ of the radius (center), and in the center of the rod (right).

Table 3-4 Parameters of the sample structure of the AISI 1045 steel sample.

Description	Homogeneous ferritic-pearlitic microstructure
Ferrite grain size	8-9 µm
Pearlite grain size	7-8 µm
Ferrite / Pearlite	25 / 75 %

Further morphological analysis has been made by FIB. By this in scanning intra-grain details can be disclosed since pearlite is shown as dark particles and plates. The effect of grains with partial pearlite structure is widely exposed along the surface, as shown in Figure 3-20. Thus, in this particular case, it is proper to use the term pearlite colony inside ferritic grains.

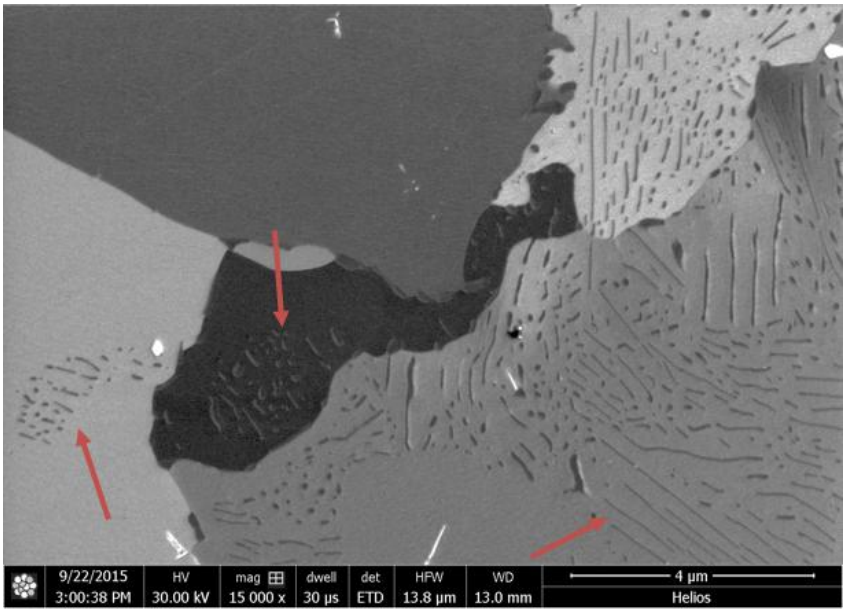

Figure 3-20 FIB micrograph of different pearlite colonies (red arrows) which are nucleated near the grain boundaries.

Another effect observed is the pearlite polymorphism. In Figure 3-21 it can be observed grains that develops pearlitic microstructures with different morphologies, i.e., lamella, discontinued and spheroidal grades.

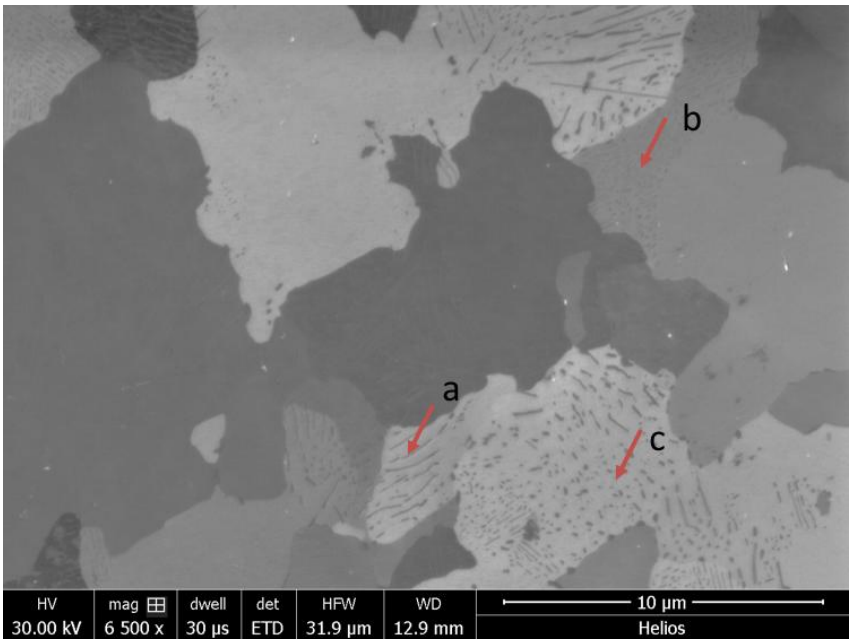

Figure 3-21 Several pearlite morphologies are present (a) lamellar, (b) discontinued plates and (c) spheroidal.

The reason for that arrangement of the cementite particles in pearlite colonies could be based in the diffusion of carbon atoms at temperatures close to austenization while cooling. As long as ferrite tries to push away the carbon, those atoms go to the grain boundaries. Thus, the carbon density varies inside the grains and the formation of pearlite is not homogeneous.

The EBSD orientation maps do not show a remarkable preferential orientation in this sample. In Figure 3-22 it is shown that there is a wide range of grain sizes. In addition, it can be observed small deviations in orientation inside the grains. Figure 3-23 shows an area where this effect is particularly visible.

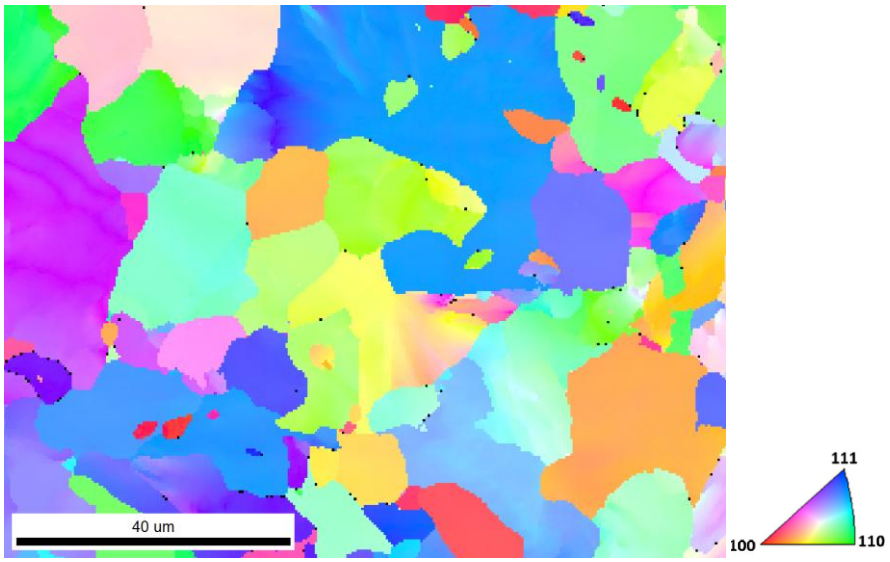

Figure 3-22 (EBSD) Orientation map of the sample. No preferential orientations are detected.

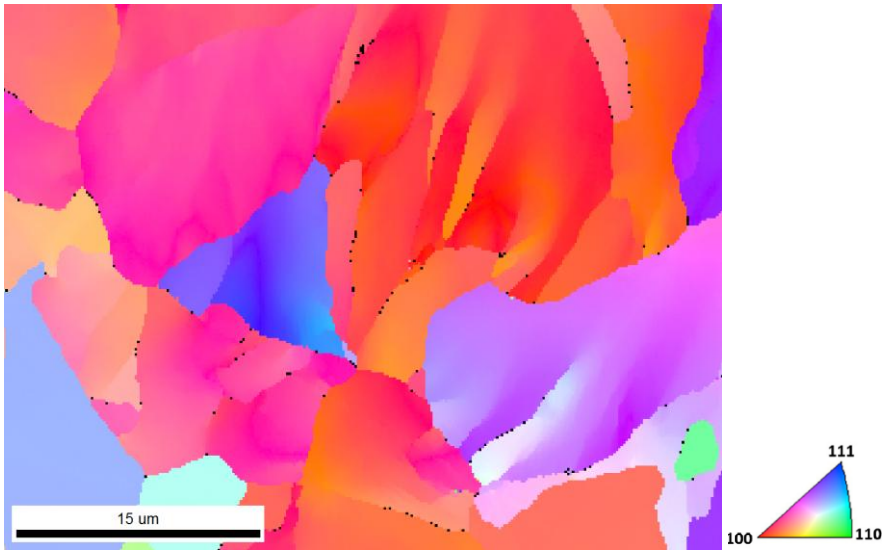

Figure 3-23 (EBSD) Several areas show small changes in the orientation inside the grains.

By Kernel Average Misorientation (KAM) post-processing applied on the EBSD data, a qualitative representation of the residual stress on the sample surface. Figure 3-24 shows the KAM post-processing on the area presented in Figure 3-23. It is depicted that some areas (inside the grains) develop string lattice deviations (green color) what probably refers to areas where the accommodations of pearlite produced more constrain.

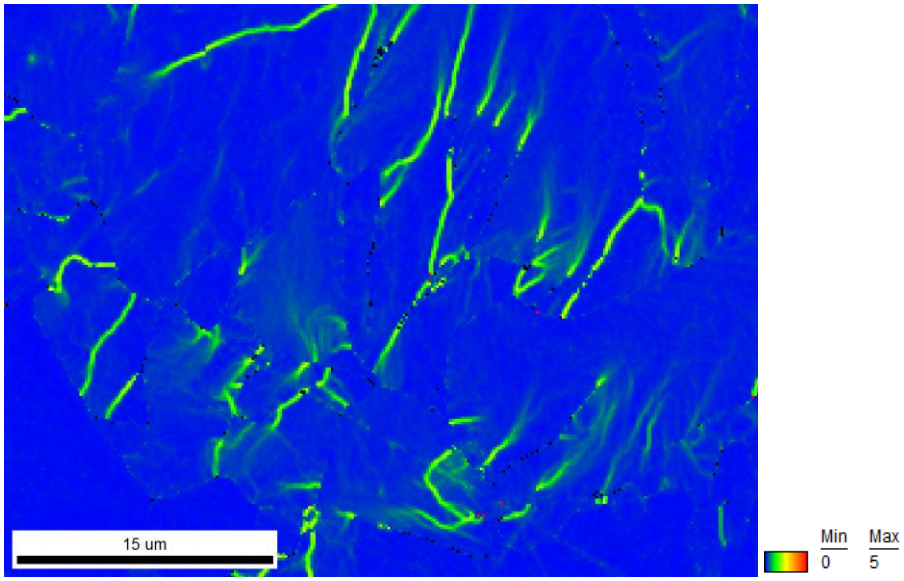

Figure 3-24 (EBSD-KAM) The misorientation map reveals the areas with higher dislocation density. In the color scale, blue refers to a misorientation angle of cero, and red to 5 degrees.

3.2.2 7475 Aluminum

These experiments were made with commercially available Aluminum 7475. As received, the material had been treated by two hardening processes. First, it has been annealed to precipitate Guinier-Preston particles, visible in Figure 3-25. Second, it has been mechanically thinned to refine the grains structure Figure 3-26.

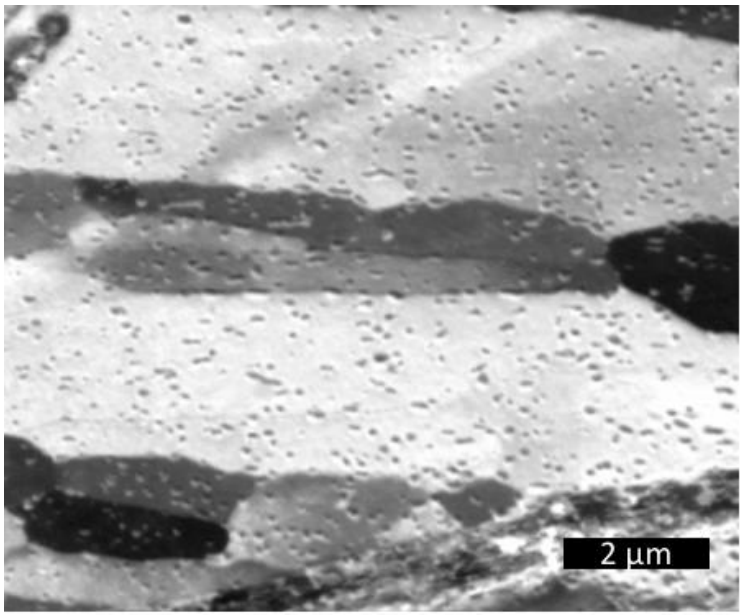

Figure 3-25 Ion scanning image of aluminum 7475 as received.

In Figure 3-25 a relatively large distribution of particles, with no particular affinity to grain boundaries can be observed after the first hardening step. Particles size rounds hundreds of nanometers, relatively large values for Guinier-Preston alloys. After the second step the

microstructure of the material develops a structure consisting of fibrils with a thickness of approximately 20 µm. Figure 3-26 depicts the structure of the material perpendicular and parallel to the mechanically produced fibrils.

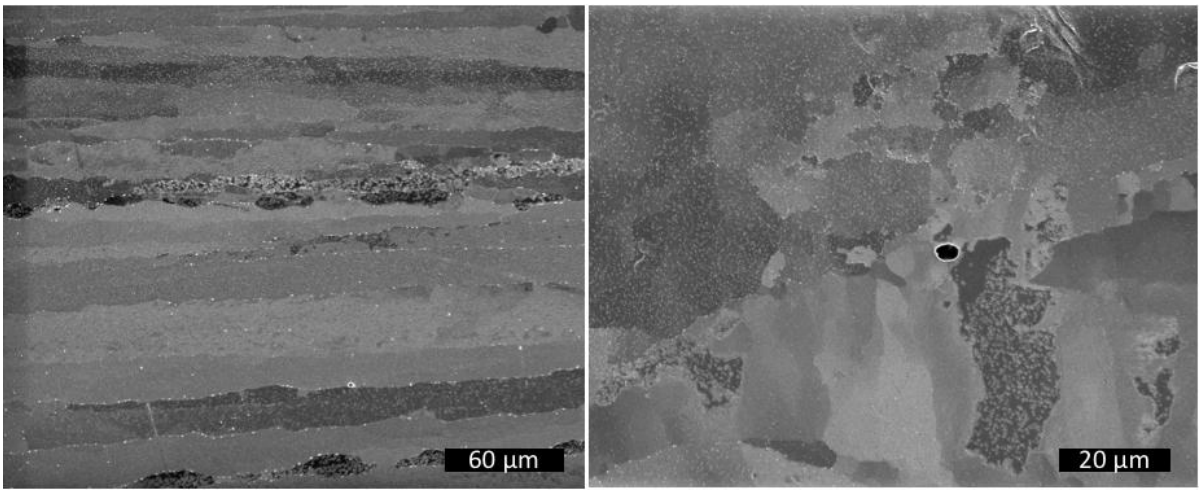

Figure 3-26 (a) Ion scanning image of the microstructure of the material as received (scale bar 50 µm). (b) Image of the surface perpendicular to the fibrils (scale bar 10 µm).

As observed in Figure 3-26, the microstructure of the material as received develops a structure of fibrils with a thickness of approximately 20 µm.

This material is generally used in the aeronautic industry as a light, ductile and strong material. After processing the alloy received develops the properties described in Table 3-5.

Table 3-5 Properties of material under testing (Aluminum 7475)

Elastic modulus	Yield stress	Ultimate tensile stress	Fracture elongation
74.1 GPa	429 MPa	534 MPa	9.9 %

Aluminum 7475 has been used to perform in-situ SEM machining tests. This material suits for this purpose due to its homogeneity, which leads to forces of cut relatively low and stable. In addition, aluminum alloys induce low wear in the micro-tool.

3.3 Equipment for machining

The equipment to perform industrial-like machining is a center of machining with computer numerical control (CNC) from Fagor, model 8070.

In the case of AISI 1045 steel, high-speed machining is performed by vertical milling machine using tubular samples, as shown in Figure 3-27. Tests were carried out in dry conditions with uncoated P15 grade carbide cutting tools, reference WIDIA TPUN 160308

TTM. The tool is holed by a dynamometer Kistler 9121 for force registering, and the process is filmed by an infra-red camera Flir Titanium 550M.

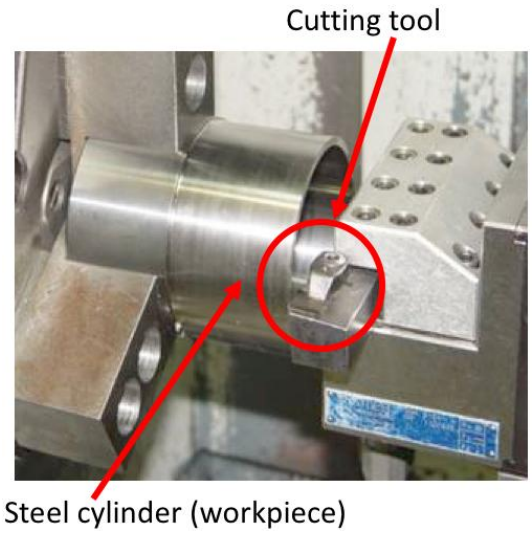

Figure 3-27 Setup for steel machining by turning a workpiece in form of cylinder.

Linear machining of aluminum has been made in order to compare ex-situ and in-situ SEM tests. For linear cutting of aluminum 7475 samples, the tool used has been a Sandvik TPUN 160308 H13A. Samples are mounted on a dynamometer Kistler 91299AA, as shown in Figure 3-28. The process of cutting is filmed by a high-speed camera.

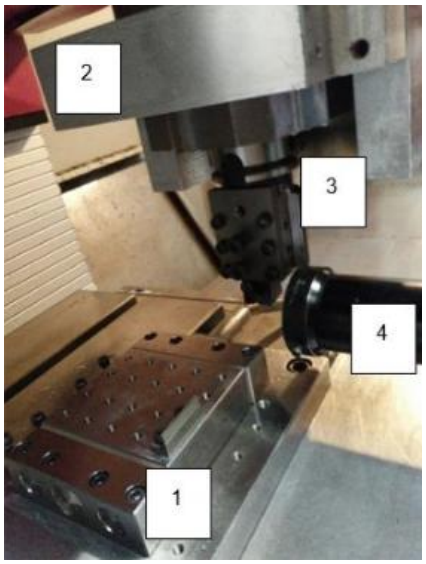

Figure 3-28 Setup for ex-situ cutting. (1) Kistler dynamometer, (2) holder, (3) tool, (4) high-speed camera.

4 Microstructural aspects of the transition between two cutting regimes in AISI 1045 steel

In depth understanding of tool-chip friction behavior is a significant aspect for tool wear performance in steels. In the present chapter the microstructure of the chip obtained in the cutting process is used to get the understanding of the plasticity mechanisms involved in tool/work piece interaction. There were multiple experimental evidences over the last 50 years for existence of qualitatively different cutting regimes existing in orthogonal machining of annealed AISI-1045 steel with uncoated P15 carbide cutting tool in dry conditions at cutting speed between 5 and 200 m/min. These two regimes involve substantially different cutting forces and result in qualitatively different surface finish. Besides obvious practical importance, up to now there is no clear understanding of the reasons causing the transition from one regime to another. In this chapter the existence of these two regimes is correlated to built-up edge appearance and to the dynamic recrystallization appearance. Discussion lay in fundamental aspects of metal plasticity.

4.1 Introduction

Understanding the phenomena occurring in the tool-chip contact area is a key for improving the machining process. Tool wear, and subsequently tool life, are notoriously affected by the thermomechanical loads occurring in this zone. However, direct experimental assessment of the conditions in the tool-chip contact area during machining presents two major challenges: (i) the small dimension where the phenomena are occurring and (ii) the extreme values of strain, strain-rate, temperature, pressure and stress reached. Although recent research has provided new insights for experimental assessment of temperature (Arrazola et al. 2015) or strain (Lee et al. 2006) values, there is still quite a few quantitative experimental data available for the other parameters. Variables like pressure or stress are inaccessible by the existing experimental measuring techniques. This fact hampers an in-depth analysis of what happens directly at the tool-chip contact area. There has been a substantial effort devoted to studies of tool-chip processes aiming to understand tool wear (Childs et al. 2000; Ernst and Merchant 1941; Jaspers and Dautzenberg 2002; Merchant 1945), non-linear friction effects depending on cutting speed and feed rate (Podgornik, Hogmark, and Sandberg 2004; Rech et al. 2013; Seker, Kurt, and Çiftçi 2004) and tribological regimes between tool and workpiece material (Ben Abdelali et al. 2012). In particular, two distinct cutting regimes were identified for orthogonal cutting of AISI 1045, AISI 4142, AISI 304L steels, leading either to discontinuous chip formation and a rough workpiece finish at low cutting speed, or to a continuous chip and smooth finishing at high speed (Rech et al., 2013). Besides giving a clear link between input and output parameters of the processes, classical macroscopic characterization techniques were not able to disclose the microscopic mechanisms for observed phenomena, and thus to gain a fundamental understanding of the processes underlying complex manufacturing processes.

In-depth studying of the microstructure of the material pieces involved in the cutting process, the chip being the most informative of those, has been already realized (Courbon et al., 2013) as an essential instrument to face above challenges. Though the chip is wasted in the machining process, it stores the stark signatures of the conditions which were present directly during cutting, especially in the secondary shear zone (SSZ), which has been in the direct contact to the tool.

A number of authors have accessed the structure of SSZ of the chips at the microscopic scale after machining steels. It was shown that the crystal structure in the SSZ of the chip in the proximity of the rake surface presents a particular grain shape and distribution. At low cutting speed the material is refined, laminated and hardened, leading to depositions in the tool edge, the so called “built-up edge” (BUE) phenomenon (Childs et al., 2000; Wallbank, 1979; Zorev, 1966). In contrast, at higher speed (starting from 50-60 m·min-1) these depositions disappear and the chip slides directly against the tool. In that case the grains of SSZ are refined to about 200 nm and tend to equiaxity in the proximity of the tool, in contrast to rest of the chip (Courbon et al., 2013). This region is commonly referred to as white layer, since it appears as a bright band near the chip surface on optical images (Griffiths, 1987). Appearance of equiaxial grains in SSZ was proposed to be due to recrystallization or phase transition (Pu et al., 2015; Subramanian et al., 2002) and this recrystallization in turn was utilized to explain softening effect appearing in the material during high speed machining. It has been pointed out that these phenomena depend on the cutting speed and take place only in certain chip locations (Jaspers and Dautzenberg, 2002). The main challenge in characterization of the structure of material in SSZ is the size of the grains often going below 100 nm. This makes high-resolution techniques like electron microscopy the only option for addressing this challenge. Due to complexity and limited availability of such methods for metalworking community, structural and mechanical characterization works happened to be separated and thus important link between the structure, material properties and machining conditions has not been clearly established by now.

In this chapter it is presented a composite study which includes characterization of the evolution of microstructure in the SSZ with the cutting speed and its correlation with such parameters of the cutting process as chip morphology, cutting and feed forces, chip/tool temperature and tool-chip contact length. In agreement with previous works we observe an abrupt transition of the tool-tip interaction regime at ~50 m/min cutting speed, correlate it to the microstructure evolution and discuss a microscopic nature of above transition.

4.2 Experimental procedure

4.2.1 Machining

Bars of AISI 1045 annealed steel with 58 mm diameter were employed in this study. The material had a hardness of 300HB, a mean grain size of 7-9 μm, and microstructure of 75% perlite and 25% ferrite as has been described in detail in chapter 3.2.1.

Orthogonal cutting tests were performed in a vertical milling machine using tubular samples 65 mm long, 58 mm in outer diameter, and 2 mm in thickness with a 15 mm long

solid base for clamping (see Figure 3-27 and Figure 4-1 for a schematic of the set-up). Tests were carried out in dry conditions with uncoated P15 grade carbide cutting tools (rake angle = 6 degrees and cutting-edge radius = 40 µm). The feed rate was kept constant to 0.2 mm/rev, while the cutting speed was varied: 5, 10, 25, 50, 75, 100 and 200 m/min. Three trials of every experiment were carried out in order to determine repeatability. A fresh cutting edge was used for each test to prevent wear effects. For every cutting experiment we monitored feed and cutting force, tool tip temperature, chip morphology and thickness, chip microstructure and tool-chip contact length. A Kistler 9121 dynamometer was used to measure the cutting and feed forces at the sampling rate of 5000 Hz and 300 Hz cut-off filter. The tool and tool holder were mounted on the dynamometer. The dynamometer was fixed to the table of the machine. The workpiece was clamped to the machine spindle, which provided the rotational movement and vertical feed, as described in (Armendia et al. 2010).

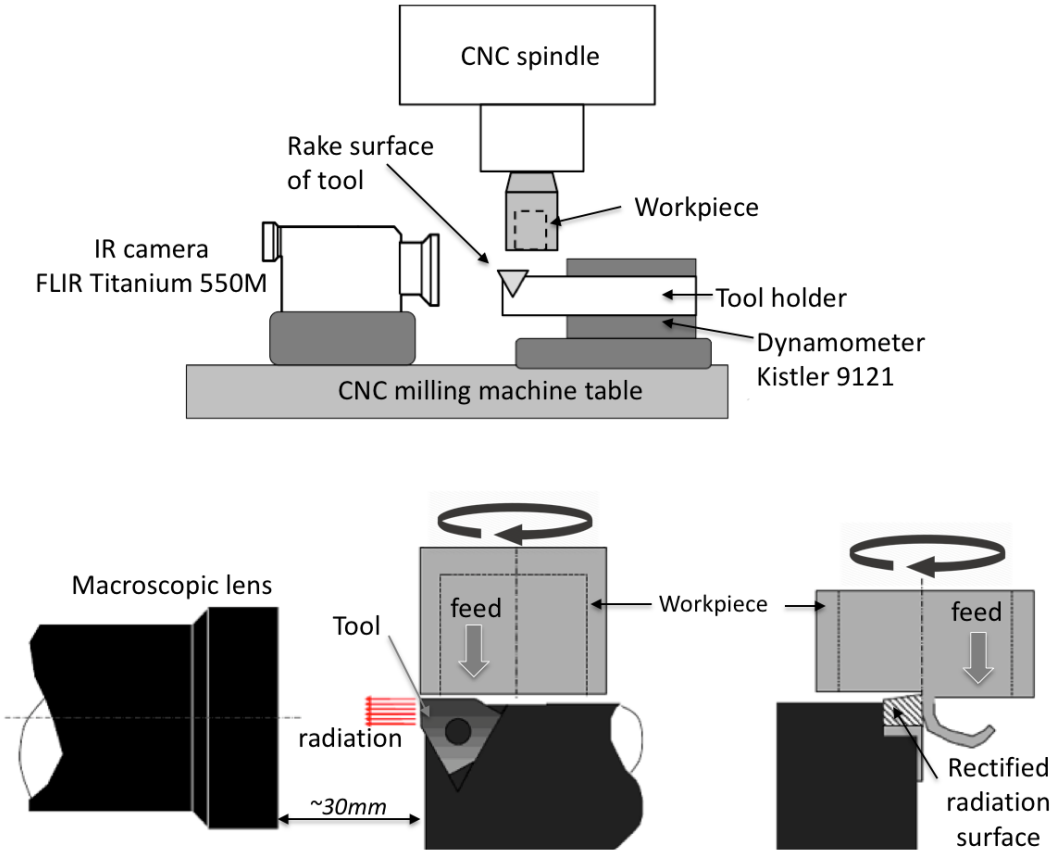

Figure 4-1: Experimental set-up for orthogonal cutting tests. The set-up is composed of tool and tool holder mounted on a dynamometer, a workpiece mounted in the splinter, and the infrared camera (upper sketch). While tool remains fixed, workpiece turns to generate the chip perpendicularly to the camera (bottom sketch).

The temperature was measured by a FLIR Titanium 550M infrared camera mounted to the machine table. The camera was equipped with a macroscopic lens giving a spatial resolution of 1 pixel = 10 µm. A narrow-band filter in the IR spectral range of 3.97-4.01 µm was applied. In order to have sufficient data to evaluate temperature evolution over time, it is necessary to have a high acquisition frame rate (fr). However, a high fr implies reducing

camera resolution and therefore the field of vision. In the present study the frame rate was fr=1000 Hz which allowed thermographies of 160x128 pixels to be recorded.

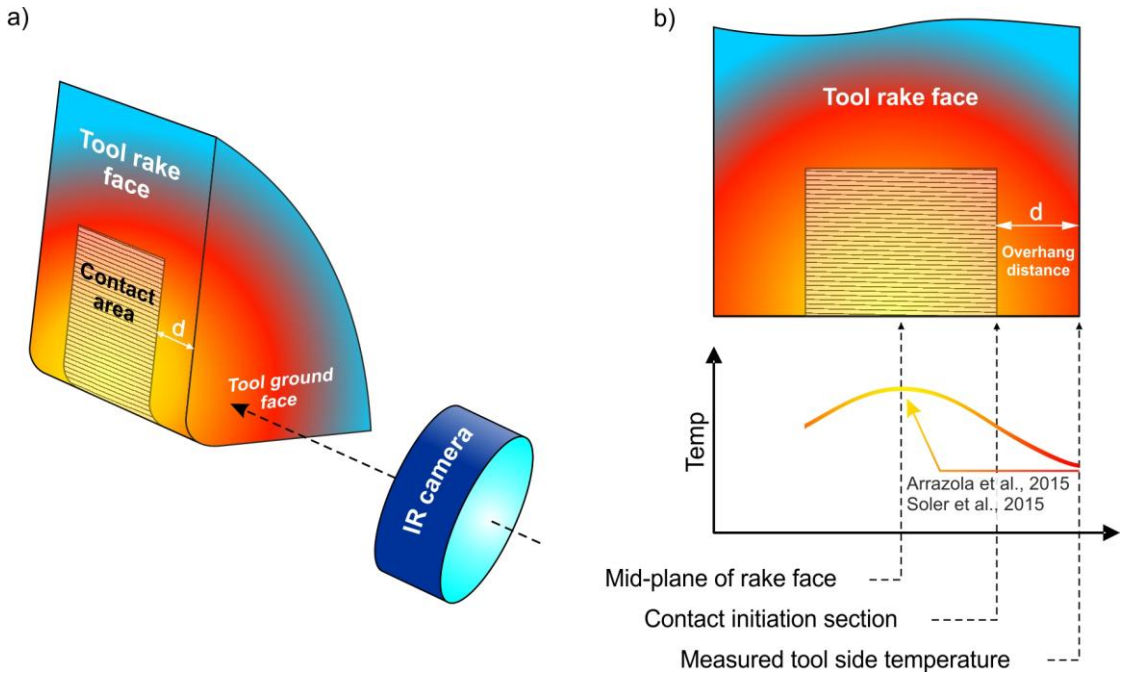

Figure 4-2 a) Schematic view of tool and camera for infrared photography of tool side face. b) Temperature correction from tool side to the mid plane of the rake face.

To prevent a nonlinear detector response, the integration time was selected depending on radiation values as 60, 100, 200, 300 and 150 µs (without filter for a v_c = 5 m/s). The cutting time for each test was 5 s, which was long enough to ensure a temperature steady state condition and short enough to prevent oxidation on the tool insert. In order to relate the camera recorded data with the real temperature the calibration method proposed by (D Soler et al. 2018) was followed. The tool temperature was measured in the groundside face of the insert (see Figure 4-2a). In order to estimate the temperatures on the mid-plane of the rake face (see Figure 4-2b) two approximations were applied. First, based on the experimental procedure developed in (Daniel Soler et al. 2015), the temperature from the tool side was interpolated to the contact initiation section. As a result, the effect of the overhang distance (*d* on Figure 4-2b) was corrected from *d*=0.3mm to *d*=0mm. Secondly, based on the analysis carried out on (Arrazola et al. 2015), the previously corrected temperature was multiplied by a ratio to take into account the increase in the tool temperature form the contact initiation section to the middle section due to the friction effects. From the results obtained in Arrazola et al. it was extracted that the temperature increases from the contact initiation section to the mid-plane of the rake face by 10% for a cutting speed of 75 m/min and a 25% for 250 m/min in the case of an AISI-4140. According to those published results, previously corrected experimental temperatures were increased by 10-25% depending on the cutting condition.

Chip thickness was measured from low magnification SEM images of polished chip cross-sections. Tool-chip contact length was measured from the wear of the tool, see information in Appendix A for details. The measurement uncertainties were ± 10N in forces, ± 100 ºC in tool temperature, ± 0.02 mm in chip thickness and ± 0.2 mm in tool contact length.

4.2.2 Modeling

A model set-up in Abaqus/Explicit™ (v6.14), described in(Arrazola 2003; Arrazola et al. 2007) was employed to obtain quantitative information of cutting and feed forces, temperatures and plastic strain. Coupled mechanical and thermal analysis was done using the Arbitrary Lagrangian Eulerian (ALE) formulation.

Material behavior was determined by a Johnson-Cook flow stress model. The parameters of the constitutive model were characterized with experimental dynamic compression tests, as described in previous works (Saez-de-Buruaga et al. 2017).

The Coulomb friction law governs mechanical aspects at the tool-chip interface contact. This was set-up in function of sliding velocity, as carried out in (Rech et al. 2013). Heat transfer was allowed at the tool chip contact area and at the backside of the tool. Workpiece material and tool thermal properties were characterized in function of temperature, as described in previous publications (Saez-de-Buruaga et al. 2017). Figure 4-3 illustrates the steady state temperature distribution in the chip, based on the conditions detailed above for the case of cutting at 75 m/min. Note the particularly refined mesh applied in the tool edge contact.

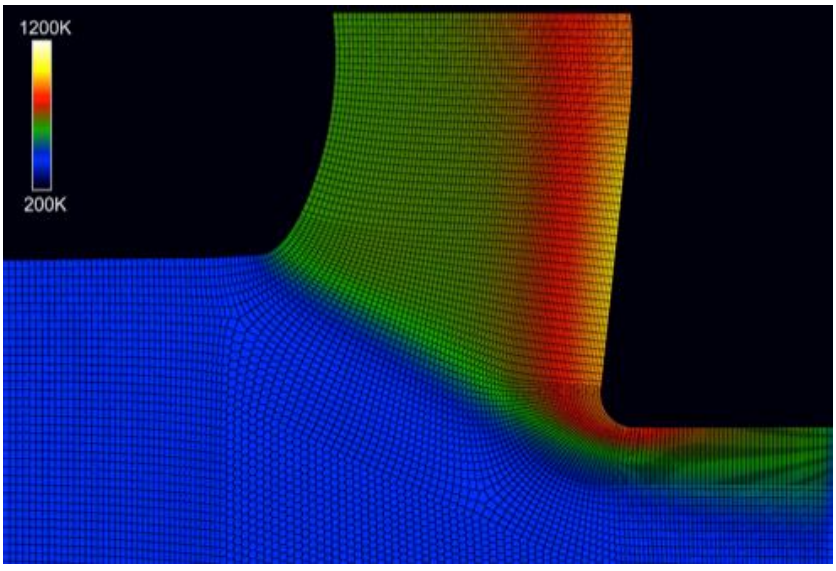

Figure 4-3 Temperature distribution obtained in FEM for Steel 1045 when machining at 75 m/min.

In order to reduce computational time, the mass scaling option was used, which basically increases material density in a controlled manner to reduce stable-time increment.

A numerical comparison carried out to verify differences when using this option showed differences lower than 1% in the most relevant variables like temperature, cutting forces or Von Mises stresses. The option Variable Mass Scaling proposed in Abaqus/Explicit™ (v6.14) was set up so as the lower time increment attained the value of 10-9 s. This option allowed reducing computational time by more than 10 times (Arrazola et al. 2007). Entry parameters for material, contact and cutting process are shown in Table 4-1.

Table 4-1. Entry parameters regarding material, contact and cutting process parameters

Parameters			AISI 1045
Material properties	Johnson Cook parameters	A_{JC} [MPa]	546
		B_{JC} [MPa]	452.2
		n	0.3514
		C_{JC}	0.0308
		m	0.6146
	Inelastic heat fraction (β)		0.9
	Density (ρ) [$Kg \cdot m^{-3}$]		7764 (293K) 7684 (573K) 7569 (873K)
	Young modulus [MPa]		$210 \cdot 10^3$
	Poisson coefficient (ν)		0.3
	Conductivity (λ) [$W \cdot m^{-1} \cdot K^{-1}$]		36.1 (293K) 34.3 (573K) 23.2 (873K)
	Specific heat (c) [$J \cdot Kg^{-1} \cdot K^{-1}$]		395.8 (293K) 545.1 (573K) 632.6 (873K)
	Thermal expansion coef.		$6.62 \cdot 10^{-6}$ (293K) $12.5 \cdot 10^{-6}$ (573K) $14.8 \cdot 10^{-6}$ (873K)
Contact prop.	Thermal cond. [$W \cdot m^{-2} \cdot K^{-1}$]		10^8
	Heat transfer coefficient (Γ)		0.5
	Friction (μ)		0.8-0.55
	% heat friction energy (η)		100
Tool parameters	Cutting edge radius (rh) [μm]		40
	Rake angle [º]		6
	Relieve angle [º]		6
	Density (ρ) [$Kg \cdot m^{-3}$]		10600
	Young modulus [MPa]		$520 \cdot 10^3$
	Poisson coefficient (ν)		0.22
	Conductivity (λ) [$W \cdot m^{-1} \cdot K^{-1}$]		25 (293K)
	Specific heat (c) [$J \cdot Kg^{-1} \cdot K^{-1}$]		200 (293K)
	Thermal expansion coef.		$7.2 \cdot 10^{-6}$ (673K)
Cutting speed [$m \cdot min^{-1}$]			25-200
Feed [$mm \cdot rev^{-1}$]			0.2

4.2.3 Sample preparation and microscopy

A sample of workpiece material was diced by diamond saw and the surface was polished with diamond disks and aluminium oxide suspension. A final chemical-mechanical polishing was made by oxide polishing suspension (Struers OPS nondry). In order to prepare the chip cross sections, chips were embedded in conductive silver epoxy (Chemtronics CW2400). This reduces drift and sample charging in electron microscope as compared to a standard epoxy. Then the embedded chips were polished using the same procedure as for workpiece material.

Chips surface being in contact with the tool was optically examined with a Leica DM4000M microscope. The microstructure of workpiece and chip was studied by SEM and FIB techniques. SEM was used to reveal the major morphological features of the samples like shape of the interface surfaces and cracks. In turn the crystallinity of the samples, i.e. the size and the shape of crystallites, was studied by FIB imaging utilizing channeling contrast as described in Chapter 3.1.5. It was found, that ion beam produces substantially higher channeling contrast than electron beam yet preserving sufficient resolution at low beam currents (1.5-40 pA). We utilized 5 kV acceleration voltage for electron beam and 30 kV for ion beam.

The EBSD technique was used to build maps of crystallographic orientation, texture and kernel average misorientation (see Chapter 3.1.4). Scanning was performed at 20 kV acceleration voltage and step size of 50 nm. Subsequent data analysis was made by OIM Analysis software.

4.3 Results

This work presents a multi-approach study. On the one hand, the material was observed before and after machining by optical and electron microscopy. On the other hand, multiple characteristics and parameters were measured during machining experiments: feed force (F_f), cutting force (F_c) chip thickness (t) and temperature. Figure 4-4 gives a schematic of the parameters been monitored and their relation to the particular parts of experimental setup.

The central sketch of Figure 4-4 illustrates in the origin of the images of the present chapter, where (a) is the cross-section of the chip, (b) is the workpiece and (c) is the chip surface sliding over the tool rake angle.

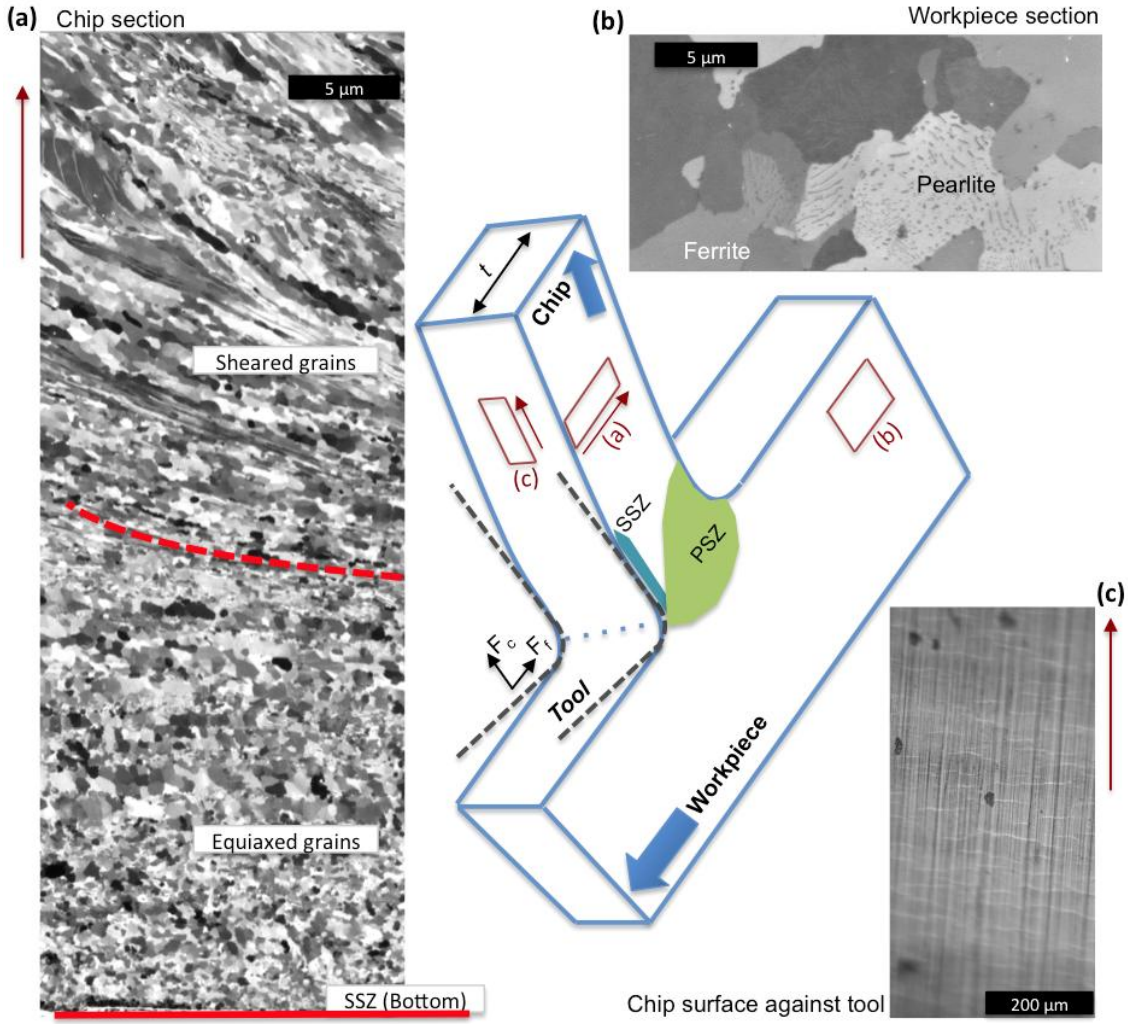

Figure 4-4 In the middle is the sketch of different areas and parameters of the chip under study. (a) Ion image of chip cross-section when machining at 100 m/min. Red dashed line is an estimation of PSZ - SSZ boundary. (b) Ion image of workpiece section. (c) Optical image of the chip surface sliding against tool when machining at 100 m/min.

The typical FIB image of the microstructure of a workpiece sample before machining is depicted in Figure 4-4b, where pearlite colonies cover 75 % of the sample area (more details in Section 3.2).

Figure 4-4a shows an overview FIB image of the cross-section of a chip machined at 100 m·min-1. The surface being in contact with the tool is at the bottom of the image. A characteristic feature of the structure is pronounced shape anisotropy, with the long axis of the crystals changing direction from the shear angle of the PSZ to angles almost parallel to the surface in the proximity of SSZ. The other peculiar structural feature is the existence of the so called “white layer” (the name coming from optical images of cross-sections) (Griffiths 1987) – the area at the tool-chip contact surface where crystallites are very small and do not show pronounced shape anisotropy (Courbon et al. 2013). Hereafter, this area will be studied, as it is particularly this, which reflects specific thermomechanical conditions of the cutting

process at the very proximity of the tool. Figure 4-4c gives an example of an optical image of the chip surface at the rake side of the chip produced at 100 m/min cutting speed.

4.3.1 Microscopy of the SSZ microstructure at different cutting velocities

Figure 4-5 summarizes morphological and structural features of the chips obtained at cutting velocities from 5 to 200 m/min. The left column depicts optical images of the bottom chip surface that has been in contact with the rake surface (corresponding to position of Figure 4-4c). There are two different morphologies present: at 50 m/min and above the chips are smooth and are not fragmented; however, at cutting speeds of 25 m/min and bellow chip surface develops cracks perpendicular to the direction of chip movement. In the middle column optical images of the chip cross-sections reveal a typical lamellar structure characteristic for the PSZ. The lamellae direction is changing from parallel to the surface at the tool-chip interface to its bulk value, which is specific for every cutting speed.

Right column of Figure 4-5 depicts FIB images of the chip cross-section in the area in the proximity of the rake surface, which reveal the grain distribution down to sub-100 nanometer size in SSZ at the tool-chip interface (corresponding to position of Figure 4-4a). For chips cut at 25 m/min and below the grains in this region develop lamellae type structure with a strong shape anisotropy. In the vicinity of the tool-chip interface the lamellae are almost parallel to the surface. Furthermore, in chips machined at low speed one can observe the features directly related to BUEs. Figure 4-6 shows a complete BUE, which detached from the tool tip and was trapped inside the chip when machining at 5 m/min. Similar signatures of BUE were present also at 10 and 25 m/min cutting speeds. It is notable that the lamellae structure is significantly finer inside the BUE, that in the rest of the chip. In addition, figure 4-6 demonstrates a change in the cutting geometry, as in the presence of BUE chip slides against nose with an angle of 20 ±5 degrees instead of the rake angle of the tool of 6 degrees.

As seen from Figure 4-5, at the speed of 50 m/min lamellae in SSZ start to lose their integrity, breaking apart into smaller grains. This process is most pronounced close to the rake surface where almost equiaxial grains are visible, while deeper into the chip the lamellar structure is still preserved. At the higher cutting speeds, the region of equiaxiality extends deeper into the chip to about 10 micrometers depth (dependence of the thickness of this region from the cutting speed is plotted at Figure 4-8). It is notable that the size of equiaxial grains increases from the surface to the depth of the chip from sub-100 nm to a few hundred nanometers across.

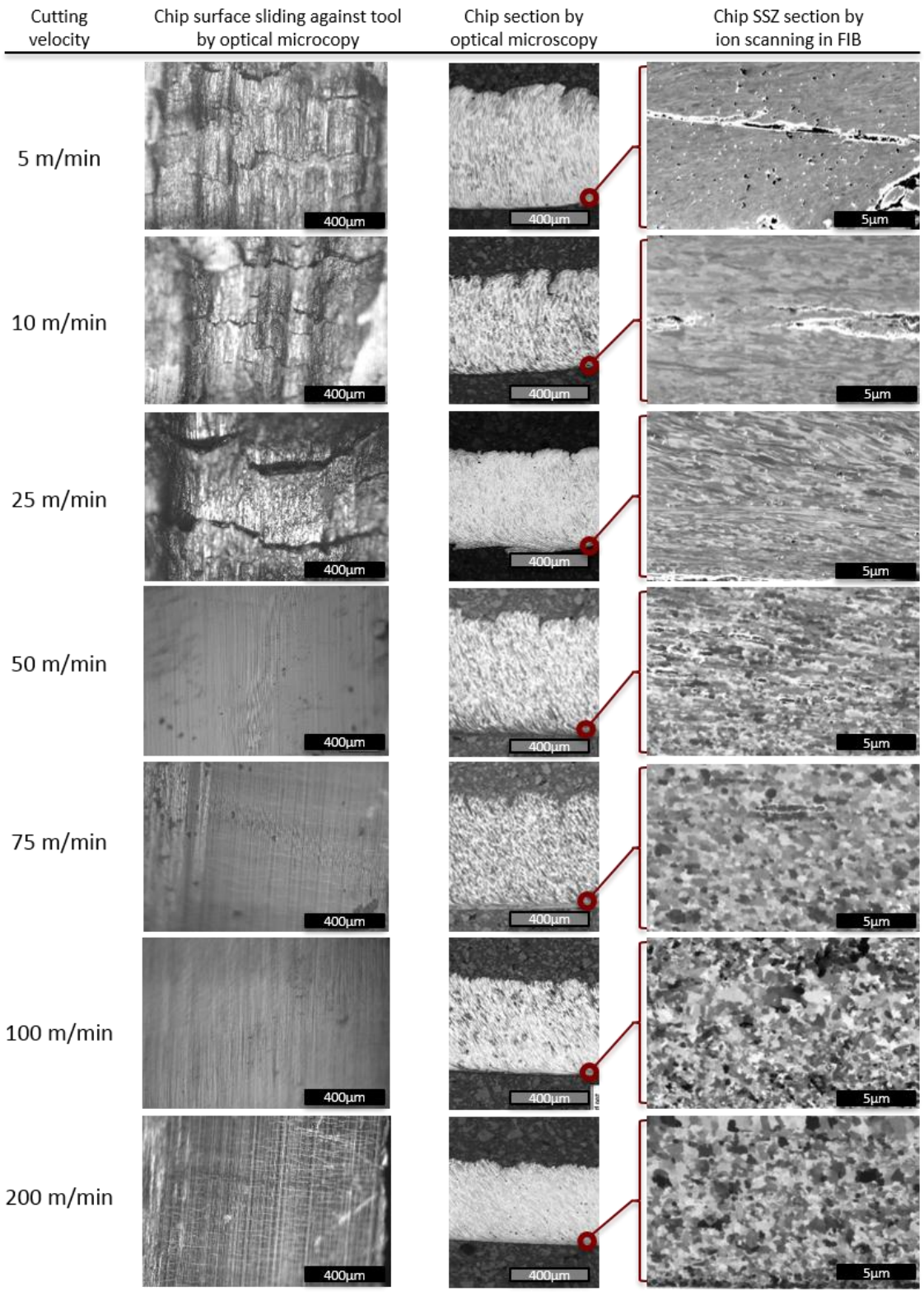

Figure 4-5 Chips made by cutting with feed 0.2 mm and cutting speeds from 5 to 200 m·min-1. Left column - images of the chip surface sliding against the tool (location of Figure 4-4c). Middle column – optical images of the complete chip cross-section. Right column - FIB images of the SSZ area (the bottom corresponds to the chip rake surface) (location of this area is indicated on Figure 4-4a).

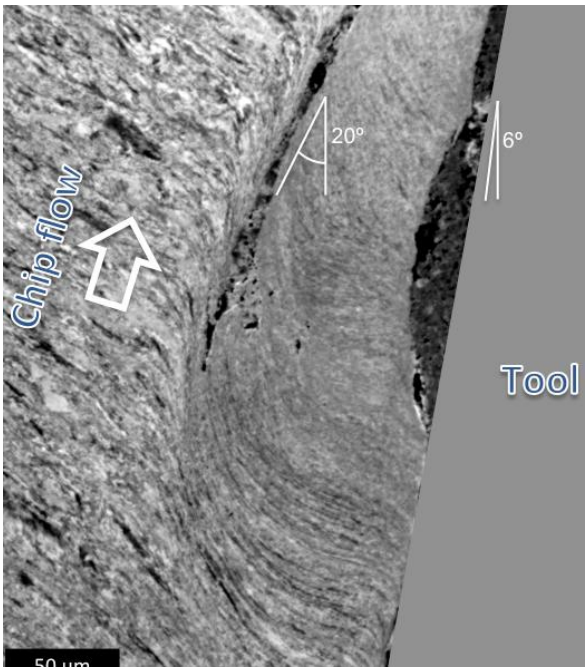

Figure 4-6 BUE attached to a chip machined at 5 m/min (tool is overlapped on image for clarification).

Figure 4-7 presents the data obtained by analysis of EBSD patterns. The upper row shows color coded orientation maps of SSZ of the chips cut at different speeds. These maps confirm the observations made by FIB channeling contrast – starting from 50 m/min cutting speed a layer of equiaxial small crystals starts to develop at the rake surface of the chip, and its thickness increases with growing cutting speed. At the same time the size of the grains, which develop equiaxiality increases with growing speed. The varying distribution of grain sizes with the depth below the rake surface is also visible. The black color in the proximity of the rake surface at 200 m/min cutting speed indicates that the grain sizes in this region are below the resolution limit of EBSD, which was of the range of 100 nm.

The polar maps in the middle row of Figure 4-7 result from the statistical analysis of orientation maps and reflect the probability to find particular crystallographic orientation in the ensemble of crystals. Clustering of the points on these plots indicate the presence of preferential orientations/texture. As is seen on the middle row of Figure 4-7 the pole figures become more diffused when the cutting speed grows from 50 to 200 m/min reflecting more stochastic distribution of the grains orientation. Thus, increase in cutting speed not only leads to disintegration of lamellae to small crystals, but also to rotation of these crystals inside the matrix. This can be also visually detected on the orientation maps at the top row of Figure 4-7 as a more uniform color distribution with the increase of cutting speed.

The bottom row of Figure 4-7 shows the outcome of kernel average misorientation (KAM) analysis of the same EBSD data. KAM represents the distortions of orientation inside individual grains and can be related to density of geometrically necessary dislocations

(Calcagnotto et al. 2010). Blue color on KAM maps corresponds to relaxed grains, while green areas depict deformed regions corresponding to high dislocation density. It is seen, that lamellar structure still existing at 50 m/min cutting speed preserves much more dislocations than equiaxial grains obtained between at 100 and 200 m/min. Thus, the process of lamellae disintegration leads also to dissipation of stored defects and relaxation of stored strain energy created upon shear deformation of SSZ.

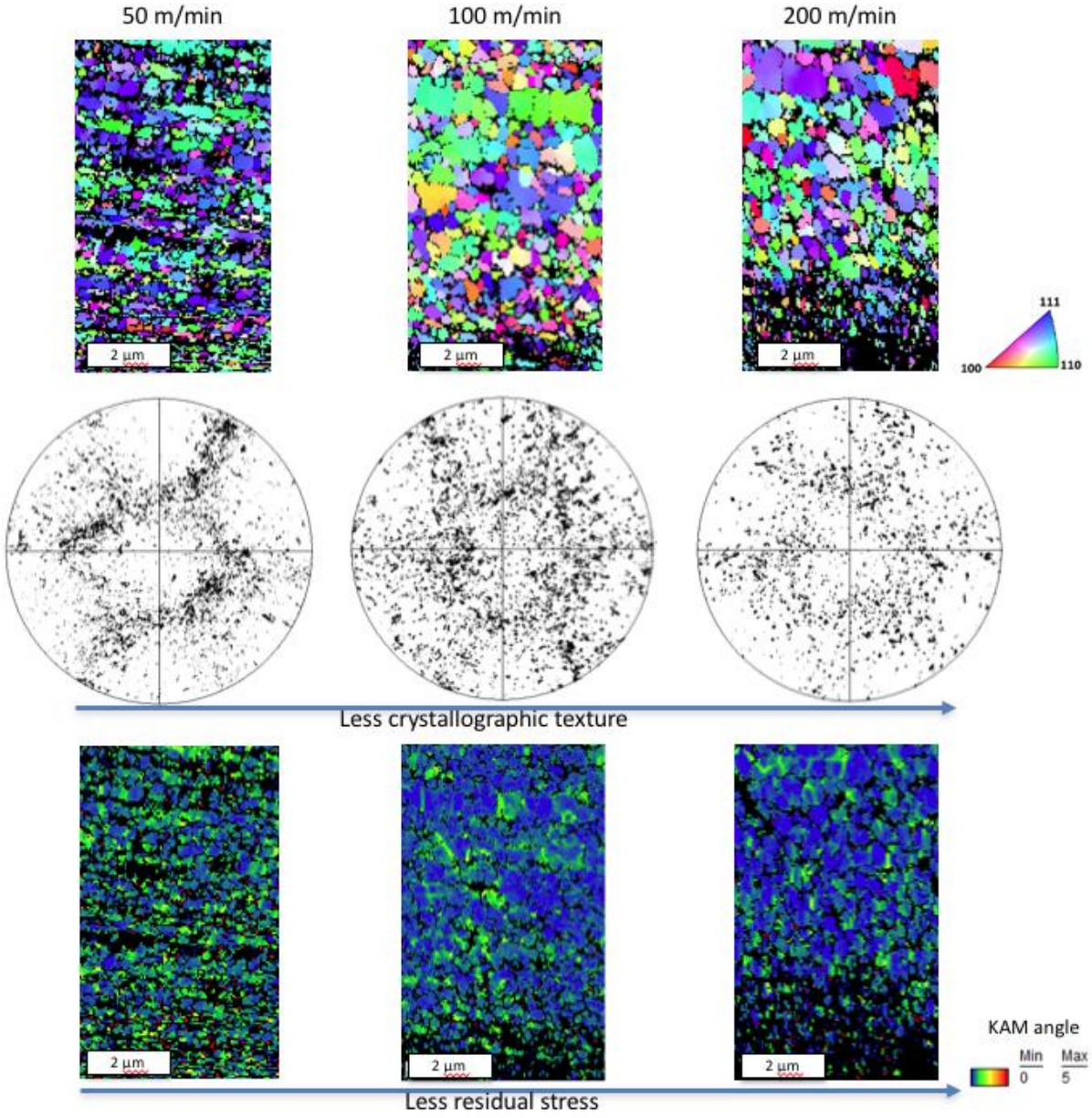

Figure 4-7 Crystallographic orientation study by EBSD on SSZ (bottom of the images corresponds to chip-tool contact surface) on chips cut at 50, 100 and 200 m/min. Top row shows inverse pole figure (IPF) colored maps. The middle row plots the pole figures (PF). The bottom row represents the kernel average misorientation (KAM).

To summarize the microstructural study, we can conclude that the processes taking place at tool-chip contact develop different surface and microstructural morphologies in SSZ for chips generated below and above 50 m/min. This is related to the chip surface changing

from cracked discontinuous to smooth as well as the appearance of the subsurface area with equiaxial crystallites morphology and reduced density of stored defects.

4.3.2 Machining output

In the experiments in the machining bench the forces, tool temperature, chip thickness and tool-chip contact length were measured for each cutting speed. The data obtained is depicted in Figure 4-8 except for the tool-chip contact length. In-line with the machining output data the thickness of the layer with equiaxial grains determined from FIB images is also plotted on Figure 4-8 (see Appendix A for the method of measuring this thickness).

The cutting and feed forces, along with chip thickness show a general decreasing trend with increasing cutting speed. However, this tendency presents a sharp transition. Between 25 and 50 m/min the cutting force abruptly increases by 10 %, recovering the decreasing trend further on. The feed force also has a transition between 25 and 50 m/min. Between 5 and 25 m/min the force remains constant, and at 50 m/min increases by 33 %. From 50 m/min on it monotonically reduces with the increase of cutting speed. The values of chip thickness present a similar feature between 25 and 50 m/min at which point the thickness increases by 50 %. This feature coincides with the onset of the formation of layer of equiaxial grains. Temperature shows a monotonic growth without singularities reaching about 550 ºC at 50 m/min.

4.4 Discussion

4.4.1 Compliance with the literature data

The trend in forces and chip thickness shown above is consistent with the transition from a cutting regime where chip slides against BUE, to the regime where chips slides directly against the cutting tool (Childs et al. 2000; Zorev 1966). Confirmation for existence of BUE at low cutting speeds is found in detached BUE structure trapped in the chip at 5 m/min (Figure 4-6). We observe the abrupt transition between these two regimes at about 50 m/min, which is in a good agreement with the results of Childs et al. However, (Kümmel et al. 2014) observed a gradual reduction of BUE size at higher velocities in the range of 50 to 100 m/min, which may be related to a very small feeding rate used in that study, resulting in lower temperatures at the tool.

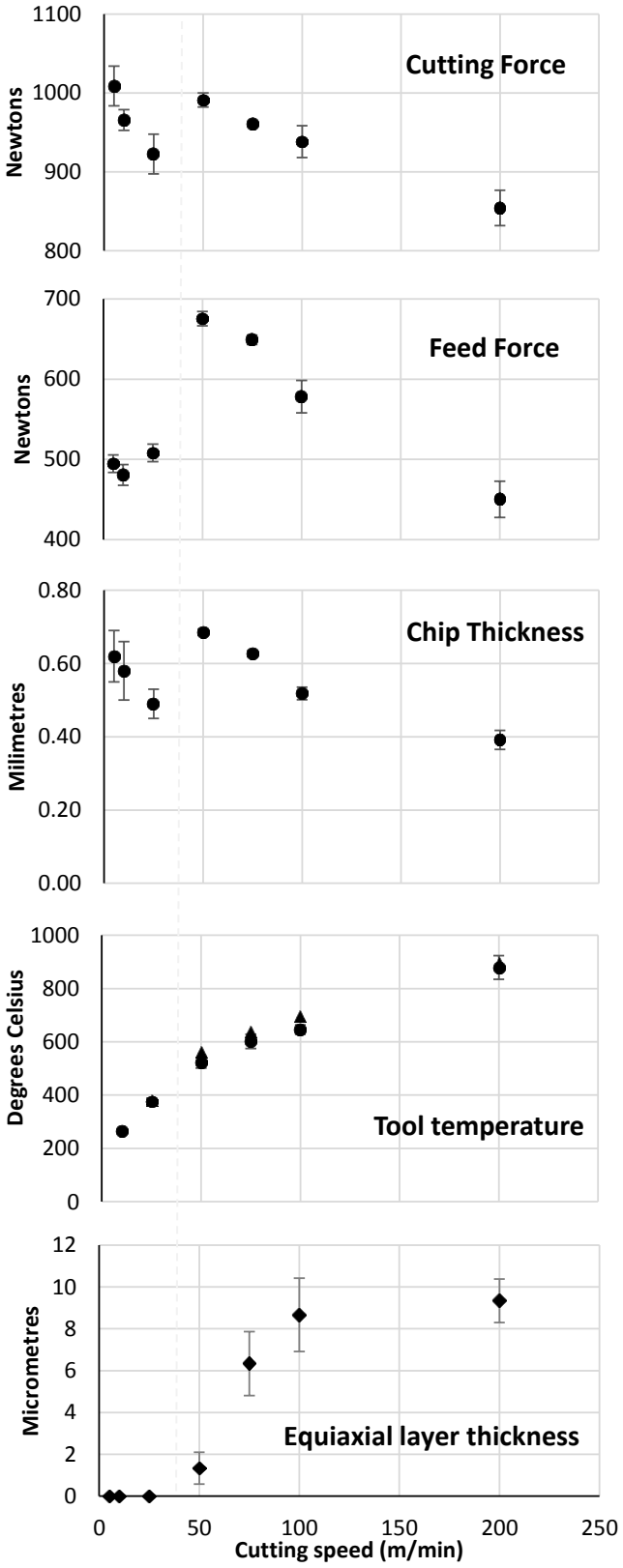

Figure 4-8 Cutting force, feed force, chip thickness, tool temperature in chip-tool contact, and equiaxial grains layer thickness experimentally obtained by machining steel AISI 1045, feed 0.2 mm and cutting speed from 5 to 200 m/min. The error bars reflect the standard deviation of multiple measurements. Additionally, triangles on the tool temperature plot represent temperature values obtained in simulation (for cutting speed 50 m/min and above).

A simple picture for the singularity in behavior of macro-mechanical parameters observed experimentally can be found in (Childs, 2013), where from simulations of the flow velocities in the chip it is evident that BUE acts as effective tool tip, effectually increasing the rake angle. Hence the BUE, shown on Figure 4-6, increases the effective rake angle from 6 to 20 degrees reducing cutting force (F_c) by 8% and feed force (F_f) by 35%, as well as chip thickness by 40%. (Arrazola, 2003) predicted an increase of approximately 1-2 % and 5-10 % for cut and feed forces respectively for every 1 degree of decrease of the rake angle. For our case this would mean expected increase of forces by 14-28 % and 70-140 % for cut and feed forces respectively. There is an obvious two-fold discrepancy between expectations and observations. In the same way, (Childs 2013) has reported approximately 2-fold discrepancy of experimental and simulated value for forces increase during transition. Both estimations (Arrazola 2003) and (Childs 2013) took into account the difference in temperature softening due to different conditions in the cutting area in two regimes, though this seems to be not sufficient to explain experimentally observed small growth of forces. There should exist other and stronger softening mechanism, which switches on during transition and results in a substantial reduction of friction.

The structure of BUE has been under extensive investigation (J. Kümmel et al. 2014) and Figure 4-6 is consistent with the results obtained in that paper. BUE has a very fine lamellae structure with the lamellae thickness down to 100 nm scale indicating high values of strain in this region. Due to the strain hardening of the material (which may reach 200 – 300 % according to (Kümmel et al. 2014)) the BUE is harder than the workpiece and the rest of the chip, and thus can act as an effective tool tip as discussed above.

On the other side of transition, i.e. above 50 m/min cutting speed, we observe a white layer under the rake surface of the chip, which is microscopically composed of equiaxial grains with the sized down to sub-100 nm scale and random crystallographic orientation. This is consistent with earlier studies of the structure of white layers obtained for different types of strain loads for different materials (Sakai et al., 2014). The genesis of this sub-surface region was associated with high strain, high strain rate and elevated temperature (Landau et al., 2016). The origin of the layer was controversially discussed in terms of phase transition (Greenwood and Johnson, 1965; Subramanian et al., 2002) or dynamical recrystallization (DRX) (Sakai et al., 2014). By now it is well accepted that the equiaxiality and random orientation of sub-micrometer crystallites in this layer is achieved via rotational DRX (Meyers et al., 2003; Perez-Prado et al., 2001). It was suggested that DRX may take place at notable rate already at half melting temperature (in Kelvin) (Meyers et al. 2003)– this is close to the transition temperature we observe in our experiments (see Figure 4-8).

4.4.2 Origin of the BUE to non-BUE transition

A number of hypotheses have been proposed to describe the transition between two cutting regimes (Childs 2013; Da Silva 1998; Iwata and Ueda 1980; Tomac et al. 2005; Wallbank 1979). Most of them utilize the effect of thermal softening, i.e. gradual reduction of the strength of a material with the increasing temperature (Campbell and Ferguson 1970). This would lead to a scenario in which the secondary shear zone gradually becomes softer and thus less and less able to support the BUE. At the same time tribological experiments of (Ben Abdelali et al., 2012) and (Rech et al., 2013) showed that in the similar cutting speed range a friction coefficient of AISI 1045 steel abruptly decreases more than twice. In a later work the same group (Ben Abdelali et al. 2013) found a clear correlation between tribological measurements and the appearance of the white layer. Though they still attributed the decrease of friction to thermal softening of the steel, these results clearly showed that the observed transition corresponds to qualitative change of the friction mechanism, which at low speed is determined by plastic deformation in the contact layer, while at higher velocities it is accompanied by DRX and thus dynamical microstructural softening (Griffiths 1987; Subramanian et al. 2002), which overperforms the effect of thermal softening (Landau et al. 2016), leading to a step-like increase of ductility.

In this scenario, the temperature, rather than acting as a direct softening factor, triggers the DRX and thus dynamically creates a soft “lubricant” layer between the tool and the workpiece. Thus, DRX is a missing piece of a puzzle which can explain the discrepancy between observed and predicted forces increase after transition from BUE to direct sliding mode.

Figure 4-9 depicts a summary of the relations observed between DRX, BUE and friction evolution depending on the cutting speed. Experiments in tribometers, have shown a continuous decrease in the friction of tool – AISI 1045 steel above ~50 m/min (Rech et al. 2013), in good agreement with the activation of DRX observed experimentally in the present work, and with the absence of BUE as well. Here we propose that the same DRX mechanism that reduces the friction, is responsible for the initiation of the transition between BUE and non-BUE regimes in orthogonal cutting experiments. In order to clarify a possible contribution of DRX in the change of cutting regimes we look in more detail into conditions for DRX onset and evolution.

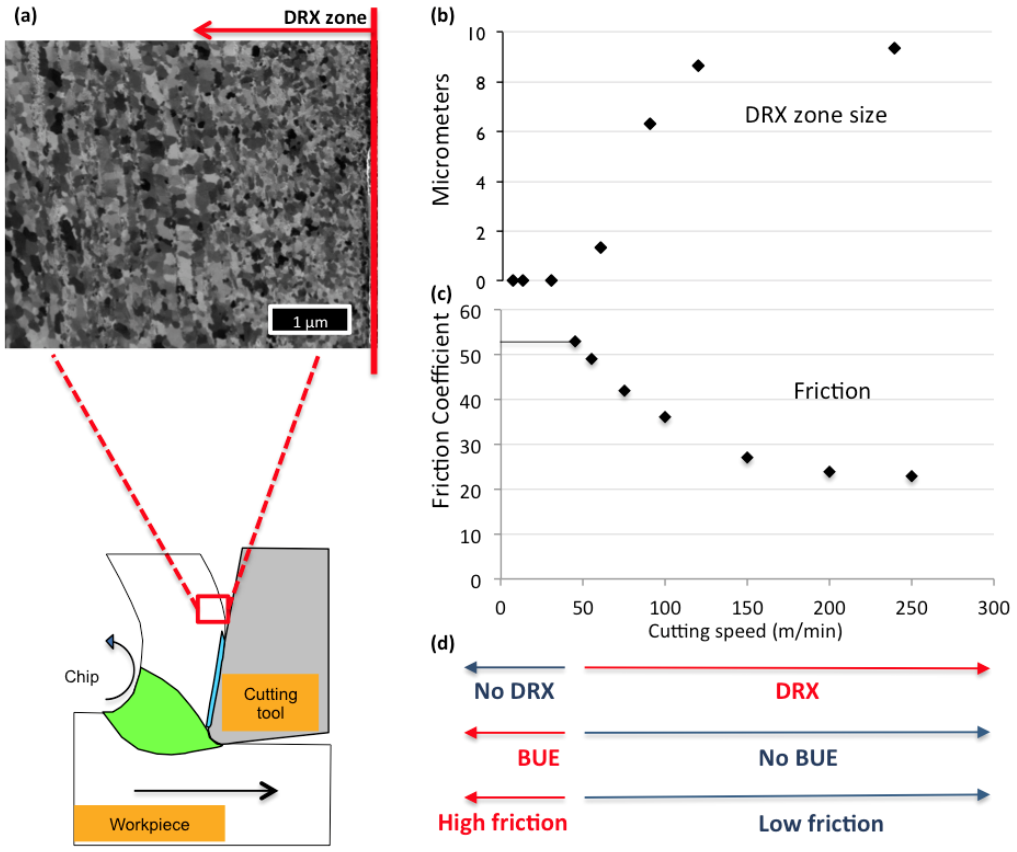

Figure 4-9 (a) Image of the area affected by DRX in the SSZ of a chip. (b) and (c) represent the effect of cutting speed in the size of DRX layer and tool-chip friction. Data of (c) has been obtained from (Rech et al. 2013). (d) DRX and BUE have shown as mutually excluded, in agreement with evolution of tool-chip friction.

4.4.3 DRX initialization and evolution in orthogonal cutting

DRX is a very common phenomenon at the conditions, when crystalline materials are subjected to high strains at high strain rates and elevated temperatures. It has been argued (Hines and Hines 1997) that DRX taking place in metals during high speed processing (punching, hot rolling, high speed cutting) has rotational nature in contrary to migrational recrystallization. The time frames for the later are a few orders of magnitude larger than for the former and there is simply not enough time for substantial boundary migration (governed by lattice diffusion) during a few milliseconds, which is a typical timescale in high speed processing (for instance tool-chip contact time at 5 m/min is approximately of 33 milliseconds, 7 milliseconds at 25 m/min, 3.4 millisecond at 50 m/min, and 0.46 milliseconds at 200 m/min. Rotational recrystallization in turn is governed by boundary diffusion, which is much faster than lattice one and typically has an activation energy twice as low (Frost and Ashby 1982). To describe the onset of DRX in orthogonal cutting we will use a simple model proposed by (Meyers et al. 2003) for rotational DRX. We assume here that DRX is a key and limiting stage in the process of material softening, i.e. all necessary preliminary steps, like dynamical recovery, take place before DRX onset without substantial time consumption. This is a

reasonable assumption as activation energy for these processes (Kuo and Lin 2007; Sakai et al. 2014) is typically much lower than for DRX. Meyers has described the rotation angle of a grain boundary during rotational DRX as

$$f(\theta) = \frac{4\delta D\gamma}{LkT}t \qquad \text{Eq. 4-1}$$

where f(θ) is a complex function (Meyers et al. 2003) of rotation angle θ only, δD is a product of grain boundary thickness and grain boundary diffusion coefficient, γ is the surface energy, L is the length of the grain face, k is a Boltzmann constant, T is the temperature and t is the duration of the process. δD is defined via grain boundary mobility δD_0 as:

$$\delta D = \delta D_0 exp\left(-\frac{Q}{RT}\right) \qquad \text{Eq. 4-2}$$

where Q is an activation energy for grain boundary diffusion and R is a gas constant.

Though parameter L in Eq.(4-1) is not exactly the grain size, it can be used if the relative comparison is made. Resolving equation (1) relative to L and combining it with Eq.(4-2) we get equation:

$$L = \frac{4\delta D_0 exp\left(-\frac{Q}{RT}\right)\gamma}{f(\theta)kT}t \qquad \text{Eq. 4-3}$$

which describes the size of the grains accessible to rotational DRX at particular temperature over the time period t.

The parameters used in the equations above for α-Fe are: a product of grain-boundary mobility and thickness δD0 = 1.1×10 12 m^3/s (Frost and Ashby, 1982); activation energy for grain-boundary diffusion Q = 174 kJ/mol (Frost and Ashby, 1982), surface energy at 300K γ ~ 2.4 J/m^2 (Schönecker et al. 2015).

The function $f(\theta)$ has a singularity at 30º (at complete relaxation), so it is not convenient to deal with. For further discussion we will rather use any other value close to 30º, for example 29º, and monitor how the DRX evolves for different size of the crystallites.

Figure 4-10 shows the plot of Eq. (4-3) for f(29º) calculated for the process time t interpolated from experimental data (between 0.5 and 33 ms). The function has a smooth onset at about 400 ºC indicating that around this temperature DRX starts for the smaller sub-100 nm grains structurally leading to equiaxial nanocrystallites with random orientation. What is more important, DRX results in dynamical softening of the material, which undergo

recrystallization (Osovski et al. 2012). Figures 4-4 and 4-5 show that at low cutting speeds the finest anisotropic/lamellae crystals are found in SSZ at the proximity of rake surface and also they constitute the BUE. So, the onset of DRX will start in this region, making it softer than the rest of the material and thus efficiently preventing the formation of BUE.

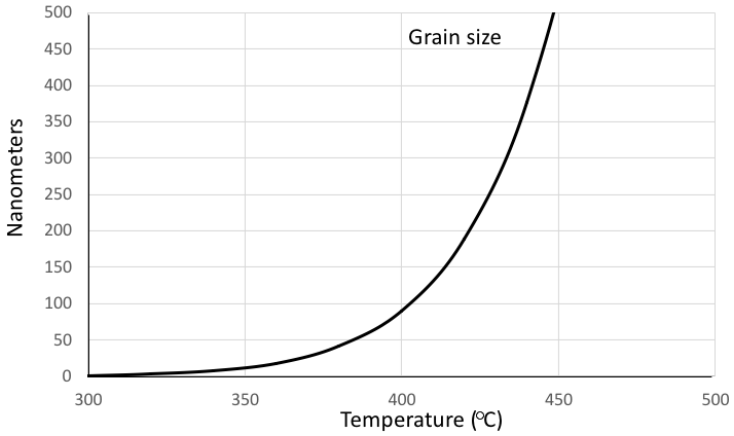

Figure 4-10 The size of the grains accessible to rotational DRX (L in Eq.(4-3)) vs temperature.

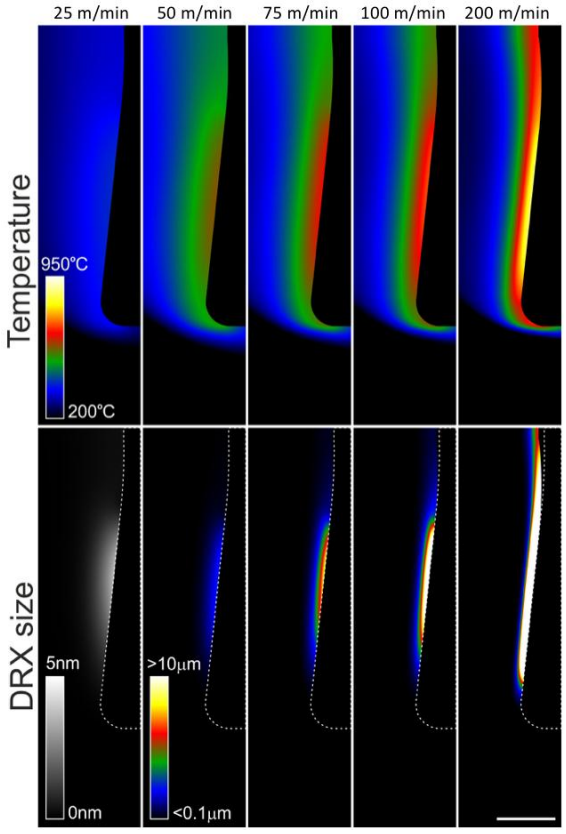

Figure 4-11 Upper row – simulated temperature distribution in the chip for different cutting speeds assuming a direct sliding mode. Lower row – the map of crystal sizes accessible to rotational DRX calculated from temperature distributions according to equation (3). The scale bar corresponds to 100 μm for all images. Note a different color codding for the bottom left image.

With the increasing cutting speed, the size of the crystallites accessible by DRX grows exponentially, which should seemingly lead to recrystallization of the whole chip. However,

as is evident from the top row of Figure 4-11 (numerical values obtained from the FEM simulations described in section 4.2), with growing cutting speed high temperatures become more and more localized close to the rake surface of the chip. The bottom row of Figure 4-11 represents these temperature distributions recalculated in accordance to Eq. (3), i.e. represents the distributions of the sizes of the crystallites accessible to rotational DRX at different cutting speeds. At 25 m/min the crystallites accessible to DRX are less than 5 nm in size, meaning that practically DRX does not take place, and rather the strain hardening develops leading to the formation of BUE at these conditions. Starting from 50 m/min DRX acts on larger and larger grains, yet staying confined in 10-20 μm rake subsurface region even at highest velocities. This observation is in close agreement to the observed saturation of the thickness of the equiaxial/white layer with cutting speed to the value of about 10-15 μm (Figure 4-8).

It is remarkable that the grain size does not increase in the proximity of the contact as a result of DRX as is evident from figure 5 and especially from Figure 4-7. This gives a strong argument for the rotational nature of DRX, which simply converts crystals severely elongated due to the share stress into equiaxial grains of similar dimensions. Grain boundary migration, which would be responsible for the grains growth, is still not activated at these temperatures as was pointed out by a number of authors (Capdevila et al. 2003; Taheri et al. 2005).

4.4.4 Combined description of two cutting regimes

Thus, the role and evolution of DRX in orthogonal dry cutting of AISI 1045 steel may be qualitatively described as follows. The temperature threshold for the onset of rotational DRX separates the cutting conditions into two distinct regimes. Surprisingly, this threshold is very well described by a simple model for rotational DRX (Meyers et al. 2003) utilizing activation energy for grain boundary diffusion. If cutting conditions (besides the cutting speed this can be a feed rate, yet not studied in this work) are so, that the threshold temperature is not reached, the extreme share stress in SSZ leads to strain hardening of the rake surface of the chip, which sticks to the surface of the tool and promotes the growth of BUE. BUE then acts as an effective tool tip, increasing the rake angle and thus decreasing the forces acting on a tool. Instability of the BUE and its periodic detachment can result in a rough surface of the chip (and the workpiece, yet not shown in this work).

When the temperature threshold is reached, the dynamical softening due to DRX first develops at the very proximity of the contact between the chip and the tool, thus canceling the strain hardening and preventing the formation of BUE. As is seen from Figure 4-11,

conditions for DRX are first reached not directly on the tip itself, but at some distance up the tool rake surface, which may lead to a gradual decrease of BUE size with cutting speed (as was observed e.g. in (Kümmel et al., 2014)), rather than to an abrupt transition. It should be pointed out, that even at the highest cutting speed studied in this work (200 m/min), the area close to the tool apex is not accessible by DRX and thus the tool surface is always in contact with the strain hardened material, though the area of this contact decreases at higher speed.

The transition from BUE mode to the direct sliding of the chip against tool surface is accompanied by a decrease of effective rake angle (in our case from 20 to 6 degrees as was discussed in section 4.4.1) leading to the stepwise increase of cutting forces and increase of chip thickness. With the further increase of cutting speed the thickness of soft DRX layer (which acts as a lubricant) increases together with the temperature at SSZ, leading to a gradual decrease of the cutting forces and chip thickness. The thickness of DRX layer saturates already at 200 m/min due to a strong localization of high temperature near chip-tool interface. The micro-nano-structure of the DRX layer, namely preservation of the size of the crystallites during recrystallization, gives a strong argument for purely rotational nature of DRX process.

4.5 Conclusions

The area of the secondary shear zone that develops dynamic recrystallizations has been matter of a multi-approach analysis. Morphological, structural and mechanical studies have been performed.

Samples of AISI 1045 steel were studied under machining at cutting speeds between 5 and 200 m/min. The combination of several information sources, from the machining tests to the ion scanning microscopy, successfully revealed the succession of events that drives the chip flow regime at mid-high cutting speeds.

- The change of the cutting mode at a speed between 25 and 50 m/min was observed for the orthogonal dry cutting of AISI 1045 steel with uncoated P15 carbide cutting tools, which reflected in the abrupt change of cutting forces, chip thickness and chip microstructure. According to the concepts existing in the literature this change was attributed to a transition between the BUE formation mode and the direct sliding mode.

- The microstructure observed in the chips produced below the transition speed was characteristic for cold working and showed drastically strained lamellae structure in the SSZ. Chips produced over the transition speed showed the presence of the layer of equiaxial grains down to 100 nm size, which is characteristic for the DRX process. The independence of the grain size in relation to the cutting speed pointed to the rotational nature of the DRX.

- It was proposed that it is a temperature onset of the DRX which causes the transition from the BUE to the non-BUE mode and described a complete scenario of the transition between the two modes.

- FE simulations reproduced the onset and further evolution of the DRX layer, demonstrating that the onset of DRX coincides with the activation of the diffusion conducted through the grain boundaries, which is an underlying mechanism for rotational recrystallization.

The potential of the complex approach including systematic microstructural characterization for understanding of the processes taking place in the confined space and at the extreme conditions during orthogonal cutting was demonstrated. The present study provides new insights into the machining process, alluding to fundamental microstructural effects to explain the evolution of the tool-chip contact. This could help solving tool-chip friction issues in future simulations and practical experiments.

5 Characteristics of microstructure obtained by ultra-fast recrystallization during high-speed steel cutting

Metal cutting represents a process where ultra-high-speed deformation is present, particularly in the proximity of the cutting tool. In the present work attention has been paid to the characteristics of chip material in contact with the rake surface in the tool, which presents a unique ultra-refined microstructure consequence of a recrystallization. The evaluation of microstructure morphology, defects density, mechanical properties, and chemistry revealed an extreme refinement of the grain size, well under the typical sizes after industrial recrystallization. This microstructure has demonstrated a particular mechanical behavior, including an uncommon reduction of the elastic modulus. The condition of the microstructure has similitudes with both hot and cold severe forming. It has been argued that the microstructure refined down to grains sizes of 70 nm, and the re-solution of carbon in the ferrite lattice induce certain amorphization on the material what lead to the elastic modulus reduction and enhanced strength.

5.1 Introduction

Industrial metal cutting presents one of the largest strain-rates among of the whole range of materials processing techniques. While the industrial relevancy has fed metal cutting research for decades, the extreme thermo-mechanical conditions and the small area of contact have made invisible the phenomena in the proximity of the cutting edge. There, material hits the tool at velocities well over 1 m/s, and deforms more than 100 % in a fraction of millisecond (Frost and Ashby 1982). Hence, a process happening locally in front of the tool edge reaches strain-rates over 10^3 s^{-1} in common operations. Such phenomena induce in the chip SSZ a microstructure refined down to the nanometer scale, as shown in previous chapter, promoted by a DRX process.

The nanostructure of the recrystallized layer in the SSZ has been subject of investigation in the last few years (Courbon et al. 2014; Pu et al. 2016), disclosing grains of 200 nm of diameter in the edge proximity. Furthermore, in the present work (chapter 4) structures down to 70 nm has been observed after high-speed cutting, remarking the unique structure developed in the proximity of the contact with the tool. This structure, consequence of the contact between tool and workpiece material, may be produced in the different sides in which material slides against the tool. Hence, a nano-structured material could be induced in machined surfaces. This last has been demonstrated by Liao et al. (2018), who by microscopy works on machined nickel alloys have shown that the recrystallized layer of material is also present in the surface of industrial parts (Liao et al. 2018). Thus, this recrystallized layer may induce special mechanical properties in the surface of industrial parts.

Recrystallization traditionally enhance the mechanical properties in metals and alloys. It has been exploited by different paths. By thermal mechanical loads material's structure can reassembled into a new microscopic distribution, leading to smaller grains and more dispersed particles (Barani et al. 2007). In contrast to that, over the past two decades another method of new grain formation has been studied extensively; this takes place under conditions of severe plastic deformation (Sakai et al. 2014). In this case, the ultrafine grained structures are developed at relatively low temperatures. In some cases, this technique applied in pearlitic lead to what has been call super-saturated ferrite (Nematollahi et al. 2016), referring to a state where carbon atoms of cementite re-dissolve into the ferrite overcoming the saturation limit. Contrary to these two recrystallization processes, the effect of recrystallization observed in metal cutting has been claimed, with only recent attention for further characterization study (Liao et al. 2018). Liao et al. show that the layer affected by DRX develops an average grain size of 300 nm homogeneously distributed along the surface.

This material, tested by pillar compression, doubles the stress (1% strain) depicted by the original bulk material, thus providing special mechanical properties in the parts surface.

This strength increasement coincides with the trend observed in grain refined materials which, down to certain size, tend to have higher flow stress (Hall 1951) that the micro-crystalline counterpart. Furthermore, it has been demonstrated that in the regime of tens of nanometers or diameter the mechanisms of plasticity may change. (Grewer and Birringer 2014) have shown that dislocations are not there anymore the dominant mechanisms, giving some importance to grain boundary migration. Moreover, not only the plastic, but also the elastic response may be altered by the large volume fraction of boundaries (Giallonardo et al. 2011). Thus, a number of different aspects may be involved in the mechanical properties of the layer of workpiece material in contact with the cutting tool after machining, which may lead to unique properties in the coating surface.

In this work we present a composite study which includes characterization of the microstructure in the SSZ affected by DRX in a steel cutting process at high speed. Morphological, structural, chemical and mechanical tests have been performed on the material, i.e., machining-induced recrystallized AISI 1045 steel.

5.2 Experimental procedure

5.2.1 Machining

The material used has been the same exposed in Chapter 4. Cutting tests have been made in dry conditions with uncoated P15 grade carbide cutting tools (WIDIA TPUN 160308 TTM with rake angle = 6 degrees and cutting-edge radius = 40 μm). The feed rate was fixed to 0.2 mm/rev, while the cutting speed was 200 m/min. A fresh cutting edge was used for each test to preserve tool properties.

5.2.2 Sample preparation

A sample of workpiece material was diced by diamond saw and the surface was polished with diamond disks and aluminum oxide suspension. A final chemical-mechanical polishing was made by oxide polishing suspension (Struers OPS nondry). In order to prepare the chip cross sections, chips were embedded in conductive silver epoxy (Chemtronics CW2400). This reduces drift and sample charging in electron microscope as compared to a standard epoxy. Then the embedded chips were polished using the same procedure as for the workpiece material.

Samples embedded in silver epoxy have been used for chip section analysis, series of nano-indentations and to build and test micro-pillars. In this last case, the micro-pillars have been cut by ion beams. They were located in the proximity of the chip edge where dynamic recrystallizations develop. In order to test the different structure outside and inside the DRX layer, a number of pillars have been constructed at a distance of 3 to 60 micrometers from the edge, as seen in Figure 5-1. These pillars have been made by ion milling in two steps. Primary, with currents up to 9 nA it has been performed a rough milling. Subsequently, each pillar has been defined one by one using current down to 0.1 nA.

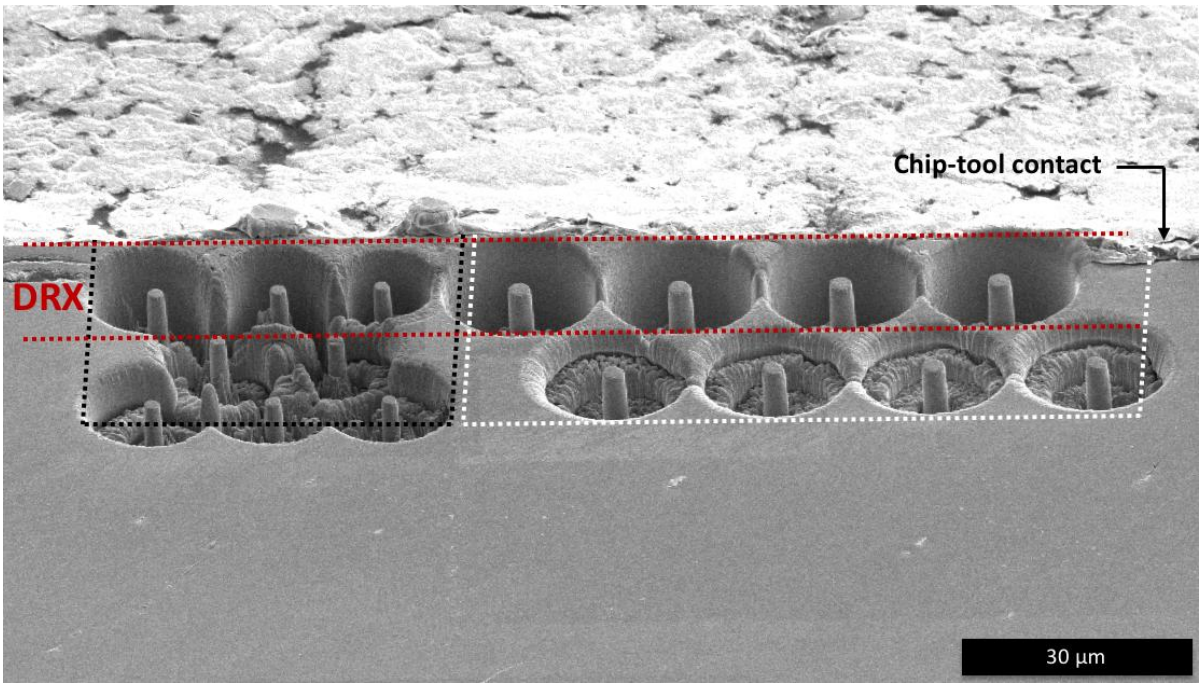

Figure 5-1 Pillars of 2 (left) and 3 µm (right) cut by ion beam in the proximity of the chip edge.

While chip embedding can be used to perform pillar cutting, this kind of preparations is not suitable for building TEM lamellae and beams for bending. In the first case, to obtain a lamella by FIB it is required accessing the chip from the sliding surface, perpendicular to the section to analyze. In the case of beams, they have to be built in the sample edge in order to give access to the ion column for milling from two sides, this in order to remove the material behind the beam for in-situ bending tests (shown in Figure 5-2). In that case, chip was prepared by direct glue to a holder by wax, polished, and finally detached and cleaned by acetone. The polishing method follow the same steps as for the workpiece material.

Beams have been milled by FIB following the steps to pillars. A first rough milling at high current (9 nA), and afterwards fine milling bellow 1 nA.

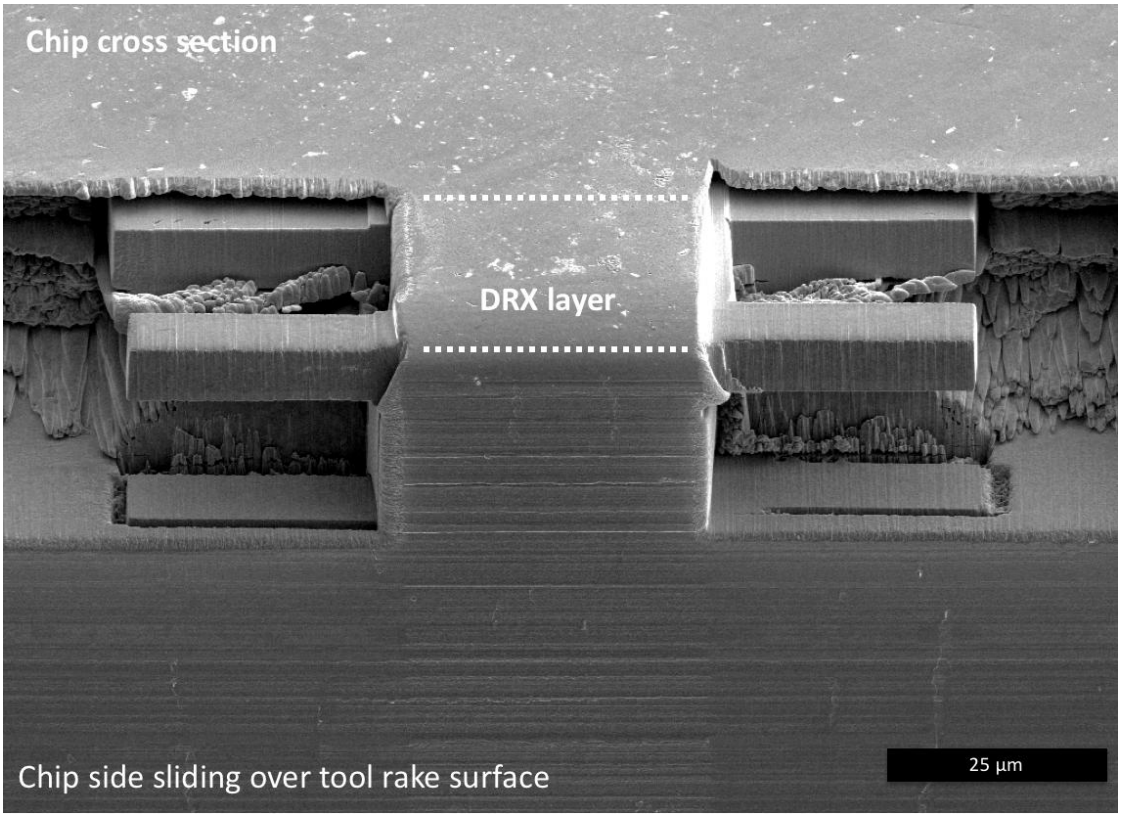

Figure 5-2 Beams of 5 µm side constructed in the SSZ, where DRX is developed during machining.

5.2.3 Microscopy

The microstructure of workpiece and chip was studied by SEM and FIB techniques similar to the study presented in chapter4. SEM was used to reveal the major morphological features of the samples like shape of the interface surfaces and cracks. In turn the crystallinity of the samples, i.e. the size and the shape of crystallites, was studied by FIB imaging utilizing channeling contrast (Canovic, Jonsson, and Halvarsson 2008). We utilized 5 kV acceleration voltage for electron beam and 30 kV for ion beam. FIB was also used to mill pillars and beams for micro-mechanical testing, in that case ion were accelerated by 30 kV. After mechanical tests pillars has been analyzed by SEM and low current ion scanning.

The EBSD technique was used to build maps of grains orientation, crystallographic texture and kernel average misorientation in a similar way as described in Chapter 4. Scanning was performed at 20 kV acceleration voltage and step sizes of 50 nm. Subsequent data analysis was made by OIM Analysis software. Experiments by the transmission electron microscope (TEM) were used to study the microstructure in detail, particularly grain distribution and particles. To study the chemical composition of material's features. It has been used a FEI Titan 60-300 equipped with an Edax EDX RTEM detector for x-ray analysis.

5.2.4 Mechanical testing

Original material and chips produced by the machining process have been characterized by nanoindentation as described in 3.1.7. In the pristine material a matrix of 36 indentations has been performed for statistical calculation of material hardness and elastic modulus. In the case of the chip, a line of 20 indentations has been performed across the chip from the side being in contact with the tool into the depth of the chip. In addition, the area affected by recrystallization has been characterized on a finer matrix of 15 indents to precisely estimate mechanical properties trend in this particular area. A Berchovich tip has been used and the indentation depth has been set to 140 nm to overcome the indentation size effect (Greer and Hosson 2011), leading to an indentation diameter rounding 600 nm. Hysitron TriboIndenter TI 900 has been used for these tests.

In order to test the pillars in the chip, the same nano-indenter has been fitted with a flat punch tip. 12 pillars have been successfully compressed by displacement control at a strain rate of approximately 40 s^{-1}. Sneddon criteria has been used for the correction of the base material deformation (Sneddon 1965).

The experiments of beam bending have been made in-situ in the chamber of the microscope Zeiss Sigma SEM. The testing device in that case was an Asmec nano-indenter UNAT-SEM2. Nanoindenter was equipped with a tungsten tip milled by FIB to perform bending tests (Figure 5-3).

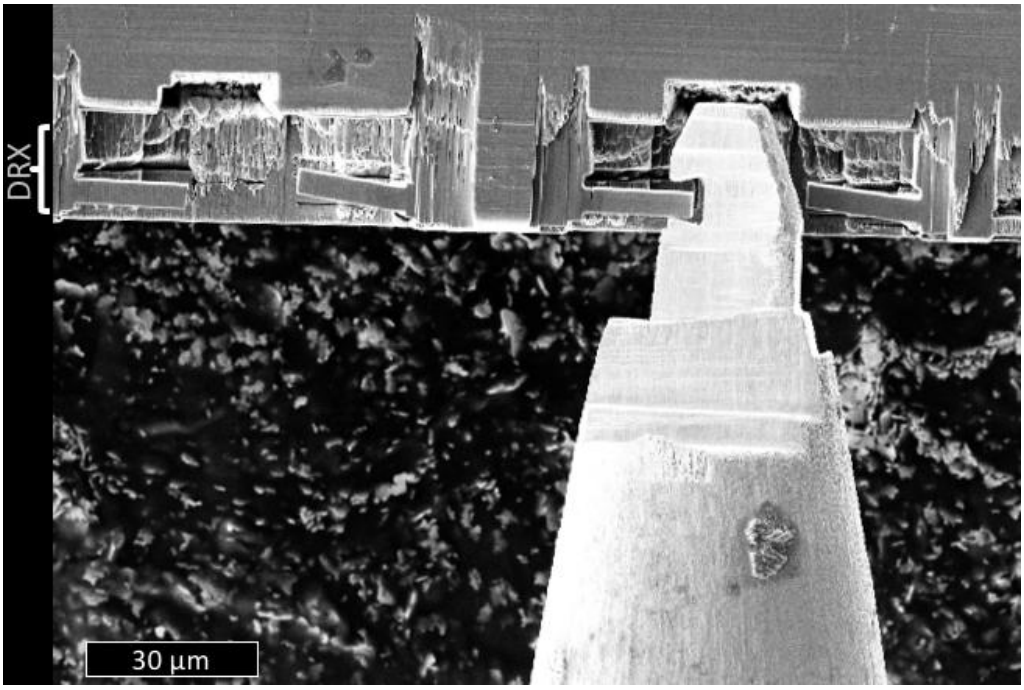

Figure 5-3 Setup for beam bending in-situ in the SEM.Tip fabricated by FIB milling of a tungsten needles.

5.3 Results

Here the results of investigation of the particular structure developed in the chip during metal cutting by multiple approaches are presented. Signal-based techniques like SEM, FIB, SEM-EBSD and EDX, and equipment for mechanical test like nanoindenter and in-situ SEM indenter have been used to characterize the area of interest. The original material, in addition to the microscopic analysis of Chapter 3.2.1, here is subject of analysis by nanoindentation to determine hardness and approximated elastic modulus. The chip is also investigated by microscopy and nanoindentation, but also by pillar compression and beam bending. Figure 5-4b gives a schematic of the chip area being monitored. Indentations and pillar compression test extend across SSZ and PSZ up to 60 µm from the edge, while beam bending concentrates in the SSZ side of the chip (Figure 5-4a)

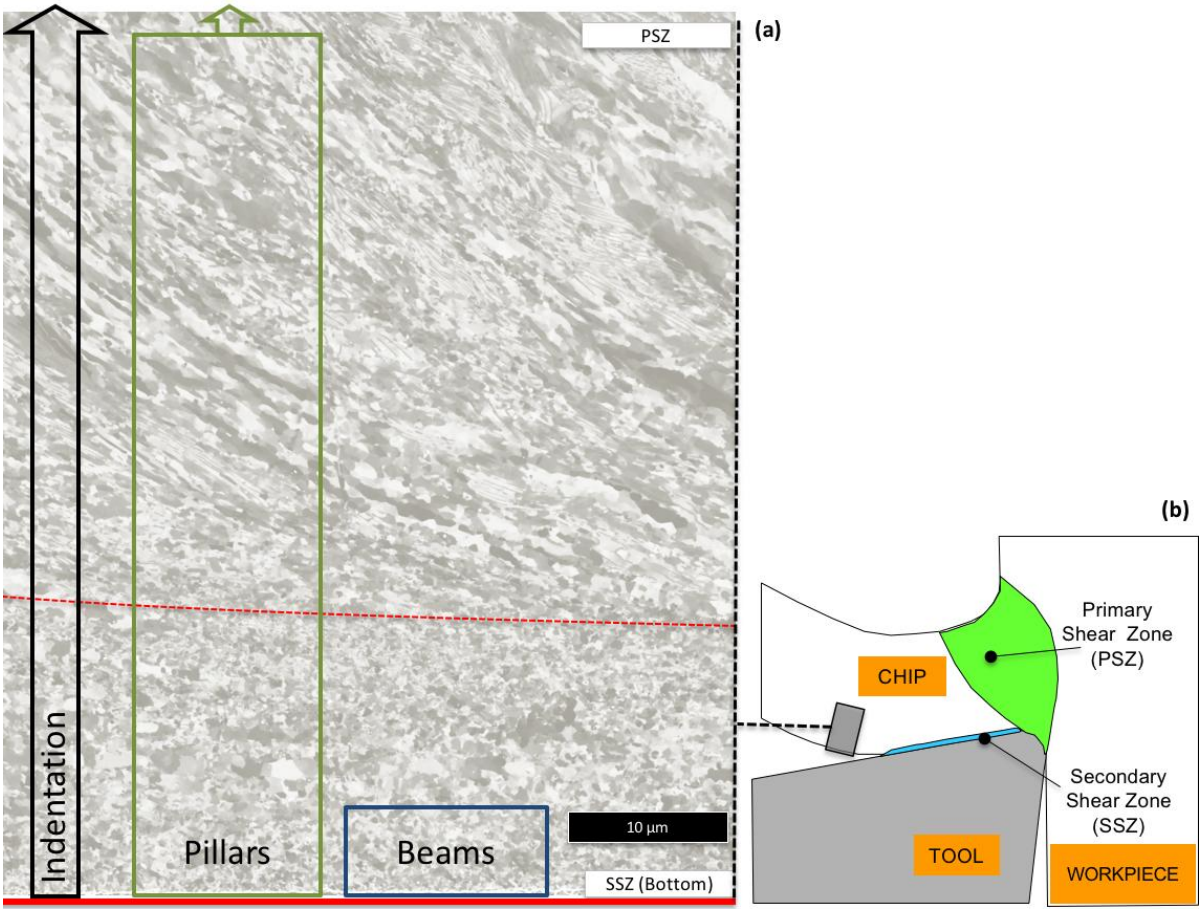

Figure 5-4 (a) Ion image of chip cross-section when machining at 200 m/min. Red dashed line is an estimation of PSZ - SSZ boundary. (b) Sketch of area of the chip under study.

It should be noted that nanoindenations in chip have been performed in two ways, by a line of tests perpendicular to the edge, as shown in Figure 5-4a, and also by a matrix of 3x4 indents restricted to the SSZ. This last in order to provide an accurate set of hardness values in the SSZ (Figure 5-9c,d).

5.3.1 Microscopy

Material present in the proximity of the chip-tool contact, where DRX is developed, has been morphologically analyzed by FIB imaging. Figure 5-5 depicts the microstructure developed in the SSZ after a DRX process revealed by this technique. Chip-tool contact corresponds to the bottom side of the image, as in the sketch of Figure 5-4a.

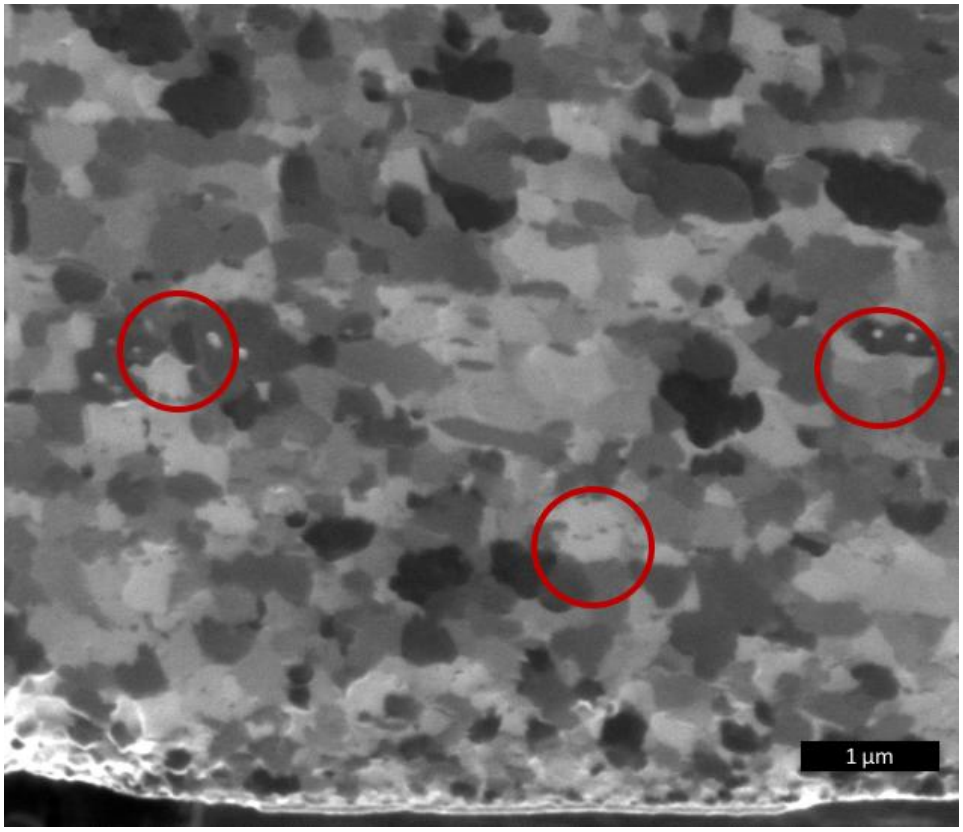

Figure 5-5 Detail of the SSZ by ion scanning of chip cross-section when machining at 200 m/min. Crystals tend to equiaxity and the diameter is consistently in the sub-micrometer regime. Some carbides are present in the structure (red cycles). In the proximity of the bottom this trend is remarked by grains in the order of 100 nm.

Figure 5-5 reveals a grain distribution down to sub-100 nanometer size in SSZ at the tool-chip interface, which comparing to the original material structure (Section 3.2.1) denotes a dramatic reduction in grain size. In addition, certain gradient of grain sizes is present, since grains in the contact proximity develop much smaller grain size as compared to e.g. 5 µm depth. This material developed after recrystallization presents a lack of cementite lamellae and few visible carbides. This is in contrast to the original material, which has pearlite colonies in 75 % of the volume, mostly lamellar pearlite.

The crystallographic structure has been analyzed by SEM – EBSD (see Section 3.1.4). Figure 5-6 depicts in the left side (a) a crystallographic orientation map in the proximity of the tool contact, including SSZ in the bottom side, and PSZ in the top. The PSZ region shows a structure with a prominent shear deformation, where grains/sub-grains with similar orientation

are aligned in lamellae at oblique angle to the contact surface. In contrast, the grains in SSZ tend to have equiaxial shape without prominent signs of shear. Moreover, the grains at the bottom side does not show a preferential orientation, they are oriented randomly.

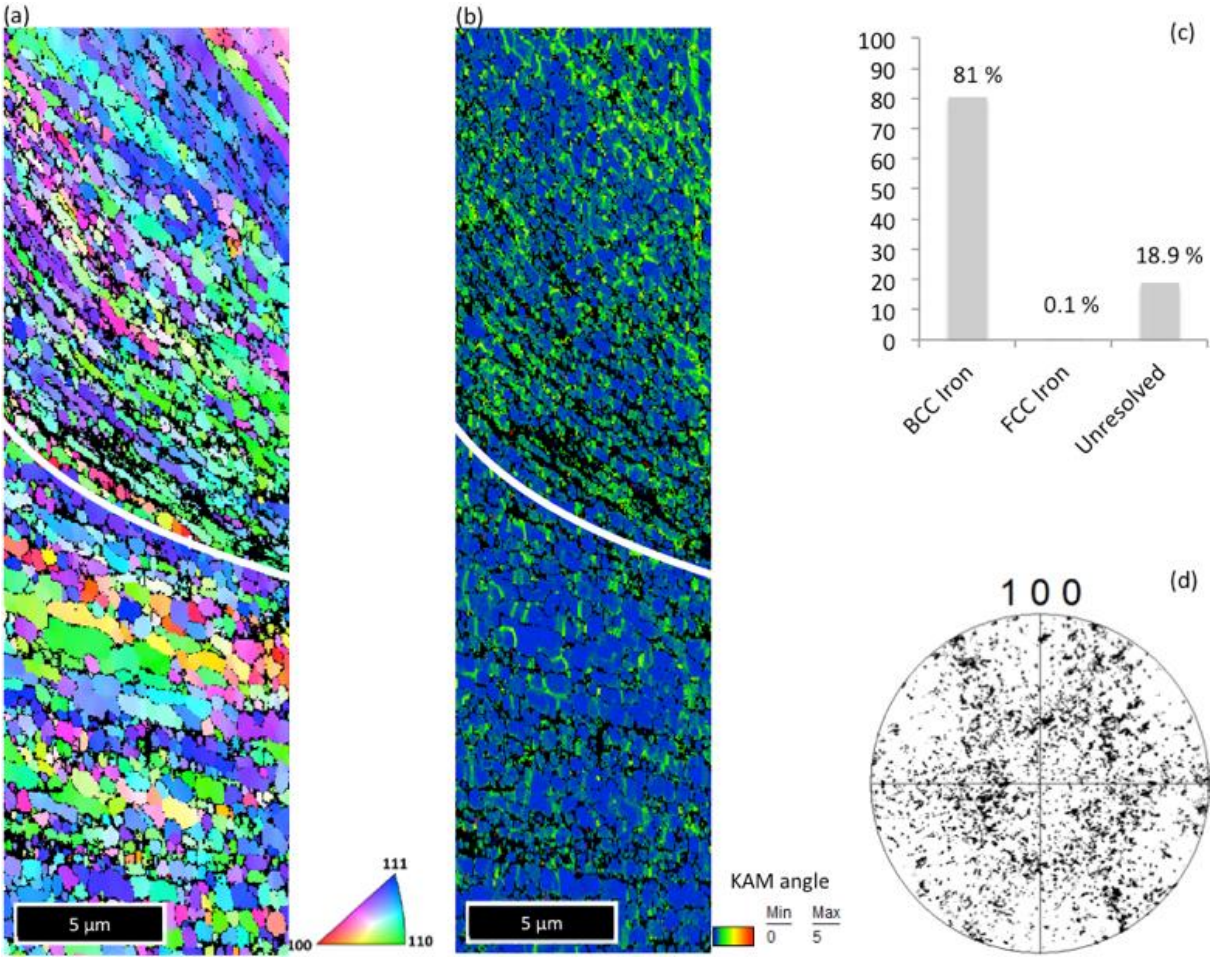

Figure 5-6 Crystallographic orientation study by EBSD on SSZ (bottom correspond to chip-tool contact surface) on chips cut at 200 m/min. (a) Inverse pole figure (IPF) colored maps, where SSZ depict a refined structure. Shear is only obvious in the upper side. (b) Kernel average misorientation (KAM) map, typically related to the density of geometrically necessary dislocations and thus associated strain energy. (c) Percentage of each iron phase, almost 100 % of detected points refer to BCC iron. (d) Plot the pole figures (PF), indicating a low crystallographic texture in SSZ.

The post-processing of EBSD data by the kernel average misorientation method is an illustrative indicator of density of geometrically necessary dislocations. A major fraction of them is produced by the plastic deformation during chip generation. Figure 5-6b depicts the KAM map obtained from the same region as Figure 5-6a. While the density of dislocation is generally large in whole section, the SSZ part shows a larger amount of grains free of them. The pole figure in Figure 5-6d depicts certain texture in the structure, however a specific orientation is not promoted. In terms of phase distribution, the software resolved 81.1 % of

the grain structure, being the structure of BCC present in almost all the section. 18.9 % of the points scanned have produced poor Kikuchi lines and led to unresolved crystallinity.

The secondary shear zone has been analyzed by scanning transmission electron microscopy. Figure 5-7 depicts a group of grains in SSZ visible in transmission (left), and EDX maps for iron (center) and carbon (right) obtained from the same region (see Section 3.1.6). Transmission image reveal grains, grain boundaries and a dark particle located on a boundary. The chemical analysis revealed that iron is not homogeneously distributed in the sample, but in the particle. The map of carbon also shows a homogeneous distribution with no particular segregation in the grain boundaries. Only in the particle it was observed a larger amount of carbon. Though quantitative analysis is hardly possible at this scale, the particle is most probably a residual of cementite.

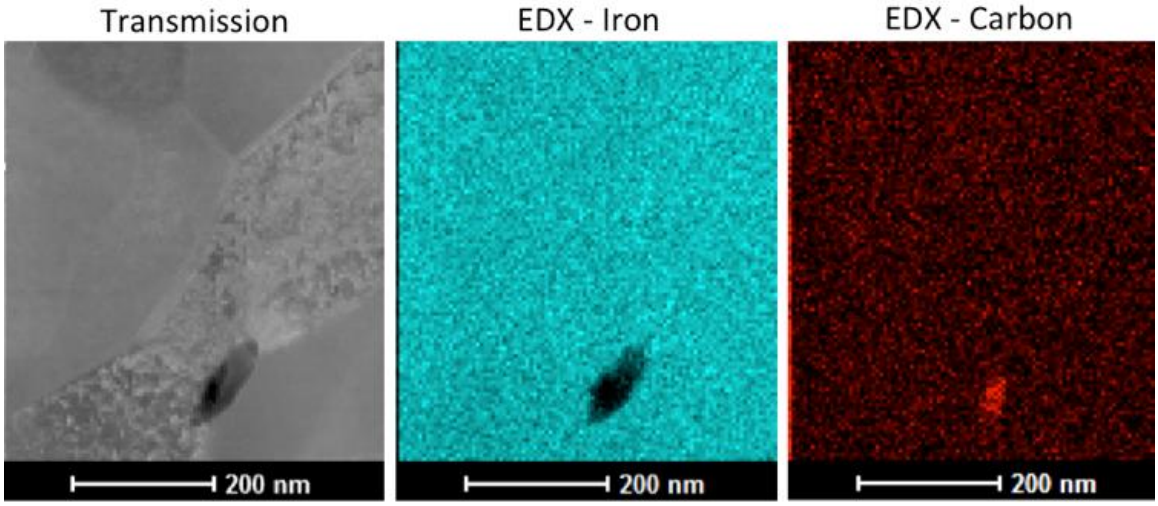

Figure 5-7 Images of TEM obtained from the SSZ area. Transmission image shows the intersection of several grain boundaries and a particle in one of them. Chemical scans by EDX (center and right side) depict the distribution of iron and carbon atoms. The particle shows a lack of iron and a larger concentration of carbon, however grain boundaries do not depict a particular concentration of the elements.

5.3.2 Mechanical testing

Series of nanoindentation have been performed in the pristine material (workpiece) and in the chip produced by the cutting process. Mean values with standard deviations of hardness and elastic modulus are depicted in Figure 5-8. It has been observed that mean hardness values before machining is 2.9 GPa and the standard deviation 0.52 GPa. After machining the material develop a mean hardness of 3.5 GPa with a similar value of standard deviation. Contrary to hardness, elastic modulus lightly decreases after the deformation induced by cutting. Mean value decrease from 208 to 197 GPa, with a standard deviation rounding 15 GPa in both cases.

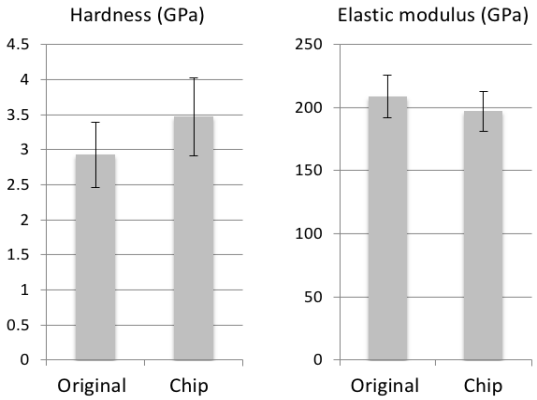

Figure 5-8 Plot of mean values and standard deviations of hardness and elastic modulus of series of nano-indentations in the pristine material (workpiece) and the material removed (chip).The deformation induced in the chip induced a hardness increase in the material, while the values elastic modulus lightly decreased.

In the case of indentations in the chip, they have been performed along the chip cross section. Figure 5-9 depicts the values of hardness and elastic modulus obtained by indentations at incrementing distance to the chip-tool contact edge, according Figure 5.4a. Generally, the results show a relevant scattering along the section, particularly in hardness (Figure 5-9a). In the case of elastic modulus (Figure 5-9b), while the scattering is there, certain reduction of the elastic modulus is appreciated in the proximity of the SSZ.

In order to increase the amount of data in the proximity of the SSZ, series of indentations have been made closer to the tool contact (according to criteria of minimum distance between indents of Table 3.1). Figures 5-9c and 5-9d depict the corresponding values of hardness and elastic modulus. Results show that in this area elastic modulus follow a decreasing trend, well under 200 GPa. Hardness does not have a remarkable trend apart of certain stabilization of values around 4 GPa, comparing to the more stochastic results present in Figure 5-9a.

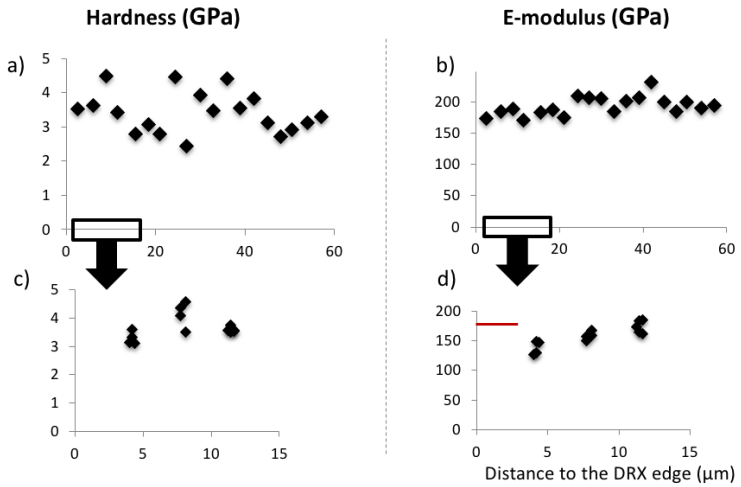

Figure 5-9 Series of indentations at progressive distance to the edge where DRX is developed. Up to 60 µm from the edge (a) hardness and (b) elastic modulus depicted depending on the position. Indents in the proximity of the edge (DRX layer) of (c) hardness and (d) elastic modulus (red line is the modulus by beam bending).

In order to obtain an accurate value of the elastic modulus it has been performed experiments of beam bending in the proximity of the edge, inside SSZ. Four beams with a witch of 5 µm and 25 µm long have been fabricated by FIB. Afterwards, they have been bended in-situ SEM as it is shown in Figure 5-10. Calculations of elastic modulus have been made following the procedure described by (Demir et al., 2010). In comparison to the values obtained from indentation, beam bending tests have led to consistent values of elastic modulus rounding 178 GPa, with a standard deviation of 5 GPa (red line in Figure 5-9d).

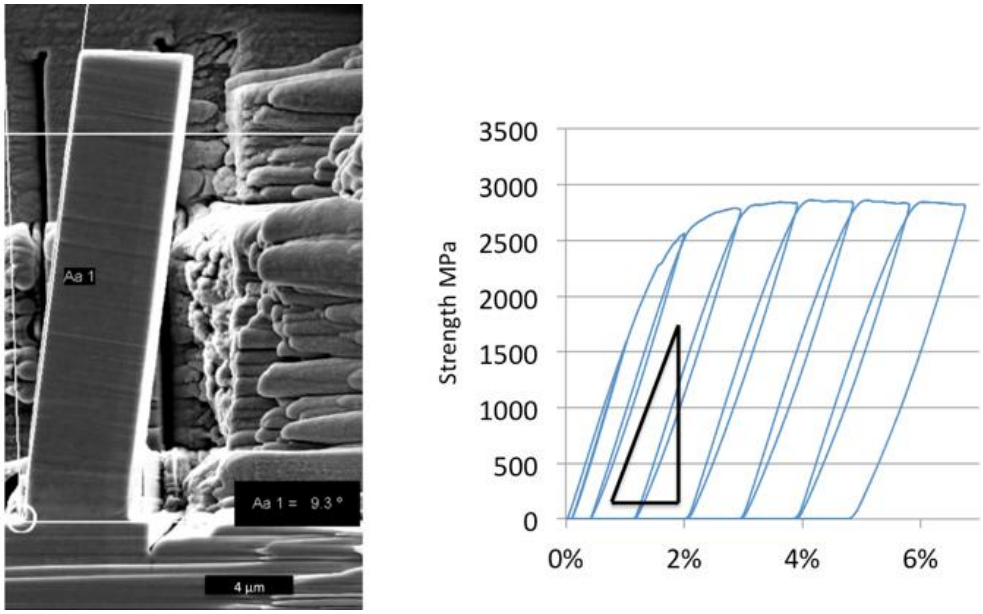

Figure 5-10 Beam bending experiments for elastic modulus calculation. By force and displacement values, and deformation geometry strength-strain curve was calculated following the method of (Demir et al., 2010). Based on that it was obtained a consistent elastic modulus of 178 GPa.

It is of importance to mention that in beam-bending there is a situation of size effect of strength similar to the one described in the section 3.1.7.2 for nanoindentations. The localized curvature represents a sharp strain gradient in micro-beams, since the angular strain in each lattice step increases inversely with the size. This promotes a large density of geometrically necessary dislocations, which contribute to the strength of the material and leads to an exaggerated value of flow stress.

In this material, a more adequate method to calculate the flow stress is pillar compression. The proximity of the chip edge has been also tested mechanically by this method. Pillars of 6, 3 and 2 µm of diameter have been milled by FIB in the proximity of the edge, up to 63 µm away. For each case, pillar strength has been calculated at a strain of 4 %. Values have been corrected by the method of Seddon, taking into account the pillar base size and substrate modulus. Figure 5-11 shows the values of strength depending on the distance to the edge.

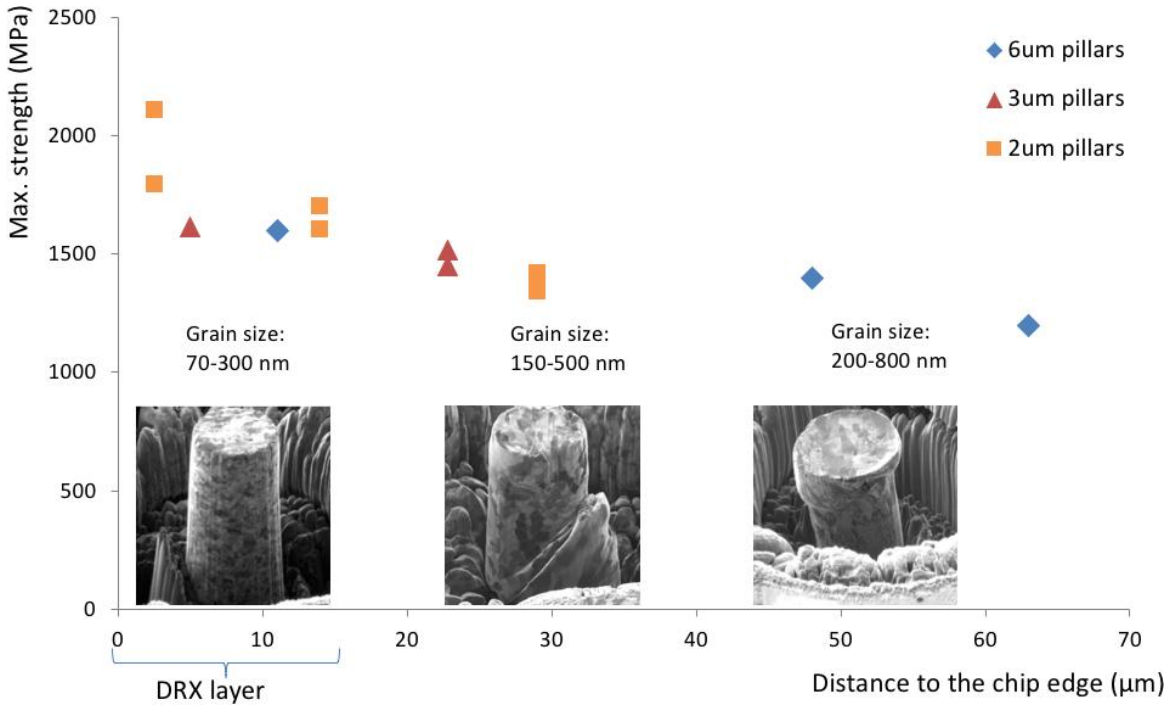

Figure 5-11 Pillars of 2, 3 and 6 µm of diameter in the proximity of the SSZ area of the chip. Pillar diameter does not have a major influence in the strength, however pillar closer to the edge (smaller grain size) have depicted larger strength.

It has been observed that pillar diameter does not make an influence in the measured strength, so the influence of the dislocation starvation (see section 3.1.8.2) may be neglected. The measurements have revealed a strong dependence of the strength on the distance to the edge. While outside of the layer affected by DRX maximum strength rounds 1300 MPa, inside DRX zone the values of strength exceed 1500 MPa. In this last case, FIB images of pillars showed a regular structure of nano-grains that deform homogeneously.

In the case of pillars build in the area not affected by DRX, micrographs depict pillars composed by a heterogeneous structure, a combination of pearlite and refined ferrite. This makes the deformation by pillar compression inhomogeneous. It has been seen that pearlite colonies tend to remain undeformed, while strain is absorbed by the ferritic fraction.

5.4 Discussion

5.4.1 Effect of dynamic recrystallization on structure of the material

In a static recrystallization processes, the pristine structure disintegrates into a new one with refined features, i.e., smaller grains and a more homogeneous distribution of particles (Sakai et al. 2014). However, rather than a sequential process, the dynamic character of DRX assumes the continuous rearrangement of the material features. This is possible by the combination of high temperature and sustained strain: while large strains break down the microstructure into smaller and defective grains, high temperature promotes diffusive

repairing of crystallographic defects (Elsey, Esedo, and Smereka 2009). The continuous action of these two effects leads to successive reduction of the grain size. However, the smaller are the grains the larger is the trend of grain coarsening. Thus, the achievable grain size (also known as grain size of saturation) is defined by the competition between rates of structure breaking and grain coarsening (Stüwe, Padilha, and Siciliano Jr 2002).

Typical grain sizes achieved by dynamic recrystallization rounds units of micrometers, depending on the conditions (Guo-zheng 2013), then it is remarkable that the microstructure observed in the SSZ of the chip have the grain sizes in the range of 100 nm. That locates the saturation grain size obtainable in the cutting process one order of magnitude under typical values, indicating that the rate of structure breaking is much larger than the rate of grain growth. This rate of structure breaking is consequence of the large strain-rate, which push down the grain size of saturation (Gottstein et al. 2003). Thus, the large values of strain-rate typically observed in the SSZ during high speed cutting (Arrazola et al. 2003) would likely be the responsible of the extreme refinement of the microstructure in SSZ.

DRX not only refines a microstructure to a smaller grain size, but also result in redistribution of the precipitates in an efficient manner (Sakai et al. 2014). This effect can be observed in the images of SSZ (Figure 5-5), where there is very little presence of disintegrated cementite phase.

Taking into account that in the pristine material developed pearlite colonies occupy 75 % of the volume, it can be concluded that a complete disintegration of the carbides happens during DRX. This lack of carbides could lead to a scenario where carbon atoms diffuse to grain boundaries. However, the chemical analysis of the SSZ area (Figure 5-7) did not detect an excess of concentration of carbon in grain boundaries. Hence, carbon is mostly homogeneously distributed in the matrix of ferrite. This is coherent with several authors that reported a super-saturated state of ferrite after cold working of pearlitic steel caused by severe plastic deformation (Li et al. 2014; Nematollahi et al. 2016) . This state of ferrite corresponds to a lightly deformed BCC lattice to locate a larger amount of carbon atoms per cell. In addition to a huge plastic deformation similar to cold working, the material affected by DRX during cutting experience also a structural relaxation according to the EBSD measurement of Figure 5-7. Thus, the material of SSZ can be defined as a nano-crystalline ferrite supersaturated by carbon, that has been partially relaxed, and showing no dominant crystallographic texture.

5.4.2 Mechanical properties of recrystallized material

During machining material severely deforms, what changes the microstructure and mechanical properties. In terms of hardness, nano-indentation tests in the chip show an increment of 0.6 GPa over the values in the original alloy. However, no particular trend has been observed in the SSZ. Contrary to that, in the case of elastic modulus, values are smaller in the SSZ comparing to the rest of the chip. This is reinforced by the indentation data of Figure 5-9d, where modulus is consistently under the typical values for steel (210 GPa). Nevertheless, the nanoindentation technique has been criticized because of the large susceptibility to the substrate in E-modulus calculations, with large scattering of results in composite material (Constantinides and Ulm 2004). Thus, to ensure the low values of modulus in the SSZ the proof of a second technique is needed.

The method of beam bending has demonstrated to be suitable for elastic modulus calculation in small scales. It provides low sensitivity to specific features and, contrary to pillar compression, it is relatively agnostic to small geometric misalignments. By this method it has been calculated an elastic modulus in the SSZ rounding 178 GPa. These values confirm a remarkable reduction over the original steel of 15%. In comparison to other studies, which have reported variations up to 7 % after metal rolling or tensile test (H. Y. Yao, Yun, and Fan 2013), this represents a notable decrease. At this regard, it has been reported that nanocrystalline materials tend to reduce the elastic modulus, however this has been observed below a threshold of 20 nm of crystallite size (Giallonardo et al., 2011). In our case study, the re-solution of carbon into the ferrite matrix could lead to a lattice supersaturation (Zhang et al. 2011), what may act distorting lattice symmetry, leading to certain atomic amorphization. In addition, grains depict sizes down to 70 nm, the same order of magnitude pointed by Giallonardo et al. These two factors could be the responsible of the elastic modulus reduction measured in the recrystallized layer.

In terms of material strength, the trends observed in Figure 5-11 reveal that the typical size effect in pillar compression is not relevant in these tests. This is coherent with the results obtained by Fritz et al., with no strength effects for pillars much larger than the grain size (Fritz et al., 2016). In contrast, results show that grain boundary hardening is dominant, and, as the pillars seems to not be been affected by the prove size effect, this can be interpreted as the bulk strength of the material. Contrary to the pristine material, which develops an ultimate strength rounding 560 MPa, the process of recrystallization leaded to a microstructure with more than 1.5 GPa of strength, i.e., three times the typical of undeformed AISI 1045 steel.

5.4.3 Use of focus ion beam in structure analysis

Some of the difficulties of material characterization relates to revealing the crystallographic details without a specific sample preparation. While some techniques like transmission electron microscopy (TEM) provide plenty of crystallographic details, it is limited by a very specific lamella preparation. More accessible are sample examinations by electron back-scattered diffraction (EBSD), where sample surface can be scanned directly. Nonetheless, it typically demands that the whole surface under study is tilted 70 degrees to the electron column in order to optimize back-scattered electrons collecting (Maitland and Sitzman 2006). This limits the study of non-flat surfaces.

Another option to distinguish microstructure details resides in taking benefit from the beam channeling contrast effect (Canovic, Jonsson, and Halvarsson 2008). While it provides qualitative information, this effect highlights contrast by crystallographic orientation and lattice structure, thus revealing grains boundaries and second phases.

Channeling contrast is particularly relevant in scans by large-particle beams, then the use of an ion beam instead of an electron beam will enhance this effect. Hence, scanning by a focus ion beam (FIB) can reveal plenty of details of the microstructure. In contrast, this technique presents some other disadvantages. On the one hand, ion scans may induce surface damage and atomic implantation, limiting the number of scans over the same area. On the other hand, it does not provide quantitative information since a number of crystallographic orientations may produce the same contrast. The drawback comparing to EBSD, is that FIB scans cannot provide maps of orientation or phases. On the positive side collecting secondary electrons generated by ion scanning leads to better image magnification in a fraction of the time needed by EBSD. FIB can also access microstructures of complex geometries, since no specific surface tilting is needed. Thus, the analysis of cross sections or 3D structures is possible.

Figure 5-12 depicts images of the pillar after compression, where the left side presents the scan of electron beam, and the right side the scan of gallium ion beam. In both cases secondary electrons are detected. While in the first case, image depicts mostly topographic information, in the ion image the grain distribution and the presence of cementite is clearly visualised. This gives the opportunity of locating the pillar shear line in the proximity of a colony of pearlite. In addition, at high magnification some details of pearlite are accessible, such as the crystal subdivision observed in the ferritic phase in between cementite lamellae, likely produced during the machining process.

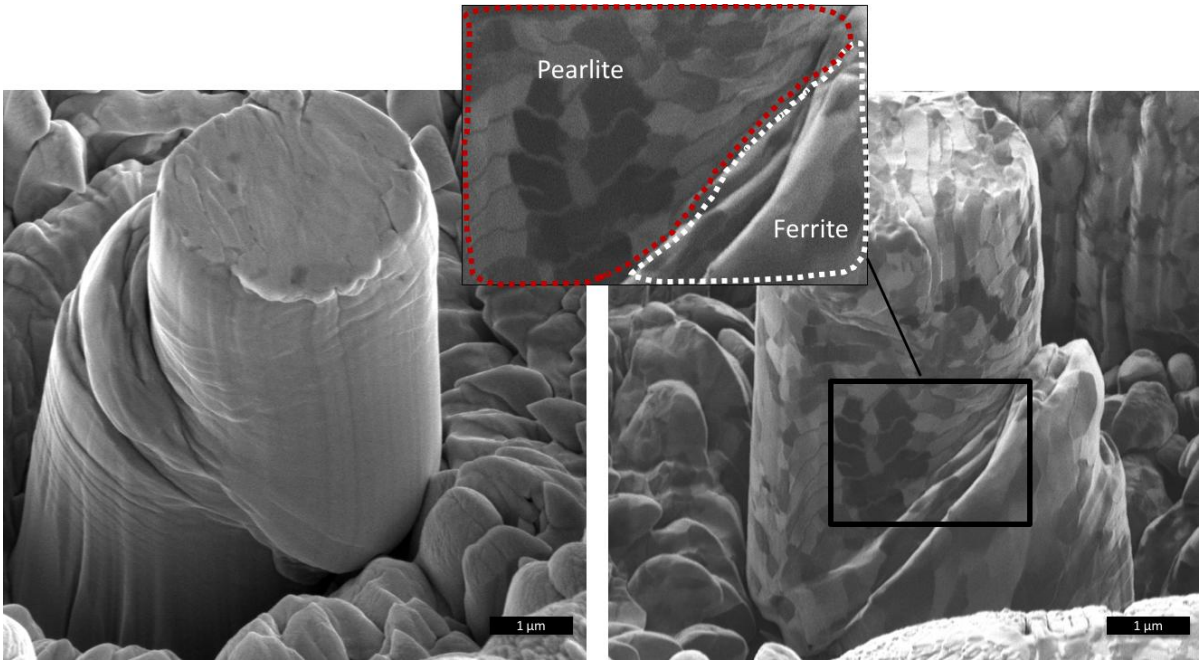

Figure 5-12 The same pillar scanned in the left side by an electron beam, and in the right side by Ga+ beam – in both cases collecting secondary electrons. Right image reveals the grain distribution and the position of pearlite lamellae, locating the area of shear in the interface between ferrite and pearlite.

5.5 Conclusions

Machining represents a fabrication method where ultra-high strain-rate govern deformation in the proximity of the cutting edge. The present chapter pays attention to the unique nano-structured material obtained in SSZ area of the chip. Morphological, structural, mechanical and chemical studies have demonstrated unique mechanical properties of this material in the proximity of the tool-chip contact when machining at high cutting speed.

- The assessment of the microstructure morphology reveals an extreme refinement of the grain size, well under the typical sizes after industrial recrystallization.

- EBSD post-processing has demonstrated a relatively low density of dislocations. This supports the presence of recrystallization, which acts as a strong softening effect, even when strains rate approaches 10^3 s^{-1}.

- Experiments of nanoindentation have been performed across the chip section. They point to an evident material hardening in the chip in respect the original material on the one hand, and on the other hand, certain reduction of the elastic modulus in the tool contact proximity, as compared to the rest of the section.

- Micro-bending experiments of the material affected by DRX have reliably demonstrated of 15% decrease of elastic modulus as compared with unprocessed AISI-1045 steel - from 210 GPa in unprocessed material to 180 GPa in the nanocrystalline area of the chip.

- Chemical analysis of the SSZ, performed by X-ray analysis in transmission electron microscope, showed a homogeneous distribution of carbon. No signs of regular pearlite have been found, and carbon has not diffused to grains boundaries. This points to the re-solution of carbon in the ferrite matrix, leading to a metastable microstructure rich in carbon.

- The process of recrystallization produced a microstructure that develops a bulk strength over 1.5 GPa, three times over the typical value of unprocessed AISI 1045 steel.

The results present in this work shed some light on the material properties induced during machining in the SSZ, and open the possibility of subsequent studies in other sides of the contact, like PSZ and fabricated parts surface. Furthermore, it could open new paths to obtain ultra-refined microstructures by high strain-rate treatments of alloys.

6 Machining in the nanometer regime: built and use of an in-situ electron microscope cutting setup

While the post-analysis of the microstructure of the chips provides an integral picture of the mechanism that governed the tool-workpiece interaction, microscopic aspects of this process like dependence on grain orientation, grain boundaries and phases distribution in the workpiece falls off this integral picture. The possibility to look on the process itself on a microscopic scale could shed light on the intimate details of the cutting process, though, as it is emphasized in the introduction, this is an extremely challenging task. In an attempt to address this challenge, this thesis studies the potential of direct observation of metal cutting in-situ in electron microscope. A proof of concept device to perform lineal cutting inside an electron microscope's vacuum chamber has been designed, constructed and tested. Based on this device, experiments on in-situ machining have been successfully performed, and have shown that the crystallographic orientation may in fact influence the thickness of material deformed under the cutting tool. Furthermore, the effect of cutting in the sub-micrometer regime has been studied. There, tool and chip have demonstrated a stronger interaction in comparison with macroscopic cutting, leading to proportionally larger SSZ and TSZ than their counterparts in macroscopic cutting. Finally, a multi-scale analysis of the influence of the cutting-edge radius on the specific cutting energy has been performed, and it has been shown that the size effect in cutting is strongly related to the geometry of the tool.

6.1 Introduction

Material removal by mechanical means, referred as machining, has become and remains relevant since the age of the industrial revolution. Since that time the research community has been always on pursuit of new methods to elucidate the succession of events leading to metal cutting. The process itself has been acceded for investigating in different manners. In many cases it has been studied by empirical methods, analysis of tool, workpiece and chip after machining, or computational simulations, a range of techniques in constant growth.

The difficulties on that study relies on that removing material by machining imposes deformation work in a small volume of the workpiece. In addition of the limited dimensions of the area of interest, there is also a limited time of interest, i.e., during the chip generation process the material is usually deformed in terms of milliseconds. In top of that, there is an uncertainty in regard to mechanical behavior. The material is self-heated by contact friction and deformation work, and rapidly cooled once the stimulus disappears. This entails to ephemeral mechanical properties only present during the process. Neither the pristine material nor the resultant one depicts the properties present during machining. Thus, a full knowledge of the mechanism of material removal is hampered by limited access to the cutting area and in-process mechanical properties in the available time window.

All these aspects have pushed the development of specialized direct observation methods for metal cutting, the ones that can access the mechanism of cut during the process. On that regard, much effort has been devoted to exploiting high-speed optical cameras, which provide visual access to the chip generation with high temporal resolution. By this equipment (List et al. 2013) afforded the analysis of strain and strain-rate along a section of the 2D system workpiece-chip-tool, being observed a gradient in strain-rate in the proximity of the cutting tool. In further studies by high speed cameras, material feature tracking by video post-processing showed detailed trajectories of the material flow in the primary shear zone (PSZ) and secondary shear zone (SSZ) (Y. Guo, Compton, and Chandrasekar 2015). Additionally, infrared high-speed cameras have opened the possibility of tracking the field of temperatures during the process of cutting in conditions similar to industrial machining (Arrazola et al. 2015). All these techniques have had access to the whole chip generation in the microscopic scale, with a typical spatial resolution of the units of micrometers. However, significant part of microstructural features in materials and related events in cutting have smaller scales down to 100 nanometers, out of perception of optical microscopy.

To overcome limitation in image resolution, some effort has been devoted on experimental machining to be performed under monitoring in an SEM. (Heo 2004) developed a set-up of micro-machining to be installed inside a SEM chamber. This set-up used a turning workpiece of tungsten carbide cut by a polycrystalline diamond tool, where observations of cutting progress were performed by images taken when stopping the process every 10 meters. In further studies, (Heo 2008) assessed the mechanism of WC-Co cutting in lubricated conditions as well, and more recently, (Fang, Liu, and Xu 2015) used a linear cutting setup to study surface roughness of parts after micro-machining of AISI 1045 steel. These few works represent occasional approaches to in-situ SEM machining, with limited progress because of the complexity of micro-devices building on the one hand, and the little availability of these kind of microscopes for metal processing community on the other hand.

The scanning nature of image construction in SEM (Section 3.1.1) entails to low frame-rates during image acquiring, what hampers temporal resolution of machining monitoring. To overcome this drawback, eventual quick-stop (sudden stop of cutting for taking and snapshot of the system) has been used for material imaging. This has pushed the efforts on exploiting the advantages of in-situ machining to a deep microstructural analysis of the cutting process. This is based on that SEM based techniques offer large options of spectroscopy and characterization. On the other hand, cutting is performed in a vacuum chamber, an unreactive environment that can preserve many of the microstructural features produced during cutting, enlarging the possibilities to resolve the mechanics of cutting. As most of the efforts were aimed to the analysis of the microstructure during/after micro-cutting, such important aspect as the forces involved in the process have not been addressed at all so far.

6.2 Setup for in-situ SEM machining

6.2.1 Concept

In order to face the challenges highlighted in the introduction the in-situ micro-cutting device should fulfill two major requirements: it has to be possible to perform and to observe cutting experiments at the dimensions smaller than the characteristic grain size of a workpiece material, and it should be possible to measure at least a cutting force. In our design the device is placed in a dual beam microscope chamber, in which FIB column is inclined by 52 degrees in respect to electron column. By placing the workpiece surface horizontal top and side views of the cut may be achieved. Workpiece remains fixed to the sample holder. The tool is hold by an in-situ nano-manipulator that pushes the tool for metal cutting and retracts for the workpiece inspection.

Piezoelectric systems, though being the state of the art in force measurements in nano to micro Newton range, have two severe drawbacks: the cost, which may go up to 100k euros, and limited operating stroke. We have used conceptually different approach for in-situ force measurement based on measurement of the deflection of a calibrated spring system. The workpiece has been held by a spring with a known elastic constant, *k*; the displacement of the workpiece, *x*, is monitored by SEM imaging; the force parallel to the surface (cutting force) can be then calculated as $F=k \cdot x$. Figure 6-1 depicts a sketch of the tool, the workpiece, and the spring holder.

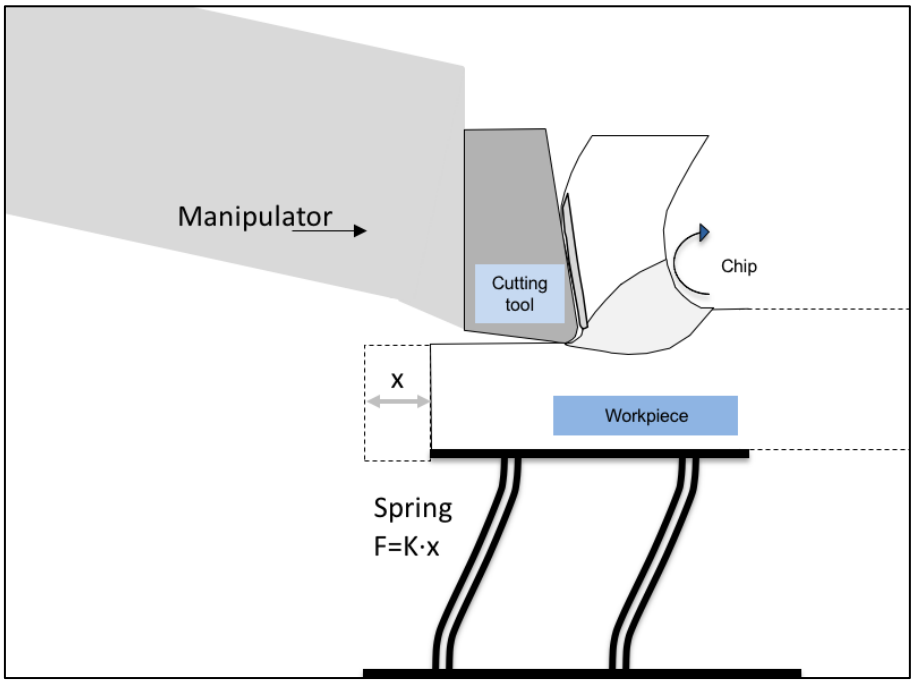

Figure 6-1 Sketch of the working principle of the mechanisms of force calculation.

6.2.2 Device

The device is based on Kleindiek STFMA spring-table system in combination with Kleindiek MM3A-EM micromanipulator and custom made cutting micro-tool. The device is constituted by manipulator, counterweight, tool holder, a grid-holder, elevator and the spring holder in which the sample is placed. The device can be mounted in the SEM chamber as shown in Figure 6-2.

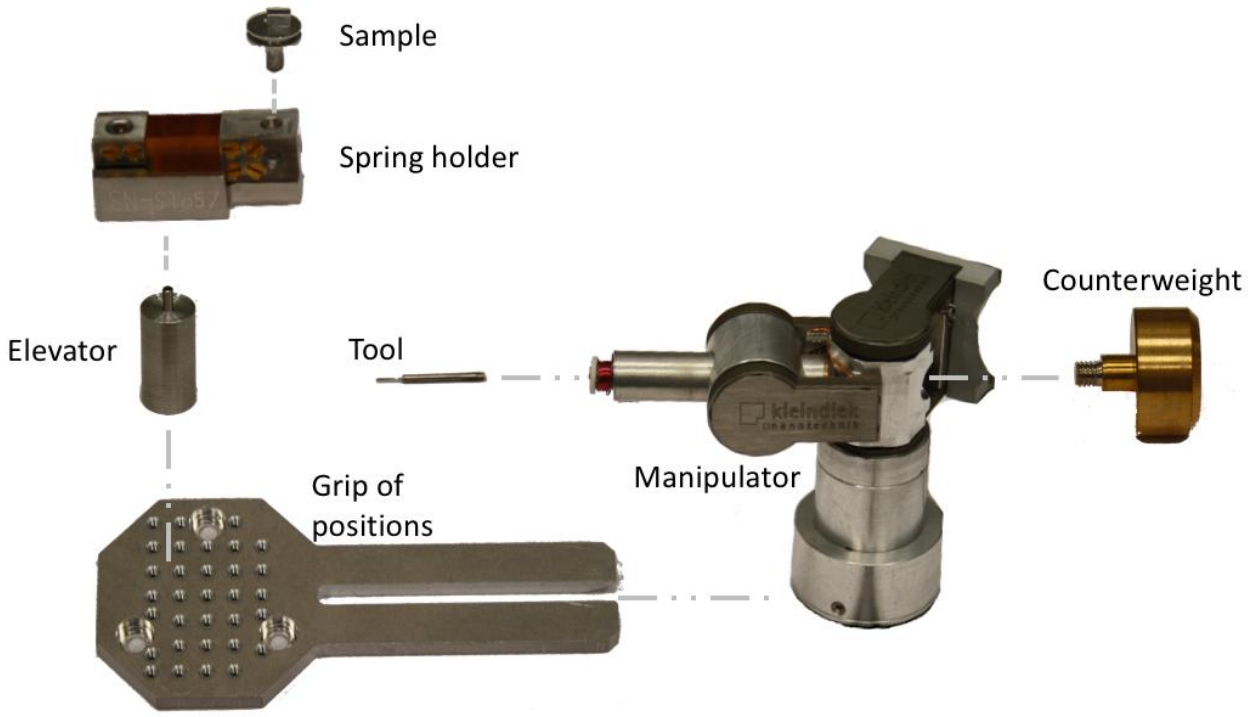

Figure 6-2 Mounting sketch of the Kleindiek MM3A-EM micromanipulator and STFMA spring-table adopted and assembled for in-situ SEM cutting.

The cutting tool is fixed on the arm of Kleindiek MM3A-EM micromanipulator (see section 6.2.3 for details of tool fabrication) The arm provides two axes of rotation and one additional axis of longitudinal displacement. Rotational axes are used for tool feeding and retracting. The longitudinal displacement axis is used to generate a cutting force against the workpiece. The design of the spring table in the form of double flat parallel spring limits possible movements of the spring holder to a linear motion parallel to the holder surface. By design this direction coincides with the axis of cutting. The approximated elastic constant of the spring used is 1059 N/m. The cutting parameters (the width of the tool, the tip radius and the feed) are optimized in order to achieve spring displacements of the order of 10s of microns. Figure 6-3 shows the cutting setup already assembled.

As mentioned before, the cutting force can be measured during machining based on the tracking of the workpiece displacement. This displacement can be measured by the workpiece position on the sequential micrographs during cutting relative to the initial position. Position measurement is achieved with subpixel accuracy by custom made software, reaching precision of nanometers.

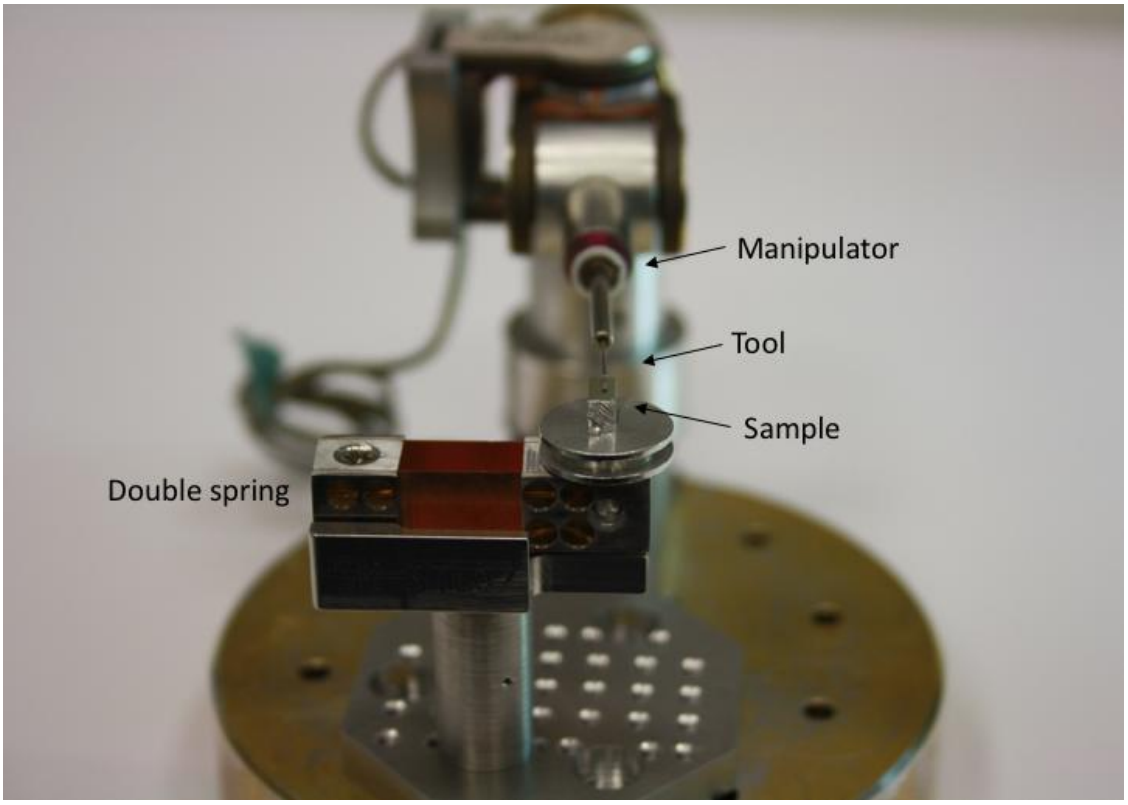

Figure 6-3 Setup built in position of cutting. It should be noted that the longitudinal axis of the manipulator should be strictly parallel to the workpiece surface, which in turn is perpendicular to the share movement of the double spring.

The device has been mounted on the sample stage inside FEI Nanolab Helius 600 dual beam (electron and ion Ga+ beam) instrument. Both beams have been used for monitoring purposes, electrons have been accelerated by 5 and 10 kV, and ions by 30 keV.

6.2.3 Tool fabrication

The cutting tool has been fabricated ad-hoc in a FIB microscope FEI Nanolab Helius 450. The material used for the tool is WC-Co H13A (Figure 6-4) – typical material of inserts for macroscopic cutting experiments. Initially, a block of 80x30x10 µm has been cut by FIB at 30 keV ions energy and currents between 9 and 60 nA. The block has been cut all around leaving one side connected to the sample, and an aluminum holder fixed in the arm of micromanipulator has been advanced to the block. Then the block has been welded to the aluminum holder by deposition of platinum in the interface. After this, the final cut was made completely detaching the tool from the WC-Co H13A piece.

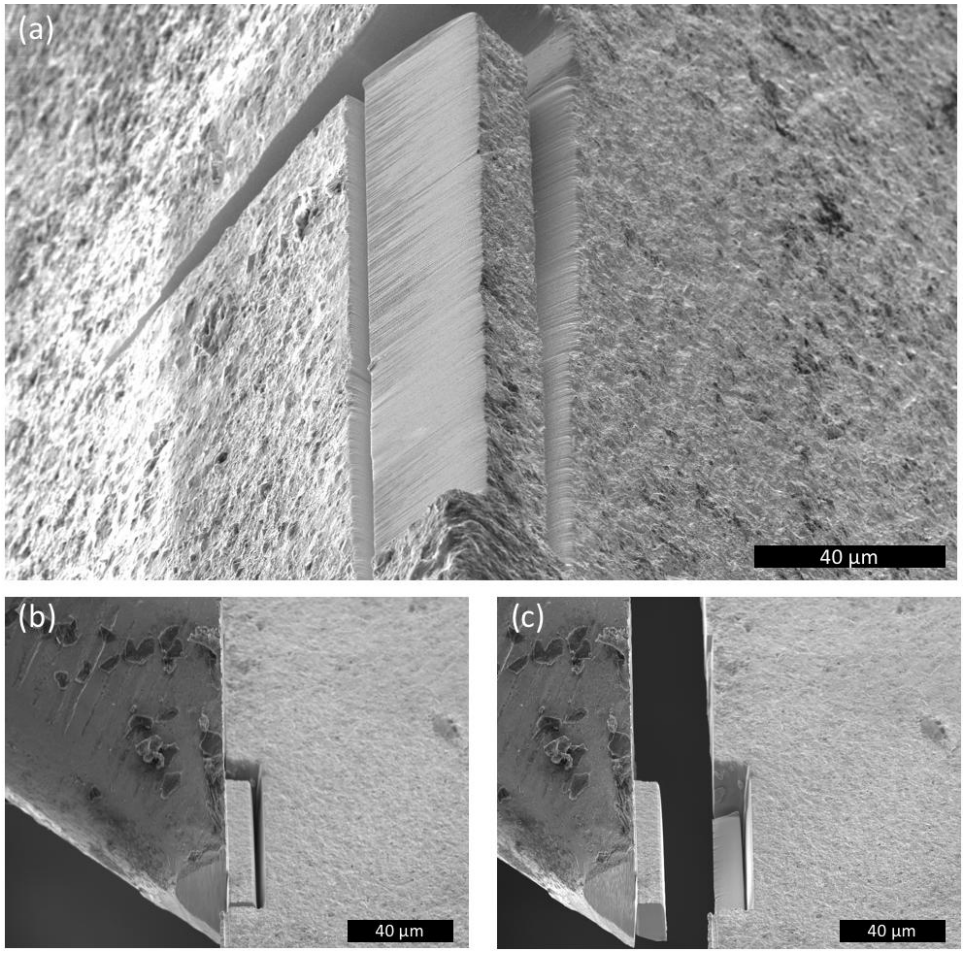

Figure 6-4 (a) Block of a WC-Co specimen milled with an ion beam. (b)Engagement of the block to the tool holder for welding by Pt deposition. (c) Extraction of the tool for further sharping operations.

In order to give to the tool the proper surface quality and edge angle, the block has been shaped by the ion beam with currents between 9 and 1 nA. By this last procedure, a cutting-edge radius of 120 nm has been obtained, as well as a clearance angle of 40 degrees, when the rake angle is fixed to -9º.

It should be noted that the fabrication of the cutting tool requires considerable time of ion beam operation, being this time for milling in a large fraction, but also for welding by ion induced platinum deposition. The following table shows the approximated working time for each step:

Table 6-1 Hour consumed for cutting tool fabrication

Task	Hours of ion beam on
Milling cutting tool material (Figure 6-4a)	15
Prepare tool holder surface	5
Platinum welding of holder-tool	4
Tool edge sharping	4
Total	28

6.2.4 System assembly

In order to guarantee adequate setup, the system must be assembled with the rotation axes of the arm located at the same height as the sample surface, ensuring that the longitudinal displacement of the manipulator moves parallel to the sample surface, hence cutting with a constant feed. The system is placed horizontally on the microscope stage, which in turn can be tilted from -9 to 60 degrees, providing access to electron beam and ion beam from different perspectives for imaging or material cutting. Figure 6-5 depicts the position in which the cut can be monitored from the side with the electron beam.

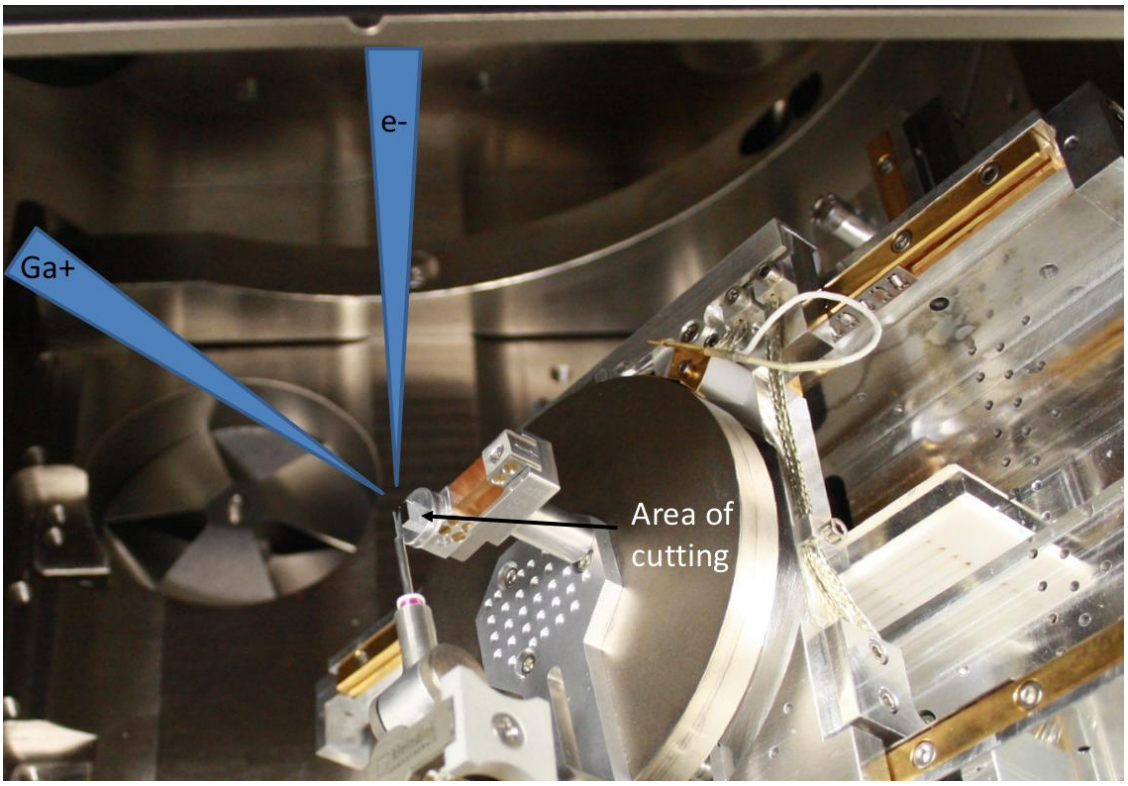

Figure 6-5 Device mounted in the chamber of the microscope. The cut is performed in the top of the sample. During cutting operations, the device is tilted to observe the chip growth with the electron beam, which provides higher scanning rates than the ion beam.

Neither the tool nor the workpiece holder has had a feedback, thus exact measurements of feed and cutting depth are made by SEM imaging post-processing. In order to avoid unnecessary angular corrections to feed and force measurements, cutting direction has been be aligned with the tilt axis of the microscope, as shown in Figure 6-5.

Figure 6-6 shows SEM image of the tool located to perform experiments of material removal. Note that the cutting part is welded at the bottom of the manipulator.

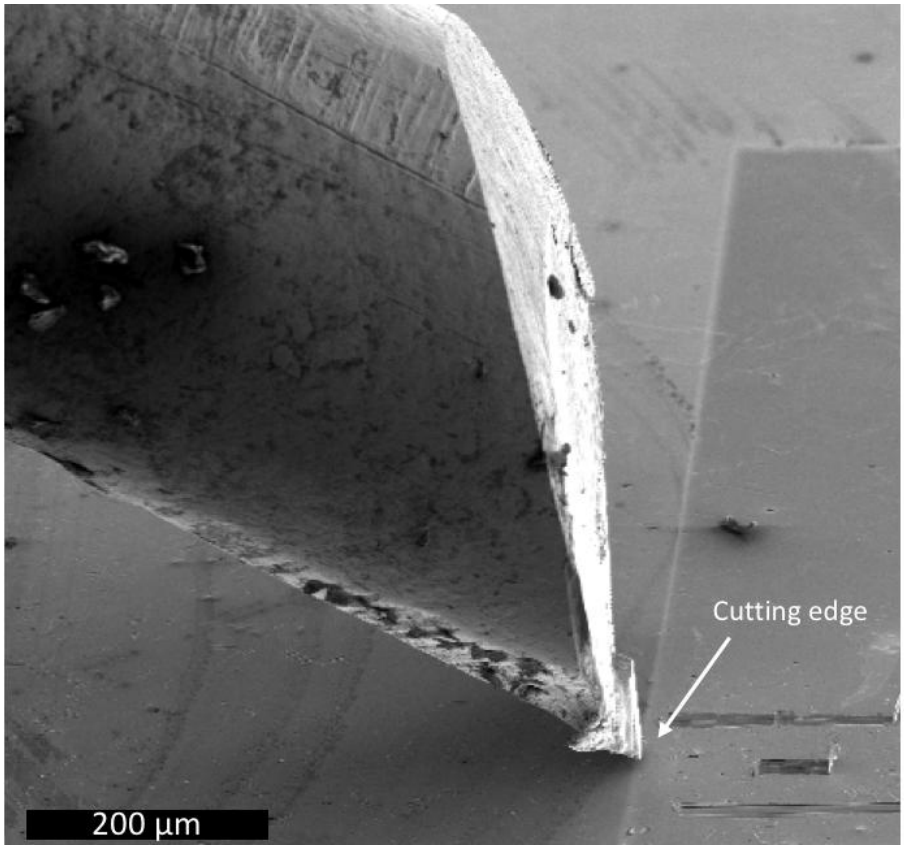

Figure 6-6 Tool in position for cutting from the perspective of from the electron beam in the position show in Figure 6-5.

6.3 Experimental

The set-up previously described has been used in cutting experiments with a feed size in the regime of units of micrometers. These experiments have been made in commercially available Aluminum 7475. The use of aluminum in this research is conditioned by the necessity of a relative soft metal which can preserve the integrity of the tool during this proof of concept, and in addition an alloy which may develop strain-hardening, hence able to reproduce many of the mechanisms discussed in chapters 4 and 5. As described in Section 1.5, as received the material was treated by two hardening processes: hardening by particle precipitation, and mechanical forming.

Machining experiments have been made in-situ by the set-up developed for the present work (described in section 6.2) on the material already processed as above. For comparison metal cutting experiments with the same material has been carried out on industrial equipment and commercially available tools with cutting radius of 11 and 5 µm (see Section 3.3).

In the experiments carried out in-situ SEM, 17 cuts have been made with a tool rake angle of -9 degrees, and a clearance angle of 35 degrees. A cutting speed of proximately 10

µm/s has been used, with quick stops for imaging. Afterwards, chip and workpiece have been examined for deeper analysis of cutting mechanics.

The input parameters in the cutting experiments are the cutting speed, the depth of cut and the geometry of the cutting tool. It has to be taken into account that the manipulator that holds the tool does not have positioning feedback, so the exact values of cutting feed and cutting speed have to be measured by image analysis after each experiment.

6.4 Results

6.4.1 In-situ cutting experiments

The experiments of in-situ cutting show all features characteristic to the macroscopic counterpart. Once the chip is developed, most of the chip deforms in a constant manner by shear strain from the tip edge to the free surface (Figure 6-7).

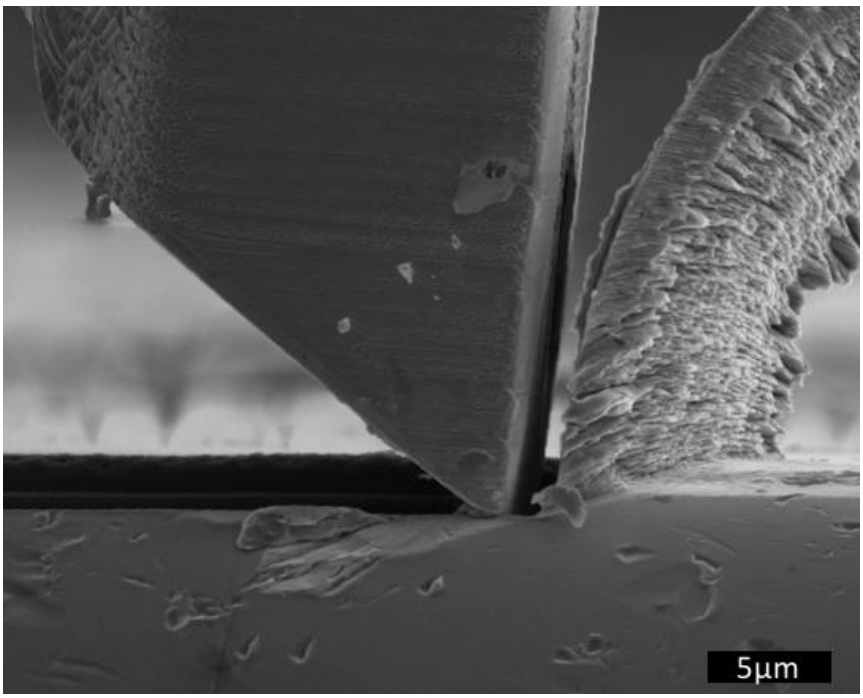

Figure 6-7 Lateral view of the system workpiece-chip-tool. It can be observed that chip appear in front of the tool in a similar manner as in macroscopic cutting.

While the tool advances, the chip is constantly generated according the description provided earlier (Section 2.1). Interesting peculiarities are observed at the very early state, i.e., during the tool-workpiece impact: a larger volume of the material is affected by the tool pressure without clear sings of chip generation. In this transitory regime the amount of material affected plastically is larger than that when the shear zone is developed. Figure 6-8 depicts a quick stop during this transitory state, when the material is compressed immediately after tool has contacted the workpiece (at 10 µm/s), and before a clear shear is developed.

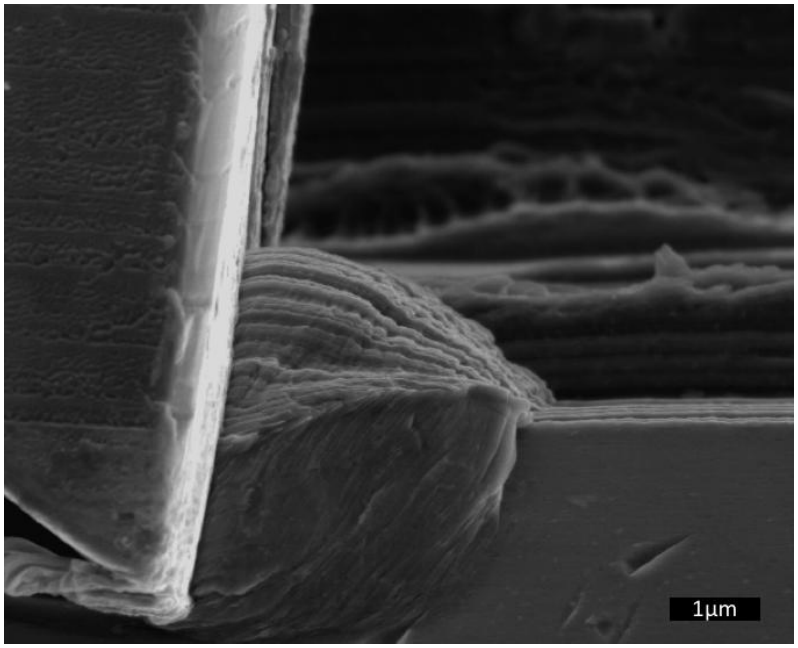

Figure 6-8 Material compressed by tool first contact with workpiece material.

The images of chip generation when the primary shear zone is fully developed (it will be further referred to as the permanent regime, in opposition to the transitory one) show the material deformation concentrated over the line of shear. Figure 6-9 shows the chip generation by cut with 1.18 µm feed at 10 µm/s cutting speed. In this case, contrary to the transitory regime, less volume is simultaneously affected by deformation. In addition, it can be intuited a straight area of shear in the PSZ, indicating that this shear affects only a small volume of material at once, and that the deformation process of chip generation is performed sequentially in that small steps.

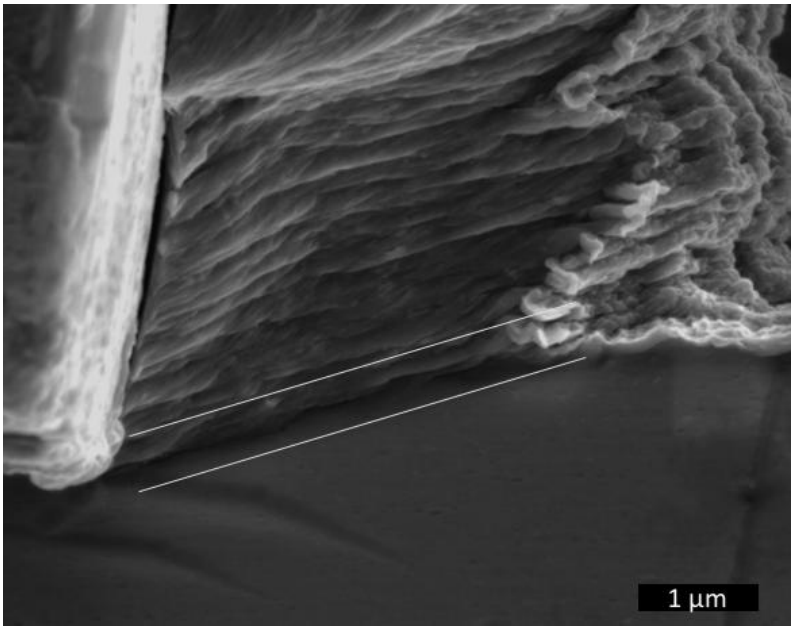

Figure 6-9 After bulk compression effect disappears, PSZ is dominated by shear phenomena.

6.4.2 Microstructure of chip section

Cutting experiments have been monitored in-situ from a lateral direction by electron been scanning (as in the sketch on Figure 6-1). In order to analyze the resulting microstructure the cross-sections of the samples after the cuts have been prepared by ion milling. The material was removed until reaching half of the cutting depth, i.e. the cross-section represents the structure in the middle of the cut. The grain structure in the cross-section has been accessed by FIB imaging exploiting the channeling contrast (see Chapter 3.1.3 and 3.1.4 for description). Figure 6-10 shows a cross-section of the chip cut at rounding 50 µm/s with a feed of 0.5 µm. It should be mentioned that the milling beam hits the sample from the top, been necessary to mill more material over the chip than over the free sample surface. This produces an artifact in a shape of a step in the cross section, as present below the left side of the chip in Figure 6-10.

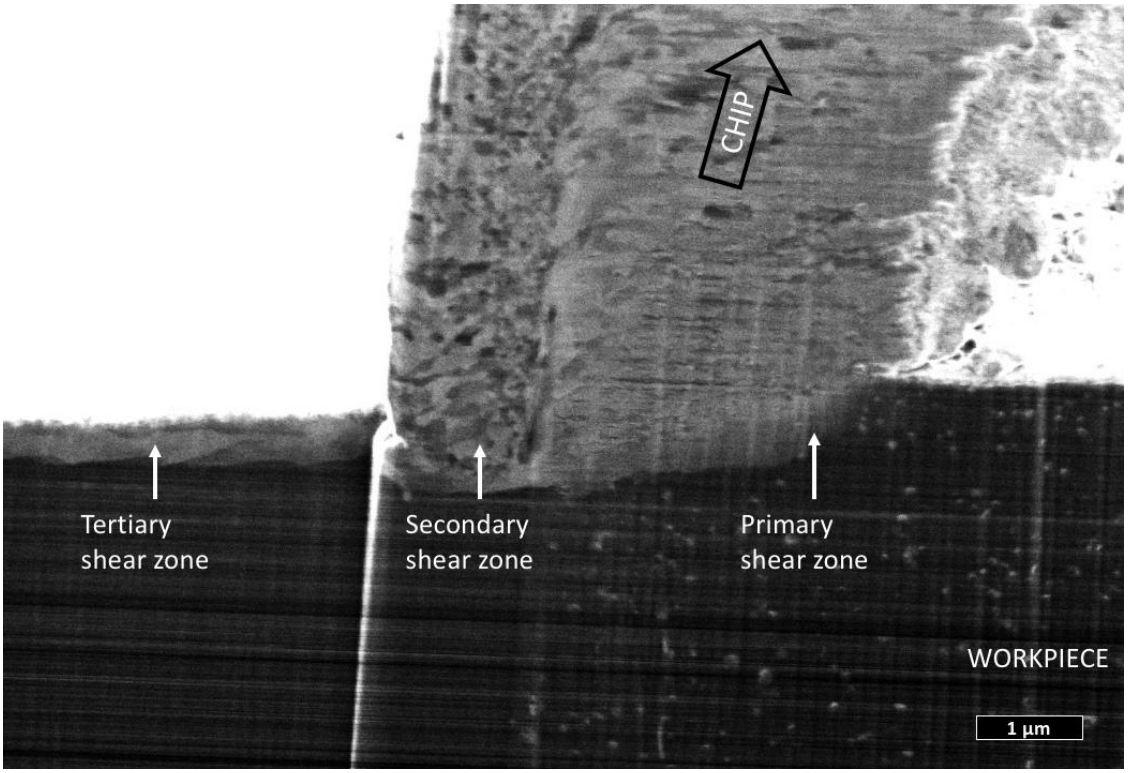

Figure 6-10 FIB cross-section of a chip cut with 500 nm of feed.

In Figure 6-10 the aluminum grain over which the cutting is performed (dark contrast at the bottom of the image) changes the contrast by the action of cutting, showing a deformation-induced change in the crystallographic orientation. This is happening in the primary and secondary shear zones in the chip, and tertiary shear zone on the surface of the workpiece.

The SSZ in Figure 6-10 is identified by a refined microstructure, with little signs of shear and no dominant grain orientation. It can be observed that the size of the SSZ is

approximately one third of the total chip thickness. Like in Figure 6-9, it has been seen in chips cut with a cutting speed over 50 µm/s proportionally large shear zones in the proximity of the tool-chip contact.

It can be also elucidated that the cutting also introduces a plastic deformation in a thin top layer of the workpiece. This layer of deformed material under the cutting tool, commonly referred as the tertiary shear zone (TSZ), develops in this case a thickness rounding 200 nm. Nanocrystals in this layer are elongated along the surface indicating the presence of the shear strain. The size of the TSZ layer changes significantly from one grain to another depending on the crystal structure orientation. Figure 6-11 shows a cross section of a surface after in-situ machining in SEM. The cut was made over the boundary of two different grains with different orientation as evidenced by the difference in channeling contrast. The thickness of the TSZ differ by almost a factor of two on both sides of the boundary.

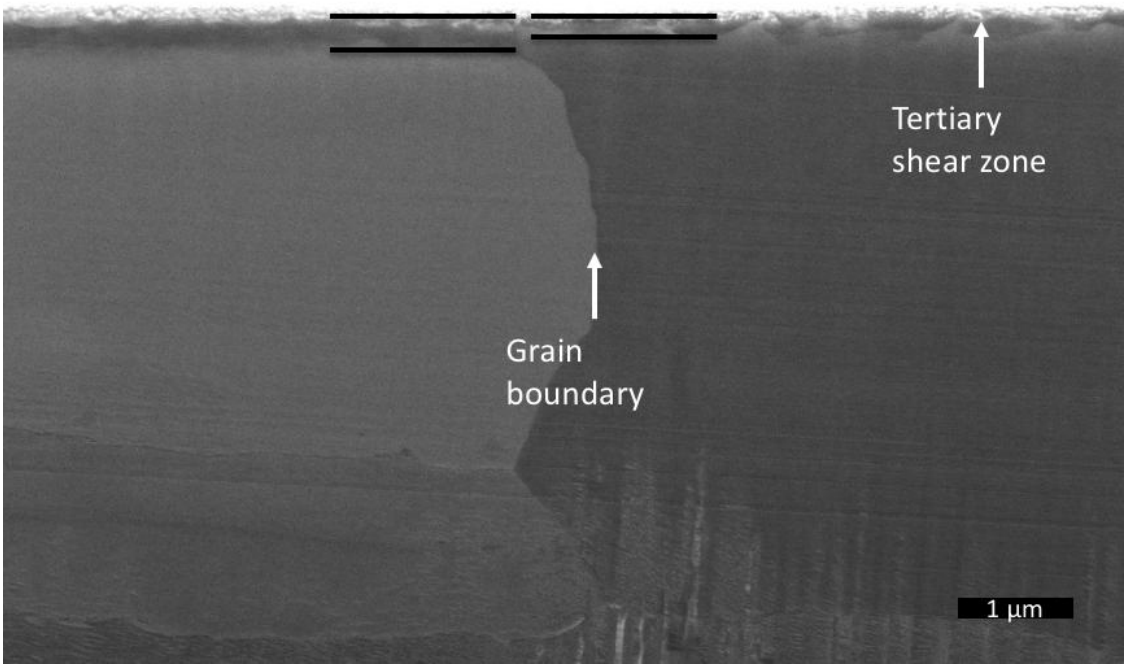

Figure 6-11 Tertiary shear zone after cutting action on two grains with different orientation.

6.4.3 Force measurements

Cutting force calculations during cutting have been made based on the tracking by SEM imaging of workpiece displacement, and the value of spring constant, *k*, of the sample holder. The spring used has an elastic constant of 1059 N/m. This value, multiplied by the displacement, lead to the plot of Figure 6-12, which shows a typical (reproduced in multiple

experiments with different tooling parameters) force–“tool displacement” curve, obtained by cutting with a feed of 1.1 µm, and cutting depth of 12 µm.

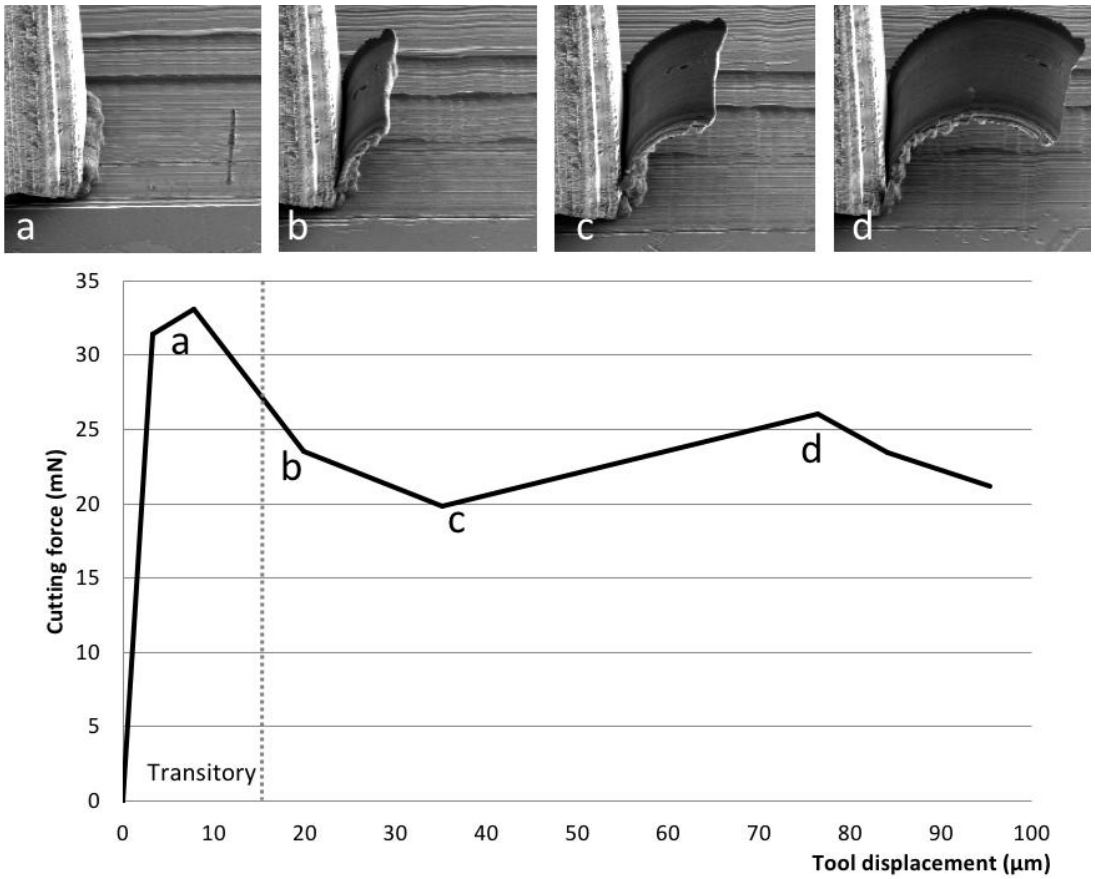

Figure 6-12 Representation of cutting force - cutting displacement for a feed of 1.1 µm.

Force measurements at the beginning of cutting have typically higher values which agrees with the transitory regime proposed on the base of Figure 6-8. Force values tend to stabilize after tens of micrometers of cutting. A value of characteristic cutting force of the experiment is calculated in this stable state, when force does not change substantially.

In order to make a link between microscopic and macroscopic cutting experiments, a set of experiments in the macroscopic regime have been made in a commercial machining bench, the same as described in Chapter 3.3. In this case, the average values of cutting force have been extracted by a force sensor. Experiments have been performed with two different tools, one with a cutting-edge radius of 11 µm and another with a radius of 5 µm. The cutting speed of 500 mm/min represents the minimum of the equipment. Table 6.2 presents the summary of the parameters used in all experiments and corresponding values of the measured cutting force. For a proper comparison of the values of forces obtained in in-situ SEM and in the machining bench, the cutting force has been normalized to the cutting depth in all the cases, which is in the order of micrometers for in-situ cutting and in the millimeter range for the machining bench.

Table 6-2 Measurements perform with cutting tools of 11, 5 and 0.02 µm of radius. It should be noted that in the first two cases experiments have been performed ex-situ in industrial machining equipment, while for the last case experiments have been performed in the in-situ SEM cutting device.

	Tool Radius	Feed	Cutting speed	Feed/Radius	Depth (width) of cut	Cutting force	Kc
	µm	mm	mm/min	-	mm	N	N/mm²
Ex-situ	11.00	0.7000	500.00	63.64	3.00	2055.80	978.95
	11.00	0.5000	500.00	45.45	3.00	1573.00	1048.67
	11.00	0.5000	500.00	45.45	3.00	1592.00	1061.33
	11.00	0.5000	500.00	45.45	3.00	1593.60	1062.40
	11.00	0.2000	500.00	18.18	3.00	865.70	1442.83
	11.00	0.0010	500.00	0.09	3.00	28.07	935.67
	5.00	0.1000	500.00	20.00	3.00	242.40	808.00
	5.00	0.1000	500.00	20.00	3.00	250.90	836.33
	5.00	0.0067	500.00	1.34	3.00	43.00	2139.30
	5.00	0.0056	500.00	1.12	3.00	40.50	2410.71
	5.00	0.0036	500.00	0.72	3.00	31.40	2907.41
	5.00	0.0009	500.00	0.18	3.00	16.70	6185.19
	5.00	0.0017	500.00	0.34	3.00	25.30	4960.78
In-situ	0.12	0.0065	0.60	54.17	0.01	0.07	852.07
	0.12	0.0049	0.60	40.83	0.01	0.06	879.12
	0.12	0.0040	0.60	33.33	0.02	0.09	965.91
	0.12	0.0037	0.60	30.92	0.01	0.04	1257.86
	0.12	0.0034	0.60	28.33	0.03	0.09	1058.82
	0.12	0.0030	0.60	25.00	0.02	0.07	1166.67
	0.12	0.0020	0.60	16.83	0.01	0.04	1443.89
	0.12	0.0020	0.60	16.67	0.02	0.05	1071.43
	0.12	0.0020	0.60	16.67	0.02	0.08	1739.13
	0.12	0.0013	0.60	10.83	0.02	0.05	1573.43
	0.12	0.0012	0.60	9.83	0.01	0.03	2118.64
	0.12	0.0011	0.60	9.17	0.01	0.02	1666.67
	0.12	0.0005	0.60	3.92	0.02	0.02	2026.34
	0.12	0.0003	0.60	2.50	0.02	0.02	2380.95
	0.12	0.0003	0.60	2.33	0.02	0.02	2678.57
	0.12	0.0003	0.60	2.17	0.01	0.01	3205.13
	0.12	0.0002	0.60	1.92	0.03	0.02	4000.00

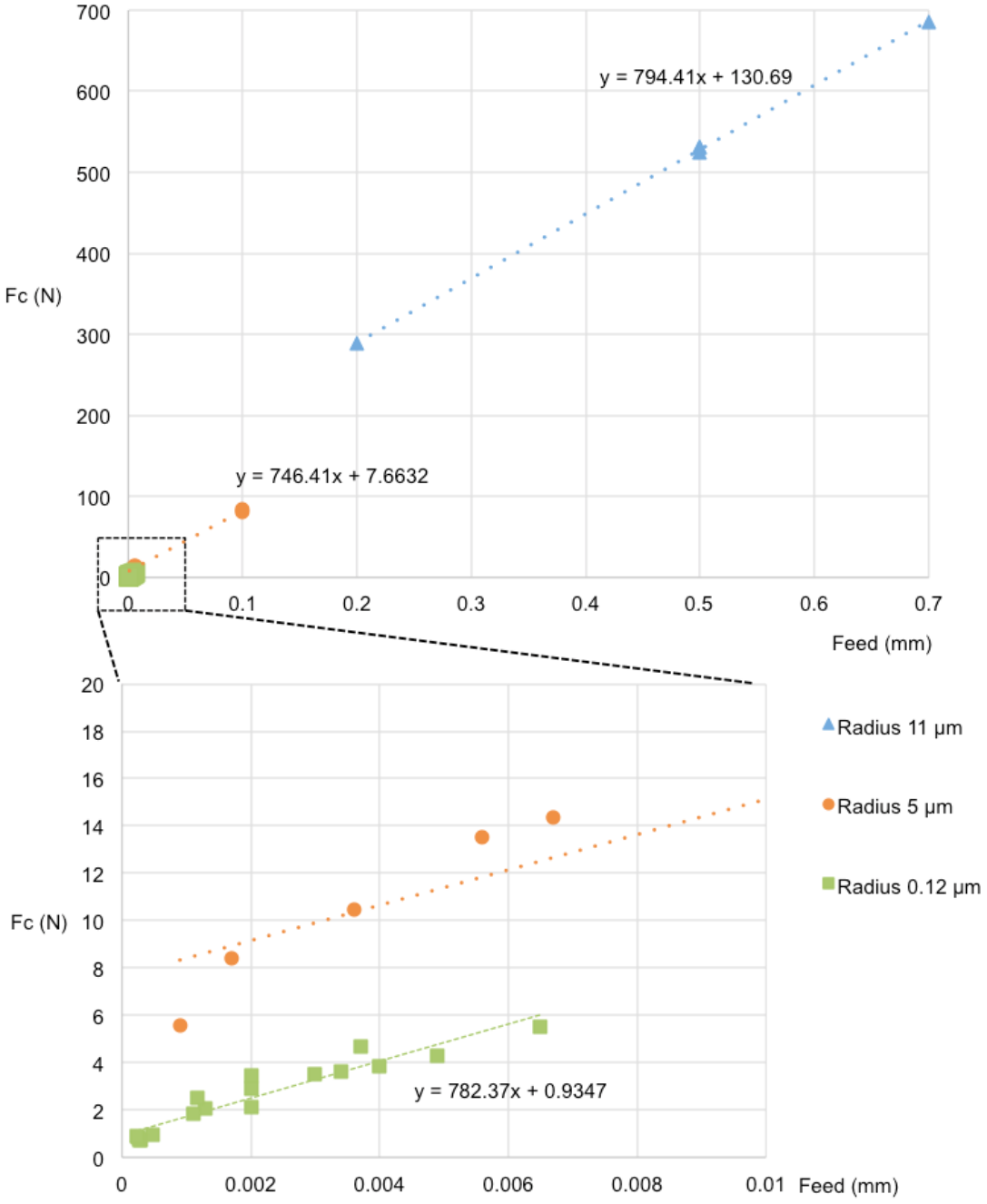

Figure 6-13 Representation of the cutting forces depending on the cutting feed. It should be taken into account that the force is divided by the cutting depth in order to been able to compare results.

Figure 6-13 shows a graphical representation of dependence of the cutting force from the feed for different tool tip radius. It can be seen that for every tip radius the dependence can be approximated by straight line. The coefficients of these three linear fits are very close to each other, but the free term is strongly dependent on the tip radius.

6.5 Discussion

6.5.1 Suitability of the setup for machining analysis

It has been shown that the setup presented allows performing experiments of orthogonal cutting in the vacuum chamber of a scanning electron microscope. That presents certain advantages in terms of microstructure analysis. On the one hand, the pressure in the chamber in testing conditions can be better than 10^{-5} Pa, leading to a very inert environment. Hence, no oxidation reactions are present in the new aluminum surfaces obtained by cutting. This gives access to the microstructure of the new surfaces without an oxide layer, which is typically amorphous (Davis 2001).

As presented in the sketch on Figure 6-1, the setup is constituted by simple and commercially available elements. Such simple construction favors versatility in terms of in-situ analysis of chip and workpiece. During experiments, in a first stage tool can be used for cutting, and subsequently retracted away from the sample in a second stage for further characterization, i.e., after machining experiments the whole workpiece-chip frame can be made available for FIB scanning or cross-sections milling and analysis without opening the vacuum chamber.

In addition to monitoring the cutting process at sub-micron scales and accessing the microstructure of the products, the setup allows to mount the workpiece on a spring-holder, what makes the cutting force available for measurements during cutting. Since the spring elastic constant has been characterized, the displacement of the workpiece has a direct link with the force applied. Thus, SEM monitoring has also the function of measuring the cutting force, with the force resolution being related yet exceeding the pixel resolution of imaging, thanks to sub-pixel position tracking.

The strategy afforded in this work has been cutting quick stops, which has clearly shown that can preserve much of the features in the PSZ, SSZ and TSZ. Such strategy slows on the one hand to perform extended chip exploration and on the other hand to obtain sample displacement and subsequently values of cutting force.

6.5.2 Chip generation in the small scale

Experiments of machining in the nanometer regime have demonstrated a chip generation process that is geometrically similar to that at the macroscopic scale. As predicted

by (Woon and Rahman 2010) and (Ducobu, Filippi, and Riviere 2009), the main limitation of chip generation at the sub-micron scales lies in the cutting-edge geometry. Since the fraction of material that flows under the tool depends on the edge curvature, for a feed size below the radius of the tool edge the chip will have difficulties to progress over the rake face of the tool. In the present study, even by reducing the cutting feed size down to 230 nm, chip has been properly generated, since the cutting-edge radius (120 nm) is a fraction of that size.

However, some microstructural particularities are presented in the nanometer regime as compared to macroscopic cutting. The most prominent is the relatively strong interaction of the tool with the material, which is seen in Figure 6-10 as a layer of material in contact with the tool that depicts a refined microstructure without signs of shear. Since the deformation in this area seems to be highly influenced by the tool contact friction, it can be assumed that this layer corresponds to the secondary shear zone. It is remarkable that SSZ thickness in this case has the same order of magnitude as the PSZ. This contrasts with the macroscopic cutting, where SSZ is typically relatively much smaller, below 10% of the chip thickness (Courbon et al 2014). Though the depth of strong friction interaction between tool and chip seems to be in the order of units of micrometers both in the macro- and nano-regime, the size of the whole chip mostly depends on the cutting feed. A number of variables (tool roughness, cutting speed or edge radius) may lead to this phenomenon, thus in order to disclose the origin further test would be needed.

In Figure 6-10 the tool-chip contact side shows a SSZ with refined and equiaxed grains. This structure points out to certain material recrystallization, which has been seen in high-speed metal cutting. In contrast, in this case machining has been performed at approximately 10 µm/s, far for typical fast machining. In the case presented in Chapter 4, DRX was activated in steel at 450 ºC approximately, hence 0.4 times the melting temperature. If we consider that aluminum melts at 660 ºC (933 K), then the corresponding 0.4 *Tm* points to approximately 100ºC (373 K). This would be an easily reachable temperature for in-situ machining if it is considered a local generation of heat close to the tool edge and accounting the vacuum condition (no heat transfer to the environment). Then it could be argued that the conditions for triggering recrystallization are reachable.

The large shear interaction between tool and workpiece material, seen in the SSZ of the chip, should also induce a large tertiary shear zone on the surface of the workpiece. The results confirm the existence of TSZ, which is observed in Figure 6-10 and Figure 6-11, though the grain sizes in the TSZ are larger than in the SSZ probably due to different mechanical properties of the initial material: large relaxed grains of the workpiece for TSZ and highly strained and already refined PSZ material for the case of SSZ. It is remarkable

that the thickness of the TSZ changes from one workpiece grain to another. This effect is probably related to the mechanical anisotropy of cubic lattices. In the case of pure aluminum, in terms of resolved shear the flow stress varies up to 100 % from one orientation to another (Hosford, 2006). Then, the movement of dislocations is restricted to certain planes, and hence the direction perpendicular to surface can be favored or not for strain propagation depending on the crystallographic orientation.

Small-scale cutting experiments have shown a mechanics of cutting consisting in an initial stage with characteristics similar to pure compression (Figure 6-8), and a second steady stage with well-developed primary shear zone. For the first stage, it can be argued that the tool rake face impacts the workpiece material and punches the whole feed surface at once. Contrary to that, in a steady state mode, when PSZ has been already developed, the deformation is concentrated in a relatively small area with a height corresponding to the thickness of a shear band of the chip visible e.g. on Figure 6-9. This would lead to a reduction of the cutting force as in fact measured experimentally and shown in Figure 6-12, and a sequential growth of the chip layer by layer.

6.5.3 Cutting force, specific energy and tool radius

The effect of tool edge radius in metal cutting has been a matter of extensive research. While a strong contribution of the edge radius in forces and other cutting characteristics is commonly assumed, no reliable quantitative relation between them has been established so far. Plotting of cutting force vs the feed, as shown in Figure 6-13, tends to produce a straight line for each tool radius. In this common representation, it is generally assumed that the intersection of this line with the ordinate axis corresponds to the pure contribution of a rounded cutting edge to the overall cutting force (Ducobu, Filippi, and Riviere 2009). In the present study by decreasing the tool radius down to 120 nm the pure contribution of the edge radius has been reduced by one order of magnitude, which goes in-line with above assumption. The pure contribution of the tool radius to the overall cutting force is represented in Figure 6-14 for the data over two orders of magnitude of edge radii.

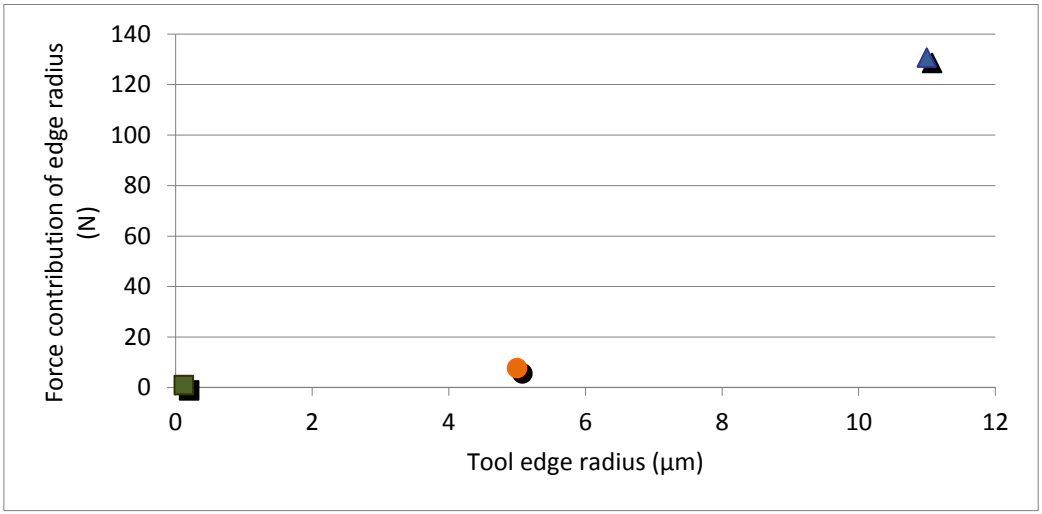

Figure 6-14 Plot of the edge radius contribution in terms of force for radius values of 0.12, 5 and 11 µm.

While individual machining parameters like tool wear, forces acting on the cutting tools, material removal rate, temperature or chip ratio can help evaluating and optimizing the process of machining, they do not provide an integral measure of the efficiency of machining. The criterion called specific cutting energy (also known as specific cutting force) has become a reliable way to quantify the convenience of certain cutting conditions (Sarwar et al. 2009). This criterion is expressed as follows:

$$K_c = \frac{F_c \cdot \cancel{displacement}}{t_1 \cdot a_p \cdot \cancel{displacement}} \qquad \text{Eq. 6-1}$$

Here K_c is the specific cutting energy, F_c is a cutting force, t_1 is the feed size and a_p is the depth (width) of cut.

The specific energy of metal cutting can be described as the energy needed for removing a unit volume of material. In aeronautic aluminum alloys it is known to be slightly below 1000 N/mm^2 with the dependence on tool radius, feed and cutting speed (Sarwar et al. 2009). In recent years certain cutting size effect, in terms of specific cutting energy, have been observed when machining at very small scales, and have been the matter of controversy in interpretation of the results. While some authors have pointed that this effect is purely a geometric effect of the tool radius (Woon and Rahman 2010), it has been also suggested that a certain material hardening size effect could have a major influence (Weber et al. 2008).

In the present study a variation of the specific cutting energy depending on the feed size has been observed. Figure 6-15 depicts the values of specific cutting energy vs feed for each experiment made with edge radii of 11, 5 and 0.12 µm (it should be noted that the feed size is plotted in logarithmic scale). For each cutting radius an increase from values around 1000 to several thousands of N/mm^2 is observed. Remarkable, that the larger is the edge

radius, the stronger is the increase of specific energy with decrease of the feed size. Though the trend in the size effect in specific energy is clear from the Figure 6-15, these plots does not reveal the origin of the effect.

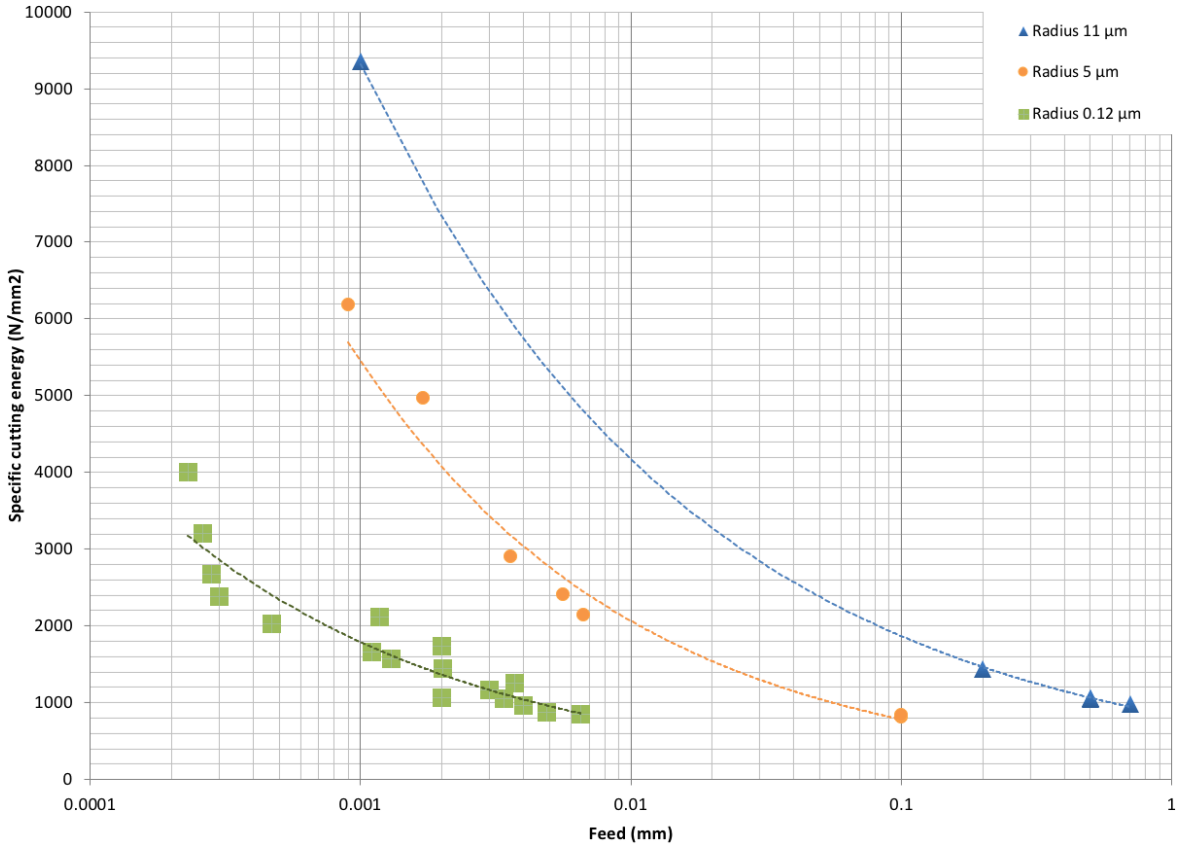

Figure 6-15 Plot of the measured specific cutting energy depending on the feed size. Note that the abscise axis is in logarithmic scale.

The picture becomes clearer if the feed size is normalized by the tool-edge radius, in order to have a dimensionless quantity for every experiment. The renormalized data shown in Figure 6-16 demonstrate almost complete overlap meaning independence of the size effect from the absolute dimensions, thus ruling out the contribution of the material specific scales into the increase of specific energy. This brings the tool geometry as the major driving factor for the size effect.

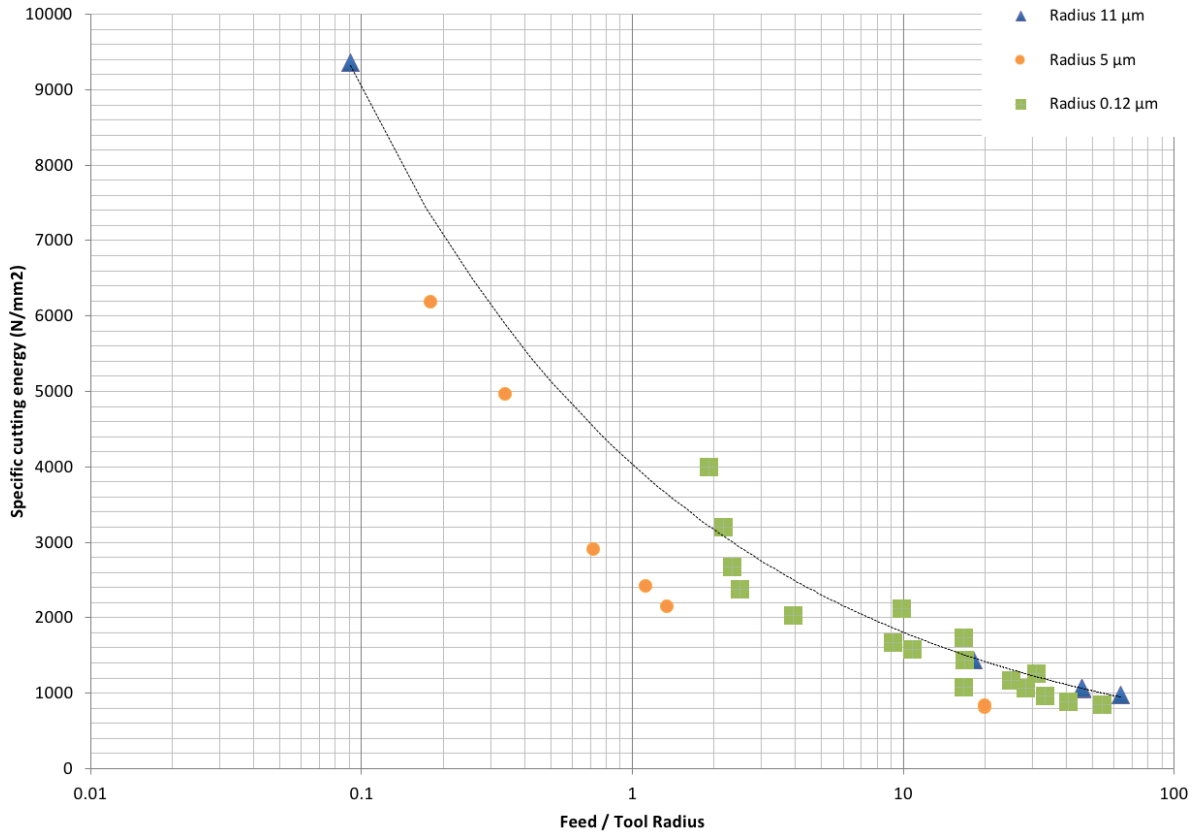

Figure 6-16 Plot of the specific cutting energy depending on the normalized feed size (feed/radius). Note that the abscise axis develops in logarithmic progression.

6.6 Conclusions

In the present study, a new cutting device that allows cutting experiments down to the sub-micrometer size has been developed. Such device can be located in a scanning electron microscope for in-situ monitoring of the cutting process at the sub-micron scales. Works have been concentrated on investigating the system in two ways, on the one hand for analysis of the microstructural effects taking part in the proximity of the tool. On the other hand, a cutting force have been measured in micro-cuttings and compared to the counterpart in the macroscopic level. This last has led to clarification of the feed-size effect in specific cutting energy. The following highlights can be extracted:

- The setup presented has been built by a simple arrangement of commercially available elements except for the cutting tool itself. Cutting experiments with the feed between 200 nm and 6 µm has been successfully performed. In addition, the system has been used to measure cutting forces in-situ in slow speed experiments.

- A clear boundary between primary and secondary shear zones has been observed even in sub-micrometer scale machining. As in macroscopic material removing processes, strain in the material far ahead of the tool edge is governed by the shear, while the material in the proximity of the tool develop more complex deformation largely influenced by the chip-tool friction.

- The feed-size effect in the specific cutting energy (exponential increase of the cutting energy at small cutting feed) has been demonstrated for three different groups of experiments. It has been concluded that this cutting energy increase is mainly due to the interaction between workpiece and the cutting radius of the tool edge.

7 Machining phenomena analysis by atomistic simulations

During the process of metal cutting, the phenomena in the tool edge governs the tool-chip interaction. Despite the enormous effort to disclose these phenomena experimentally, many aspects remain hidden to experimental observation. In this regard, the development of methods to simulate machining have been of great help to reveal the cutting conditions. These simulations are typically performed with the finite element method (FEM), which address the behavior of materials from the perspective of continuum mechanics. However, while this methodology has been used to approximate temperature, forces and strain in areas experimentally hampered, aspects of materials behavior related to crystals cannot be reproduced in the continuum, but in the discrete regime of individual atoms of a lattice. In this chapter the method of molecular dynamic (MD) is tested as a technique to simulate the tool interaction with the aluminum atoms of a workpiece. Cuts up to 40 nm of feed have been performed to evaluate influence of tool geometry and feed size during machining. It has been observed that, while small cuts induce simple mechanisms of plasticity, when the number of atoms under consideration growth the multiple mechanism permit more complex deformation. This complexity increases if the tool-chip friction increases, leading to recrystallization in SSZ and PSZ.

7.1 Introduction

Some phenomena in machining science are not easily observed or not subject to direct experimentation, hence initially the influence of a number of process parameters has to be studied by empirical correlation, or more recently simulations. While finite element simulations have been of large relevance to disclose the distribution of this parameters (stress, strain, displacement or temperature in the workpiece and chip), several aspects of matter interaction are hidden under the parachute of continuum mechanics. The phenomena of crystals mechanics that triggers a number of macroscopic behaviors are not directly represented in FEM. These material behaviors are represented in FEM simulations (like in chapter 4) by an elasto-plastic law where material flow stress depends on strain, strain-rate and temperature, or in case of friction by normal load and velocity gradient (Coulomb law). Nevertheless, effects related to the metal lattice are not taken into account. Thus, while FEM can accurately approach the behavior of statistically representative matter, the different mechanisms of crystal plasticity cannot be simulated.

Since the mechanisms of lattice plasticity are defined in the regime of atoms, this regime has to be considered for proper representation of microstructural phenomena. On this regard, the method of molecular dynamics (MD) can simulate relative movement of atoms guided by the potential (forces) that interact among them (Alder and Wainwright 1959). This approach does not consider sub-atomic effects, being the interaction purely Newtonian. However, it has been proved that this approach leads to an accurate representation of lattice mechanics, and the forces involved in material's deformation (Kato et al. 2017; Gunsteren and Mark 1998).

Some aspects hamper the applicability of this simulations for real cases. On the one hand, the computational power needed by MD is much larger than the one in other techniques like FEM simulations, in terms of processing power and in terms of system memory. Hence, the upscaling needs a considerable amount of resources. The fundamental aspects which impact in the consumption of these resources are the number of atoms, the accuracy of the method to estimate the potential between atoms and the period of time to be simulated. For a given method, the size of the sample to be simulated is limited by the amount of memory, and for a given method and sample size, the rate of simulation-time calculated depends on the processing power.

On the other hand, MD simulations needs a mathematical description of the potentials acting between atoms. These potentials have to be calculated previously by other techniques. Generally, first-principles (ad-initio) simulations are used. In addition, the potentials are applicable only for the case of design. This has entailed that building of potentials

concentrates in cases of interest, normally organic chemistry, small inorganic systems of few elements or pure metals. However, complex systems tend to be orphan of an adequate potential, thus making MD simulations not possible.

In the case of metals, many of them can be simulated in pure state. Nevertheless, potentials for binary and tertiary alloys are scarce, and industrial alloys are far from been reproducible in the context of MD. Hence, most of the simulations nowadays concentrate on pure metals, which are the base of other industrial alloys. In the case of the cutting simulations of Inamura et al. (1992) 204 atoms for 1.5 nanoseconds of simulation-time have been simulated, and a relative simple Morse potential (Morse 1929) has been used for pure cooper. Since that time, further research of simulation techniques has been accompanied by a progressive increase of the power of available computers. With this, bigger models have been replicated, and more realistic aspects have been considered.

In molecular dynamics the systems do not exchange heat with the environment, they are adiabatic unless a mechanism of heat transfer is provided. During machining the heat generated by material deformation is remarkable, hence a dissipation system is necessary in order to simulate heat disipation into a large workpiece. The method of use in most of the cases is the declaration of thermostat atoms, which have a fixed temperature along the whole simulation. As described by (Maekawa and Itoh 1995), these atoms in the boundary can successfully simulate the dissipation of heat in a simulation of machining.

Another point of controversy has been the potential of use, the manner atoms interact. In first approximations of MD to machining, pairs-potentials were used (Maekawa and Itoh 1995; Kim and Moon 1996; Inamura and Takezawa 1992). However, (Pei et al. 2006) demonstrated that the embedded atom method (EAM) can reproduce better the forces in metals. The EAM potential, which was developed from the density function theory, is based upon the recognition that the attractive force of metal atoms is governed by the pairing potential of the nearest neighbor atoms, and also by embedding energy related to the sea of electrons which covers the atoms. Based on this, recent examples of machining make use the EAM method (Pei, Lu, and Lee 2007; Goel et al. 2015; Ghomi and Odeshi 2012; Wang et al. 2015).

MD is a method that needs a large amount of resources to simulate models with a comparable size to real experiments. Hence, some authors studied methods to reduce the number of atoms under consideration. Goel et al. also make use of periodic conditions in the plane perpendicular to the cut. This technique induces mirror forces at both sides of the plane, leading to conditions similar to the ones in the center of a chip (Goel et al. 2015). This allows

to reduce the number of atoms of the simulation on the one hand, and to force a situation of plane deformation.

The aspects considered above have helped to approximate atomistic simulations to real metal cutting. This effort responds to the necessity of disclosure of the response of the material in the nanometer regime, and the mechanics of cutting in terms of lattice deformation. Nevertheless, the feed size represented in prior research (less than 10 nm) could hamper a validation with machining experiments.

This thesis affords the use of molecular dynamics simulations in order to evaluate the goodness of this method to disclose some of the phenomena related to lattice mechanisms, which cannot be resolved by continuum mechanics. As presented in chapter 4, these mechanisms guide part of the response of the workpiece material to the action of the cutting tool. However, such mechanisms are hidden by the scarce access in-process to the material under cutting. This chapter tries on the one hand to evaluate the suitability of MD for machining simulations purposes, and on the other hand to hypothesis the phenomena in nano-scale cutting of aluminum.

7.2 Methodology

Simulations have been performed by the software LAMMPS (Plimpton 1995). The potentials file is an EAM for pure aluminum (Mendelev et al. 2008), where the relaxed lattice constant is defined to 4.049 angstroms in FCC lattice. This potential defines the interaction of “Newton atoms”. Atoms which are then allowed to follow Newtonian dynamics by the method LAMMPS NVE dynamics, which resolves the movement of atoms according to the second law of Newton without external energy exchanges - LAMMPS manual (Plimpton et al. 2018).

The simulations are based on a configuration of orthogonal cutting, where the rake face of the tool is perpendicular to the direction of motion. The workpiece simulated consists of a thin plate of aluminum of 225 nm of length, 83 nm of height and 3 nm of thickness. This leads to a workpiece of 2.2 million atoms located following a (100) lattice (according to axis *x*), as shown in Figure 7-1. In terms of boundary conditions, it has been stablished periodic force conditions in the direction perpendicular to the plate. This makes the material deform only in the plane of the plate, thus reproducing a 2D system.

As shown in Figure 7-1, the tool is fixed in *x* and *y* directions. The action of cutting is then induced by the movement of the workpiece, which is constrained in the *y* axis but moves against the tool along the *x* axis at constant speed.

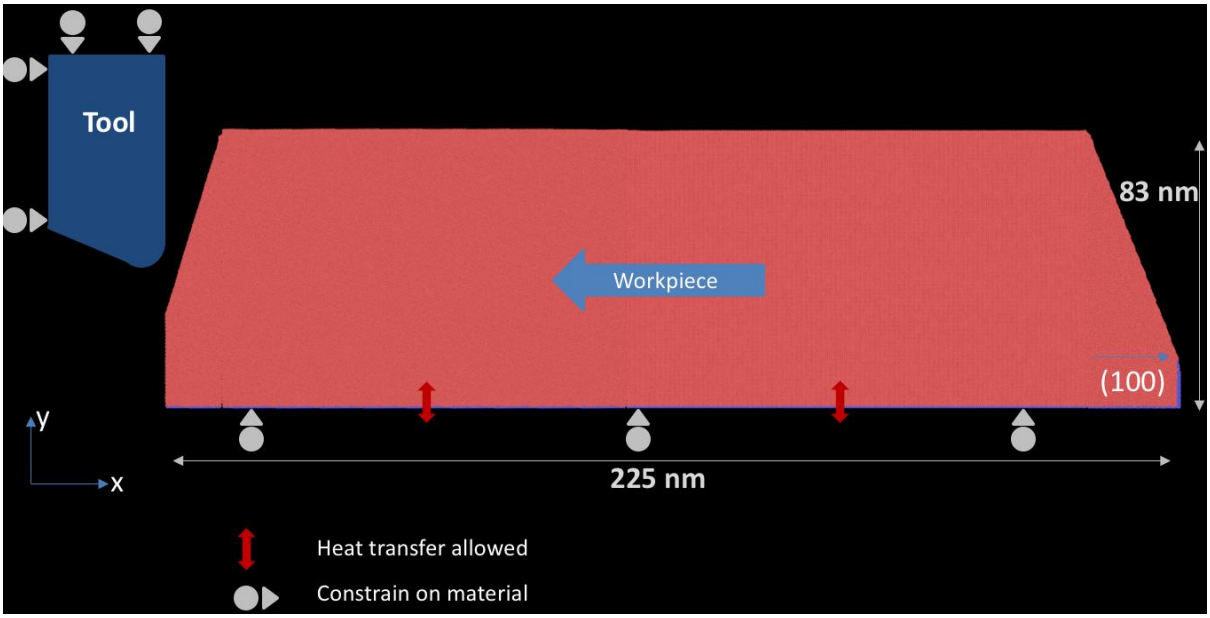

Figure 7-1 Workpiece and tool sketch. Workpiece is made of 2.2 million atoms of aluminum. It has 225 nm of length, 83 nm of height and 3 nm of thickness.

Heat transfer is allowed only in the bottom part of the workpiece. There workpiece is constituted by fixed atoms working as thermostat (LAMMPS NVT dynamics) (Figure 7-2). The purpose of these atoms is to dissipate the heat generated in the simulation volume.

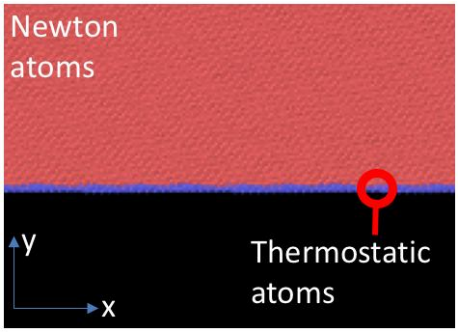

Figure 7-2 Detail of the bottom of the workpiece, which is largely constituted by Newton atoms, which behave based on Newtonian dynamics defined by the EAM potential. Thermostatic atoms have a fixed temperature along the simulation, and absorb heat generated during simulation.

The temperature induced in thermostatic atoms is 400 K, adjusted every 100 simulations steps. The simulation step time, the period between system evaluations, is 0.001 femtosecond. The atoms of the workpiece move direction *"-x"* at speeds around 20 m/s (1200 m/min respectively), which are typical machining speeds for aluminum alloys (Byrne, Dornfeld, and Denkena 2003). It has been used values of feed size between 9 and 40 nm.

The tool of use is not made by atoms, instead it is an ideal rigid surface with certain topography. It has been used two geometries, a tool with quasi-straight vertical surface with an edge radius of 4 nm and roughness Ra=0.04 on the one hand, and on the other hand a tool with irregular surface, a roughness of approximately R_a = 1.0 nm and an edge radius of 15 nm. By this model the friction between tool and workpiece is entirely given by the interaction of the workpiece and the topography of the tool.

During cutting, every 1000 steps of simulation two types of data are generated, a file with the force in *x* and *y* directions along the tool, and another one with the position of all the atoms. The data generated in this last file has been afterwards visualized and analyzed by the software OVITO (Stukowski 2010). This software has been used in the present work to plot the workpiece-chip scene, plot atom trajectories, track lattice rotations or approximate lines of dislocations for Sections 7.3.1 and 7.3.2. The analysis of the force data is evaluated in section 7.3.3.

7.3 Results and discussion

7.3.1 Chip generation

The action of material removing by the pressure of the workpiece against a fixed tool has produced in all the cases the typical generation of chips of material, as shown in Figure 7-3. In this figure it is observed a cutting process with an ideal tool and 9 nm of feed.

Figure 7-3 Workpiece cut and chip generation in case of 9 nm of feed. The tool of use has 4 nm of radius.

In this case, with the straight tool, friction forces between tool and workpiece are low. The relatively small number of atoms involved in the cut and the reduced friction lead to a constant chip generation with well-defined deformation regions.

Figure 7-4 shows a slide on atoms of the primary shear zone (PSZ). There, it can be observed that in the free side of the chip atoms deforms in an ordered way. However, while most of the atoms deform in the primary shear zone by pure shear, this process takes two steps. These steps are marked in Figure 7-4.

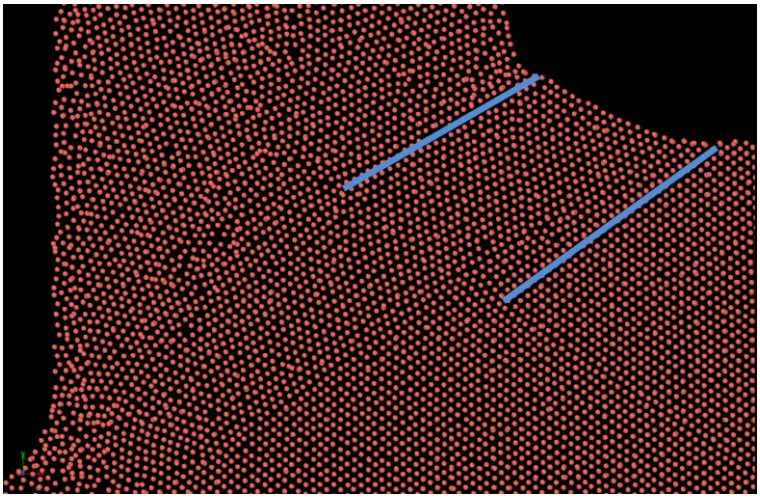

Figure 7-4 Cross-section of 1-layer atoms of the scene presented in Figure 7-3. The primary shear zone is here observed to be constituted by two lines of shear.

The trend of a primary shear zone with two lines of shear can be clearly observer if the trajectories of the atoms are plotted for the whole process of cutting (Figure 7-5). This representation shows the two-steps shear in PSZ, which exhibit variable width.

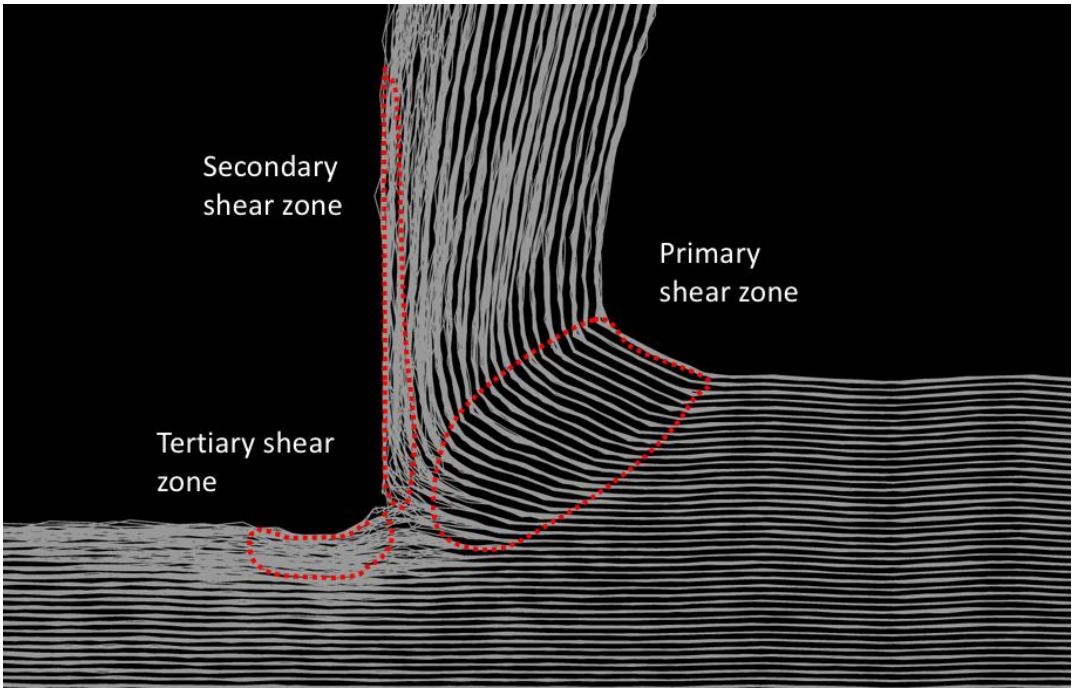

Figure 7-5 Plot of trajectories of the atoms from the workpiece to the chip. Dashed lines localize the approximate position of the primary, secondary and tertiary shear zones.

Figure 7-5 shows that the trajectories of atoms remain parallel in most of the workpiece and the chip, indicating well-defined mechanisms of lattice deformation. In contrast, lines cross themselves in the proximity of the tool. This points out that movement of the atoms have some component perpendicular to the general flow, and this component is not common for all the atoms. This last represents a more complicate mechanism than the one in the PSZ. While in this system the friction does not play a major role, a large gradient of stress in the edge proximity could be the governing factor in this case.

In order to study the effect of the model size, a similar simulation to the previous one have been carried out, with the difference of a feed size increased. Figure 7-6 presents a cut with the same tool and cutting speed as Figure 7-3, but a feed size of 40 nm instead of 9 nm. Here it can be observed that in the proximity of the tool edge the material develops voids and surface roughness. This could be consequence of a severe gradient of stress when atoms cross a sharp edge.

Figure 7-7 presents the total trajectory of a column of atoms during the whole simulation. For a constant velocity, the length of the trajectory should be constant for all the atoms. However, it can be seen that trajectories close to the tool develops shorter lengths. Hence, there is a velocity gradient in the proximity of the tool edge, what entails an increase of strain. This points that in the proximity of the flow separation kinetics can be largely reduced without the intervention of a tool-material friction factor. In addition, it can be observed that there is no clear PSZ, and a more complex chip generation process is present.

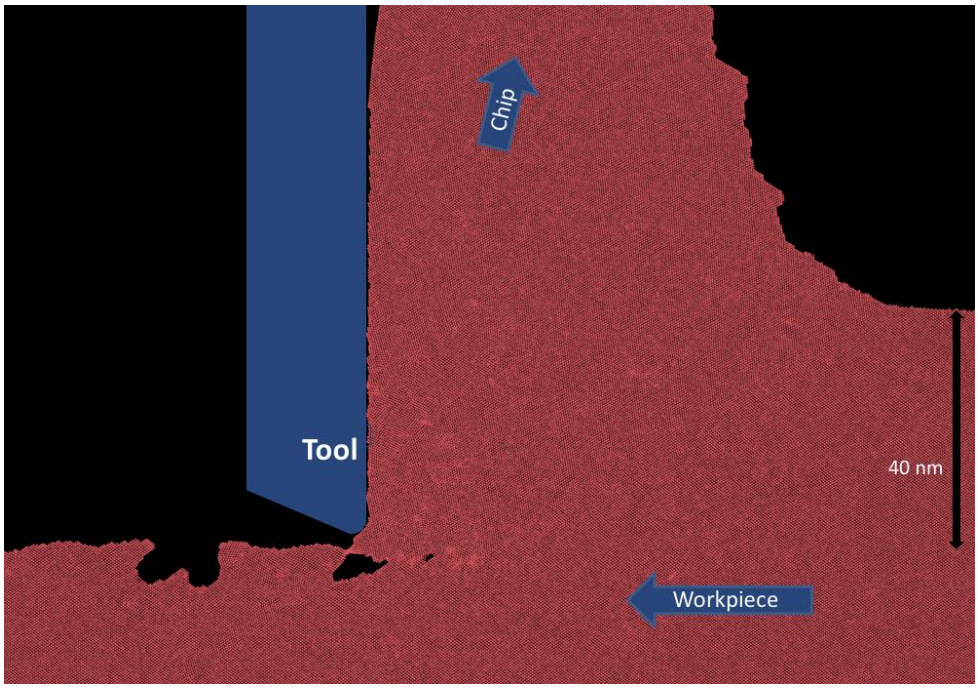

Figure 7-6 Workpiece-chip system of a cut of 40 nm of feed.

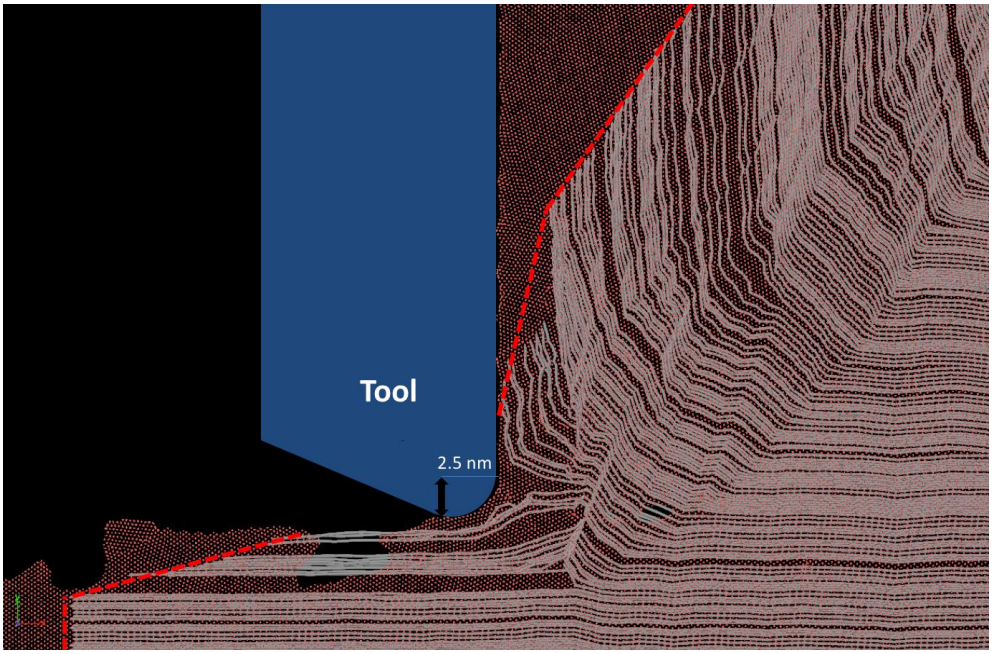

Figure 7-7 Atom trajectories of the simulation presented in Figure 7-6. A trajectory line (white) represents the total displacement of an atom during the simulation. Redline marks the approximated final location of the atoms, pointing to shorter trajectories for the atoms in the proximity of the tool. The point of flow separation in this case is approximately 2.5 nm over the bottom tool edge.

Such complexity could be related to a question of dimension. It should be mention that typical deformation effects in real materials are size-dependent. In metals, only a limited number of mechanisms are available, and real material deforms by a combination of these mechanisms. While a reduced number of atoms can only coordinately act according to one or few mechanisms (Grewer and Birringer 2014), a large number of atoms can accommodate multiple kind of defects at the same time, allowing geometrically complex deformations. Hence, a more complicated crystal deformation could be expected in a process with a significantly large number of atoms, hence leading to different mechanical response. (Giallonardo et al. 2011) showed that in an FCC metals like nickel, yield modulus remains constant for any grain size above 20 nm, being in decreasing trend below this size. Moreover, while typically grain size reduction tends to increase the material strength according to the Hall-Petch law (Hall, 1951; Petch, 1953), more recently (Pande and Cooper 2009) pointed out that metals escape from this law when the grain size is reduced under 25 nm. Since this is consequence of the number of atoms-defect interactions, simulations with a high enough feed size should permit a large number of inter-atomic mechanisms acting simultaneously, thus reproducing a behavior closer to the one expected from real experiments.

In addition to more representative cutting size, following simulations make use of a rough tool, which should develop tool-chip friction. With the same feed and speed as previous simulation, the representation in Figure 7-8 corresponds to a simulation that makes use of the tool with 15 nm of edge radius and rough surface. There, trajectories are plotted together

with the atoms in their last position. As can be seen, none of the atoms reach the surface. This could mean that other atoms, previously located in front of the tool, remains quasi stationary against the rest of the atoms.

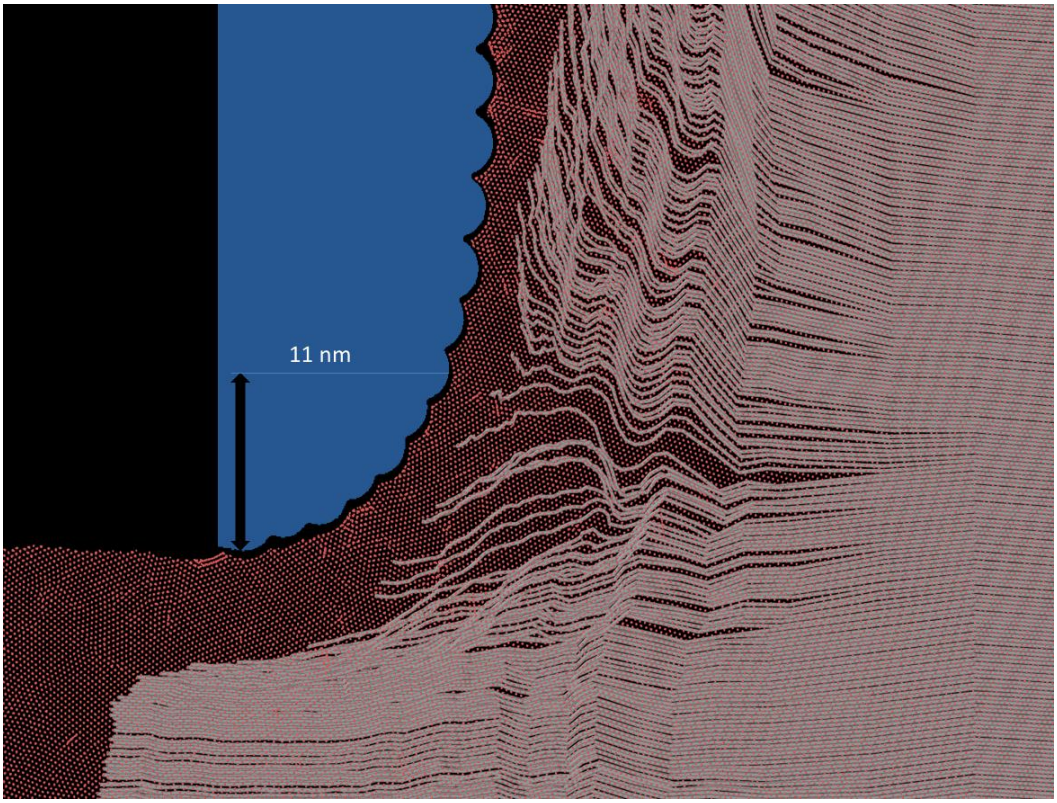

Figure 7-8 Trajectories of the atoms in the approximation to the rough cutting tool. It can be seen that trajectories do not reach the tool, as other atoms remain quasi stationary in front of the edge. The point of flow separation is approximately 11 nm over the bottom tool edge.

The results suggest that the friction introduced in this simulation reduces the mobility of the atoms in close proximity of the tool. This, up to the point of inducing a layer of low atomic mobility over which the rest of the atoms of the workpiece slides. This would make the friction to be governed by two factors, relative movement against the tool, and internal friction between aluminum atoms.

Figures 7-7 and Figure 7-8 also shows different behaviors in the tertiary shear zone (under the cutting tool) with voids and irregularities in the first case, and a smooth surface in the second case. These effects could be explained by the tool radius, since a sharper edge would induce larger gradients of stress in the surrounded material than a rounded one. In this last case with friction, if it is considered the larger edge radius and assumed a layer of quasi-static atoms in top of that, it could be expected a smoother gradient of stress under the tool. This would induce other mechanisms of deformation instead of fracture. An analysis of crystallography could shed some light on the phenomena in the proximity of the tool.

7.3.2 Effect of recrystallization in the SSZ and TSZ

As it has been seen in chapter 4, 5 and 6, the action of cutting induces large values of deformation in the close proximity of the tool. This has led to crystallographic changes in the material, in some cases structure refinement and material recrystallization.

These effects, not treated in predictive techniques based in continuum mechanics, have demonstrated to be of great importance to determine de conditions of the tool-chip contact. Here, MD results are analyzed with OVITO to evaluate phenomena of recrystallization. In order to predict the crystallographic orientation it has been used structural identification by polyhedral template matching (Larsen, Schmidt, and Schiøtz 2016) for cuts with smooth and rough surfaces (Figure 7-9 and 7-10 respectively).

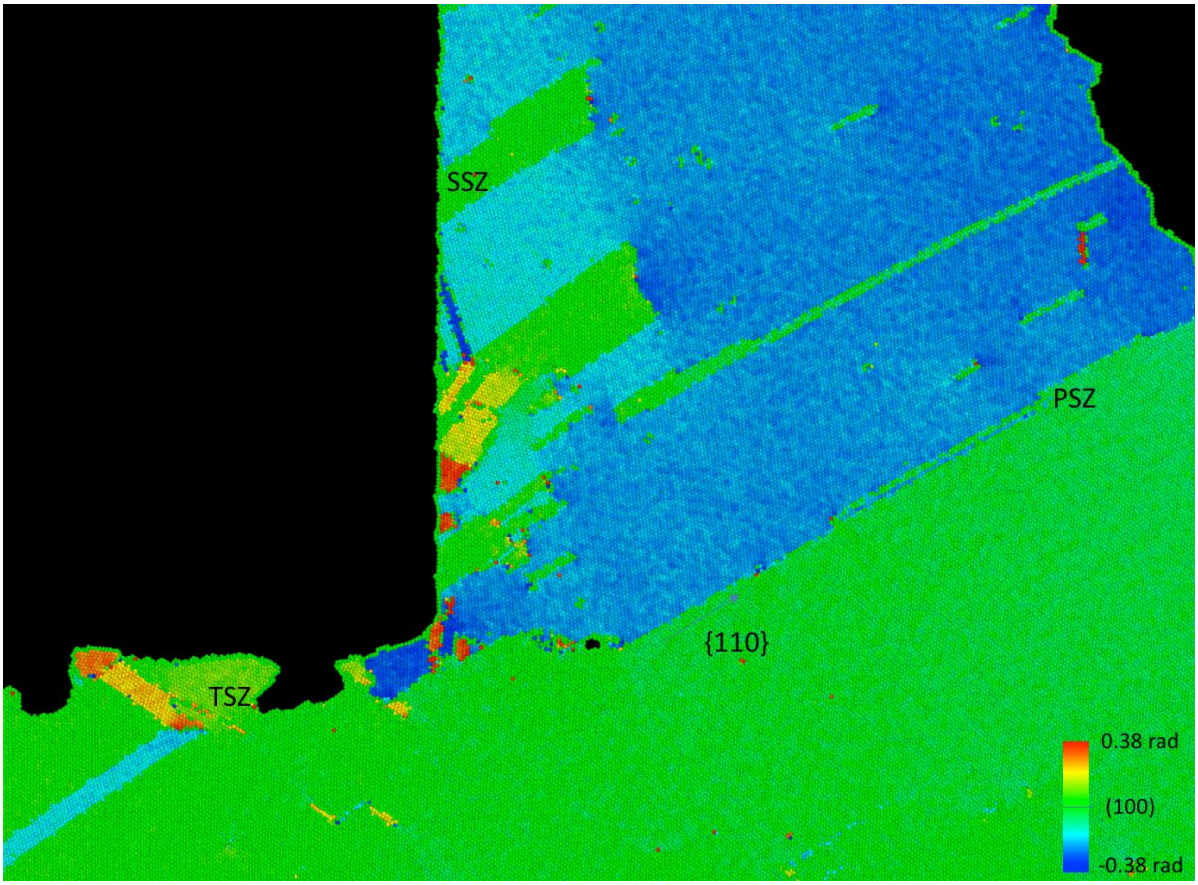

Figure 7-9 Crystallographic rotations (around the axis perpendicular to the scene) during the cut made with smooth surface. Green color refers to the original (100) orientation.

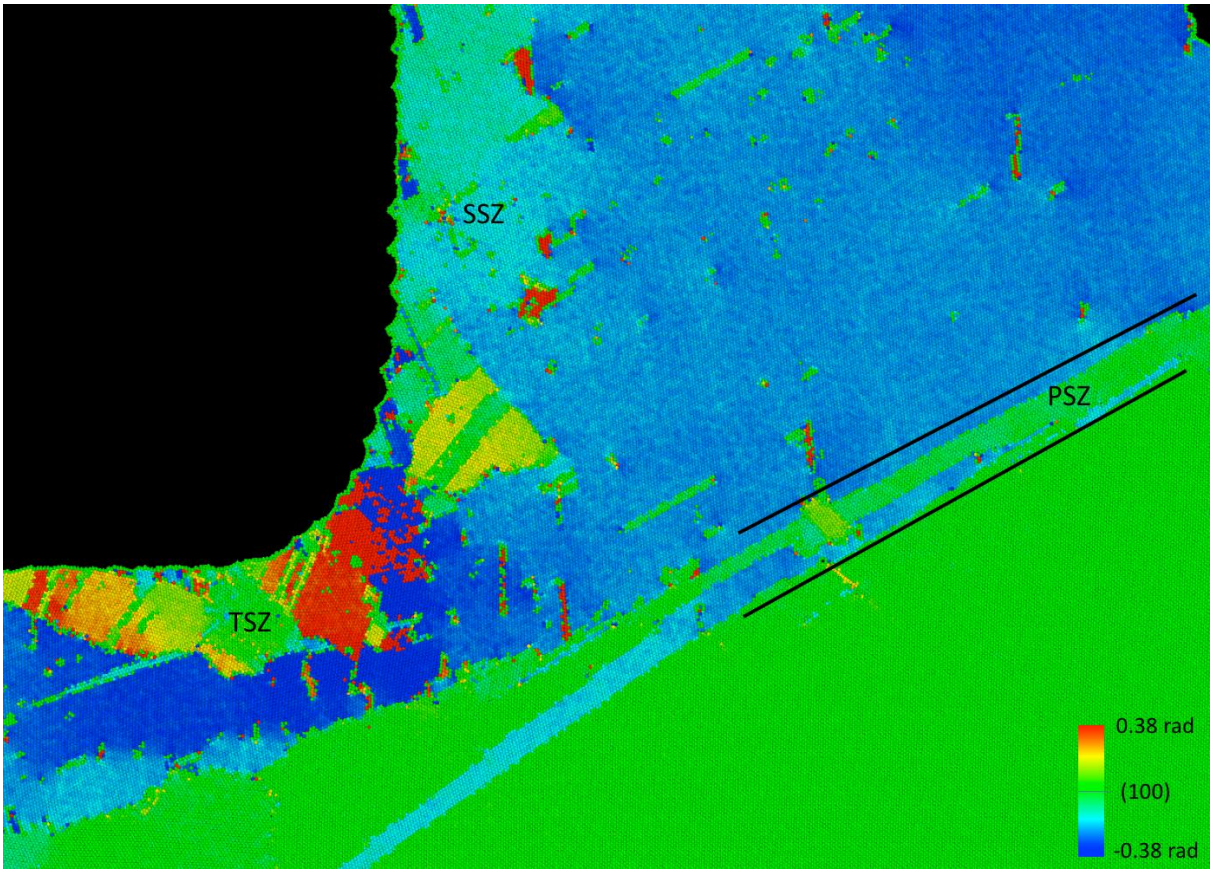

Figure 7-10 Crystallographic rotations (around the axis perpendicular to the scene) during the cut made with rough surface.

Figure 7-9 depicts a PSZ in which the material of the workpiece (100) shears across the plane (-111), direction of shear of the family {110} expected for FCC metals (Callister and Rethwisch 2007). This makes PSZ to stick to a well-defined line. Nevertheless, another kind of deformation can be seen close to the edge. As shown in Figure7-7, in this area the material slowdowns as consequence of the tool proximity, and it can be argued that PSZ is not anymore the responsible of the deformation, being in contrast the SSZ. Here, the gradient of stress in the tool proximity would be responsible of certain recrystallization, however fracture is a preferred mechanism particularly under the tool.

In case of cutting with the rough tool, Figure 7-10 shows a more complex scenario than in the previous case, since single mechanisms can roughly explain PSZ, SSZ and TSZ. In the first case, a combination of multi-step shears is observed, while being these steps diversely distributed along PSZ. On the other hand, the vicinity of the chip depicts a stochastic distribution of grains and orientations compared to Figure 7-9. This seems to be generated in the proximity of the point of flow separation, where lower mobility has been observed. Such area could be the responsible of feeding SSZ and TSZ of recrystallized matter. It has been seen that in this area the field of particle velocities change, what entail an increase in the strain. This could be the responsible of the localized recrystallization, particularly evident

where materials flow separates. These considerations could open new interpretation about an origin of the DRX strictly related to the tool edge.

7.3.3 Force and friction

The mechanism of friction in this study is strictly generated by surface topography. This represents, to the knowledge of the author, an approach not present in the literature. To study the goodness of this method, the approximated value of the friction coefficient is calculated to compare with real tribological values. For that, normal and tangential force has been extracted from the vertical section of the tools, where chip slides. If the model of Coulomb is used, an approached coefficient of friction can be calculated by:

$$\mu = \frac{F_t}{F_n} \qquad \text{Eq. 7-1}$$

where μ is the coefficient of friction, F_n is the force normal to the surface and F_t is the tangential one.

As Figure 7-11 depicts, the smooth tool developed a friction coefficient of 0.05, while the rough one 0.4, thus a difference of one order of magnitude. The value of friction obtained by the rough tool is comparable to values of friction obtained experimentally by tribometers in similar conditions to high-speed machining, rounding 0.4 (Faverjon, Rech, and Leroy 2013).

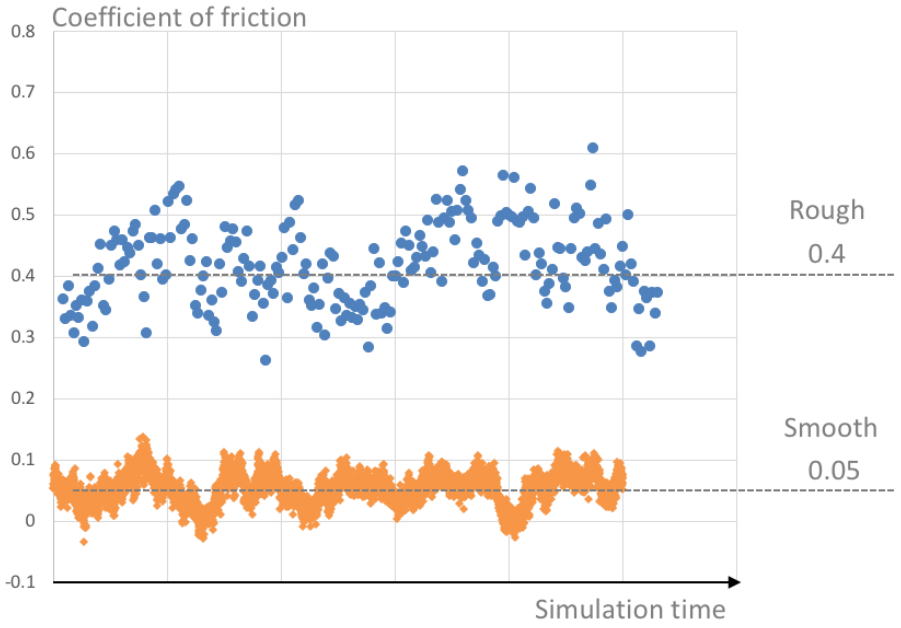

Figure 7-11 Values of friction coefficient calculated for each simulation step. A mean value of 0.05 and 0.4 has been found for the smooth and rough tool respectively.

In order to evaluate the data in MD cutting, the scales present in this chapter make complicate to figure out the validity of the values of force. However, as seen in Chapter 6, a relatively reliable characteristic for comparing multi-scale cutting is the specific cutting energy K_c. This variable K_c is calculated as in previous chapter, by equation 6-1, leading to the following plot (Figure 7-12)

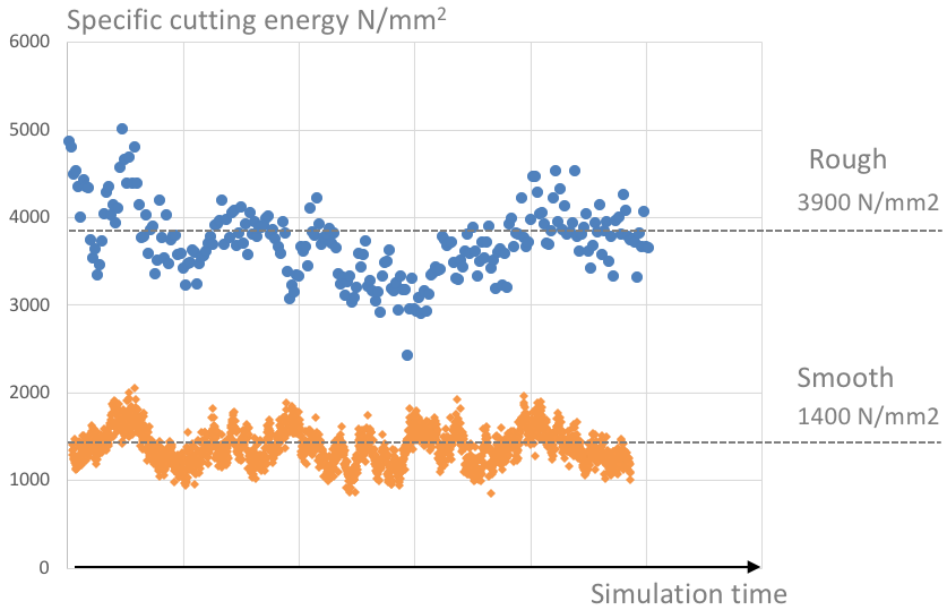

Figure 7-12 Values of specific cutting energy calculated each calculation step, where the rough tool led to 3900 N/mm^2 and the smooth one 1400 N/mm^2.

Values of specific cutting energy tend to round 1000 N/mm^2 in aluminum alloys, hence the values presented here are relative high, moreover since pure metals tend to be softer than commercial alloys.

In order to correctly evaluate these values, it should be considered the effect of the cutting radius. As shown in previous chapter, the relation between cutting feed and edge radius has a prominent effect in specific cutting energy. Hence, to compare with the experimental data, feed-to-radius relation should be considered. This can be observed in Figure 7-13, where the points obtained in MD simulations overlay the data obtained experimentally on the Figure 6-16 of previous chapter, and particularly the values obtained for the smallest radius, acquired in-situ in the SEM. This supports feed-to-radius as a multi-scale parameter, suitable to consider cutting energy in nano y macro regimes. And furthermore, these results also support, up to certain point, the validity of atomistic simulations based on molecular dynamics to reproduce mechanical machining, which accordingly with experiments has reproduced recrystallization in SSZ and PSZ in the previous section, as well as reasonable cutting energy values in the present one.

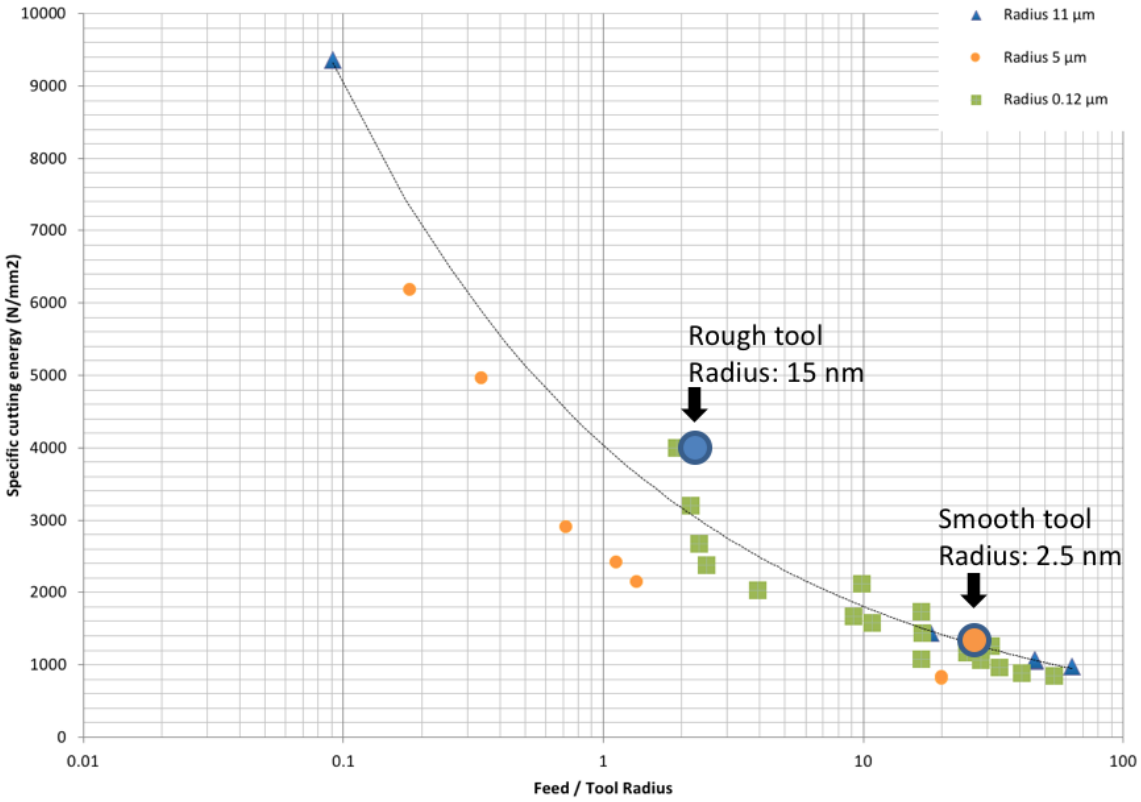

Figure 7-13 Specific cutting energy calculated in the present chapter represented over the Figure 6-16 of previous chapter.

7.4 Conclusions

In this chapter it has been studied the feasibility of an atomistic method of simulations to predict crystallographic phenomena during machining. The method of use has been molecular dynamics (MD), which provides matter representation down to atom lattices, at a reasonable computation cost.

MD has been used to reproduce a process of cutting over aluminum with cuts up to 40 nm of feed. It has been observed that, while small cuts induce simple mechanisms of plasticity, when the number of atoms under consideration growth the multiple mechanism permits more complex deformation. The following highlights can be extracted:

- When the cut involves a reduced number of atoms (feed of 9 nm) deformation sticks to simple mechanisms of deformation. This leads to well-defined shears, particularly in the PSZ.

- In case the number of atoms enrolled in a process of deformation growths, it could be activated a number of distinct slip systems. While PSZ may still be

governed by shear, in the proximity of the tool a more complex mechanism is observed. This may produce fracture or recrystallization.

- It has been observed that friction plays a major role in terms of deformation, since large values induce a large gradient of particle velocity in the proximity of the tool. This would lead to large strain values and, as observed in the orientations map, a deep recrystallization in SSZ and TSZ.

- It has been demonstrated that a friction model based strictly in surface topography may reproduce real values of friction in MD. This friction may induce a layer of atoms with very low mobility in front of the tool.

- The specific cutting energy, while being relatively high for a pure metal, follows the trend of experimental calculations, being coherent with the results of chapter 6 if the tool radius is taken into account.

8 Conclusions

The aim of the present work is exploring the potential of nano-science research methods for revealing the atomic mechanisms of metals plasticity in machining conditions, in particular, the mechanics of the tool-chip contact. In-line with this aim methodologies have been designed to reconstruct the microstructural events taking place in the tool edge proximity (Chapter 4 and 5); a micro-scale cutting device has been constructed to perform machining experiments *in-operando* inside an electron microscope, that has provided an access to chip generation at sub-microscopic scales (Chapter 6); finally, the method of molecular dynamics has been applied to reproduce lattice distortions in the proximity of the tool during cutting, i.e. to afford machining simulations on the atomic level (Chapter 7).

More in detail, this thesis dissertation yields the following conclusions:

-Chip-tool contact mechanics:

Sudden reduction in the cutting friction in orthogonal dry cutting of AISI 1045 steel reported in the literature has been in this work associated with the initiation of the dynamic recrystallization process in the tool/chip contact area. Dynamic recrystallization induces a strong microstructural softening effect which supports and overperforms the effect of thermal softening. After initiation of dynamic recrystallization at a certain cutting speed a softer layer is developed in the contact area between the chip and the tool, which works as a lubricant that absorbs most of the deformation and reduces the friction.

A complete thermomechanical description of the process of AISI 1045 steel cutting has been proposed, which include formation of a build-up edge at low cutting speeds, annihilation of built-up edge at transition cutting speed due to onset of dynamic recrystallization, and a direct chip on tool sliding mode promoted by existence of dynamically soft recrystallizing layer at the tool/chip contact.

It has been shown, that the onset of dynamic recrystallization is solely defined by the temperature rise at the tool/chip contact area. In the time-window available in high speed machining only recrystallization of the rotational type can be initiated, which finds its experimental confirmation in the preservation of the grains size after the process. Rotational recrystallization has atoms diffusion along grain boundaries as underlaying atomic mechanism, and in this work it was shown that knowing the grain boundary diffusion coefficient and the surface energy, both being intrinsic properties of the material, it is possible

to predict the onset temperature for dynamic recrystallization and thus a speed for mode transition in orthogonal dry cutting of AISI 1045 steel.

-Structural and mechanical characterization of nano-crystalline material obtained as a result of dynamic recrystallization:

The secondary shear zone (SSZ) in chips has been matter of a multi-approach characterization. A set of morphologically, microstructurally, mechanically and chemically analysis has demonstrated, for the tested conditions, its unique microstructure in comparison with the original structure as well as with any microcrystalline metal obtained by other methods.

It has been elucidated that, in contrary to the rest of the chip, SSZ is built by nano-sized equiaxial grains obtained as a result of dynamic recrystallization. This tendency is particularly remarkable in the proximity of the chip edge, where grains reduce the size down to 70 nm. EBSD measurements show that dynamic recrystallization promotes material relaxation reducing the number of dislocations inside the grains.

Local mechanical properties of this nano-crystalline material have been characterized by nanoindentation and micro-bending. It was found that the hardness of the chip is higher than of unprocessed bulk material, which is consistent with expected strain hardening. Particularly interesting have been a 15% reduction of the elastic modulus in the nano-crystalline region as compared to the expected modulus for this steel. This has been attributed to the high-volume fraction of the grain boundaries, and thus a higher degree of disorder, since a number of authors has shown that amorphous structures tend to reduce elastic modulus.

Chemical analysis of the nano-crystalline material, performed by EDX in scanning transmission electron microscope, showed a homogeneous distribution of carbon. No signs of pearlitic structures have been found, and carbon has not segregated in grains boundaries. This indicates the complete re-solution of carbon in the ferrite matrix. Thus, the material in the secondary shear zone has been defined as nano-crystalline ferrite super-saturated by carbon.

-In-situ SEM set-up for machining:

An in-situ in SEM setup for microscopic linear orthogonal cutting experiments has been designed and assembled, and its functionality has been tested. The setup is based on commercially available micromanipulator, spring table and a custom-made cutting head.

Proposed design allows for advancement and positioning of the cutting tool in respect to the sample, linear travel of the tool in the cutting direction, continuous force measurement between the tool and the workpiece in the direction of the cut (cutting force) and harmless withdrawal of the tool from the workpiece for further inspection of the cut.

Cutting force measurement has been performed by the measurements of displacement of the spring table with the known spring constant. This displacement has been directly obtained from the SEM imaging during cutting. Subpixel accuracy of positioning by custom made algorithms has provided 10 μN resolution and tens of mN measurement range in forces.

Customized cutting tools have been fabricated from WC-Co H13A piece by FIB. This technology has allowed controlling the feed and clearance angle and tip radius down to 120 nm. Multiple cutting experiments have been performed with this tool at different cutting feeds.

Direct observation of the micro-cutting process assisted by force measurement lead to discrimination of two stages in cutting: a transitory regime at the moment of insertion of the tool into the workpiece, when the whole feed surface is deformed, leading to high cutting force, and a steady state regime, when the material is sequentially deformed in the narrow shear band along the shear plane, which results in decreased cutting force as compared to transitory regime.

Based on the cutting force measurements in micro- and macro-cutting experiments a specific cutting energy has been calculated in dependence of feed size for a range of almost three orders of magnitude of cutting edge radii. It was found that the size effect observed for the specific energy can be fully attributed to the geometry of the tool.

Direct observations of the cutting process allowed tracking microstructure’s behavior. Effects like crack nucleation and propagation have been monitored by the scanning electron microscope.

-Approaching the cutting process by atomic simulations:

In machining science, the finite elements method (FEM) has been successfully used to predict multiple parameters. Nevertheless, this last assumes the continuum mechanics approach of the material, which cannot reproduce lattice-related effects. In the present thesis the method of molecular dynamics (MD) has been tested for simulation of a process of high-speed cutting. Contrary to FEM, MD assumes that the matter is made of atoms controlled by simple potential forces, what makes capable to reproduce atomic mechanism of plasticity without necessity to know/fit macroscopic material properties.

The outcome of the simulations has allowed to track the particles trajectories along the whole primary and secondary shear zones, which in microscopic terms corresponds to material flow. It has been elucidated that, while in the primary shear zone the plasticity is largely governed by pure shear, in the secondary zone the deformation is more stochastic, and singular shear can be hardly defined.

It has been observed that the depth of material affected by residual stress in the secondary and tertiary shear zones is strongly affected by the cutting-edge radius and topography. For sharp edges the density of defects remains relatively low, while increasing the radius and topography leads to deeper and more relevant permanent deformations.

Very remarkable finding has been that the specific cutting energy obtained by MD simulations in chapter 7 is in good agreement to the experimental values of chapter 6 for similar the normalized feed values. This result uncovers huge potential of MD methodology for industrially relevant metal cutting processes and inspires future research in this direction.

9 Future lines

This thesis develops connections between material behavior under the cutting conditions and the atomic mechanisms of plasticity. This has been afforded along this work by different approaches. Each could represent a future line to develop better tool-chip interaction understanding, as discussed below.

The case presented in chapter 4 shows the potential of a reconstructive analysis of the SSZ conditions based on the traces that machining induces in the microstructure. Theses traces reflect certain processes related to the temperature and the atom mobility not taken into account before. This has been done for the case of orthogonal cutting of AISI 1045 steel, by dry cutting, at cutting speeds between 5 and 200 m/min with a feed size of 0.1 mm/rev. Such a case, while having the potential to be representative in terms of the phenomena involved, represent a very particular case. In order to expand and exploit the benefits of this methodology it can be proposed the following.

- To evaluate how input parameters like feed modifies the constitution of a recrystallized layer in AISI 1045 steel. It could be expected that the speed of transition, the size of the layer, and the depth of recrystallization vary.

- To experiment the effects of lubrication and coatings in the cutting tool in the development of recrystallization in the SSZ.

- To study, down to the nanometer regime, the effects of the steel additives that increase machinability. These additives use to reduce the friction with the tool, however, in order to understand which processes are activated, an study of the microstructure developed in the SSZ could resolve some of the phenomena.

- To determine, for other steels, the response of the microstructure in the SSZ. It could be expected other mechanisms from other steels, particularly it they are based on metastable phases or if they are based in a FCC matrix rather than a BCC one.

- To proceed with the methodologies with other aluminums, nickel or titanium-based alloys.

In chapter 5 it has been shown that in the SSZ a unique microstructure has been developed. The mechanical properties exceed the ones observed in the pristine material. While it is known that a refined microstructure also produced in the TSZ, this could affect the

properties of the surface of the parts after certain machining processes. Thus, further analysis of SSZ and TSZ could be valuable.

- To perform deeper mechanical test in SSZ and TSZ, stablishing the linking between material's refinement and strength.
- To study new parameters to define the response of the parts to mechanical loads. Of particular interest could be the fatigue life, since material of study would be in the surface, which is a typical origin of fatigue cracks.
- To consider the conditions in which DRX has been developed in the SSZ, for further applications in the materials treatments.

The setup for in-situ machining in electron microscopes presented in chapter 6 has demonstrated being applicable for the study of chip generation. This has been a first design with large possibilities of optimization and expansion in the operational procedure and in the features available:

- To define standard procedures for device installation in the SEM, use of the manipulator and extraction and processing of the data.
- To increase the control of the manipulator by the use of scriptable movements.
- To use of different tool geometries to identify the response in the PSZ, SSZ and TSZ for clearance and rake angles of other values.
- To develop new fabrication methods for the tool. While the process described in chapter 6 has been of great value, it consumes considerable amount of time. In addition, other materials could be explored as candidates for the tool.

In chapter 7 it has been described the use of the method of molecular dynamics for the potential use in simulations of machining. This has represented a firsts approach to cutting experiments with relatively large feed size (in the order of 40 nm). However, simulations have been primary used to demonstrate a "proof of concept", where much of the microscopical mechanisms seen in previous chapter can be reproduced. Further development of the technique could make possible to correlate data from chapter 6 with simulations:

- To design of a simulation and an experiment to compare and validate the method. It should be taken into account that the lack of some potentials makes

only affordable simulations for some aluminum alloys, ideally pure aluminum. Thus, the same material should be used in simulations.

- To develop the properties of the cutting tool to reproduce with fidelity the condition of real tool-chip interaction. Of particular importance the thermal conditions.

- To increase the amount of data which can be extracted and post-proceeded from each simulation. Now feed force and cutting force can be extracted, however parameters like temperature of the workpiece material present more difficulties, since at the atomic level temperature is not a property of an atom, but from a group of atoms.

10 Dissemination

Publications

(Minor revision) Microstructural aspects of the transition between two machining regimes in orthogonal cutting of AISI 1045. B. Medina-Clavijo, M. Saez-de-Buruaga, C. Motz, A. Chuvilin, P-J. Arrazola. Journal of materials processing technology.

(In preparation) Characteristics of ultra-fast recrystallization's microstructure by steel cutting. B. Medina-Clavijo, J. Rafael-Velayarce, M. Saez-de-Buruaga, C. Motz, P. J. Arrazola, A. Chuvilin

(In preparation) Machining in the nanometer regime: built and use of an in-situ electron microscope cutting setup. B. Medina-Clavijo, Andres Sela, Gorka Ortiz-de-Zarate, Andrey Chuvilin, Pedro J. Arrazola

Conferences

In SEM testing of mechanical properties of Steel and Shape Memory Alloys. B. Medina, E. Modin, I. Rodriguez, V. A. Chernenko, P. J. Arrazola, A. Chuvilin. Kleidiek meeting 2017. Reutlingen (Alemania).

Reconstructing thermo-mechanical loads of machining – Poster session. B. Medina, P. J. Arrazola, A. Chuvilin. 5th Dresden Nanoanalysis Symposium: In-situ Microscopy. 1.Sep.2017 - Fraunhofer Cluster Nanoanalysis (Germany)

11 References

Aarnts, M. P., R. A. Rijkenberg, F. A. Twisk, D. Wilcox, M. J. Zuijderwijk, A. Arlazarov, D. Barbier, et al. 2011. *Microstructural Quantification of Multi-Phase Steels (Micro-Quant)*.

Abouridouane, M., F. Klocke, and D. Lung. 2014. “MICROSTRUCTURE-BASED 3D FE MODELING FOR MICRO CUTTING FERRITIC- PEARLITIC CARBON STEELS,” 1–8.

Alder, B J, and T E Wainwright. 1959. “Studies in Molecular Dynamics. I. General Method.” *The Journal of Chemical Physics* 31 (2): 459–66. doi:10.1063/1.1730376.

Armendia, M., A. Garay, A. Villar, M.A. Davies, and P.J. Arrazola. 2010. “High Bandwidth Temperature Measurement in Interrupted Cutting of Difficult to Machine Materials.” *CIRP Annals - Manufacturing Technology* 59 (1): 97–100. doi:10.1016/j.cirp.2010.03.059.

Arrazola, P. 2003. “Modélisation Numérique de La Coupe: Étude de Sensibilité Des Paramètres d’Entrée et Identification Du Frottement Entre Outil-Copeau.” Universite de Nantes. http://www.sudoc.fr/081180950.

Arrazola, P, Patxi Aristimuno, Daniel Soler, and Tom Childs. 2015. “Metal Cutting Experiments and Modelling for Improved Determination of Chip/Tool Contact Temperature by Infrared Thermography.” *CIRP Annals - Manufacturing Technology* 64 (1). CIRP: 57–60. doi:10.1016/j.cirp.2015.04.061.

Arrazola, P, T. Özel, D. Umbrello, M. Davies, and I.S. Jawahir. 2013. “Recent Advances in Modelling of Metal Machining Processes.” *CIRP Annals - Manufacturing Technology* 62 (2): 695–718. doi:10.1016/j.cirp.2013.05.006.

Arrazola, P, D Ugarte, J Montoya, A Villar, and S Marya. 2005. “Finite Element Modeling of Chip Formation Process with Abaqus/Explicit 6.3.” *VII International …*. http://congress.cimne.com/complas05/admin/Files/FilePaper/p173.pdf.

Arrazola, P, A Villar, D Ugarte, and S Marya. 2007. “Serrated Chip Prediction in Finite Element Modeling of the Chip Formation Process.” *Machining Science and Technology* 11 (November 2010): 367–90. doi:10.1080/10910340701539882.

Ashby, M. F., C. Gandhi, and D. M R Taplin. 1979. “Fracture-Mechanism Maps and Their Construction for f.c.c. Metals and Alloys.” *Acta Metallurgica* 27 (5): 699–729. doi:10.1016/0001-6160(79)90105-6.

Ashby, Michael F., and David R. H. Jones. 1996. “Engineering Materials.” In *Engineering Materials 1*, edited by Elsevier, 2nd editio. Butterwoth-Heinemann.

———. 1998. “Engineering Materials.” In *Engineering Materials 2*, edited by Elsevier, 3rd

editio. Butterwoth-Heinemann.

Askeland, Donald R., Pradeep P. Fulay, and Wendelin J. Wright. 2010. “The Science and Engineering of Materials.” In *The Science and Engineering of Materials*, edited by Cengage Learning, 6th editio, 949.

Babu, Bijish. 2008. “Physically Based Model for Plasticity and Creep of Ti-6Al-4V.” Lulea University of technology.

Bakshi, S Das, A Leiro, B Prakash, and H K D H Bhadeshia. 2014. “Dry Rolling / Sliding Wear of Nanostructured Bainite.” *Wear* 316 (1–2): 70–78. doi:10.1016/j.wear.2014.04.020.

Barani, A. Ardehali, F. Li, P. Romano, Dirk Ponge, and D. Raabe. 2007. “Design of High-Strength Steels by Microalloying and Thermomechanical Treatment.” *Materials Science and Engineering: A* 463 (1–2): 138–46. doi:10.1016/j.msea.2006.08.124.

Ben Abdelali, H., W. Ben Salem, Joël Rech, A Dogui, and Philippe Kapsa. 2013. “Characterization of the Friction Coefficient and White Layer at the Tool-Chip-Workpiece Interface Using Experimental and Numerical Studies during Friction Tests of AISI 1045.” *Lecture Notes in Mechanical Engineering* 1: 69–77. doi:10.1007/978-3-642-37143-1.

Ben Abdelali, H., C. Claudin, J. Rech, W. Ben Salem, Ph Kapsa, and A. Dogui. 2012. “Experimental Characterization of Friction Coefficient at the Tool-Chip-Workpiece Interface during Dry Cutting of AISI 1045.” *Wear* 286–287. Elsevier B.V.: 108–15. doi:10.1016/j.wear.2011.05.030.

Benson, David J. 1997. “A Mixture Theory for Contact in Multi-Material Eulerian Formulations.” *Computer Methods in Applied Mechanics and Engineering* 140 (1–2): 59–86. doi:10.1016/S0045-7825(96)01050-X.

Benson, David J., and Shigenobu Okazawa. 2004. “Contact in a Multi-Material Eulerian Finite Element Formulation.” *Computer Methods in Applied Mechanics and Engineering* 193 (39–41): 4277–98. doi:10.1016/j.cma.2003.12.061.

Bhadeshia, H.K.D.H., and Sir Robert Honeycombe. 2006. *Steels*. *Steels*. Elsevier. doi:10.1016/B978-075068084-4/50013-3.

Boneti-Toldo, L L, Marcio Ferreira-Hupalo, Selauco Vurobi-Junior, and Adriano Murilo Rosário. 2017. “Influence of Casting Heterogeneities on Microstructure and Mechanical Properties of Austempered Ductile Iron (ADI).” *Revista Materia* 22 (3).

Brunzel, and Fomin. 1997. “Effect of the Pearlite Strcture of Structural Steel on Its Machinability.” *Metal Science and Heat Treatment* 39 (2): 39–41.

Byrne, G I, D I Dornfeld, and B Denkena. 2003. “Advancing Cutting Technology.” *CIRP Annals - Manufacturing Technology* 2 (52): 483–507.

Bytyqi, Arsim, Nusa Puksic, Monika Jenko, and Matja Godec. 2011. “Characterization of the

Inclusions in Spring Steel Using Light Microscopy and Scanning Electron Microscopy" 45 (1): 55–59.

Calcagnotto, Marion, Dirk Ponge, Eralp Demir, and D. Raabe. 2010. "Orientation Gradients and Geometrically Necessary Dislocations in Ultrafine Grained Dual-Phase Steels Studied by 2D and 3D EBSD." *Materials Science and Engineering: A* 527 (10–11): 2738–46. doi:10.1016/j.msea.2010.01.004.

Callister, William D., and David G. Rethwisch. 2007. *Materials Science and Engineering: An Introduction*. Edited by Inc. John Wiley & Sons. *Materials Science and Engineering*. 7th editio. doi:10.1016/0025-5416(87)90343-0.

Campbell, J D, and W G Ferguson. 1970. "The Temperature and Strain Rate Dependence of the Shear Strength of Mild Steel." *Philos. Mag.* 21 (September 2013): 63–82.

Canovic, S, T Jonsson, and M Halvarsson. 2008. "Grain Contrast Imaging in FIB and SEM." *Journal of Physics: Conference Series* 126 (EMAG 2007): 012054. doi:10.1088/1742-6596/126/1/012054.

Capdevila, C., Y. L. Chen, a. R. Jones, and H. K. D. H. Bhadeshia. 2003. "Grain Boundary Mobility in Fe-Base Oxide Dispersion Strengthened PM2000 Alloy." *ISIJ International* 43 (5): 777–83. doi:10.2355/isijinternational.43.777.

Chen, Yong-jun, Jarle Hjelen, and Hans J. Roven. 2012. "Application of EBSD Technique to Ultrafine Grained and Nanostructured Materials Processed by Severe Plastic Deformation: Sample Preparation, Parameters Optimization and Analysis." *Transactions of Nonferrous Metals Society of China* 22 (8): 1801–9. doi:10.1016/S1003-6326(11)61390-3.

Childs, T. H C. 2013. "Ductile Shear Failure Damage Modelling and Predicting Built-up Edge in Steel Machining." *Journal of Materials Processing Technology* 213 (11). Elsevier B.V.: 1954–69. doi:10.1016/j.jmatprotec.2013.05.017.

Childs, T.H.C., K. Maekawa, T. Obikawa, and Y. Yamane. 2000. *Metal Machining, Theory and Applications*. Elsevier.

Constantinides, Georgios, and Franz-Josef Ulm. 2004. "The Effect of Two Types of C-S-H on the Elasticity of Cement-Based Materials: Results from Nanoindentation and Micromechanical Modeling." *Cement and Concrete Research* 34 (1): 67–80. doi:10.1016/S0008-8846(03)00230-8.

Courbon, C., T. Mabrouki, J. Rech, D. Mazuyer, F. Perrard, and E. D'Eramo. 2013. "Towards a Physical FE Modelling of a Dry Cutting Operation: Influence of Dynamic Recrystallization When Machining AISI 1045." *Procedia CIRP* 8: 516–21. doi:10.1016/j.procir.2013.06.143.

Courbon, C., T. Mabrouki, J. Rech, D. Mazuyer, F. Perrard, and E. D'Eramo. 2014. "Further Insight into the Chip Formation of Ferritic-Pearlitic Steels: Microstructural Evolutions

and Associated Thermo-Mechanical Loadings.” *International Journal of Machine Tools and Manufacture* 77. Elsevier: 34–46. doi:10.1016/j.ijmachtools.2013.10.010.

Courtney, Thomas H. 2005. *Mechanical Behavior of Materials*. Waveland Press.

Da Silva, Marcio Bacci. 1998. “LUBRICATION IN METAL CUTTING UNDER BUILT-UP EDGE CONDITIONS.” University of Warwick.

Davis, Joseph R. 2001. “Aluminum and Aluminum Alloys.” In *Alloying: Understanding the Basics*, 351–416. ASM International. doi:10.1361/autb2001p351.

Demir, Eralp, and Dierk Raabe. 2010. “Mechanical and Microstructural Single-Crystal Bauschinger Effects: Observation of Reversible Plasticity in Copper during Bending.” *Acta Materialia* 58 (18). Acta Materialia Inc.: 6055–63. doi:10.1016/j.actamat.2010.07.023.

Demir, Eralp, Dierk Raabe, and Franz Roters. 2010. “The Mechanical Size Effect as a Mean-Field Breakdown Phenomenon: Example of Microscale Single Crystal Beam Bending.” *Acta Materialia* 58 (5). Acta Materialia Inc.: 1876–86. doi:10.1016/j.actamat.2009.11.031.

Ducobu, François, Enrico Filippi, and Edouard Riviere. 2009. “Chip Formation and Minimum Chip Thickness in Micro-Milling.”

Durst, Karsten, Björn Backes, Oliver Franke, and Mathias Göken. 2006. “Indentation Size Effect in Metallic Materials: Modeling Strength from Pop-in to Macroscopic Hardness Using Geometrically Necessary Dislocations.” *Acta Materialia* 54 (9): 2547–55. doi:10.1016/j.actamat.2006.01.036.

Durst, Karsten, G Mathias, and George M Pharr. 2008. “Indentation Size Effect in Spherical and Pyramidal Indentations.” *Journal of Physics D: Applied Physics* 074005. doi:10.1088/0022-3727/41/7/074005.

Elsey, Matt, Selim Esedo, and Peter Smereka. 2009. “Diffusion Generated Motion for Recrystallization and Grain Growth,” no. 2: 1–24.

Ernst, H., and M. E. Merchant. 1941. “Chip Formation, Friction, and High Quality Machined Surfaces.” *American Society of Metals* 29: 299–378.

Espinosa-Zúrñiga, L A, F A Pérez-González, O Zapata, N F Garza-Montes-de-la-Oca, and S Haro. 2016. “Surface Quality Evaluation of Hot Deformed Aluminum.” *Materials Research Society* 1816. doi:10.1557/opl.2016.63.

Eurostat, European Union. 2016. “Archive : Manufacture of Fabricated Metal Products Statistics - NACE Rev . 2,” no. April 2013: 1–9. http://ec.europa.eu/eurostat/statistics-explained/index.php?title=Manufacture_of_fabricated_metal_products_statistics_-_NACE_Rev._2&oldid=249508.

Fang, Fengzhou, Bing Liu, and Zongwei Xu. 2015. “Nanometric Cutting in a Scanning Electron Microscope.” *Precision Engineering* 41. Elsevier Inc.: 145–52.

doi:10.1016/j.precisioneng.2015.01.009.

Faverjon, Pierre, Joël Rech, and René Leroy. 2013. “Influence of Minimum Quantity Lubrication on Friction Coefficient and Work-Material Adhesion During Machining of Cast Aluminum With Various Cutting Tool Substrates Made of Polycrystalline Diamond , High Speed Steel , and Carbides.” *Journal of Tribology* 135 (October): 1–8. doi:10.1115/1.4024546.

Fibics-Incorporated. 2016. “Grain Orientation Contrast.” http://www.fibics.com/fib/tutorials/grain-orientation-contrast/6/.

Fritz, R., V. Maier-Kiener, D. Lutz, and D. Kiener. 2016. “Interplay between Sample Size and Grain Size: Single Crystalline vs. Ultrafine-Grained Chromium Micropillars.” *Materials Science and Engineering: A* 674. Elsevier: 626–33. doi:10.1016/j.msea.2016.08.015.

Frost, H J, and M F Ashby. 1982. *Deformation-Mechanism Maps : The Plasticity and Creep of Metals and Ceramics*. Edited by Oxford. Oxford [Oxfordshire]; New York: Pergamon Press.

Ghomi, Homa Mostaghimi, and Akindele G. Odeshi. 2012. “The Effects of Microstructure, Strain Rates and Geometry on Dynamic Impact Response of a Carbon-Manganese Steel.” *Materials Science and Engineering A* 532. Elsevier B.V.: 308–15. doi:10.1016/j.msea.2011.10.096.

Giallonardo, J.D., U. Erb, K.T. Aust, and G. Palumbo. 2011. “The Influence of Grain Size and Texture on the Young’s Modulus of Nanocrystalline Nickel and Nickel–Iron Alloys.” *Philosophical Magazine* 91 (36): 4594–4605. doi:10.1080/14786435.2011.615350.

Goel, Saurav, Xichun Luo, Anupam Agrawal, and Robert L. Reuben. 2015. “Diamond Machining of Silicon: A Review of Advances in Molecular Dynamics Simulation.” *International Journal of Machine Tools and Manufacture* 88. Elsevier: 131–64. doi:10.1016/j.ijmachtools.2014.09.013.

Goldstein, Joseph, Charles E Lyman, Dale E Newbury, Eric Lifshin, Patrick Echlin, David C Joy, and Joseph R Michael. 2003. *Scanning Electron Microscopy and X-Ray Microanalysis*. 3rd ed.

Goponenko, A. 2014. “Berkovich Tip.” *Biomechanics, Biomaterials and Biomedicine Instrumentation Facility.* http://bm3.unl.edu/hysitron-nanoindenter.

Gornostyrev, Yu N, and M I Katsnelson. 2015. “Misfit Stabilized Embedded Nanoparticles in Metallic Alloys.” *Physical Chemistry Chemical Physics* 17. Royal Society of Chemistry: 27249–57. doi:10.1039/C5CP04641F.

Gottstein, G, E Brunger, M Frommert, M Goerdeler, and M Zeng. 2003. “Prediction of the Critical Conditions for Dynamic Recrystallization in Metals.” *Zeitschrift Fur Metallkunde* 94 (5): 628–35.

Greer, Julia R, and Jeff Th.M De Hosson. 2011. “Plasticity in Small-Sized Metallic Systems : Intrinsic versus Extrinsic Size Effect.” *Progress in Materials Science* 56 (6). Elsevier Ltd: 654–724. doi:10.1016/j.pmatsci.2011.01.005.

Grewer, M., and R. Birringer. 2014. “Shear Shuffling Governs Plastic Flow in Nanocrystalline Metals: An Analysis of Thermal Activation Parameters.” *Physical Review B - Condensed Matter and Materials Physics* 89 (18): 1–8. doi:10.1103/PhysRevB.89.184108.

Griffiths, B. J. 1987. “Mechanisms of White Layer Generation With Reference to Machining and Deformation Processes.” *Journal of Tribology* 109 (86): 525. doi:10.1115/1.3261495.

Guinier, André. 1938. “Structure of Age-Hardening Aluminium-Copper Alloys.” *Nature* 142: 569–70. doi:10.1038/142569b0.

Gunsteren, Wilfred F Van, and Alan E Mark. 1998. “Validation of Molecular Dynamics Simulation.” *Journal of Chemical Physics* 108 (15). doi:10.1063/1.476021.

Guo-zheng, Quan. 2013. “Characterization for Dynamic Recrystallization Kinetics Based on Stress-Strain Curves.” *Recent Developments in the Study of Recrystallization*, 61–64. doi:10.5772/54285.

Guo, Wei, Eric Jägle, Jiahao Yao, Verena Maier, Sandra Korte-Kerzel, Jochen M. Schneider, and Dierk Raabe. 2014. “Intrinsic and Extrinsic Size Effects in the Deformation of Amorphous CuZr / Nanocrystalline Cu Nanolaminates.” *Acta Materialia* 80: 94–106. doi:10.1016/j.actamat.2014.07.027.

Guo, Yang, W Dale Compton, and Srinivasan Chandrasekar. 2015. “In Situ Analysis of Flow Dynamics and Deformation Fields in Cutting and Sliding of Metals.” *Proceeding of the Royal Society A* 471. doi:http://dx.doi.org/10.1098/rspa.2015.0194 or.

Hall, E O. 1951. “The Deformation and Ageing of Mild Steel: III Discussion of Results.” *Proceedings of the Physical Society. Section B* 64 (9): 747. http://stacks.iop.org/0370-1301/64/i=9/a=303.

Haušild, P., a. Materna, and J. Nohava. 2013. “Characterization of Anisotropy in Hardness and Indentation Modulus by Nanoindentation.” *Metallography, Microstructure, and Analysis* 3 (1): 5–10. doi:10.1007/s13632-013-0110-8.

Heo, Sung Jung. 2004. “Micro Cutting of Tungsten Carbides with SEM Direct Observation Method.” *KSME International Journal* 18 (5): 770–79.

———. 2008. “Environmentally Conscious Hard Turning of Cemented Carbide Materials on the Basis of Micro-Cutting in SEM : Stressing Four Kinds of Cemented Carbides with PCD Tools.” *Journal of Mechanical Science and Technology* 22 (7). Elsevier B.V.: 1383–90. doi:10.1007/s12206-008-0411-z.

Hines, J a, and J a Hines. 1997. “Recrystallization Kinetics within Shear Bands Adiabatic.”

Acta Metallurgica 45 (2): 635–49.

Hosford, William F. 2010. “Mechanical Behavior of Materials.” In *Mechanical Behavior of Materials*, Second edi, 419. Cambridge university press.

Inamura, T, and N Takezawa. 1992. “Atomic-Scale Cutting in a Computer Using Crystal Models of Copper and Diamond.” *CIRP Annals - Manufacturing Technology* 41 (1): 121–24.

Iwata, Kazuaki, and Kanji Ueda. 1980. “Fundamental Analysis of the Mechanism of Built-up Edge Formation Based on Direct Scanning Electron Microscope Observation.” *Wear* 60: 329–31.

Jaspers, S. P F C, and J. H. Dautzenberg. 2002. “Material Behaviour in Metal Cutting: Strains, Strain Rates and Temperatures in Chip Formation.” *Journal of Materials Processing Technology* 121 (1): 123–35. doi:10.1016/S0924-0136(01)01227-4.

Kato, Koichi, Tomoki Nakayoshi, Shuichi Fukuyoshi, Eiji Kurimoto, and Akifumi Oda. 2017. “Validation of Molecular Dynamics Simulations for Prediction of Three-Dimensional Structures of Small Proteins.” *Molecules* 22 (1716). doi:10.3390/molecules22101716.

Kim, Jeong-Du, and Chan-Hong Moon. 1996. “A Study on the Cutting Mechanism of Microcutting Using Molecular Dynamics.” *The International Journal of Advanced Manufacturing Lechnology*, 319–24.

Klocke, F., L. Hensgen, A. Klink, J. Mayer, and A. Schwedt. 2014. “EBSD-Analysis of Flexure Hinges Surface Integrity Evolution via Wire-EDM Main and Trim Cut Technologies.” *Procedia CIRP* 13: 237–42. doi:10.1016/j.procir.2014.04.041.

Kümmel, Johannes, Jens Gibmeier, Erich Müller, Reinhard Schneider, Volker Schulze, and Alexander Wanner. 2014. “Detailed Analysis of Microstructure of Intentionally Formed Built-up Edges for Improving Wear Behaviour in Dry Metal Cutting Process of Steel.” *Wear* 311 (1–2). Elsevier: 21–30. doi:10.1016/j.wear.2013.12.012.

Kuo, Chen-Ming, and Chih-Sheng Lin. 2007. “Static Recovery Activation Energy of Pure Copper at Room Temperature.” *Scripta Materialia* 57 (8): 667–70. doi:10.1016/j.scriptamat.2007.06.054.

Landau, P., S. Osovski, A. Venkert, V. Gartnerova, and D. Rittel. 2016. “The Genesis of Adiabatic Shear Bands.” *Scientific Reports* 6. Nature Publishing Group: 3726. doi:10.1038/srep37226.

Larsen, Peter Mahler, Søren Schmidt, and Jakob Schiøtz. 2016. “Robust Structural Identification via Polyhedral Template Matching.” *Modelling and Simulation in Materials Science and Engineering* 24.

Lee, Seongeyl, Jihong Hwang, M. Ravi Shankar, Srinivasan Chandrasekar, and W. Compton. 2006. “Large Strain Deformation Field in Machining.” *Metallurgical and Materials Transactions A* 37 (5): 1633–43. doi:10.1007/s11661-006-0105-z.

Li, Yujiao, Dierk Raabe, Michael Herbig, Pyuck-Pa Choi, Shoji Goto, Aleksander Kostka, Hiroshi Yarita, Christine Borchers, and Reiner Kirchheim. 2014. “Segregation Stabilizes Nanocrystalline Bulk Steel with Near Theoretical Strength.” *Physical Review Letters* 113 (September): 1–5. doi:10.1103/PhysRevLett.113.106104.

Liao, Zhirong, Dragos Axinte, Maxime Mieszala, Rachid M’Saoubi, Ali Abelhafeez, Johann Michler, and Mark Hardy. 2018. “On the in Fl Uence of Gamma Prime upon Machining of Advanced Nickel Based Superalloy.” *CIRP Annals - Manufacturing Technology* 1730. CIRP: 1–4. doi:10.1016/j.cirp.2018.03.021.

List, G., G. Sutter, X.F. Bi, A. Molinari, and A. Bouthiche. 2013. “Strain, Strain Rate and Velocity Fields Determination at Very High Cutting Speed.” *Journal of Materials Processing Technology* 213 (5): 693–99. doi:10.1016/j.jmatprotec.2012.11.021.

Ma, A., F. Roters, and D. Raabe. 2006. “On the Consideration of Interactions between Dislocations and Grain Boundaries in Crystal Plasticity Finite Element Modeling – Theory, Experiments, and Simulations.” *Acta Materialia* 54 (8): 2181–94. doi:10.1016/j.actamat.2006.01.004.

Maekawa, K., and a. Itoh. 1995. “Friction and Tool Wear in Nano-Scale Machining—a Molecular Dynamics Approach.” *Wear* 188 (1–2): 115–22. doi:10.1016/0043-1648(95)06633-0.

Maitland, Tim, and Scott Sitzman. 2006. “Electron Backscatter Diffraction (EBSD) Technique and Materials Characterization Examples.” In *Scanning Microscopy for Nanotechnology, Techniques and Applications*, edited by Weilie Zhou and Zhong Lin Wang, First edit, 41–76.

Melkote, Shreyes N, Wit Grzesik, Jose Outeiro, Joel Rech, Volker Schulze, Helmi Attia, P Arrazola, Rachid M’Saoubi, and Christopher Saldana. 2017. “Advances in Material and Friction Data for Modelling of Metal Machining.” *CIRP Annals - Manufacturing Technology* 66 (2). CIRP: 731–54. doi:10.1016/j.cirp.2017.05.002.

Mendelev, M I, M J Kramer, C A Becker, and M Asta. 2008. “Analysis of Semi-Empirical Interatomic Potentials Appropriate for Simulation of Crystalline and Liquid Al and Cu.” *Philosophical Magazine* 88 (12). Taylor & Francis: 1723–50. doi:10.1080/14786430802206482.

Merchant, M Eugene. 1945. “Mechanics of the Metal Cutting Process. I. Orthogonal Cutting and a Type 2 Chip.” *Journal of Applied Physics* 16 (5): 267–75. doi:10.1063/1.1707586.

Meyers, M. A., Y. B. Xu, Q. Xue, M. T. Pérez-Prado, and T. R. McNelley. 2003. “Microstructural Evolution in Adiabatic Shear Localization in Stainless Steel.” *Acta Materialia* 51 (5): 1307–25. doi:10.1016/S1359-6454(02)00526-8.

Modi, O P, N Deshmukh, D P Mondal, A K Jha, A H Yegneswaran, and H K Khaira. 2001.

"Effect of Interlamellar Spacing on the Mechanical Properties of 0 . 65 % C Steel." *Materials Characterization* 46: 347–52.

Morse, Philip M. 1929. "Diatomic Molecules According to the Wave Mechanics. II. Vibrational Levels." *Phys. Rev.* 34 (1). American Physical Society: 57–64. doi:10.1103/PhysRev.34.57.

Mukhopadhyay, Sharmila M. 2003. *Sample Preparation for Microscopic and Spectroscopic Characterization of Solid Surfaces and Films*.

Nematollahi, Gh. Ali, Blazej Grabowski, Dierk Raabe, and Jörg Neugebauer. 2016. "Multiscale Description of Carbon-Supersaturated Ferrite in Severely Drawn Pearlitic Wires." *Acta Materialia* 111: 321–34. doi:10.1016/j.actamat.2016.03.052.

Nix, William D, and Huajian Gao. 1998. "Indentation Size Effects in Crystalline Materials: A Law for Strain Gadient Plasticy." *Journal of the Mechanics and Physics of Solids* 46 (3).

Oliver, W.C., and G.M. Pharr. 2011. "Measurement of Hardness and Elastic Modulus by Instrumented Indentation: Advances in Understanding and Refinements to Methodology." *Journal of Materials Research* 19 (01): 3–20. doi:10.1557/jmr.2004.19.1.3.

Osovski, S., D. Rittel, P. Landau, and A. Venkert. 2012. "Microstructural Effects on Adiabatic Shear Band Formation." *Scripta Materialia* 66 (1). Acta Materialia Inc.: 9–12. doi:10.1016/j.scriptamat.2011.09.014.

Oxley, P.L.B. 1961. "Mechanics of Metal Cutting." *International Journal of Machine Tool Design and Research* 1 (1–2): 89–97. doi:10.1016/0020-7357(61)90046-4.

Pande, C S, and K P Cooper. 2009. "Progress in Materials Science Nanomechanics of Hall – Petch Relationship in Nanocrystalline Materials." *Progress in Materials Science* 54 (6). Elsevier Ltd: 689–706. doi:10.1016/j.pmatsci.2009.03.008.

Pardal, J.M., S.S.M. Tavares, M. Cindra Fonseca, J.A. de Souza, R.R.A. Côrte, and H.F.G. de Abreu. 2009. "Influence of the Grain Size on Deleterious Phase Precipitation in Superduplex Stainless Steel UNS S32750." *Materials Characterization* 60 (3): 165–72. doi:10.1016/j.matchar.2008.08.007.

Pei, Q. X., C. Lu, F. Z. Fang, and H. Wu. 2006. "Nanometric Cutting of Copper: A Molecular Dynamics Study." *Computational Materials Science* 37 (4): 434–41. doi:10.1016/j.commatsci.2005.10.006.

Pei, Q. X., C. Lu, and H. P. Lee. 2007. "Large Scale Molecular Dynamics Study of Nanometric Machining of Copper." *Computational Materials Science* 41 (2): 177–85. doi:10.1016/j.commatsci.2007.04.008.

Piispanen, Väinö. 1948. "Theory of Formation of Metal Chips." *Journal of Applied Physics* 19 (10): 876–81. doi:10.1063/1.1697893.

Plimpton, Steve. 1995. “Fast Parallel Algorithms for Short – Range Molecular Dynamics.” *Journal of Computational Physics* 117 (March): 1–42.

Plimpton, Steve, Aidan Thompson, Stan Moore, and Axel Kohlmeyer. 2018. “LAMMPS Manual.”

Podgornik, B., S. Hogmark, and O. Sandberg. 2004. “Influence of Surface Roughness and Coating Type on the Galling Properties of Coated Forming Tool Steel.” *Surface and Coatings Technology* 184 (2–3): 338–48. doi:10.1016/j.surfcoat.2003.11.002.

Preston, G. D. 1938. “The Difraction of X-Rays by Age-Hardening Aluminium Copper Alloys.” *Proceeding of the Royal Society A* 167 (931): 526–38. doi:10.1098/rspa.1938.0152.

Pu, C. L., G. Zhu, S. B. Yang, E. B. Yue, and S. V. Subramanian. 2016. “Effect of Dynamic Recrystallization at Tool-Chip Interface on Accelerating Tool Wear during High-Speed Cutting of AISI1045 Steel.” *International Journal of Machine Tools and Manufacture* 100: 72–80. doi:10.1016/j.ijmachtools.2015.10.006.

Püschl, W. 2002. “Models for Dislocation Cross-Slip in Close-Packed Crystal Structures : A Critical Review.” *Progress in Materials Science* 47: 415–61.

Rech, J., P. J. Arrazola, C. Claudin, C. Courbon, F. Pusavec, and J. Kopac. 2013. “Characterisation of Friction and Heat Partition Coefficients at the Tool-Work Material Interface in Cutting.” *CIRP Annals - Manufacturing Technology* 62 (1). CIRP: 79–82. doi:10.1016/j.cirp.2013.03.099.

Rittel, D., P. Landau, and a. Venkert. 2008. “Dynamic Recrystallization as a Potential Cause for Adiabatic Shear Failure.” *Physical Review Letters* 101 (16): 2–5. doi:10.1103/PhysRevLett.101.165501.

Saez-de-Buruaga, M., J.A. Esnaola, P. Aristimuno, D. Soler, T. Björk, and P.J. Arrazola. 2017. “A Coupled Eulerian Lagrangian Model to Predict Fundamental Process Variables and Wear Rate on Ferrite-Pearlite Steels.” *Procedia CIRP* 58. The Author(s): 251–56. doi:10.1016/j.procir.2017.03.194.

Sakai, Taku, Andrey Belyakov, Rustam Kaibyshev, Hiromi Miura, and John J Jonas. 2014. “Dynamic and Post-Dynamic Recrystallization under Hot , Cold and Severe Plastic Deformation Conditions.” *Progress in Materials Science* 60. Elsevier Ltd: 130–207. doi:10.1016/j.pmatsci.2013.09.002.

Sarwar, Mohammed, Martin Persson, Hakan Hellbergh, and Julfikar Haider. 2009. “Measurement of Specific Cutting Energy for Evaluating the Efficiency of Bandsawing Different Workpiece Materials.” *International Journal of Machine Tools and Manufacture* 49: 958–65. doi:10.1016/j.ijmachtools.2009.06.008.

Schönecker, Stephan, Xiaoqing Li, Börje Johansson, Se Kyun Kwon, and Levente Vitos. 2015. “Thermal Surface Free Energy and Stress of Iron.” *Scientific Reports* 5. Nature

Publishing Group: 14860. doi:10.1038/srep14860.

Seker, Ulvi, Abdullah Kurt, and Ibrahim Çiftçi. 2004. “The Effect of Feed Rate on the Cutting Forces When Machining with Linear Motion.” *Journal of Materials Processing Technology* 146 (3): 403–7. doi:10.1016/j.jmatprotec.2003.12.001.

Simoneau, A., E. Ng, and M.A. Elbestawi. 2006. “Chip Formation during Microscale Cutting of a Medium Carbon Steel.” *International Journal of Machine Tools and Manufacture* 46 (5): 467–81. doi:10.1016/j.ijmachtools.2005.07.019.

Sneddon, I A N N. 1965. “The Relaxation between Load and Penetration in the Axisymetric Boussinesq Problem for a Puch of Arbitrary Profile.” *International Journal of Engineering Science* 3 (638): 47–57.

Soler, D, P X Aristimuño, M Saez-de-Buruaga, A Garay, and P J Arrazola. 2018. “New Calibration Method to Measure Rake Face Temperature of the Tool during Dry Orthogonal Cutting Using Thermography.” *Applied Thermal Engineering*. doi:10.1016/j.applthermaleng.2018.03.056.

Soler, Daniel, Patxi Aristimuño, Ainhara Garay, and Pedro J. Arrazola. 2015. “Uncertainty of Temperature Measurements in Dry Orthogonal Cutting of Titanium Alloys.” *Infrared Physics & Technology* 71. Elsevier B.V.: 208–16. doi:10.1016/j.infrared.2015.04.001.

Stukowski, Alexander. 2010. “Visualization and Analysis of Atomistic Simulation Data with OVITO–the Open Visualization Tool.” *Modelling and Simulation in Materials Science and Engineering* 18 (1): 15012. http://stacks.iop.org/0965-0393/18/i=1/a=015012.

Stüwe, H P, A F Padilha, and F Siciliano Jr. 2002. “Competition between Recovery and Recrystallization.” *Materials Science and Engineering A* 333: 361–67.

Subramanian, S. V., H. O. Gekonde, G. Zhu, and X. Zhang. 2002. “Role of Microstructural Softening Events in Metal Cutting.” *Machining Science and Technology* 6 (3): 353–64. doi:10.1081/MST-120016250.

Sutherland, John W. 2016. “Mechanics of Machining.” Accessed January 1. http://www.mfg.mtu.edu/cyberman/machining/intro/mechanics/introduction.html.

Szabó, Peter J, and Attila Bonyár. 2012. “Effect of Grain Orientation on Chemical Etching.” *Micron (Oxford, England : 1993)* 43 (2–3): 349–51. doi:10.1016/j.micron.2011.09.015.

Taheri, M. L., D. Molodov, G. Gottstein, a. D. Rollett, Y. Huang, and F. J. Humphreys. 2005. “Grain Boundary Mobility under a Stored-Energy Driving Force: A Comparison to Curvature-Driven Boundary Migration.” *Zeitschrift Für Metallkunde* 96 (7): 1166–70. doi:10.3139/146.101157.

Tomac, N., K. Tonnessen, F.O. Rasch, and T. Mikac. 2005. “A Study of Factors That Affect the Build-Up Material Formation.” *Adavanced Manufacturing Systems and Technology*, no. 486.

Torrents Abad, Oscar, Jeffrey M. Wheeler, Johann Michler, Andreas S. Schneider, and

Eduard Arzt. 2016. “Temperature-Dependent Size Effects on the Strength of Ta and W Micropillars.” *Acta Materialia* 103. Elsevier Ltd: 483–94. doi:10.1016/j.actamat.2015.10.016.

University of Iowa. 2016. “Scanning Electron Microscopy.” http://cmrf.research.uiowa.edu/scanning-electron-microscopy.

Wallbank, J. 1979. “Structure of Built-up Edge Formed in Metal Cutting.” *Metals Technology* 6 (1): 145–53. doi:10.1179/030716979803276426.

Wang, Bing, Zhanqiang Liu, Guosheng Su, Qinghua Song, and Xing Ai. 2015. “Investigations of Critical Cutting Speed and Ductile-to-Brittle Transition Mechanism for Workpiece Material in Ultra-High Speed Machining.” *International Journal of Mechanical Sciences* 104. Elsevier: 44–59. doi:10.1016/j.ijmecsci.2015.10.004.

Weber, M, H Autenrieth, J Kotschenreuther, P Gumbsch, V Schulze, and J Fleischer. 2008. “Influence of Friction and Process Parameters on the Specific Cutting Force and Surface Characteristicsin Micro Cutting.” *Machining Science and Technology*, no. January 2015: 37–41. doi:10.1080/10910340802518728.

Woon, Keng Soon, and Mustafizur Rahman. 2010. “The Effect of Tool Edge Radius on the Chip Formation Behavior of Tool-Based Micromachining.” *International Journal of Advanced Manufacturing Technology*, 961–77. doi:10.1007/s00170-010-2574-x.

Wright, S, M Nowell, and D P Field. 2011. “A Review of Strain Analysis Using EBSD.” Microscopy and microanalysis.

Yang, J, J J Roa, M Schwind, M Odén, M P Johansson-Jõesaar, J Esteve, and L Llanes. 2016. “Thermally Induced Surface Integrity Changes of Ground WC-Co Hardmetals.” *Procedia CIRP* 45. Elsevier B.V.: 91–94. doi:http://dx.doi.org/10.1016/j.procir.2016.02.092.

Yao, Hai Yan, Guo Hong Yun, and Wen Liang Fan. 2013. “Size Effect of the Elastic Modulus of Rectangular Nanobeams: Surface Elasticity Effect.” *Chinese Physics B* 22 (10): 1–5. doi:10.1088/1674-1056/22/10/106201.

Yao, Nan. 2007. *FOCUSED ION BEAM SYSTEMS Basics and Applications*. Cambridge university press.

Ye, G.G., Y. Chen, S.F. Xue, and L.H. Dai. 2014. “Critical Cutting Speed for Onset of Serrated Chip Flow in High Speed Machining.” *International Journal of Machine Tools and Manufacture* 86: 18–33. doi:10.1016/j.ijmachtools.2014.06.006.

Ye, G.G., S.F. Xue, M.Q. Jiang, X.H. Tong, and L.H. Dai. 2013. “Modeling Periodic Adiabatic Shear Band Evolution during High Speed Machining Ti-6Al-4V Alloy.” *International Journal of Plasticity* 40: 39–55. doi:10.1016/j.ijplas.2012.07.001.

Ye, G.G., S.F. Xue, W. Ma, M.Q. Jiang, Z. Ling, X.H. Tong, and L.H. Dai. 2012. “Cutting AISI 1045 Steel at Very High Speeds.” *International Journal of Machine Tools and*

Manufacture 56 (May): 1–9. doi:10.1016/j.ijmachtools.2011.12.009.

Zhang, Xiaodan, Andy Godfrey, Xiaoxu Huang, Niels Hansen, and Qing Liu. 2011. "Microstructure and Strengthening Mechanisms in Cold-Drawn Pearlitic Steel Wire." *Acta Materialia* 59 (9). Acta Materialia Inc.: 3422–30. doi:10.1016/j.actamat.2011.02.017.

Zorev, Nikolaĭ Nikolaevich. 1966. *Metal Cutting Mechanics*. Pergamon Press Inc.

Appendix A

Estimation of the thickness of DRX layer

The existence of DRX was evaluated based on the criterion of equiaxiality, which (in order to avoid complicated and not robust grain shape analysis) was reformulated in terms of equivalent representation of every direction of the grain boundaries. Figure A1 represents a raw ion beam image of the cross-section of the chip cut at 100 m/min, the rake surface is at the bottom of the image. Figure A2 represents the grain boundaries refined from this image by Sobel function.

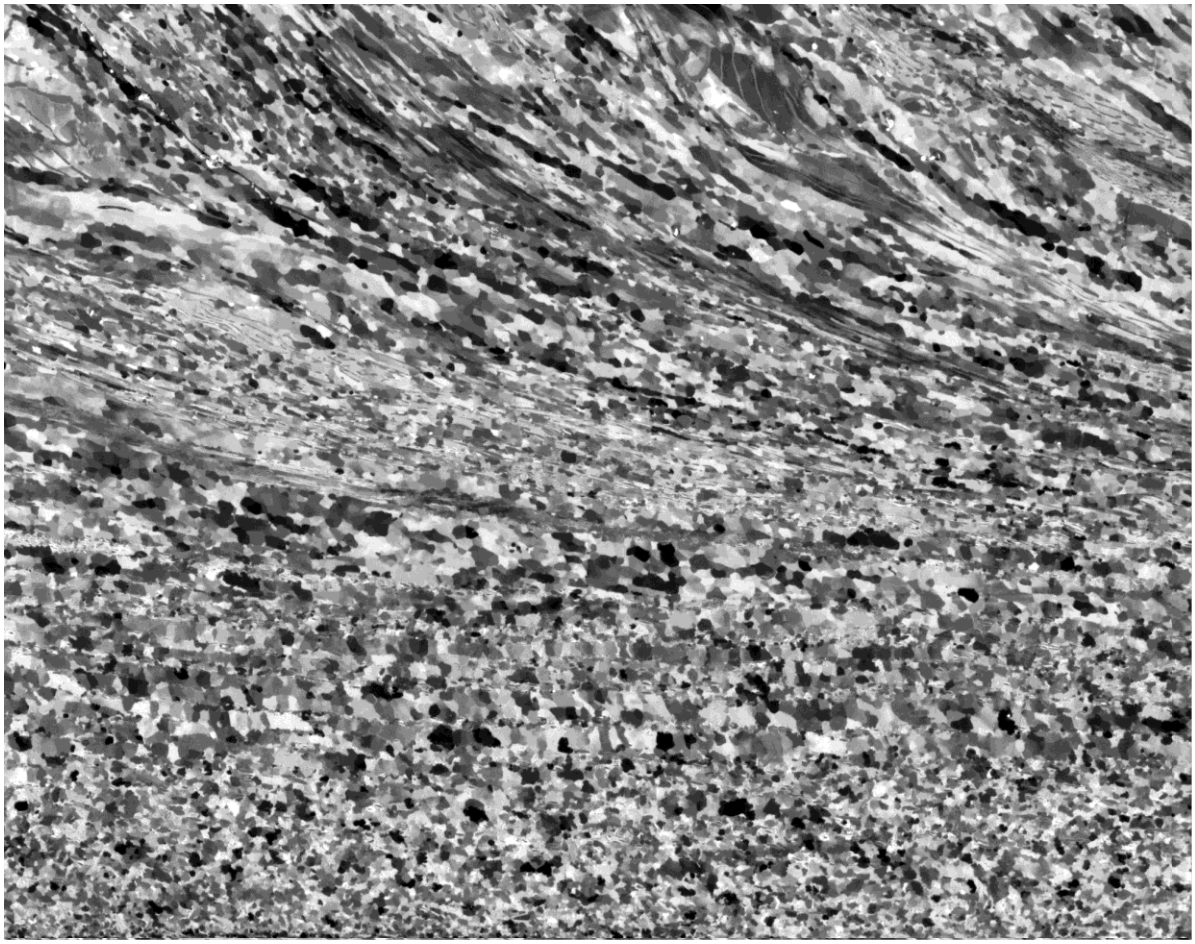

Figure A1. Ion beam image of the cross-section of the chip cut at 100 m/min.

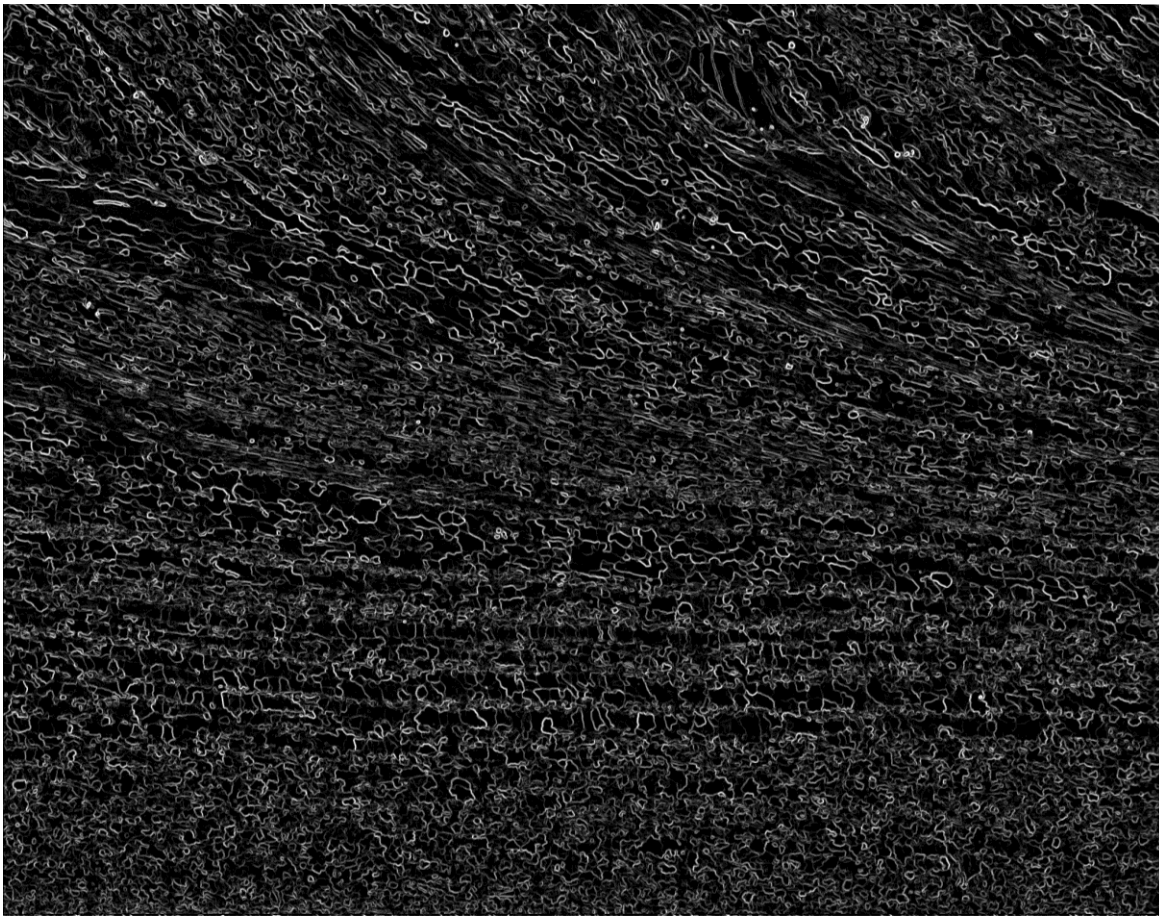

Figure A2. Sobel function applied to the image on figure A2.

Thus, obtained image of grain boundaries was processed by local 2D Fourier transformation. Every narrow line on the image produces a sharp line on a Fourier image, which goes in perpendicular direction, see Figure A3 for illustration.

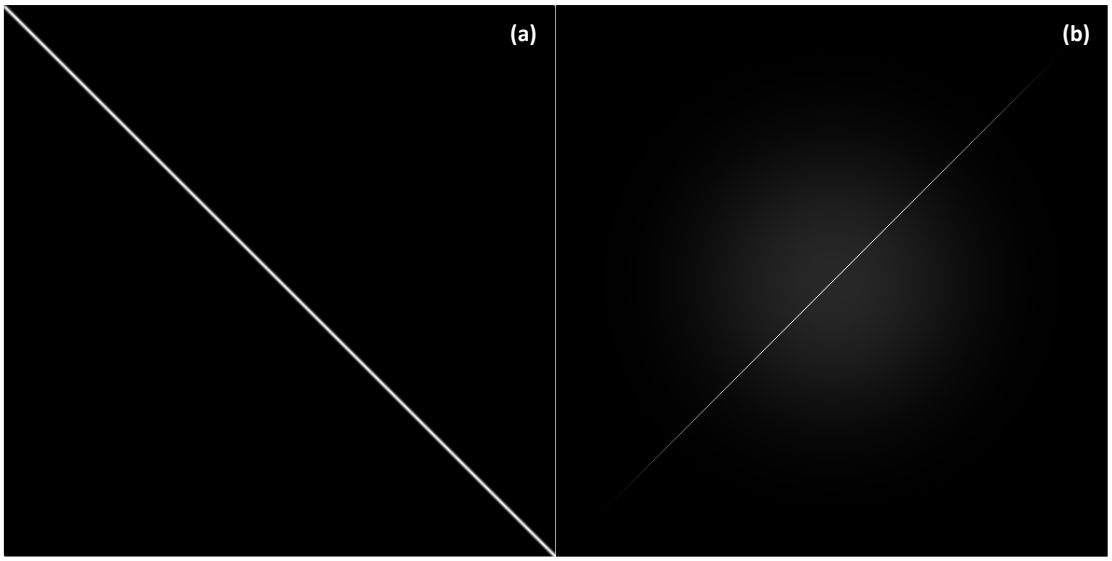

Figure A3. (a) An example image of a narrow line; (b) 2D Fourier transformation of image (a).

If multiple lines are present on the image its Fourier representation will contain multiple stripes going through the center in corresponding directions. Thus analyzing the azimuthal

distribution of intensity one can draw conclusions about average preferential directions of the lines on original image.

Figure A4 demonstrates how such analysis is made (left to right): narrow areas are selected on the image at different depth from the rake surface, 2D Fourier transformation is made from these areas (patterns are shown in the middle of Figure A4), azimuthal intensity distribution is calculated for every Fourier pattern and fitted by cosine function. Color image at the right of Figure A4 shows azimuthal distributions calculated for every depth and assembled in 2D plot. The thickness of DRX layer is clearly visible on this plot as the position where texture maxima start to vanish.

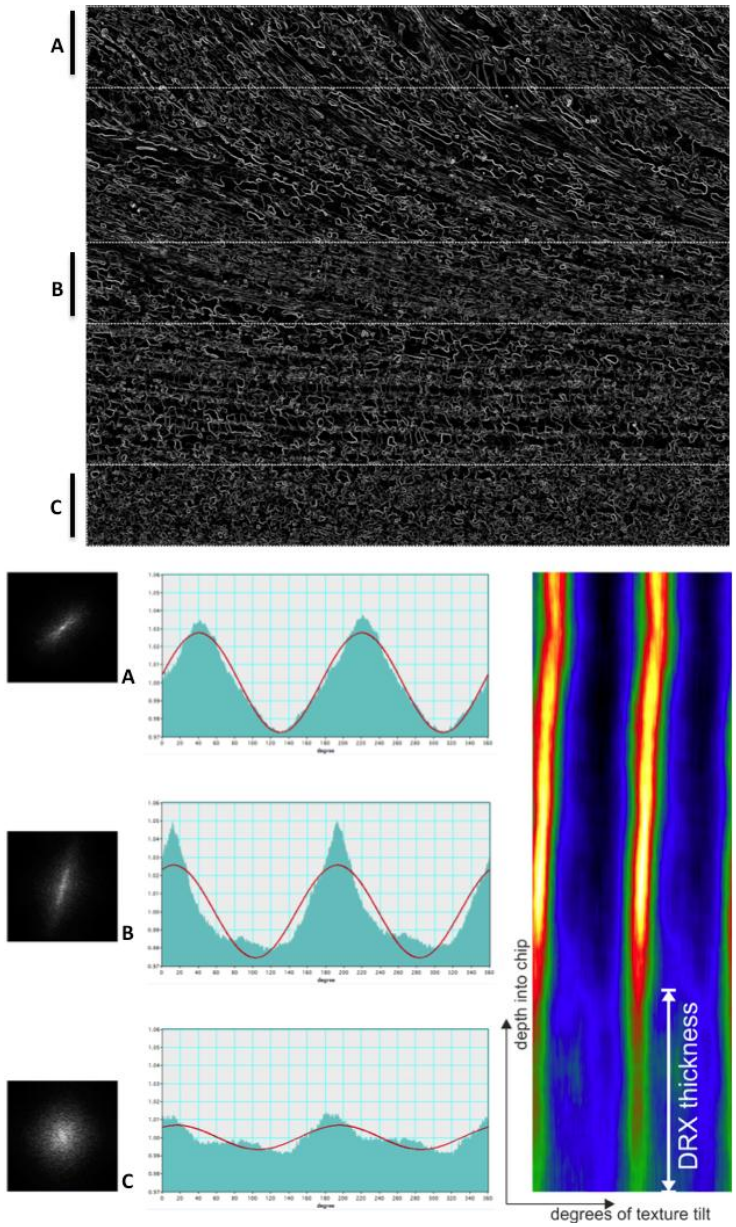

Figure A4. Texture analysis of the images (left to right): Sobel function of raw image for 100 m/min cutting speed with 3 different areas marked; 2D Fourier patterns from marked areas; azimuthal intensity distributions of Fourier patterns (texture plots) scaled to the same intensity limits with fitting cosine functions overlayed in red; 2D assembly of all texture plots for every depth in the chip.

More quantitative estimation can be obtained by plotting amplitude of fitting cosine as a function of depth, see Figure A5.

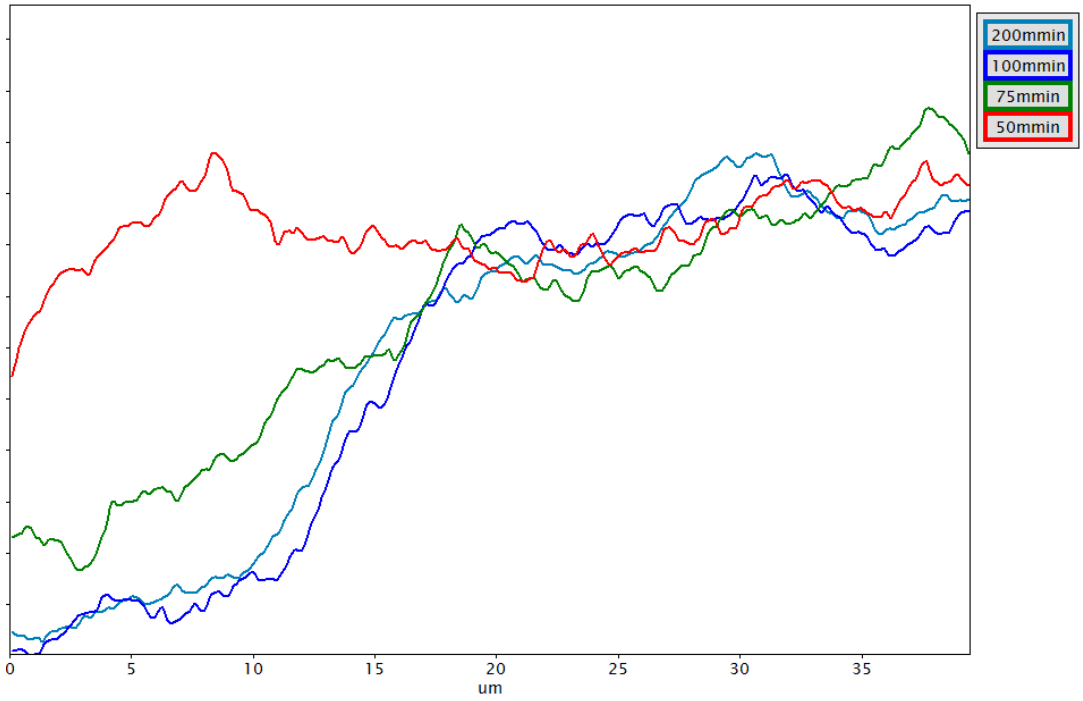

Figure A5. Amplitude of fitting cosine function plotted against the depth into the chip for different cutting speeds.